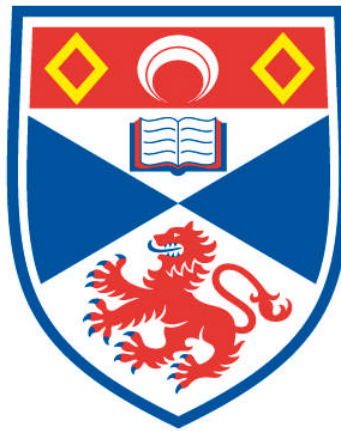


DEVELOPMENT AND CHARACTERISATION OF AN A-SITE DEFICIENT PEROVSKITE AS ALTERNATIVE ANODE MATERIAL FOR SOLID OXIDE FUEL CELLS

Ahmed D. A. Aljaberi

**A Thesis Submitted for the Degree of PhD
at the
University of St Andrews**



2013

**Full metadata for this item is available in
Research@StAndrews:FullText
at:**

<http://research-repository.st-andrews.ac.uk/>

Please use this identifier to cite or link to this item:

<http://hdl.handle.net/10023/3690>

This item is protected by original copyright

**This item is licensed under a
Creative Commons License**

**Development and Characterisation of an A-site
Deficient Perovskite as Alternative Anode
Material for Solid Oxide Fuel Cells**

A thesis submitted for the degree of Ph.D.

by

Ahmed D. A. Aljaberi



University of
St Andrews

University of St Andrews

Supervised by Professor John T. S. Irvine

Submitted in November 2012

Declarations

I, Ahmed D. A. Aljaberi, hereby certify that this thesis, which is approximately 37000 words in length, has been written by me, that it is the record of work carried out by me and that it has not been submitted in any previous application for a higher degree.

I was admitted as a research student in January 2008 and as a candidate for the degree of Ph.D. in January 2009; the higher study for which this is a record was carried out in the University of St Andrews between 2008 and 2012.

Date..... signature of candidate.....

I hereby certify that the candidate has fulfilled the conditions of the Resolution and Regulations appropriate for the degree of Ph.D. in the University of St Andrews and that the candidate is qualified to submit this thesis in application for that degree.

Date..... signature of supervisor.....

In submitting this thesis to the University of St Andrews I understand that I am giving permission for it to be made available for use in accordance with the regulations of the University Library for the time being in force, subject to any copyright vested in the work not being affected thereby. I also understand that the title and the abstract will be published, and that a copy of the work may be made and supplied to any bona fide library or research worker, that my thesis will be electronically accessible for personal or research use unless exempt by award of an embargo as requested below, and that the library has the right to migrate my thesis into new electronic forms as required to ensure continued access to the thesis. I have obtained any third-party copyright permissions that may be required in order to allow such access and migration, or have requested the appropriate embargo below.

The following is an agreed request by candidate and supervisor regarding the electronic publication of this thesis:

Access to printed copy and electronic publication of thesis through the University of St Andrews

Date..... signature of candidate.....

Date..... signature of supervisor.....

Abstract

The research presented in this thesis is a collection of many different, yet connected, parts that stemmed from the development of a new alternative material intended to be utilised as anode material in solid oxide fuel cells. The main part is the research conducted in the development and characterisation of the novel A-site deficient $\text{La}_{0.2}\text{Sr}_{0.7-x}\text{Ca}_x\text{TiO}_3$. Calcium introduction resulted in reducing this perovskite unit cell volume which, at the beginning, enhanced its electrical conductivity in reducing conditions. However, the ideal cubic symmetry could not be maintained, as in the starting material $\text{La}_{0.2}\text{Sr}_{0.7}\text{TiO}_3$, as a result of the increased A-site ionic radius mismatch and two lower symmetries were observed at room temperature. These were the tetragonal $I4/mcm$ for compositions with $0.1 \leq x \leq 0.35$ and orthorhombic $Pbnm$ for those with $0.4 \leq x \leq 0.7$. Neutron powder diffraction (NPD) studies conducted at elevated temperatures, up to 900°C , showed that the orthorhombic samples transformed into higher symmetries with $Pbnm \rightarrow I4/mcm \rightarrow Pm3-m$ phase transitions. Detailed crystallographic analysis is discussed; where the different unit cells showed changes to the tilts of the BO_6 octahedra, along with small distortions to these octahedra. DC conductivity measurements showed a high electrical conductivity of 27.5 S/cm for a pre-reduced composition of $\text{La}_{0.2}\text{Sr}_{0.25}\text{Ca}_{0.45}\text{TiO}_3$ at 900°C and $p\text{O}_2 = 10^{-19} \text{ atm}$. This material showed very encouraging features which makes it a very promising anode material for SOFCs.

A study was also done which explores the best renewable energy options for the United Arab Emirates given its local climate and other aspects. The reliance on seawater desalination is argued to be un-sustainable for different reasons. Thus, water security

should be a main element in the planning process for adopting renewable energy technologies. A system that combines different technologies; with a focus on fuel cells technology; is outlined which is thought of to be a very promising basis for a broader system that will secure power and water in a very environment friendly way.

Different compositions of the system $\text{La}_{0.2}\text{Sr}_{0.7-x}\text{Ca}_x\text{TiO}_3$ were also studied using AC impedance spectroscopy in order to establish whether or not this system can show a ferroelectric behaviour. Results showed a variation in the dielectric constant of different samples with temperature; however, no Curie point was observed. Nonetheless, the results did show that the different compositions were very homogeneous when fully oxygenated and there were some indications of possible symmetry changes at sub-ambient temperatures.

The final part of this thesis outlined the work done towards the development of a new analytical instrument. An existing TGA instrument was altered in order to provide a simultaneous thermogravimetric analysis and DC conductivity measurement for solid solutions at controlled temperature and oxygen partial pressure. Results were obtained for different samples of the system $\text{La}_{0.2}\text{Sr}_{0.7-x}\text{Ca}_x\text{TiO}_3$ which showed a great dependence of the electrical conductivity on the oxygen stoichiometry in these oxides. Also, a direct method is possible with this instrument to estimate the oxygen chemical diffusion coefficient using the electrical conductivity relaxation method. This new setup will be very useful for different electrochemical and thermal studies which can broaden the understanding of the different mechanisms that affect the performance of different solid state materials.

I dedicate this work to my beautiful wife, Noura, who endured with me throughout these years. I thank her for her love, support, encouragement, patience and for always being there for me. I also dedicate this to my lovely children, my daughter Alia and my son Abdulla who both flourished my life with joy and gave it a greater purpose.

Acknowledgement

First of all, all thanks shall be made to God who blessed me with everything that I am.

There are many people that I wish to thank and show my appreciation to. First and most, I am really grateful and thankful to my dear supervisor Professor John Irvine who gave me this opportunity and embraced me with his vast knowledge, experience, guidance and patience where I learned so much from him. I thank him for his continuous support and guidance throughout the years; which made my time in St Andrews very unique. I also thank him for the special way he was treating us, his students, which helped greatly in adjusting fairly quickly away from home.

I like to thank my sponsors, the government of the United Arab Emirates, who sponsored and supported me through the years.

I also would like to thank and acknowledge my friends in the JTSI research group and in the chemistry department at the University of St Andrews. Most of all, many thanks are for my dear friend Cristian Savaniu who taught me almost everything and for his friendship and making me feel right at home. I also wish to thank Martin Smith for his friendship and encouragement and the good times I had with him. Many thanks to Maarten Verbraeken, Abul Azad, Paul Connor, Julie Nairn and David Miller for their guidance and help with different aspects of this research. Also, not to forget, I'd like to thank Jim Rennie, George Anthony, Bobby Cathcart and Brian Walker for the help and good times I had during the development course of the TGA/DC jig. I also wish to thank my second supervisor Dr. Richard Baker for the support and useful advices he gave me through the years. Thanks are also due to both my examiners, Dr. Stephen Skinner and Dr. Mark Cassidy. Many thanks to all members of the JTSI group who became very dear friends. Finally, much thanks to all my friends in the UAE for their support and encouragement; especially Hamad Alshamsi and Mansoor Alromaiti.

Last but not least, my deepest and most heart sincere gratitude and thanks are for my parents, who believed in me since childhood and kept on encouraging and supporting me. Thank you for your endless prayers and love that made me succeed in life. Many thanks to all my brothers and sisters for their support and love.

Table of Contents

Declarations	ii
Abstract	iii
Dedication	v
Acknowledgement	vi
Table of Contents	vii
List of Figures	xi
List of Tables	xx
Chapter 1 - Introduction and Experimental Techniques	1
1.1 – Introduction	2
1.2 – Background	3
1.2.1 – Fuel Cells	3
1.2.2 – General Considerations	7
1.2.3 – The Ni-YSZ cermet	10
1.2.4 – Alternative Anodes	12
1.2.5 – Precursors of $\text{La}_{0.2}\text{Sr}_{0.7-x}\text{Ca}_x\text{TiO}_3$	15
1.2.6 – Ferroelectrics	20
1.3 – Experimental Methods	22
1.3.1 – Samples Preparation	22
1.3.2 – X-ray Powder Diffraction (XRD)	23
1.3.3 – Neutron Powder Diffraction (NPD)	24
1.3.4 – DC Conductivity Measurement	25
1.3.5 – Dilatometry	26
1.3.6 – Thermal Analysis	27
1.3.7 – Electron Microscopy	27
1.3.8 – Ferroelectricity Study	27
1.4 – References	29

Chapter 2 – The United Arab Emirates and its Energy Future A Closer Look	35
Abstract	36
2.1 – Introduction	37
2.2 – The Nature of UAE	40
2.3 – The Current Situation	42
2.4 – Is Desalination Sustainable?	45
2.5 – Addressing the Challenges	48
2.6 – Considerations	49
2.7 – Hydrogen	52
2.8 – The Proposal	53
2.9 – Conclusions	59
2.10 – References	60
Chapter 3 – Novel A-site deficient $\text{La}_{0.2}\text{Sr}_{0.7-x}\text{Ca}_x\text{TiO}_3$: Part 1 – Structural Characterisation	67
Abstract	68
3.1 – Introduction	69
3.2 – Results and Discussion	70
3.2.1 – XRD Analysis	70
3.2.2 – NPD Analysis	87
3.3 – Conclusions	111
3.4 – References	113
Chapter 4 - Novel A-site deficient $\text{La}_{0.2}\text{Sr}_{0.7-x}\text{Ca}_x\text{TiO}_3$: Part 2 – Further Analysis	115
Abstract	116
4.1 – Introduction	117
4.2 – Thermal Analysis	118
4.2.1 – Thermal Expansion	118
Results and Discussion	118

4.2.2 – TGA/DTA Analysis	124
Results and Discussion	124
4.3 – DC Conductivity Measurement	128
Results and Discussion	128
4.4 – SEM Studies	143
Results and Discussion	143
4.5 – Conclusions	147
4.6 – References	149
Chapter 5 Investigation of Possible Ferroelectricity in the A-site Deficient Perovskite $\text{La}_{0.2}\text{Sr}_{0.7-x}\text{Ca}_x\text{TiO}_3$ using AC Impedance	151
Abstract	152
5.1 – Introduction	153
5.2 – Results and Discussion	154
5.3 – Conclusions	171
5.4 – References	172
Chapter 6 - Development and Implementation of a Novel Simultaneous TGA/DC Conductivity Analysis Instrument	173
Abstract	174
6.1 – Introduction	175
6.2 – Theory	178
6.2.1 – Thermogravimetric Analysis	178
6.2.2 – DC Conductivity Measurement	178
6.2.2.1 – The 4-point probe DC Conductivity Technique	179
6.2.2.2 – The van der Pauw (vdP) Technique	180
6.2.3 – Oxygen Sensor	182
6.2.4 – Oxygen Chemical Diffusion Coefficient	183

6.3 – The Instrument	186
6.3.1 – Introduction	186
6.3.2 – Initial Issues with the SDT2960	188
6.3.3 – Alterations to the SDT2960	192
6.3.4 – Control and Logging Programmes (Software)	196
6.3.4.1 – Thermal Advantage	196
6.3.4.2 – LogTGA	197
6.3.5 – Testing Phase	199
6.4 – Experimental	206
6.5 – Results and Discussion	207
6.6 – Conclusions	219
6.7 – Future Recommendations	219
6.8 – References	221
Chapter 7 – Final Remarks and Future Recommendations	223
7.1 – Final Remarks	224
7.2 – Future Recommendations	231
Appendix A:	
Simultaneous TGA and DC Conductivity Measurement Jig – TA	233
Instruments SDT2960 - User’s Manual	

List of Figures

Figure 1.1 Schematic of a solid oxide fuel cell where hydrogen used as fuel	4
Figure 1.2 Schematic showing the TPB of a Ni-YSZ anode	8
Figure 1.3 Typical V-I characteristic for a fuel cell	9
Figure 1.4 Representation of the perovskite (ABO_3) cubic unit cell where A: green, B: blue and O: red	14
Figure 2.1 Map showing the location of the UAE; a midpoint between west and east	37
Figure 2.2 A satellite image of the UAE, showing the spread of the desert	40
Figure 2.3 Image illustrating the severity of sand storms in the UAE	41
Figure 2.4 Dubai's peak demand for electricity for 2009 and 2010	44
Figure 2.5 Flow chart representing the proposed hydrogen-based system for meeting future needs of the United Arab Emirates	56
Figure 3.1 Normalised XRD patterns of all synthesised samples of $La_{0.2}Sr_{0.7-x}Ca_xTiO_3$	70
Figure 3.2 XRD pattern of $La_{0.2}Sr_{0.6}Ca_{0.1}TiO_3$ with reflections of $SrTiO_3$ obtained from ICDD PDF card number: 35-734. Indices are those for the $SrTiO_3$ phase, S.G.: Pm3-m	71
Figure 3.3 XRD pattern for $La_{0.2}Ca_{0.7}TiO_3$ with addition to the reflections of $CaTiO_3$ obtained from ICDD PDF card number:42-423. Indices correspond to some of the reflections of the $CaTiO_3$ phase	72
Figure 3.4: Comparing the XRD patterns of the starting material $La_{0.2}Sr_{0.7}TiO_3$ to those for some of the samples of $La_{0.2}Sr_{0.7-x}Ca_xTiO_3$	73
Figure 3.5 XRD pattern of $La_{0.2}Sr_{0.6}Ca_{0.1}TiO_3$ and indexed reflections using the tetragonal symmetry I4/mcm	76
Figure 3.6 XRD patterns for samples of $La_{0.2}Sr_{0.7-x}Ca_xTiO_3$ showing the different symmetries	77

Figure 3.7 Portion of the normalised XRD patterns for samples of $\text{La}_{0.2}\text{Sr}_{0.7-x}\text{Ca}_x\text{TiO}_3$	78
Figure 3.8 Primitive unit cell parameters and volume as a function of calcium content. Unit cell parameters and volume of $\text{La}_{0.2}\text{Sr}_{0.7}\text{TiO}_3$ ($x = 0$) were obtained from ref. [66]	80
Figure 3.9 Comparison between XRD patterns of $\text{La}_{0.2}\text{Sr}_{0.6}\text{Ca}_{0.1}\text{TiO}_3$ to see the effect of reduction on the structure	81
Figure 3.10 XRD patterns of two different samples of $\text{La}_{0.2}\text{Sr}_{0.3}\text{Ca}_{0.4}\text{TiO}_3$ that were (a): fired once and (b): fired twice at 1500°C for 15 hours and 8 hours, respectively	82
Figure 3.11 XRD patterns of two samples of $\text{La}_{0.2}\text{Sr}_{0.3}\text{Ca}_{0.4}\text{TiO}_3$ that were fired at different temperatures as shown	83
Figure 3.12 Rietveld profile matching of the XRD pattern of $\text{La}_{0.2}\text{Sr}_{0.2}\text{Ca}_{0.4}\text{TiO}_3$ with I4/mcm space group with $a, b = 5.46155(22)\text{Å}$, $c = 7.73590(26)\text{Å}$. $R_p: 9.70$, $R_{wp}: 12.8$, $R_{exp}: 8.50$, $\chi^2: 2.29$	84
Figure 3.13 Rietveld profile matching of the XRD pattern of $\text{La}_{0.2}\text{Sr}_{0.2}\text{Ca}_{0.4}\text{TiO}_3$ with Imma space group with $a=5.46765(15)$, $b=7.72377(50)$, $c= 5.46369(20)$. $R_p: 10.5$, $R_{wp}: 14.0$, $R_{exp}: 8.49$, $\chi^2: 2.72$	84
Figure 3.14 Phase diagram of the ternary system CaTiO_3 - $\text{La}_{2/3}\text{TiO}_3$ - SrTiO_3 . All numbers represent calcium content. Solid symbols represent the samples studied in this work and analysed using XRD data; where shaded ones represent compositions obtained from literature	85
Figure 3.15 Observed (Red), calculated (Black) NPD pattern and the difference spectrum (in Blue) for $\text{La}_{0.2}\text{Sr}_{0.5}\text{Ca}_{0.2}\text{TiO}_3$ using I4/mcm space group	88
Figure 3.16 Unit cell volume of the studied samples of $\text{La}_{0.2}\text{Sr}_{0.7-x}\text{TiO}_3$ from NPD analysis	88
Figure 3.17 The primitive unit cell parameters of the studied samples obtained from NPD analysis	90
Figure 3.18 Phase diagram of the ternary system CaTiO_3 - $\text{La}_{2/3}\text{TiO}_3$ - SrTiO_3 . All numbers represent calcium content. Solid symbols represent the samples studied in this work and analysed using NPD data; where shaded ones represent compositions obtained from literature	92
Figure 3.19 Comparing the primitive unit cell volumes obtained from XRD and NPD; using the least square and Rietveld methods, respectively	93

Figure 3.20 Structure view along the $[00\bar{1}]$ of the tetragonal samples of $\text{La}_{0.2}\text{Sr}_{0.7-x}\text{Ca}_x\text{TiO}_3$ where A: 0.1, B: 0.2, C: 0.3 and D: 0.35 for x. The out of phase tilt angles associated with the $I4/mcm$ symmetry are shown; i.e. obtained using CrystalMaker [®]	94
Figure 3.21: Portion of the NPD patterns for samples of $\text{La}_{0.2}\text{Sr}_{0.7-x}\text{Ca}_x\text{TiO}_3$ which show a tetragonal symmetry; $0.1 \leq x \leq 0.35$; showing the $\{2\ 1\ 1\}$ reflection	95
Figure 3.22: Structure views along the $[00\bar{1}]$ showing the (A) anti-phase and (B) the in-phase tilting of the TiO_6 octahedra for the $I4/mcm$ and $Pbnm$ phases, respectively	96
Figure 3.23: Structure views along the (A) $[100]$ and (B) $[010]$ direction of the orthorhombic unit cell of $\text{La}_{0.2}\text{Sr}_{0.2}\text{Ca}_{0.5}\text{TiO}_3$; demonstrating the anti-phase tilting of the octahedra	96
Figure 3.24: The out-of-phase tilt angle values for the different compositions of $\text{La}_{0.2}\text{Sr}_{0.7-x}\text{Ca}_x\text{TiO}_3$ at room temperature	97
Figure 3.25: Bond lengths between titanium and the neighbouring oxygen anions forming the BO_6 octahedral for the different samples of $\text{La}_{0.2}\text{Sr}_{0.7-x}\text{Ca}_x\text{TiO}_3$	98
Figure 3.26: Bond lengths between the A-site cation and oxygen in the perovskite unit cell for the different samples of $\text{La}_{0.2}\text{Sr}_{0.7-x}\text{Ca}_x\text{TiO}_3$	100
Figure 3.27: NPD patterns for $\text{La}_{0.2}\text{Sr}_{0.2}\text{Ca}_{0.5}\text{TiO}_3$ showing the phase transitions at high temperatures	102
Figure 3.28: Rietveld refinement results of NPD patterns for $\text{La}_{0.2}\text{Sr}_{0.2}\text{Ca}_{0.5}\text{TiO}_3$ at (a) 900°C , (b) 300°C and (c) at room temperature	103
Figure 3.29: Unit cell parameters for a reduced sample of $\text{La}_{0.2}\text{Sr}_{0.25}\text{Ca}_{0.45}\text{TiO}_3$ as a function of temperature	105
Figure 3.30: Primitive unit cell volume of the reduced $\text{La}_{0.2}\text{Sr}_{0.25}\text{Ca}_{0.45}\text{TiO}_3$ plotted against temperature	106
Figure 3.31: Unit cell parameters for $\text{La}_{0.2}\text{Sr}_{0.2}\text{Ca}_{0.5}\text{TiO}_3$ as a function of temperature	108
Figure 3.32: Primitive unit cell volume of $\text{La}_{0.2}\text{Sr}_{0.2}\text{Ca}_{0.5}\text{TiO}_3$ as a function of temperature	108
Figure 3.33: Bond lengths between titanium and oxygen for $\text{La}_{0.2}\text{Sr}_{0.2}\text{Ca}_{0.5}\text{TiO}_3$ at high temperatures	109

Figure 3.34: NPD patterns of $\text{La}_{0.2}\text{Sr}_{0.2}\text{Ca}_{0.5}\text{TiO}_3$ at 500°C collected during (a) heating and (b) cooling. The inset shows a closer look into a portion of the same patterns	110
Figure 4.1 Thermal expansion curves of $\text{La}_{0.2}\text{Sr}_{0.6}\text{Ca}_{0.1}\text{TiO}_3$ measured in $5\%\text{H}_2$ showing TEC during heating (a) and cooling (b)	118
Figure 4.2 Thermal expansion curves of $\text{La}_{0.2}\text{Sr}_{0.25}\text{Ca}_{0.45}\text{TiO}_3$ measured while (a) heating in air and (b) cooling in $5\%\text{H}_2:95\%\text{Ar}$	120
Figure 4.3 Sintering behaviour of various samples of $\text{La}_{0.2}\text{Sr}_{0.7-x}\text{Ca}_x\text{TiO}_3$ in air	121
Figure 4.4 Sintering behaviour of $\text{La}_{0.2}\text{Sr}_{0.25}\text{Ca}_{0.45}\text{TiO}_3$ in air compared to that of YSZ	122
Figure 4.5 Plot showing the temperatures at which both materials start the sintering process	123
Figure 4.6 TGA curve of a pre-reduced sample of $\text{La}_{0.2}\text{Sr}_{0.25}\text{Ca}_{0.45}\text{TiO}_3$ during oxidation at 900°C	124
Figure 4.7: TGA curves for (a) in-situ reduction and (b) oxidation of pre-reduced samples at 900°C for samples of $\text{La}_{0.2}\text{Sr}_{0.25}\text{Ca}_{0.45}\text{TiO}_3$	125
Figure 4.8: TGA curve showing the oxidation of a pre-reduced $\text{La}_{0.2}\text{Sr}_{0.2}\text{Ca}_{0.5}\text{TiO}_3$ at 900°C	126
Figure 4.9 DTA curves for $\text{La}_{0.2}\text{Sr}_{0.25}\text{Ca}_{0.45}\text{TiO}_3$ during thermal cycling in air	127
Figure 4.10 Conductivity and $\log p\text{O}_2$ as function of time for $\text{La}_{0.2}\text{Sr}_{0.6}\text{Ca}_{0.1}\text{TiO}_3$ at 900°C	128
Figure 4.11 The conductivity of $\text{La}_{0.2}\text{Sr}_{0.6}\text{Ca}_{0.1}\text{TiO}_3$ as a function of $\log p\text{O}_2$ at 900°C	129
Figure 4.12 Thermal cycling of $\text{La}_{0.2}\text{Sr}_{0.6}\text{Ca}_{0.1}\text{TiO}_3$ at a $p\text{O}_2$ of 10^{-19} atm	130
Figure 4.13 Conductivity as a function of temperature for a pre-reduced porous pellet of $\text{La}_{0.2}\text{Sr}_{0.6}\text{Ca}_{0.1}\text{TiO}_3$ in reducing conditions	131
Figure 4.14: Response of the conductivity of the porous pellet of $\text{La}_{0.2}\text{Sr}_{0.6}\text{Ca}_{0.1}\text{TiO}_3$ at 900°C to changes to oxygen partial pressure. The line shows the point where the purging of $5\%\text{H}_2$ stopped and air was allowed to enter the furnace	132

Figure 4.15: plot of $\log(\sigma)$ vs. $\log(pO_2)$ comparing the conductivity response to pO_2 between the dense and the porous samples of $La_{0.2}Sr_{0.6}Ca_{0.1}TiO_3$ at $900^\circ C$	133
Figure 4.16: Plot of the electrical conductivity as a function of time for a dense pellet of $La_{0.2}Sr_{0.5}Ca_{0.2}TiO_3$ being reduced in-situ at $900^\circ C$ and $pO_2 = 10^{-18}$ atm	134
Figure 4.17: Oxidation of a dense sample of $La_{0.2}Sr_{0.5}Ca_{0.2}TiO_3$ at $900^\circ C$	135
Figure 4.18: Reduction of a dense sample of $La_{0.2}Sr_{0.5}Ca_{0.2}TiO_3$ at $900^\circ C$	135
Figure 4.19: Temperature dependence of the electrical conductivity of different samples of $La_{0.2}Sr_{0.7-x}Ca_xTiO_3$ in reducing conditions	136
Figure 4.20: Temperature dependence of the electrical conductivity of a dense pre-reduced pellet of $La_{0.2}Sr_{0.25}Ca_{0.45}TiO_3$ under 5% H_2 /95% Ar, $pO_2 \approx 10^{-19}$ atm	137
Figure 4.21: Temperature dependence of the electrical conductivity of $La_{0.2}Sr_{0.25}Ca_{0.45}TiO_3$ during thermal cycling in 5% H_2	138
Figure 4.22: Temperature dependence of the electrical conductivity for pre-reduced samples of $La_{0.2}Sr_{0.7-x}Ca_xTiO_3$ in reducing atmosphere	139
Figure 4.23: Comparison of the maximum conductivity at $900^\circ C$ and $pO_2 \approx 10^{-19}$ atm for all pre-reduced dense samples of $La_{0.2}Sr_{0.7-x}Ca_xTiO_3$	140
Figure 4.24: SEM micrographs of different samples of $La_{0.2}Sr_{0.7-x}Ca_xTiO_3$ sintered in air where (a): 0.1, (b): 0.35, (c): 0.4, (d): 0.45, (e): 0.6 and (f): 0.7 for x	143
Figure 4.25: SEM micrographs showing samples of $La_{0.2}Sr_{0.7-x}Ca_xTiO_3$ sintered in air at $1400^\circ C$ with 20wt% pore-former mixture; where (a): x = 0.1, (b): x = 0.2, (c): x = 0.35	144
Figure 4.26: SEM micrographs of a porous $La_{0.2}Sr_{0.6}Ca_{0.1}TiO_3$ before (left) and after (right) reduction	145
Figure 4.27: SEM micrographs for two pellets of $La_{0.2}Sr_{0.25}Ca_{0.45}TiO_3$ pressed at 1 ton (left) and 4 tonnes (right)	145
Figure 4.28: SEM micrographs showing two samples of $La_{0.2}Sr_{0.25}Ca_{0.45}TiO_3$ that were sintered once (left) and four times (right) at $1500^\circ C$	146
Figure 5.1: Impedance plots of $La_{0.2}Sr_{0.25}Ca_{0.45}TiO_3$ at $300^\circ C$ showing the results at the low frequency range	154

Figure 5.2: Impedance spectra of $\text{La}_{0.2}\text{Sr}_{0.25}\text{Ca}_{0.45}\text{TiO}_3$ at temperatures between 550° and 900°C in air	155
Figure 5.3: Frequency plots of Z'' and M'' for $\text{La}_{0.2}\text{Sr}_{0.25}\text{Ca}_{0.45}\text{TiO}_3$ at temperatures between 550° and 900°C	156
Figure 5.4: Plot of the capacitance and resistivity at different temperatures of $\text{La}_{0.2}\text{Sr}_{0.25}\text{Ca}_{0.45}\text{TiO}_3$ obtained using least square fitting of impedance data to a simple RC element (shown)	157
Figure 5.5: Temperature dependence of specific C_p at different frequencies for $\text{La}_{0.2}\text{Sr}_{0.6}\text{Ca}_{0.1}\text{TiO}_3$ at sub-ambient temperatures	158
Figure 5.6: Dielectric constant of $\text{La}_{0.2}\text{Sr}_{0.6}\text{Ca}_{0.1}\text{TiO}_3$ as a function of temperature at selected frequencies	159
Figure 5.7: Dielectric loss of $\text{La}_{0.2}\text{Sr}_{0.6}\text{Ca}_{0.1}\text{TiO}_3$ at different frequencies as a function of temperature	160
Figure 5.8: Temperature dependence of specific C_p at different frequencies for $\text{La}_{0.2}\text{Sr}_{0.6}\text{Ca}_{0.1}\text{TiO}_3$ at high temperatures	161
Figure 5.9: Dielectric loss of $\text{La}_{0.2}\text{Sr}_{0.6}\text{Ca}_{0.1}\text{TiO}_3$ at different frequencies as a function of temperature	162
Figure 5.10: C_p as a function of temperature for $\text{La}_{0.2}\text{Sr}_{0.6}\text{Ca}_{0.1}\text{TiO}_3$ at 1 kHz during thermal cycling	163
Figure 5.11: C_p vs. Frequency at different temperatures of $\text{La}_{0.2}\text{Sr}_{0.6}\text{Ca}_{0.1}\text{TiO}_3$	163
Figure 5.12: C_p vs. Frequency at different temperatures of $\text{La}_{0.2}\text{Sr}_{0.6}\text{Ca}_{0.1}\text{TiO}_3$ at high temperatures	164
Figure 5.13: Temperature dependence of C_p at different frequencies for $\text{La}_{0.2}\text{Sr}_{0.5}\text{Ca}_{0.2}\text{TiO}_3$ at sub-ambient temperatures	166
Figure 5.14: Dielectric loss of $\text{La}_{0.2}\text{Sr}_{0.5}\text{Ca}_{0.2}\text{TiO}_3$ at different frequencies as a function of temperature	166
Figure 5.15: Temperature dependence of capacity (C_p) at different frequencies for $\text{La}_{0.2}\text{Sr}_{0.4}\text{Ca}_{0.3}\text{TiO}_3$ at sub-ambient temperatures	167
Figure 5.16: Measured capacity of samples of $\text{La}_{0.2}\text{Sr}_{0.7-x}\text{Ca}_x\text{TiO}_3$ at sub-ambient temperatures at 1 kHz	168
Figure 5.17: Capacity of samples of $\text{La}_{0.2}\text{Sr}_{0.7-x}\text{Ca}_x\text{TiO}_3$ at high temperatures at 1 kHz	168

Figure 5.18: Dielectric constant of different samples of the system $\text{La}_{0.2}\text{Sr}_{0.7-x}\text{Ca}_x\text{TiO}_3$ measured at 1 kHz	169
Figure 5.19: Dielectric constant and dielectric loss plotted against temperature for $\text{La}_{0.2}\text{Sr}_{0.6}\text{Ca}_{0.1}\text{TiO}_3$	170
Figure 6.1 The geometry of a wire	179
Figure 6.2 Typical arrangement of the 4-point DC conductivity measurement technique	180
Figure 6.3 Contacts arrangement for an arbitrary shaped sample	181
Figure 6.4 Typical YSZ based oxygen sensor	182
Figure 6.5 Photograph of the SDT2960 used in this work	186
Figure 6.6 Schematic of the SDT2960 different components	187
Figure 6.7 Weight meter module	189
Figure 6.8 Image showing the by-passing of the reference weight signal	190
Figure 6.9 The plug of the reference module with the first two terminals short-circuited	191
Figure 6.10 The new sample pan with a pellet connected and lifted to show the thermocouple location; as indicated by the red arrow	192
Figure 6.11 Image showing the inside of the meter housing. The arrow points at the tip of the sample arm connected with fine wires	193
Figure 6.12 The YSZ tube used (bottom) and the improvised pO_2 sensor (top)	194
Figure 6.13 The new setup for the SDT2960	195
Figure 6.14 A screen capture of the main window of the Thermal Advantage programme	197
Figure 6.15 A screen capture of the LogTGA programme	197
Figure 6.16 Spreadsheet showing the different parameters logged by the LogTGA programme	198

Figure 6.17 Profile of the temperature programme as measured by two different thermocouples	199
Figure 6.18 Temperature programme as measured by the SDT2960 and the R-type thermocouple	200
Figure 6.19 Temperature measured using the same S-type thermocouple showing a great overlap between the two systems	201
Figure 6.20 The conductivity of dense $\text{La}_{0.2}\text{Sr}_{0.25}\text{Ca}_{0.45}\text{TiO}_3$ as a function of temperature measured in two different jigs under reducing conditions	202
Figure 6.21 New pO_2 sensor in place next to the sample arm in the SDT2960	203
Figure 6.22 Voltage generated across the new and old pO_2 sensors as a function of temperature in air	204
Figure 6.23 Voltage generated by the new sensor as a function of temperature in air; after further runs	204
Figure 6.24 oxygen partial pressure as measured by the new sensor at 932°C as the purging gas was switched as shown above	205
Figure 6.25 Electrical conductivity and the corresponding weight change of dense $\text{La}_{0.2}\text{Sr}_{0.25}\text{Ca}_{0.45}\text{TiO}_3$ through a redox cycle at 912°C	207
Figure 6.26 Electrical conductivity and the corresponding weight change of dense $\text{La}_{0.2}\text{Sr}_{0.25}\text{Ca}_{0.45}\text{TiO}_3$ through a second redox cycle at 912°C	208
Figure 6.27 Response of conductivity of the porous samples of $\text{La}_{0.2}\text{Sr}_{0.25}\text{Ca}_{0.45}\text{TiO}_3$ during reduction at 907°C	209
Figure 6.28: Conductivity and oxygen deficiency change of the ceria impregnated pellet reduction at 918°C	211
Figure 6.29: Normalised relaxation conductivity for the reduction of dense $\text{La}_{0.2}\text{Sr}_{0.25}\text{Ca}_{0.45}\text{TiO}_3$ at 900°C with the calculated oxygen chemical diffusion coefficient shown	212
Figure 6.30: Normalised relaxation conductivity for the reduction of Sample A of $\text{La}_{0.2}\text{Sr}_{0.25}\text{Ca}_{0.45}\text{TiO}_3$ at 900°C with the calculated oxygen chemical diffusion coefficient shown	213
Figure 6.31: SEM micrographs comparing the porosity of sample A and sample B, respectively	214
Figure 6.32 Normalised relaxation conductivity for the reduction of Sample B of $\text{La}_{0.2}\text{Sr}_{0.25}\text{Ca}_{0.45}\text{TiO}_3$ at 900°C with the calculated oxygen chemical diffusion coefficient shown	214

Figure 6.33: Normalised relaxation conductivity for the reduction of the ceria impregnated sample of $\text{La}_{0.2}\text{Sr}_{0.25}\text{Ca}_{0.45}\text{TiO}_3$ (Sample A) at 900°C with the calculated oxygen chemical diffusion coefficient shown	216
Figure 6.34 SEM micrographs of sample A before (left) and after (right) impregnation with ceria	217

List of Tables

Table 3.1 Space groups and primitive unit cell parameters and volumes for synthesised compositions of the system $\text{La}_{0.2}\text{Sr}_{0.7-x}\text{Ca}_x\text{TiO}_3$	79
Table 3.2 Summary of the Rietveld refinement results of NPD data for different samples of $\text{La}_{0.2}\text{Sr}_{0.7-x}\text{Ca}_x\text{TiO}_3$ at room temperature	89
Table 3.3 Summary of the Rietveld refinement results of NPD data for a reduced sample of $\text{La}_{0.2}\text{Sr}_{0.25}\text{Ca}_{0.45}\text{TiO}_3$ at different temperatures	104
Table 3.4 Summary of the Rietveld refinement results of NPD data of $\text{La}_{0.2}\text{Sr}_{0.2}\text{Ca}_{0.5}\text{TiO}_3$ at different temperatures	107
Table 4.1 Thermal expansion coefficients of different samples of $\text{La}_{0.2}\text{Sr}_{0.7-x}\text{Ca}_x\text{TiO}_3$ as measured between ambient temperature and 1000°C	119
Table 4.2 Isotropic atomic displacement parameters $\text{La}_{0.2}\text{Sr}_{0.25}\text{Ca}_{0.45}\text{TiO}_3$ and $\text{La}_{0.2}\text{Sr}_{0.2}\text{Ca}_{0.5}\text{TiO}_3$ at 900°C	141
Table 4.3 Relative density of samples of $\text{La}_{0.2}\text{Sr}_{0.7-x}\text{Ca}_x\text{TiO}_3$; which were sintered with 20wt% pore-former	144
Table 6.1 Specifications of the SDT2960	188
Table 6.2 Oxygen chemical diffusion coefficients obtained with different samples of $\text{La}_{0.2}\text{Sr}_{0.25}\text{Ca}_{0.45}\text{TiO}_3$	217

Chapter 1

Introduction and Experimental Techniques

1.1 - Introduction

Global warming is one of the most talked about phenomena around the world nowadays and the continuing growth in population, especially in developing countries, brings us to a very peculiar situation. Many are calling to lower human impact on the planet delicate ecosystem and environment. However, for many others, power is essential to survive. Different ideas and schemes are being thought of on a daily basis to combine the two necessities. Renewable energy is a term that is widely mentioned nowadays. Using renewable sources to generate power is very much achievable; whether it is solar, wind, tidal, etc.; but there is a catch. Efficiency and practicality of such technologies are essential for adopting them, especially in a world where fossil fuels are more accessible and easily used to generate power.

The majority of power generation methods employed nowadays rely on fossil fuels. Aside from the harmful environmental impact, these techniques will eventually be very expensive in the future. At the current consumption rates of hydrocarbon based fuels; the prices will eventually increase due to diminishing reserves and increasing demands. It might be more convenient today to use fossil fuels to feed energy demands of different economies, but, the question is how long it will last.

Renewable sources are up for grasp, but it becomes the duty of many scientists and engineers in different disciplines to improve and develop reliable environmentally friendly technologies. One of the most promising techniques is fuel cell technology, which has gained quite a momentum in the past few years.[1] These electrochemical devices, in principle, convert chemical energy directly into electricity without any moving parts, yielding high efficiencies. With zero emission, when used with hydrogen,

fuel cells are indeed very attractive alternatives. These can supply power as long as they are supplied with fuel, unlike other renewable technologies that depend on different natural conditions, which can be unreliable in many occasions. Fuel cells do hold the potential of providing on demand and readily available power, very efficiently and with a very low impact on the environment.

Despite the very enticing characteristics that fuel cells promise, there are many barriers; as shall be discussed herein; that need to be overcome to make this technology very competitive in current and future economical conditions and to encourage its adoption as the next generation energy production utility in the near future.

1.2 - Background

1.2.1 - Fuel Cells

As mentioned earlier, a fuel cell is a device that transforms chemical energy into electrical energy.[2,3] In 1839, Sir William Grove discovered that it was possible to generate electricity through the reversal of water electrolysis, by supplying hydrogen and oxygen to a cell, he managed to generate a weak current, thus, forming the basis of a fuel cell.[4,45] Fuel cells are offering high efficiency power generation mechanism with the by-products of a hydrogen fuel cell are just heat and water; hence, zero emission.[5] Compared to conventional energy generation mechanisms fuel cells are more efficient, reliable, fuel flexible and environmentally friendly.[6] For example, combining fuel cells with gas turbines can enhance the efficiency by up to 70%; i.e. heat from a high temperature fuel cell utilised to drive a gas/steam turbine.[3,54] A typical fuel cell is shown in figure 1.1. These cells are mainly driven by the chemical potential

difference between the fuel and the air compartments; i.e. low oxygen partial pressure and high oxygen partial pressure, respectively.[48]

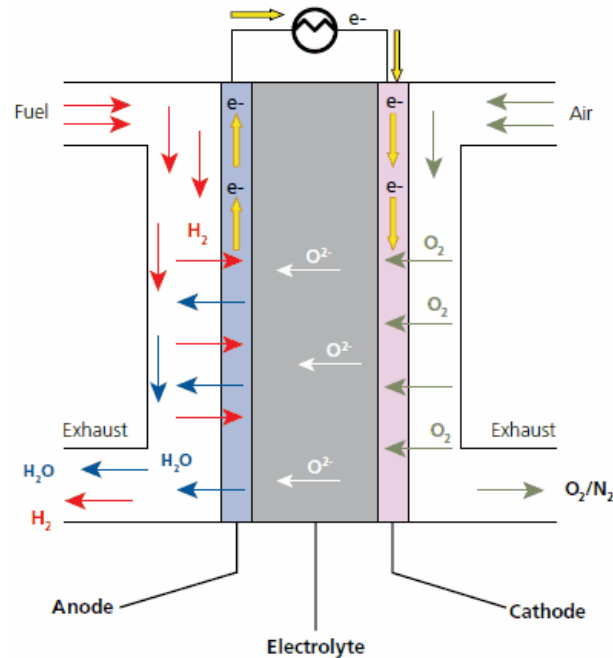
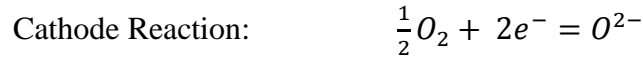


Figure 1.1: Schematic of a solid oxide fuel cell where hydrogen used as fuel.[7]

A typical fuel cell, like a battery, is made up from three parts, the anode, electrolyte and finally the cathode. Both electrodes should be porous; to allow diffusion of the different gasses; while the electrolyte must be very dense to separate and isolate the fuel and air compartments. The electrolyte should also be electrically insulating at operating conditions to avoid short circuiting the cell. Typically; i.e. in a solid oxide fuel cell; oxygen gas is reduced at the cathode and the resulting ions are transferred from the cathode through the electrolyte to the anode where they oxidise the hydrogen fuel, releasing electrons and forming water.

The reactions that take place at the electrodes of a hydrogen based fuel cell are the following:



Thus, it is already clear the potential of fuel cells towards an environmentally friendly energy production. Usually, a single fuel cell generates a small voltage and that is why many cells are stacked together to produce sufficient useful power. Depending on the application, fuel cells come in different sizes; i.e. power output; and shapes; e.g. planar, tubular. There are many types of fuel cells, mainly, Polymer Electrolyte Membrane (PEM), Alkali Fuel Cell (AFC), Phosphoric Acid Fuel Cell (PAFC), Molten Carbonate Fuel Cell (MCFC) and Solid Oxide Fuel Cell (SOFC). These types differ greatly in terms of operating temperatures, fuel types, efficiency, etc.; however, the main difference is the material of choice used as the electrolyte in those fuel cells. A good comparison between the different types of fuel cells can be found in reference [55].

While other types of fuel cells offer great properties, solid oxide fuel cell (SOFC) is one of the most promising techniques for a renewable energy generation. As the name suggest, this fuel cell is based on a solid oxide material as its electrolyte. SOFCs have high energy efficiency (60% efficiency) compared to conventional engines as well as other types of fuel cells.[8,55] One of the major challenges for adopting hydrogen fuel cells is the need for hydrogen rich or high purity hydrogen fuels.[9] Thus, having fuel flexible fuel cells is very much desirable. Fuel flexibility is a major driver in the development of fuel cells.[8] Thus, SOFCs are favoured because they show good

fuel flexibility with tolerance to impurities in fuels.[9,10,11] This flexibility comes from the high operating temperatures of SOFCs; usually higher than 650°C; which allow for internal reforming of different fuels, thus, removing the need for external purifying and reforming systems.[6,8,11,53] One of the reasons for high temperature operation is that the ionic conductivity of the electrolyte increases with temperature; as well as; the performance of the electrodes.[5,11] These high temperatures put huge strains on the different components of a fuel cell so the choice of materials is very important in designing a useful system. A major area in the research in fuel cell technology is finding alternative materials that can withstand the extreme conditions and provide the necessary performances while keeping a low cost. In general, degradation of SOFCs consists of many different mechanisms, that may include chromium poisoning of the cathode; i.e. from the interconnect steel; contact resistance, stability of the different layers/components and fuel related effects; e.g. coking and sulphur poisoning.[52] Cathodes must be compatible with the electrolyte in terms of thermal expansion coefficient, while having a high catalytic activity towards dissociation of oxygen. Also, mixed ionic and electronic conductivity is necessary for optimum conversion efficiency.[9] The electrolyte on the other hand must be very dense, stable and have a high ionic conductivity at different temperatures and atmospheres; i.e. reducing and oxidising. Finally, the anode must have high electronic conductivity, some ionic conductivity and good catalytic activity towards the oxidation of the fuel.[12] Also, it must be compatible with the electrolyte material of the cell, both mechanically and chemically. Both electrodes should have sufficient porosity to allow for easy diffusion of the different reactants/products. Currently, state of the art SOFCs are based on yttrium-stabilised zirconia (YSZ) as electrolyte, Ni-YSZ cermet as anode and strontium

doped LaMnO₃ (LSM) as cathode. Interconnects are usually made from substituted lanthanum chromites, chromium alloys and steels.[5,9] Since this work is concerned with developing a new anode material for SOFCs, the following discussions will focus on the current efforts in developing alternative anode materials.

1.2.2 - General Considerations

In most fuel cells, there are many sources of loss that lower the overall efficiency and performance. Most researchers focus on lowering these losses through materials research. If we consider a fuel cell under load, its voltage output is given by:

$$V = E^o - IR - \eta_c - \eta_a \quad (1.1)$$

Where E^o is the theoretical ideal voltage of the cell under open circuit conditions (OCV), I is the current passing through the cell, R is the ohmic resistance of the cell, η_c is the cathode polarisation loss and η_a is that of the anode.[3] The OCV of a cell can be obtained using Nernst equation and it is equal to 1.01V at 800°C with pure hydrogen at the anode and air at the cathode.[9,13] While the second term, IR , can be lowered using a thinner electrolyte, which will minimise the ohmic resistance[3], the anode and cathode losses contain many factors.

The resistance of the anode of a fuel cell comes from internal resistance, contact resistance, concentration polarisation resistance and activation polarisation resistance. Internal resistance is the resistance against the flow of electrons within the electrode which is affected by the thickness of the anode and its resistivity/conductivity. Contact resistance arises from poor contact between the anode and other components; e.g. electrolyte; which can result from poor matching of the thermal expansion coefficient between the different layers. The concentration polarisation resistance is controlled by

the porosity of the anode and how efficient its microstructure in facilitating the movement of the different gasses; e.g. hydrogen, water vapour; in and out of the anode structure. Activation polarisation resistance is dominated by the surface area of the triple phase boundary (TPB) and the catalytic activity of the anode.[3] The TPB, shown in figure 1.2, is defined as the site where the electrolyte, anode and the gas phases are in contact with each other; which is where the electrochemical reaction takes place.[9]

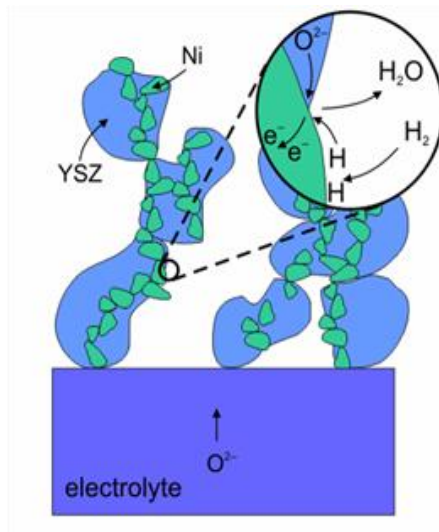


Figure 1.2: Schematic showing the TPB of a Ni-YSZ anode.[16]

In order to increase the size or extent of the TPB, many researchers are aiming at mixed ionic and electronic conductive (MIEC) materials. During operation of a typical fuel cell, at low current density, the performance of a typical fuel cell is greatly affected by the activation polarisation resistance arising from the electrodes catalytic activities. As the current density increases, the ohmic resistance decreases and dominates the operational voltage of a fuel cell. Finally, at high current densities, the concentration polarisation resistance is the one that dominates the cell performance.[3,50,51] This is best illustrated in figure 1.3; where the dominance of the different resistances is shown. Thus, to improve the performance of fuel cells, all of these losses should be minimised.

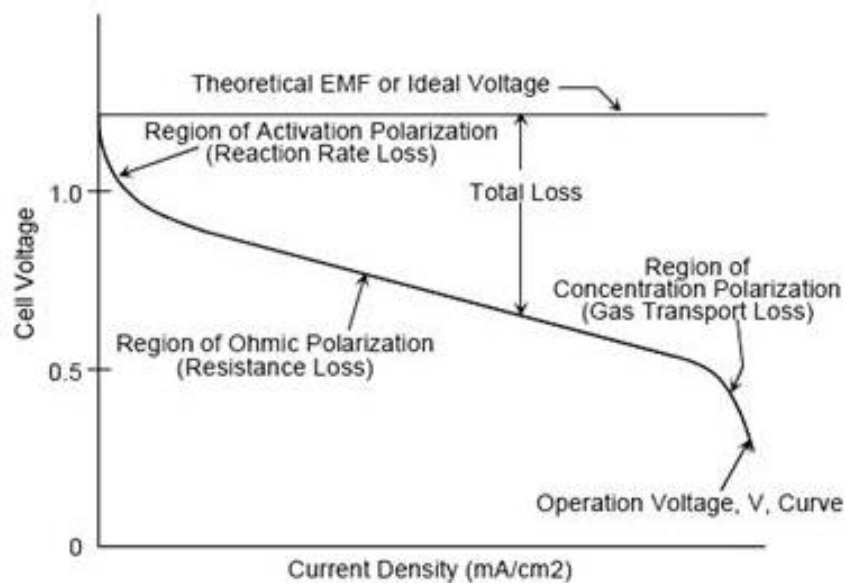


Figure 1.3: Typical V-I characteristic for a fuel cell.[49]

Taking into account all the variables that affect an anode's performance, it is clear that the challenge is difficult. For example, if we improve the TPB for example, by having higher porosity, we can increase the internal resistance since there is less conductive material that transfers the generated electrons, as well as, lowering the mechanical stability of the anode. The latter is very important in the development of electrode supported SOFCs; i.e. thinner electrolyte; to lower the ohmic resistance of the electrolyte.

Thus, it is important that SOFC anodes have high electronic conductivity, good ionic conductivity, high catalytic activity for fuel oxidation, good porosity, thermal expansion coefficient close and matching that of the electrolyte material, redox cycling stability and good chemical and mechanical stability with other components of the fuel cell; e.g. interconnects. Much of these aspects can be addressed through finding new materials or through improvements in design of existing materials that are already used in current fuel cell systems.

1.2.3 - The Ni-YSZ cermet

Ni-YSZ is the most used cermet as anode in SOFCs because it offers high catalytic activity for fuel oxidation, high electrical and ionic conductivity, chemical and mechanical stability, low cost and easy processing.[3,8,11,12] This anode can be broken into two phases, the nickel metal phase is used mainly to increase the catalytic activity of the anode towards oxidation of hydrogen and to enhance the electronic conductivity.[48] The ceramic phase YSZ is used to extend the electrochemical reaction further inside the anode away from the electrolyte by providing some ionic conductivity; which expands the triple phase boundary (TPB) surface area; thus lowering the activation polarisation resistance; as well as, matching the thermal expansion coefficient of the YSZ electrolyte.[3,48] As the properties of Ni-YSZ cermets are excellent for use in fuel cells, there are some drawbacks that should be considered.

As discussed earlier, fuel flexibility is important if fuel cells are to be used on a wider scale. Hydrogen production is majorly based on methane steam reforming; which is in a way against what fuel cells are meant to accomplish. When operated with hydrocarbon based fuels, Ni-YSZ properties deteriorate significantly. Carbon deposition on the anode and sulphur poisoning are the two major problems with Ni-YSZ.[3,8,9,11] Both can lead to severe degradation in the performance of the anode, as well as, its stability. According to Gong et al.[8], sulphur poisoning can take place in Ni-YSZ by two mechanisms. One, by the adsorption or chemisorption of H₂S by the catalytically active sites; rendering them inactive. The other, by sulfidation; which is a reaction between sulphur and the anode material that can lead to instability and poor conductivity and catalytic activity. Ni-YSZ can be affected by the smallest traces of sulphur; as small as 1-2 ppm can severely degrade the performance of the anode.[9,14]

On the other hand, carbon build-up is another issue with Ni-YSZ cermets.[12,14,15] Mainly, carbon deposits form on the surface of the nickel phase; which leads to very high activation polarisation.[3] As a result, the cell performance degrades when using hydrocarbon based fuels. Carbon build-up can be avoided by using steam reforming; however, this adds to the complexity and overall cost of a fuel cell system.[15] Generally, the metallic component of the Ni-YSZ cermet suffers from carbon deposition and sulphur poisoning.[14] Along with these issues, Ni-YSZ is not immune to mechanical failure due to volume instability of the anode during redox cycling[11,15,16,17], long term degradation due to agglomeration or coarsening of Ni particles.[12,16] The superior performance of this cermet comes from a sizeable interconnecting distribution of the Ni metallic phase, and the more of it makes the anode even less stable during operation.

It is obvious that the Ni-YSZ cermet is a very good anode if we consider hydrogen SOFCs. However, in order to make these cells more appealing to the markets, they should show great adaptability to be used with alternative fuels, especially readily available hydrocarbons; e.g. methane. The hydrogen economy is still in its infancy for it to be considered a vital fuel. Most of the hydrogen produced worldwide comes from hydrocarbons.[53] Thus, SOFCs with great fuel flexibility is very desirable, which is the major driver behind the development of new anode materials for SOFCs with comparable performances of the Ni-YSZ cermet; i.e. SOFCs operated at 800°C have shown a maximum power density of 1.7-1.8 W/cm² with Ni-YSZ used as the anode's material[56,57]; but without any of its drawbacks. A typical target is to find anode materials with electrical conductivity of 100 S/cm at operational conditions; however, this can be relaxed to even 1 S/cm with better microstructure engineering.[10,31]

1.2.4 - Alternative Anodes

There are many alternative materials that have been studied as anodes for SOFCs; we shall discuss a few of the most important. There are, generally, two approaches used to find alternative anode materials. The first is the development of new multi-phase cermets providing different enhancements; e.g. electronic, catalytic, ionic. Addressing the carbon deposition problem, for example, led to new YSZ cermets; e.g. Cu-CeO₂-YSZ/SDC.[9] Reducing the operating temperature of SOFC from 1000°C is another approach which can help reduce carbon deposition and is favourable when using thin electrolytes, which, in turn, reduces the ohmic resistance yielding high power density from the cell.[52] Then there is the approach to find new materials to replace the cermet based anodes completely.[61] There are many alternative materials that have been considered for SOFC anodes mainly materials with fluorite, perovskite, tungsten bronze and pyrochlore structures.[9,17] In general, the aim is to find mixed ionic and electronic conductors (MIEC) using oxide materials. These materials offer great advantages in extending the triple phase boundary, thus lowering the polarisation resistance, enhancing mechanical and chemical compatibility with different electrolyte materials and they show higher tolerance to sulphur.[8,12,15]

Since YSZ is the widely used material as an electrolyte in SOFCs; i.e. mainly for its ionic conductivity; many attempted to introduce electrical conductivity into YSZ by different dopants. Titanium and ceria doping were found to increase the electronic conductivity of YSZ and improve the catalytic activity of the anode.[10] Fluorite based materials; e.g. the Cu-ceria cermet; were reported to be resistant to carbon build-up due to copper being less catalytically active towards the formation of carbon bonding[10], with good catalytic activity towards the oxidation of hydrocarbon based fuels.[3,9,17]

Another good example of fluorite based materials is the gadolinium doped ceria $\text{Ce}_{0.9}\text{Gd}_{0.1}\text{O}_{1.95}$ which showed good resistance to carbon deposition and good catalytic activity for methane oxidation.[9,10] Ceria is has proven to be highly active towards the oxidation of hydrocarbons and also offer high ionic conductivity.[53,58,59] The main drawback of ceria based materials is the expansion of the lattice as a result of the reduction of the Ce ion. This leads to mechanical stresses which cause delamination and cracks that can damage the whole assembly.[3] Other types of ceramics include the pyrochlore structure. A good example is $\text{Gd}_2\text{Ti}_2\text{O}_7$, which did show high electrical conductivity values when molybdenum was substituted for titanium. This material, though, showed very poor redox stability.[9,10] Also, materials with the tungsten bronze structure; e.g. $\text{Sr}_{0.2}\text{Ba}_{0.4}\text{Ti}_{0.2}\text{Nb}_{0.8}\text{O}_3$; showed good electrical conductivity but had a lower thermal expansion coefficient to that of YSZ.[3,9,10] Thus, it is very obvious that as many materials show favourable attributes, undesirable properties do arise in many cases, which makes the task of developing alternative materials to replace the state of the art cermet Ni-YSZ in SOFCs very difficult. Nonetheless, all attempts can pave the way for better scientific understanding into the behaviour and properties of materials.

Of the many alternative materials, perovskites are attracting much of the attention in the development of new substitutes for the Ni-YSZ cermet.[3,9,10,18] A perovskite structure with the general formula ABO_3 , is simply formed of a cubic array of corner sharing octahedra with the A-site cation occupying the 12-fold body centre position, and the B-site cation in the 6-fold octahedral position[9,19], this structure is best illustrated in figure 1.4.

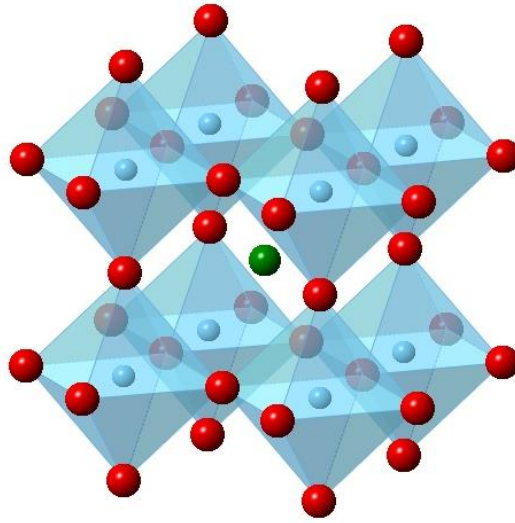


Figure 1.4: Representation of the perovskite (ABO_3) cubic unit cell where A: green, B: blue and O: red.

Perovskites offer a great advantage since the different properties can be tailored through different doping methods. Vacancies can be generated within the structure which can also support multi valence cations.[8,20] Perovskites can show electrical, dielectric, ferroelectric, piezoelectric, pyroelectric, electro-optical and magneto-optical behaviours and properties.[21] Of the most encouraging properties is that perovskite-based anodes do show a very good tolerance to carbon and sulphur containing fuels.[3] Also, these materials show good electronic conductivity, chemical and thermal compatibility with YSZ, redox stability and good performance under hydrogen and methane.[20] Many different perovskite based materials have shown very encouraging electrical conductivity values and performance. $(La_{0.75}Sr_{0.25})_{0.9}Cr_{0.5}Mn_{0.5}O_{3-\delta}$ has shown remarkable performance comparable to that of the Ni/YSZ cermet.[60,62] Also, $LaCrO_3$ have been found to be very stable in reducing conditions at high temperatures and showed good catalytic activity with methane.[63] However, chromite-based perovskites have shown very high polarisation resistance.[53] Also, the titanium-based perovskites

are interesting where $Y_{0.08}Sr_{0.92}Ti_{0.92}Nb_{0.08}O_3$ have shown a high electrical conductivity of 200 S/cm at 600°C[60], while $La_{0.3}Sr_{0.7}Sc_{0.1}Ti_{0.9}O_3$ have shown an electrical conductivity of 49 S/cm and an ionic conductivity of 0.01 S/cm at 800°C.[60] It is very important, at this stage, to mention that much care should be exercised when comparing between different materials in terms of electrical conductivity, this is because different synthesis/processing mechanisms can greatly affect the measured electrical conductivity. As we shall see in later parts of this thesis, reducing oxides at higher temperatures introduces more electrons, hence, increases the electrical conductivity. Many perovskites have, nonetheless, shown very encouraging performances. Among these, titanates have shown very encouraging performances when used with CeO_2 composites and with partial substitution of Ti on the B-site.[64] However, most important issues with these materials are the poor ionic conductivity and poor catalytic activity towards fuel oxidation.

1.2.5 - Precursors of $La_{0.2}Sr_{0.7-x}Ca_xTiO_3$

As mentioned earlier, perovskites are under much research for their attractive properties that can be used to replace the state of the art Ni-YSZ cermet. This work is concerned with the A-site deficient Ca-substituted $La_{0.2}Sr_{0.7-x}Ca_xTiO_3$ to see if it can be used as an anode material for SOFCs. Thus, it is important to see how this system has evolved.

Starting with $CaTiO_3$; regarded as the parent material of all perovskite based materials; is considered a very important material in both earth science and materials science. This perovskite is very similar to $MgSiO_3$, which is the main constituent of the lower mantle of our planet; thus, $CaTiO_3$ is extensively studied for its structural properties in different temperatures and pressures.[47] In addition, it is widely used in

Synroc (Synthetic Rock) for handling and processing of radioactive nuclear waste and it is, also, employed in the development of many electronic devices.[22,23,24] Moreover, CaTiO_3 is known to be stable at high temperatures in a wide range of oxygen partial pressures.[25] SrTiO_3 , on the other hand, is considered among different perovskites to be, when reduced, a very good electronic conductor.[10] It also shows a very good tolerance to sulphur, chemical and thermal stability.[3,5,6,26] SrTiO_3 can also be a superconductor if cooled down to temperatures close to 0K.[27] Thus, these two parent materials show great potential for being a basis for developing new materials for SOFCs anodes.

As both materials belong to the perovskite structure, doping with different cations can be accommodated and can enhance different properties. By considering the electrical conductivity, strongly reduced $\text{SrTiO}_{2.72}$ showed a conductivity of 1.7×10^3 S/cm at room temperature and showed a metallic behaviour.[27] When reducing SrTiO_3 , some of the Ti^{4+} reduces to Ti^{3+} which introduces electrons into the 3d conduction band of the titanium.[12,16,27] However, reduction of SrTiO_3 , to achieve a large proportion of Ti^{3+} , usually requires very high temperatures that exceed the operating temperature of SOFCs and can increase the complexity of processing with other cell components. Also, these strongly reduced compositions were not redox stable.[27] Thus, alternative techniques are needed, such as doping SrTiO_3 with a donor cation like La^{3+} , which makes it easier to reduce Ti^{4+} to Ti^{3+} . [6,26,27] Before reduction donor doped strontium titanate maintains electroneutrality by formation of strontium vacancies and SrO layers. And once reduced, oxygen vacancies are generated with the formation of Ti^{3+} which maintain electroneutrality and enhance the conductivity.[15,28] Reduced compositions of La-doped SrTiO_3 (LST) have shown conductivities of 100-

400 S/cm in reducing atmospheres at very high temperatures; e.g. 1000°C.[8,27] Also, $\text{La}_{0.3}\text{Sr}_{0.7}\text{TiO}_3$ showed an electrical conductivity of 220 S/cm at 800°C.[60] Moreover, LST tend to react less with YSZ; i.e. cathodes containing strontium and lanthanum reacted with YSZ forming insulating secondary phases like $\text{La}_2\text{Zr}_2\text{O}_7$ and SrZrO_3 . LST also showed very close thermal expansion coefficient, good stability in reducing atmospheres and through redox cycling, much better performance compared to chromites and other perovskites.[8,9,11,16,28] The type of dopant affects the physical and/or chemical properties of the original material in many different ways. For example, it was found that donor doping; e.g. La^{3+} and Nb^{5+} , makes SrTiO_3 a n-type semiconductor, while acceptor doping; e.g. Fe^{3+} , Co^{3+} on the Ti site; gives a p-type semiconductor.[6,28] Thus, improvements to the electronic or ionic conductivity can be obtained using different proportions of different dopants. It was shown that the conductivity of LST depends on the content of lanthanum in the structure; i.e. conductivity increases with lanthanum content; up to a content level of 0.4 where the conductivity levels off.[10] Doping strontium titanates with lanthanum leads to the incorporation of excess oxygen into the structure to maintain electroneutrality. However, high lanthanum content leads to crystallographic shear structures with oxygen rich regions forming line defects. For low lanthanum content, the defects are point-like and distributed randomly.[16] It is known that defects can affect the properties of material and that high defect concentration leads to the domination of defect-defect interactions.[29] Thus, the type of dopant and how much of it determines and affects the conductivity in this type of compound. One of the most encouraging aspects of LST is the good tolerance to sulphur [10,30], which makes it a very strong candidate for alternative anode material to Ni-YSZ. It was reported that no degradation was seen with

LST even with sulphur content as high as 5000 ppm.[16] However, many reports showed that the catalytic activity of LST towards the oxidation of hydrogen is relatively low compared to Ni-YSZ.[8,11,31] Two routes to improve the catalytic activity of LST were proposed. First, the catalytic activity can be improved through B-site doping to substitute the Ti with a multi valence cation like Mn and a fixed valence cation like Ga.[11] Doping the titanium site (B-site) with Mn and Ga showed very close performance to that of the Ni-YSZ cermet.[26] The second route is to impregnate the anode with a catalytically active phase; e.g. ceria.[31] In addition to the poor catalytic activity, LST showed poor ionic conductivity compared to Ni-YSZ.[30] Stoichiometric LST is oxygen excess before reduction, and oxygen ions need oxygen vacancies within the lattice in order to migrate within the anode. Thus, oxygen vacancies are needed to improve the ionic conductivity and increase the surface area of the TPB.[11,12,29] Creating oxygen deficiency was tried by mixed doping of the B-site of LST as in the $\text{La}_4\text{Sr}_8\text{Ti}_{11}\text{Mn}_{1-x}\text{Ga}_x\text{O}_{38-\delta}$ based compositions; which showed conductivity values of 7.9-6.8 S/cm at 900°C in reducing conditions.[11]

As LST did show promising results in terms of stability and electrical conductivity, another approach was taken to improve the poor catalytic activity and the low ionic conductivity. Since lanthanum doping creates oxygen excess compositions; which in turn increases with lanthanum content; A-site deficient compositions were considered. Through electroneutrality, a lower effective charge on the A-site of the perovskite, leads to oxygen deficiency. For example, it was found that A-site deficient strontium titanates have higher conductivity than their stoichiometric counterparts.[6,31] Moreover, with an A-site deficient LST, it is less likely for a reaction to occur with the YSZ phase of the electrolyte.[16] A-site deficiency is, also,

thought to be better for the densification of these perovskites.[6] More recently, Savaniu and Irvine[31] have reported that porous samples of $\text{La}_{0.2}\text{Sr}_{0.7}\text{TiO}_3$ had shown a conductivity of 39.75 S/cm at 750°C and $p\text{O}_2 = 10^{-21}$ atm; which was an improvement from the 2.75 S/cm conductivity of the dense counterpart. Also, impregnating this material with Gd_2O_3 -doped CeO_2 (CGO) and copper has resulted in much higher performances.[31] Thus, this material was chosen to be the basis of this study with the objective of improving the electrical conductivity through substituting strontium with calcium following the system $\text{La}_{0.2}\text{Sr}_{0.7-x}\text{Ca}_x\text{TiO}_3$. Calcium was chosen because it has the same valence as the replaced strontium, maintaining the electrical neutrality condition for this perovskite. With a smaller ionic radius, an improvement to the electrical conductivity is anticipated to be obtained through the reduction of the unit cell volume. A smaller unit cell volume shall bring the titanium d-orbitals closer to each other, thus enhancing the electrical conductivity without the need for extra dopants or changes to the microstructure of the original basis $\text{La}_{0.2}\text{Sr}_{0.7}\text{TiO}_3$. Hence, we are seeking improvements to the electrical conductivity of this perovskite through manipulation of the crystal structure, rather than through chemical routes. Since $\text{La}_{0.2}\text{Sr}_{0.7}\text{TiO}_3$ was improved through careful micro-structural changes and through impregnation with different catalysts, structural improvement to the system $\text{La}_{0.2}\text{Sr}_{0.7-x}\text{Ca}_x\text{TiO}_3$ will give a new platform for further improvements, which will have a greater potential of becoming a very serious candidate as an alternative anode material for SOFCs. Also, structural effects of calcium introduction in the unit cell are of interest since the crystal structure of this new system has not been investigated previously. Other pursued improvements to this perovskite include easier sintering, which will eventually help reduce the overall cost of fuel cells. Also, less strontium content can help in obtaining a better thermal

expansion coefficient control, since it was suggested that high strontium content can lead to abnormality in this aspect.[53]

1.2.6 – Ferroelectrics

For many years, much research was focused on finding new ferroelectric materials driven by the demand of new electrical components for new technologies. A ferroelectric material is defined as “an insulating system with two or more discrete stable or metastable states of different non-zero electric polarization in zero applied electric field”. Where it is possible to switch between these states by the application of an electric field giving rise to a hysteresis loop.[32]

Applications include capacitors, thermistors, varistors, actuators and sensors, acoustic and pressure transducers, optical modulators, energy conversion systems, piezoelectric and pyroelectric sensors, dynamic random access memory and non volatile ferroelectric random access memory (NVFRAM).[33-36] Development of ferroelectric random access memory is a major driver for ferroelectric materials research; since this type of memory offer low power non-volatile memory functionality with fast response to writing and reading and they are very scalable.[37] Lead zirconate titanate based materials are well known ferroelectrics; which are mostly used as piezoelectric materials.[38] Among the most recognizable are the zirconate-modified lead titanate (PZT), lanthanum-modified lead titanate PLT, and lanthanum-zirconate modified lead titanate PLZT.[35] However, major environmental concerns come from synthesis of these materials, where toxic lead evaporation is an issue.[35,38] Thus, much of the research is focused on finding alternatives to the lead based ferroelectrics.[39] Perovskite-based materials offer great alternatives that can be easily modified since the

perovskite structure offers great basis to alter physical and chemical properties through doping. Most useful ferroelectrics belong to the perovskite family, where BaTiO_3 is the most common perovskite ferroelectric material used in capacitors.[34,40] Barium titanate is widely used in electrical systems for its very high permittivity making it a very good capacitor.[41] It also offers good mechanical and chemical stability and shows good ferroelectric behaviour above room temperature.[33] On the other hand, the system $\text{Ca}_x\text{Sr}_{1-x}\text{TiO}_3$ showed many phases that were ferroelectric, antiferroelectric and relaxor ferroelectric, with the ferroelectric phase showing below 35K.[32,33] Since the structure of the new system $\text{La}_{0.2}\text{Sr}_{0.7-x}\text{Ca}_x\text{TiO}_3$ was, somewhat, elusive and some impedance measurements showed changes to the capacitance of some samples with temperature, different samples were analysed for the possibility of forming ferroelectric phases at different temperatures. Although the main objective of the work in this thesis was to find an alternative anode material for SOFCs, this investigation into the ferroelectricity of the new system encourages the good practice of finding multiple uses for a given material. Also, it shows the importance of identifying and interlinking structural parameters to different physical properties and vice versa. The main studies for the structural behaviour of $\text{La}_{0.2}\text{Sr}_{0.7-x}\text{Ca}_x\text{TiO}_3$ were conducted at high temperatures resembling the operating conditions of solid oxide fuel cells. And through this study, we were able to shed some light into structural changes at sub-ambient temperatures giving the experimental setup that was used. In a way, electrical behaviour is easier to detect to indicate some minute structural changes that might be elusive with conventional diffraction techniques.

1.3 - Experimental Methods

1.3.1 - Samples preparation

Synthesis of different samples of the system $\text{La}_{0.2}\text{Sr}_{0.7-x}\text{Ca}_x\text{TiO}_3$ was carried out using the solid state method. First, the starting materials of high purity of La_2O_3 (Sigma-Aldrich 99.99%), SrCO_3 (Alfa Aesar 99%), CaCO_3 (Alfa Aesar 99.5%) and TiO_2 (Alfa Aesar 99.5%) were dried in a muffle furnace in air at 300°C for 90 minutes for CaCO_3 , SrCO_3 and TiO_2 ; and at 800°C for 2 hours for La_2O_3 . The appropriate ratios of the dried powders were then weighed as soon as they were taken out of the furnace to avoid any moisture being absorbed by the powders. These were then mixed using a pestle and mortar; which were then calcined in air at 1000°C for 15 hours. The calcined powders were then ball milled for 4 hours in acetone using a planetary ball mill. After ball milling the samples were allowed to dry naturally and then dry pressed into 13mm pellets using a uniaxial press under a pressure of 4 tons. Sintering of pellets was carried out at 1500°C for 15 hours in air. Resulting pellets were crushed and ball milled after the initial sintering, then pressed again for a second sintering at the same parameters as the initial one. Very dense pellets were obtained; i.e. relative density 92-95%. Prior to analysing the samples using XRD and NPD, all pellets were crushed and ball milled for at least 4 hours. It should be noted that in order to minimise discrepancies in the prepared samples, extra care was employed during synthesis; from using the same furnace, scale and other tools to prepare the different samples.

A pore former was made from 50:50wt% mixture of glassy carbon and graphite. Porous pellets were made from chosen compositions by sintering them with 20wt% of

the pore former mixture. All pellets were uniaxially pressed under a pressure of 4 tons and subsequently sintered at 1400°C for 12 hours in air.

Prepared pellets were pre-reduced in a tube furnace under a constant flow of a gas mixture of 5% H₂/95% Ar for 72 hours minimum. Earlier samples were pre-reduced at 900°C which was then raised to 1050°C which proved more effective in obtaining a considerable reduction to the dense pellets.

1.3.2 - X-Ray Powder Diffraction (XRD)

Unit cell parameters and space groups were investigated and determined from powder XRD patterns which were collected using CuK α radiation from an 18 kW high-resolution Rigaku ATX-E four-circle diffractometer (NRL, Washington DC, USA). In order to reduce the background, the powder samples were mounted on a single Si (001) crystal which was offset in theta to avoid any of its diffraction peaks. Runs were carried out in the range of $2\theta = 20-120^\circ$ with a step size of 0.02° . Peaks were indexed using the STOE WinXPOW (ver. 1.04) software package through the least square method. The process involved carefully choosing and marking peak positions throughout the diffraction pattern, followed by indexing the peaks to given unit cell parameters and space groups, which were initially set close to the unit cell parameters of the starting material La_{0.2}Sr_{0.7}TiO₃. These parameters were refined by carefully changing them according to the refinement outcome to ensure the stability of the fitted model. In addition, phase purity of different samples was examined from XRD patterns obtained using a STOE-StadiP X-ray diffractometer, with Cu K α_1 radiation and a PANalytical Empyrean diffractometer. Diffraction patterns were collected in the range $2\theta = 10^\circ-90^\circ$ with steps of 0.1° at 300 s/step in ambient conditions.

1.3.3 - Neutron Powder Diffraction (NPD)

NPD was carried out using the D2B powder diffractometer at the Institute Laue-Langevin (ILL) at Grenoble, France. Data were collected from powder samples in vanadium containers where the angular range was $0 < 2\theta < 160^\circ$, in 0.05° steps using a neutron radiation with $\lambda = 1.594\text{\AA}$. Counting time of the patterns varied between 2 hours for normal resolution and 5 hours for high resolution runs. High temperature studies were conducted on two samples, $\text{La}_{0.2}\text{Sr}_{0.25}\text{Ca}_{0.45}\text{TiO}_3$ and $\text{La}_{0.2}\text{Sr}_{0.2}\text{Ca}_{0.5}\text{TiO}_3$; since these two were close to the phase transition boundary between $I4/mcm$ and $Pbnm$, as well as, where the maximum conductivity at 900°C in reducing atmospheres started to decrease with calcium content (Chapter 4). A reduced phase of $\text{La}_{0.2}\text{Sr}_{0.25}\text{Ca}_{0.45}\text{TiO}_3$ was analysed since it showed the highest electrical conductivity in the range of samples of the system $\text{La}_{0.2}\text{Sr}_{0.7-x}\text{Ca}_x\text{TiO}_3$. The collection temperatures were varied between $100\text{--}900^\circ\text{C}$. All patterns were analysed and refined using the Rietveld method using the software package Fullprof (version 2.05) and the included graphics utility WinPLOTR. Diffraction peaks were refined using a pseudo-Voigt function and the background with a 6-parameter polynomial. The initial unit cell parameters were set using the findings obtained from the XRD studies and the atomic positions for the different sites were set according to the space group (symmetry). B-site (Ti) atomic coordinates were kept fixed while the other sites were allowed to vary. Occupancies were initially allowed to vary through the refinement process yielding insignificant variations from the initial stoichiometries, later these were kept fixed in order to obtain more stable refinements. All models were refined to convergence with the best fits chosen by the agreement factors and stability of the refinement process.

Also, using the software CrystalMaker (Version 2.6.2) and the results of the Rietveld refinement, the obtained structures were visually represented.

1.3.4 - DC Conductivity Measurement

The electrical conductivity of samples was measured using the conventional 4-probe DC technique in a controlled atmosphere furnace. Oxygen partial pressure was measured using a zirconia sensor with air as a reference pO_2 . Samples were prepared with four electrodes made out from platinum foil; which were attached to the surface of the sample using platinum paste. The samples were then fired using a muffle furnace at 900°C for 1 hour to burn off the organic solvent in the platinum paste and solidify the electrodes on the surface. The samples were placed in the jig with all electrodes; i.e. sample and jig; in contact which was checked using a standard voltmeter. The jig was lowered into the vertical furnace and sealed. Measurements were conducted by heating the samples at a fixed rate under chosen purge gas; i.e. mainly air and 5% $H_2/95\%$ Ar; to an isotherm at 900°C ; where changes in atmosphere were taken. The conductivity was mainly measured at 4 regimes; heating, oxidation, reduction and cooling. Data were collected at a fixed time rate which was adjusted in accordance to the sample's activity. In-house built software using LabView[®] Package was used to control the experiment and record data points. The second technique that was used to measure the electrical conductivity of different samples was the van der Pauw technique. 2-3mm thick pellets were prepared with four contacts on the periphery using gold paste. Four thin rectangular gold mesh segments were cut and attached to the gold paste contacts on the pellets. This was followed by firing the pellets at 900°C for an hour to burn off the organic solvent in the gold paste and solidify the contacts. The pellets were then placed into the jig where the gold mesh electrodes were checked for contact with the platinum

wires within the jig. The jig was inserted into the furnace and measurements were conducted in the same manner as mentioned above. The data points were recorded using similar software as the one above. The porous samples conductivity was corrected using the following relation:

$$\frac{\sigma_m}{\sigma_c} = 2 \times \left(\frac{\rho_{rel}}{100} - 0.5 \right) \quad (1.2)$$

Where σ_m is the measured conductivity, σ_c is the corrected conductivity and ρ_{rel} is the relative density of the sample.[46,65] All results were processed using Microsoft® Office® Excel®.

1.3.5 - Dilatometry

Thermal expansion coefficient (TEC) was measured using a Netzsch DIL 402C dilatometer with a load of 30-35 cN.cm⁻². The samples were ~ 13mm in diameter and 2-3.5mm in thickness pellets that were sintered in air at 1500°C for 15 hours. All sample runs were corrected using a correction run that was done prior to any measurement on a standard alumina disk. Samples were heated to 1000-1050°C with a ramp rate of 2-5K/min under different atmospheres; i.e. mainly 5%H₂/95%Ar and dry air. Data were collected and corrected using the NETZSCH Measurement software (version 4.8.5) and the data were analysed using NETZSCH Proteus – Thermal Analysis software (version 4.8.5). The same instrument was used to test the sintering behaviour of powders that were pressed into the same dimensions mentioned above. These were heated to 1430°C at a ramp rate of 2-3°/min in air where the shrinkage due to sintering was recorded as a function of temperature.

1.3.6 - Thermal Analysis

Thermal Gravimetric Analysis (TGA) and Differential Thermal Analysis (DTA) were conducted on fine powder samples weighing between 100-105 mg using a NETZSCH STA 449 C. Samples were contained within an alumina crucible. All measurements were collected and corrected using the Proteus[®] thermal analysis software. TGA analysis was also conducted using a NETZSCH TG 209 on powder samples weighing between 30-40mg where the data were collected with the same software. Samples were heated with fixed ramp rates up to 900°C.

1.3.7 - Electron Microscopy

The morphology of the samples was analyzed by scanning electron microscopy (SEM) where images were collected using a JEOL 5600 microscope. Images were collected from prepared pellets at different magnifications levels. Acceleration voltage was varied between 5-20kV while the working distance was kept around 20mm.

1.3.8 - Ferroelectricity Study

Some samples were studied for the possibility of being ferroelectric where the capacitance (C_p) and dielectric loss tangent (D_{loss}) of samples was measured at different temperatures. Both measures were obtained by using AC impedance spectroscopy on 2-3mm pellets. All pellets were surfaced on sand paper and painted with face electrodes using platinum paste. These were then fired at 900°C in air for 1 hour to burn off traces of the organic solvent in the platinum paste.

Earlier impedance measurements were conducted using an HP4192A impedance analyser with the sample mounted on a horizontal jig. The jig was placed within a tube furnace. Samples were heated in air to different set temperatures and allowed in each isotherm for a minimum of 20 minutes to achieve thermal equilibrium. Data were

analysed using ZView software (version 2.90); where the analysis involved least square fitting of impedance spectra using equivalent circuits. Due to the high resistance of the prepared samples, practical and reliable impedance analysis was more difficult using this setup.

Later, two setups were used to measure the capacitance (C_p) and dielectric loss tangent (D_{loss}) at low and high temperatures. For the low temperature measurements, samples were cooled to 30K using a closed cycle He-cryocooler with a fixed rate of 2K/min. Data were collected at different isotherms over a frequency range of 100 Hz to 10MHz using an HP4192A impedance analyser. The high temperature measurements were taken for samples heated to 450°C with a rate of 2°C/min. Impedance spectra were collected at isotherms over a frequency range of 25Hz to 2MHz using a Wayne Kerr 6500B precision impedance analyser. Impedance data were collected and converted into capacitance (C_p) and dielectric loss tangent (D_{loss}) values using an in-house built software using LabView package, which automatically carries out all the calculations to obtain those two parameters. All data were plotted using Microsoft® Office® Excel®. Dielectric constant values were obtained using the capacitance values obtained from the AC impedance results and the pellets geometry by using the following relation for the capacitance:

$$C_p = \frac{\epsilon_0 \epsilon_d A}{d} \quad (1.3)$$

Where ϵ_0 is the permittivity of free space ($\epsilon_0 = 8.854 \times 10^{-12}$ F/m), ϵ_d is the dielectric constant of the material, A is the surface area of the pellet and d is its thickness.[42-44]

1.4 - References

- [1] J. T. S. Irvine, *J. Power Sources*, 2004, **136**, 203-207.
- [2] X. Li, H. Zhao, F. Gao, N. Chen and N. Xu, *Electrochem. Commun.*, 2008, **10**, 1567-1570.
- [3] W. Z. Zhu and S. C. Deevi, *Mater. Sci. Eng.*, 2003, **A362**, 228-239.
- [4] SAE International, “*History of Fuel Cells.*” Internet, available from: <http://www.sae.org/fuelcells/fuelcells-history.htm>, accessed 4 October 2012.
- [5] J. C. Ruiz-Morales, D. Marrero-Lopez, J. Canales-Vazquez and J. T. S. Irvine, *RSC Advances*, 2011, **1**, 1430-1414.
- [6] H. Zhao, F. Gao, X. Li, C. Zhang, Y. Zhao, *Solid State Ionics*, 2009, **180**, 193-197.
- [7] SIGMA-ALDRICH, “*Aldrich Materials for Solid Oxide Fuel Cell Applications.*” Internet, available from: <http://www.sigmaaldrich.com/technical-documents/articles/material-matters/aldrich-materials.html>, accessed 12 March 2013.
- [8] M. Gong, X. Liu, J. Trembly and C. Johnson, *J. Power Sources*, 2007, **168**, 289-298.
- [9] C. Sun and U. Stimming, *J. Power Sources*, 2007, **171**, 247-260.
- [10] J. W. Fergus, *Solid State Ionics*, 2006, **177**, 1529-1541.
- [11] M. J. Escudero, J. T. S. Irvine and L. Daza, *J. Power Sources*, 2009, **192**, 43-50.

- [12] J. Canales-Vazquez, S. W. Tao and J. T. S. Irvine, *Solid State Ionics*, 2003, **159**, 159-165.
- [13] A. Lashtabeg and S. J. Skinner, *J. Mater. Chem.*, 2006, **16**, 3161-3170.
- [14] R. J. Gorte and J. M. Vohs, *Curr. Opin. Colloid In.*, 2009, **14**, 236-244.
- [15] B. H. Smith, W. C. Holler and M. D. Gross, *Solid State Ionics*, 2011, **192**, 383-386.
- [16] D. Burnat, A. Heel, L. Holzer, D. Kata, J. Lis, T. Graule, *J. Power Sources*, 2012, **201**, 26-36.
- [17] J. C. Ruiz-Morales, J. Canales-Vazquez, D. Marrero-Lopez, J. T. S. Irvine and P. Nunez, *Electrochim. Acta*, 2007, **52**, 7217-7225.
- [18] X. Li, H. Zhao, N. Xu, X. Zhou, C. Zhang and N. Chen, *Int. J. Hydrogen Energ.*, 2009, **34**, 6407-6414.
- [19] S. M. Plint, P. A. Connor, S. Tao and J. T. S. Irvine, *Solid State Ionics*, 2006, **177**, 2005-2008.
- [20] S. Tao and J. T. S. Irvine, *The Chemical Record*, 2004, **4**, 83-95.
- [21] C. Ohly, S. Hoffmann-Eifert and X. Guo, *J. Am. Ceram. Soc.*, 2006, **89**[9], 2840-2852.
- [22] M. Yashima and R. Ali, *Solid State Ionics*, 2009, **180**, 120-126.
- [23] M. Yashima, *J. Am. Ceram. Soc.*, 2002, **85**, 2925-2930.
- [24] S. Qin, A. I. Becerro, F. Seifert, J. Gottsmann and J. Jiang, *J. Mater. Chem.*, 2000, **10**, 1609-1615.

- [25] V. Vashook, L. Vasylechko, N. Trofimenko, M. Kuznecov, P. Otchik, J. Zosel and U. Guth, *J. Alloy. Compd.*, 2006, **419**, 271-280.
- [26] D. N. Miller and J. T. S. Irvine, *J. Power Sources*, 2011, **196**, 7323-7327.
- [27] S. Hashimoto, F. W. Poulsen and M. Mogensen, *J. Alloy. Compd.*, 2007, **439**, 232-236.
- [28] O. A. Marina, N. L. Canfield and J. W. Stevenson, *Solid State Ionics*, 2002, **149**, 21-28.
- [29] J. C. Ruiz-Morales, J. Canales-Vazquez, C. Savaniu, D. Marrero-Lopez, W. Zhou and J. T. S. Irvine, *Nature*, 2006, **439**, 568-571.
- [30] A. Vincent, J. Luo, K. T. Chuang and A. R. Sanger, *J. Power Sources*, 2010, **195**, 769-774.
- [31] C. D. Savaniu and J. T. S. Irvine, *Solid State Ionics*, 2011, **192**, 491-493.
- [32] M. A. Carpenter, S. Rios, P. Sondergeld, W. Crichton and P. Bouvier, *J. Solid State Chem.*, 2007, **180**, 360-369.
- [33] J. Manchado, F. J. Romero, M. C. Gallardo, J. del Cerro, T. W. Darling, P. A. Taylor, A. Buckley and M. A. Carpenter, *J. Phys.: Condens. Matter*, 2009, **21**, 295903.
- [34] M. B. Smith, K. Page, T. Siegrist, P. L. Redmond, E. C. Walter, R. Seshadri, L. E. Brus and M. L. Steigerwald, *J. Am. Chem. Soc.*, 2008, **130**, 6955-6963.
- [35] F. D. Morrison, D. C. Sinclair and A. R. West, *J. Am. Ceram. Soc.*, 2001, **84**, 531-538.

- [36] A. P. Ramirez, M. A. Subramanian, M. Gardel, G. Blumberg, D. Li, T. Vogt and S. M. Shapiro, *Solid State Comm.*, 2000, **115**, 217-220.
- [37] R. Zuo, S. Su, Y. Wu, J. Fu, M. Wang and L. Li, *Mater. Chem. Phys.*, 2008, **110**, 311-315.
- [38] C. Elissalde and J. Ravez, *J. Mater. Chem.*, 2001, **11**, 1957-1967.
- [39] V. V. Lemanov, A. V. Sotnikov, E. P. Smirnova, M. Weihnacht and R. Kunze, *Solid State Comm.*, 1999, **110**, 611-614.
- [40] M. A. Subramanian, D. Li, N. Duan, B. A. Reisner and A. W. Sleight, *J. Solid State Chem.*, 2000, **151**, 323-325.
- [41] J. Liu, C. Duan, W. Yin, W. N. Mei, R. W. Smith and J. R. Hardy, *Phys. Rev. B*, 2004, **70**, 144106.
- [42] MIT Web, Physics II, “Chapter 5: Capacitance and Dielectrics.” Internet, available from <http://web.mit.edu/8.02t/www/materials/StudyGuide/guide05.pdf>, accessed 4 October 2012.
- [43] M. O. Orlandi, M. A. Ramirez, C. R. Foschini, A. A. Felix and J. A. Varela, “Giant Dielectric Constant Materials and Their Applications,” in *Sol-Gel Processing for Conventional and Alternative Energy*, ed. M. Aparicio, A. Jitianu and L. C. Klein, Springer US, New York, **2012**, 123-146.
- [44] Georgia State University, Hyper Physics, “Parallel Plate Capacitor.” Internet, available from: <http://hyperphysics.phy-astr.gsu.edu/hbase/electric/pplate.html#c1>, accessed 4 October 2012.

- [45] Cleantech magazine, “*Fuel Cells: two centuries of development.*” Internet, available from: <http://www.cleantechinvestor.com/portal/fuel-cells/9699-fuel-cells-two-centuries-of-development.html>, accessed 20 February 2013.
- [46] F. Tietz, I. A. Raj, Q. X. Fu and M. Zahid, *J. Mater. Sci.*, 2009, **44**, 4883-4891.
- [47] J. Zhao, N. L. Ross, D. Wang and R. J. Angel, *J. Phys.: Condens. Matter*, 2011, **23**, 455401.
- [48] S. McIntosh and R. J. Gorte, *Chem. Rev.*, 2004, **104**, 4845-4865.
- [49] R. Jain and B. Mandal, “*Studies on Ideal and Actual Efficiency of Solar Polymer Electrolyte Fuel Cell,*” in The Alternative Energy eMagazine, February 2007. Internet, available from: http://www.altenergymag.com/emagazine.php?issue_number=07.02.01&article=solar_polymer, accessed 25 March 2013.
- [50] F. Zhao and A. V. Virkar, *J. Power Sources*, 2005, **141**, 79-95.
- [51] S. Farhad and F. Hamdullahpur, *Electrochim. Acta*, 2012, **61**, 1-12.
- [52] N. H. Menzler, F. Tietz, S. Uhlenbruck, H. P. Buchkremer and D. Stöver, *J. Mater. Sci.*, 2010, **45**, 3109-3135.
- [53] A. Atkinson, S. Barnett, R. J. Gorte, J. T. S. Irvine, A. J. McEvoy, M. Mogensen, S. C. Singhal and J. Vohs, *Nat. Mater.*, 2004, **3**, 17-27.
- [54] J. Brouwer, “1.4: Hybrid Gas Turbine Fuel Cell Systems.” Internet, available from: <http://www.netl.doe.gov/technologies/coalpower/turbines/refshelf/handbook/1.4.pdf>, accessed 25 March 2013.

- [55] U.S. Department of Energy, Fuel Cell Technologies Program, “Comparison of Fuel Cell Technologies.” Internet, available from http://www1.eere.energy.gov/hydrogenandfuelcells/fuelcells/pdfs/fc_comparison_chart.pdf, accessed 25 March 2013.
- [56] X. Huang, H. Zhao, X. Li, W. Qiu and W. Wu, *Fuel Cells Bulletin*, 2007, **7**, 12-16.
- [57] S. C. Singhal, *Solid State Ionics*, 2002, **152-153**, 405-410.
- [58] S. Park, J. M. Vohs and R. J. Gorte, *Nature*, 2000, **404**, 265-266.
- [59] E. Lay, G. Gauthier, S. Rosini, C. Savaniu and J. T. S. Irvine, *Solid State Ionics*, 2008, **179**, 1562-1566.
- [60] P. I. Cowin, C. T. G. Petit, R. Lan, J. T. S. Irvine and S. Tao, *Adv. Energy Mater.*, 2011, **1**, 314–332.
- [61] J. C. Ruiz-Morales, J. Canales-Vázquez, C. Savaniu, D. Marrero-López, P. Núñez, W. Zhou and J. T. S. Irvine, *Phys. Chem. Chem. Phys.*, 2007, **9**, 1821–1830.
- [62] B. A. Boukamp, *Nat. Mater.*, 2003, **2**, 294-296.
- [63] S. Tao, J. T. S. Irvine and S. M. Plint, *J. Phys. Chem. B*, 2006, **110**, 21771-21776.
- [64] A. Ovalle, J. C. Ruiz-Morales, J. Canales-Vázquez, D. Marrero-López and J. T. S. Irvine, *Solid State Ionics*, 2006, **177**, 1997-2003.
- [65] H. Tagawa, J. Mizusaki, Y. Arai, Y. Kuwayama, S. Tsutiya, T. Takeda and S. Sesido, *Denki Kagaku*, 1990, **58**, 512.

Chapter 2

The United Arab Emirates and its Energy Future

A Closer Look

Abstract:

The United Arab Emirates is actively exploring the spectrum of renewable energy technologies for maintaining its growth while lowering the impact on both the environment and the economy. Given the healthy economy of the country and the abundant oil revenues, the UAE has an advantage and more freedom in trying and adopting different types of renewable energy technologies. However, power is not the sole concern for a secured future of the country. Water is widely regarded to be much more important than power. The scarcity of fresh water supply in the UAE requires a deeper and more evolved method of planning for combining different technologies in both sectors; i.e. power and water production. Hence, a plan is proposed which combines different renewable energy technologies; with an emphasis on the adoption of fuel cell related techniques; that can provide both power and fresh water in the future with minimum impact on the environment. This study gives a very clear perspective and justification to the continuous efforts that are made to find new materials for solid oxide fuel cells that improve flexibility and applicability.

2.1 - Introduction

The United Arab Emirates (UAE) is a federal union of seven different emirates; i.e. States; that was established on the 2nd of December 1971. Prior to this day, the region consisted of different sheikhdoms and tribes under the protection of the British Empire at the time. Given its location on the trade routes between the West and the Indian subcontinent, the UAE economy mainly relied on trade, fishing and the pearl industry.



Figure 2.1: Map showing the location of the UAE; a midpoint between west and east.[8]

Since the discovery of oil in the 1960s, the region evolved from dispersed Bedouin tribes throughout the desert and some fishing towns on the coast to one of the most developed countries in the world. The revenues that oil exports brought were heavily invested in developing the infrastructure of the country and the development of the welfare of its people. One of the main and intensive aspects of the country's development was lowering the dependence on oil as the main source of income. The

UAE's government invested huge amounts of funds in industry, infrastructure, services and trade. The diversification of the economy is the backbone of the development programmes in the UAE; nowadays more than 70% of the GDP comes from non-oil sectors.[1] The latest estimates show that the UAE's GDP per capita is ranked 11th in comparison with the rest of the world.[2] The latest estimates showed that the population of the UAE has more than doubled since 2005 to reach over 8.26 million people in 2010.[3] Among this, there are only 947,997 native citizens; which indicate the rapid increase in foreigners coming to the country mainly to work or for business. This growth reflects the continuous development of the UAE; which makes it a potential customer for new technologies that can help drive this development and provide future security in different aspects.

Ever since its establishment, the UAE has kept a keen eye on preserving and protecting the local environment; which made it one of the leading countries in the world when it comes to protecting the environment while sustaining development and growth. By funding diverse programmes from protecting endangered wildlife species to natural habitat restoration; the government shows a strong commitment to environmental issues. Many laws have been issued for protecting the local environment; notably the prohibition of hunting, mass grazing, mass fishing practices and uncontrolled underground water exploitation. The UAE was one of the first major oil producing countries to sign and ratify the Kyoto Protocol; which is targeted on fighting global warming.[4] In June 2009, the capital of UAE, Abu Dhabi, was chosen to be the host city for the headquarters of the International Renewable Energy Agency (IRENA).[5] The UAE government has committed to cover 42% of the agency's funding by offering a grant worth \$136 million, as well as, supporting the operational

cost of IRENA for the first 6 years.[6,7] The new agency's headquarters are to be based in Abu Dhabi's MASDAR City; the world's first green city; which is part of the MASDAR Initiative. These actions and many others are clear indications of the UAE commitment towards an environment friendly development and growth for a better future.

Sustaining a continuous development requires, ultimately, sustaining the population's well being and needs. Power on one hand is a major component of the infrastructure development in the UAE; where it is a major objective for the government to meet the current and future power demands. The local environment of the country makes it, also, very necessary to address the sustainability of fresh water. The arid climate and the natural landscape of the UAE put a huge strain on the country's water resources. Securing power supplies thus might not be the most important factor for the future of the people, or the country as a whole; water availability could be more vital in the future. Certainly, water scarcity was part of the history of the people living here; however, an increasing population requires new ways of planning ahead in order to secure both resources; while maintaining a low impact on the environment in doing so.

In this chapter, a discussion is outlined for the different options available for the UAE to sustain its growth through careful adoption of different renewable energy technologies; taking into account different aspects that are unique to this part of the world and should be considered carefully when planning for the future. Most research efforts aimed at developing very efficient and applicable renewable energy technologies outline general schemes that can be implemented all over the globe. However, it is equally important to consider specific conditions and local parameters in order to develop very enticing and convincing schemes to be embraced by certain markets and

societies. Selling an idea is very important when it comes to driving scientific research in all different disciplines forward.

2.2 - The Nature of UAE

In recent years the UAE has increased its commitment to provide sufficient resources for its growth, while keeping in mind the protection of the local environment. With growth comes higher demand for power and being one of the largest oil producing countries in the world, the cost for power generation through the use of hydrocarbons is relatively cheaper compared to leading countries in the western hemisphere. However, given the type of climate the country has; which is a very arid climate and the largest portion of the country being a desert; puts certain strains on the future of this growth. The country is mostly covered with sand desert with some mountains on the eastern part of the country. Most of the major cities are on the coast of the Gulf, with one of the emirates located on the coast of the Gulf of Oman, which is an extension of the Indian Ocean, on the east. There are a few cities and towns that originated around small oases.

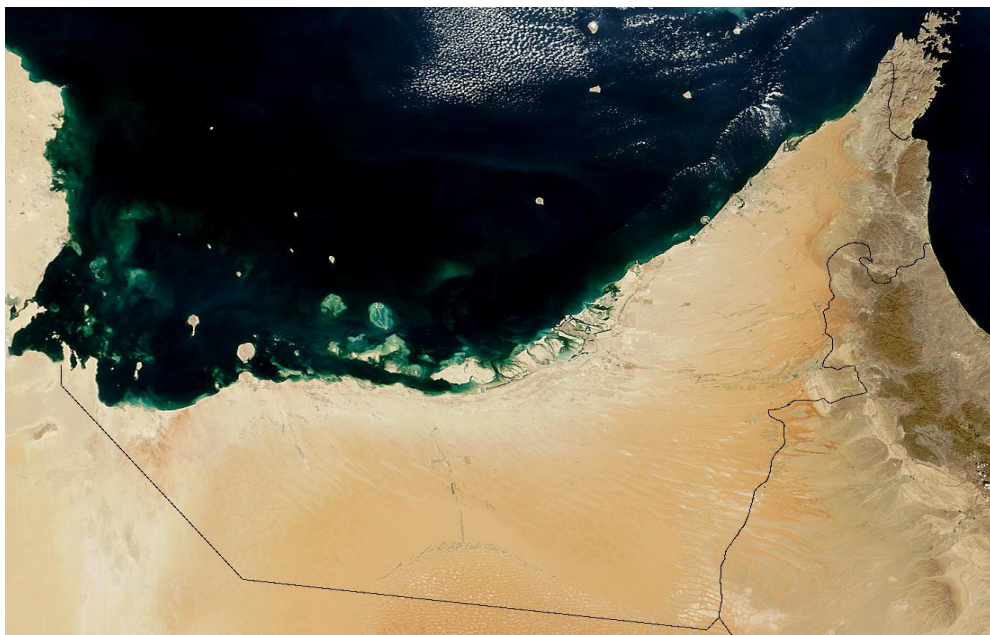


Figure 2.2: A satellite image of the UAE, showing the spread of the desert.[52]

The UAE has a very low rainfall level, high temperatures; i.e. over 30°C; most of the year and re-occurring sand storms. These storms sometimes are very severe and lead to many disruptions around the region; not to mention sand accumulation over surfaces and structures.[45]



Figure 2.3: Image illustrating the severity of sand storms in the UAE.[45]

It was estimated that the annual rainfall in the Emirate of Abu Dhabi; which is the largest emirate; is less than 100mm/year. This is reflected on the underground water recharge rate which is very low; which is only 4% of the total annual water consumption. Thus, Abu Dhabi has one of the highest water consumption rates per capita in the world.[9] In 2008, it was estimated that the annual renewable water resources of the whole country is only 0.2 km³. [10] The latest figures suggest that the annual water consumption of water in Abu Dhabi, alone, was 210183 million gallons in 2010; i.e. around 0.96 km³. [11] To address this problem, the country has invested

heavily in building desalination plants to bridge the gap between fresh water production and consumption.

Since most of the country is covered with desert sand; i.e. 80% of its total land area[12]; the government focused on increasing the spread of greenery and agriculture. Vast funds were transferred in developing water resources, irrigation methods, building water dams, agriculture and forestry. The main objective behind these efforts was to increase the country's green areas to provide better habitats for local and migrating wildlife species and to stop or slow the sand or desert movement towards inhabited areas. Citizens were encouraged to adopt farming by providing them with huge subsidies for seeds, fertilizers, irrigation systems and well digging. This proved to be a very successful policy at the time since it provided the people with an extra source of income and helped increase the green surface area around the country. Unfortunately, rainfall kept declining in the past 20 years, putting a strain on these farms and the overall underground water reserves; which are now more or less completely depleted.

Thus, it is very important to think about developing the country's water resources as well as its energy resources. Water security might be considered, in the case of UAE, to be more important than securing future energy demands.

2.3 - The Current Situation:

The UAE government is trying its best to sustain the growth of the country by providing the necessary infrastructure elements needed to sustain the very high living standard of its population. Since its formation, the country has invested extensively into building many power stations; in order to drive the country into a more diverse economy from the sole reliance on oil and gas. Today, power is readily available and

demands are met; given the current capacities of the country's power plants. Most of these plants are powered by gas turbines; where most of the natural gas used is imported through a pipeline from neighbouring Qatar. Many of these plants are combined with desalination units to compensate for the shortages of underground water reserves.

According to the ministry of energy in the UAE; the annual energy consumption has increased from 48155 GWh in 2003 to 89587 GWh in 2010, showing an increase of about 46%. [11,13] All these years, this consumption of power was met with an increase in the capacity of power generation. For the same period, the generation capacity has increased from 12217MW to 23215MW; where in 2010 it was estimated that gas turbines accounted for 19335MW of the gross power capacity; amounting to almost 83.3% of the power capacity of the country. [11,13] Thus, this shows that the UAE is increasingly relying on natural gas as the main resource for power generation. In 2006, the consumption of natural gas has reached 42.1 billion cubic metres in the emirate of Abu Dhabi alone; where electricity and water desalination have dominated with a 61% share. [14] Demand for power is expected to more than treble by 2030, according to forecasts by the Abu Dhabi Water and Electricity Authority (ADWEA). [15] The same forecasts are expecting the peak demand to grow above the 7.5% p.a. trend to 11% p.a. between the years 2009 and 2019. The peak demand for power in the UAE increases substantially during the months of summer; see figure 2.4. This increase is indicative of the increase use of air conditioning; since, as mentioned earlier, temperatures can soar to over 48°C during the day in summer, e.g. 40% of the power produced in Abu Dhabi is consumed by air-conditioning. [17]



Figure 2.4: Dubai's peak demand for electricity for 2009 and 2010.[16]

On the other hand, water demand is increasing as well and is expected to double by 2030. Between 1999 and 2009 water production has increased by 210% through mainly desalination of sea water.[15] In 2006, the annual consumption of water in Abu Dhabi was found to be 3123 million m³. Most of the water is supplied by desalination plants and the rest is from fast decreasing underground water reserves through wells. The total desalination production is 742.41 million m³. According to Abu Dhabi Environment Agency (EAD), the total production of water from the different sectors; i.e. desalination, underground and treated water; was only 3123.22 million m³; which can result in water shortages in the near future since water production and the power consumed in the different sectors may lag behind the continuous increase in water demand per year. There are more than 28 sewage treatment plants around Abu Dhabi which can produce about 150 million m³ annually; where this treated water is mainly used for irrigation of green surfaces and public parks.[9] In 2009 the total fuel consumed in generating electricity and water production was 537,215,887 MBTu; 97% of which was natural gas.[15] Thus, it is very obvious that the efforts to drive the

economy of the UAE are very costly and it could be argued that this trend cannot be sustained in the future if the predictions of growth are met; especially when it comes to providing the much needed fresh water.

2.4 - Is Desalination Sustainable?

In 2010, it was estimated that the total water production in the UAE has reached 375,663 million gallons; to meet a consumption of 344,462 million gallons. Desalination accounted for 355,964 million gallons in the same year; that is about 94.8% of the total fresh water made available in the country.[11] For now, this technique is the most obvious choice because of the arid climate the UAE has, and the limitations of the underground water aquifers. However, there are many good reasons to think that seawater desalination is not sustainable in this part of the world; especially with the high consumption rates the country has compared to other countries around the world.

The three factors that affect the cost of desalination are energy costs, feed water salinity levels and plant size.[22] In the case of UAE, almost all of the energy produced is driven by local and imported natural gas. And it is known that the price of this commodity varies according to geopolitical, economical and even natural reasons. Thus, it is nearly unpredictable how much it will cost to desalinate the same amount of seawater in the future. The latest trends in the world markets indicate that the prices of oil and gas are on the increase and it is becoming increasingly expensive to generate power using hydrocarbons. It is true that the UAE is one of the leading oil producing countries in the world and it has large amounts of natural gas reserves; but the other

factor is the impact on the environment from the existing energy and water production methods.

The second factor that affects the desalination cost is the salinity level of the seawater. The UAE main desalination plants are located along the coast of the Arabian Gulf; which is a semi-enclosed sea. The Arabian Gulf is known to have the highest number of desalination plants in the world; accounting for around 45% of the total worldwide daily production.[18] The UAE has most of these desalination plants around the gulf with a share of 26% of the world's total desalination capacity.[18] With around 120 desalination plants in the countries surrounding the Arabian Gulf; i.e. the UAE, Saudi Arabia, Qatar, Bahrain, Kuwait and Iran; these plants process more than 12 million m³ of sea water every day; however, on a daily basis, they discharge around 24 tonnes of chlorine, 65 tonnes of algae-harming antiscalant chemicals and around 300 kg of copper.[19] These quantities are alarming for the wellbeing of the eco-systems in the gulf; which in fact now has the highest saline concentration in the world apart from the Dead Sea; i.e. 45 g/l.[20,21] Given the arid climates of these countries and the semi-enclosed nature of the gulf indicates that salinity levels are to keep increasing in the future. The hot climate of the region increases the evaporation of seawater accompanied with very low rainfall, salinity level is increasing without any human intervention. Also, since the only way for water exchange with the Indian Ocean is through the narrow Strait of Hormuz; the flow of low saline water into the gulf is thought of to be very low. Thus, in addition to harming the ecological system in the gulf, currently these plants are adding to the cost of their own operation by the extensive discharges they release every day. So, it is expected that in the future these plants will require more power and

processing of the intake water in order to desalinate the same volumes of today. Not to mention the continuous release of greenhouse gasses.

Finally, the cost of desalination increases with the plant size. The size is determined by the production levels required; which are increasing by demand in the UAE. Since most of the underground water resources have been extensively exploited, along with the lack of any other fresh water resources; it is inevitable that the size of the sea desalination industry is going to expand in the future. This increase is not going to be solely in the UAE; it will be as well in the rest of the gulf countries which are developing with the same pace as the UAE. Thus more power and water will be needed in the near future; and since the cost is relatively low in this part of the world, the populations do not feel the need to lower their consumption levels; which are among the highest in the world. Experts do indeed warn that if things continue in this manner, the gulf region, and the UAE included, will face a crisis in the future if energy costs do rise.[23,24]

To conclude, desalination at the current rates does not seem to be sustainable and its effects on the environment cannot be ignored.[42] Energy is relatively cheap in the UAE nowadays and desalination might seem cost-effective. However, with the current and the predicted consumptions the country might face a crisis; unless tougher actions are to be taken. Currently, most consumers get their energy and water much cheaper than other parts of the world; due, in part, to heavy subsidies by the government; and this might be a main driver for the economic boom in the UAE. Authorities should explore new methods to encourage the consumer to save on their use of power and water; as well as; better technologies to feed the demand by the different sectors in the country.

2.5 - Addressing the Challenges

The UAE is considered one of highest energy consumers per capita in the world and that makes it one the highest CO₂ emitters in the world; ranking 30th in 2003.[25] From 2002 to 2008, the CO₂ emission of UAE has increased from 94.2 to 146.9 million tonnes.[26] This increase has led the government to act quickly to address this issue. Also, it is expected that the country will require over 40000 MW of electricity supply by 2020.[29] Thus, the government has announced its plans to build four 1400 MW nuclear reactors to cut down on its CO₂ emissions and help provide 25% of the expected demand of power.[43] The first one is expected to go online in 2017 with the rest to be completed by 2020.[30] Also, the government of Abu Dhabi has outlined in its ‘Abu Dhabi Economic Vision 2030’ to have 7% of its total energy from renewable energy sources by 2020.[27] Many of the local and federal agencies around the country have undertaken actions to lower their carbon footprint. A major driver towards this target is MASDAR; which is based in the emirate of Abu Dhabi.

MASDAR has been established from the Emirate of Abu Dhabi efforts; and the UAE as a whole; to diversify the economy from being very reliant on the oil industry. Established in 2006, MASDAR became a multimillion investment company which invests in and acquires renewable energy companies and developers around the world. This investment is mainly to bring the latest advances in the environment friendly energy technologies to the country. The company is currently involved in many different projects which include a 100MW concentrated solar power plant (CSP)[55], carbon capture and storage, wind farms and photovoltaic panels manufacturing and installations. It also provides capital for different research and development

programmes around the world.[27,28] This company has captured the interest of many people who are involved in the renewable energy sector around the world when it announced its plans to build the first carbon-neutral city in the world, MASDAR City. This city is currently housing the MASDAR headquarters and the MASDAR institute. The institute is a graduate university which offer different degrees in major disciplines within the renewable energy industry. The main power source for this city will be solar energy via PV panels and CSP, along with many innovative methods for a green community.[41] Such a novel initiative, coming from a major oil producer, shows the concerns and the commitment of the UAE government to lower its impact on the environment.

2.6 - Considerations

It is no wonder that the government of UAE has considered nuclear power as an option for providing the needed energy in the future. Nuclear power is the best alternative so far from hydrocarbon based power generation mechanisms. It is obvious what dangers nuclear power posses, especially after the late incident in Japan which resulted after a major earthquake that caused much damage and drawn the attention of the world to the dangerous aspects of this type of power generation. However, if planned carefully and managed properly nuclear power proves to be a very effective method for generating electricity compared to the current methods employed in the UAE. The country mainly relies on its huge gas reserves as well as on a large imported portion from Qatar to producing water and power. The UAE has moved from being an exporter of natural gas to an importer in order to sustain its local power demands. Although huge investments have been taken into improving the efficiency of the current

power infrastructure, the increasing demand and the future's predictions led to considering nuclear power as a major alternative. Nuclear power, however, cannot be considered to be a renewable, environmentally friendly option, since the nuclear waste that results from this method of power generation is still a major issue. Many are trying to find effective methods for handling and processing the radioactive waste of the depleted fuel rods. Nonetheless, nuclear power is considered very efficient and cost effective method for generating power.

On the other hand, the UAE can be seen to have plenty of sunshine readily available around the year giving its arid climate. This gives the impression that solar energy is the way forward. But, if we consider the current efficiencies of many of the state of the art PV panels that are available in the market; which are very low; this means that large areas would be converted to accommodate more of these panels. Being relatively expensive and by taking large areas to provide sufficient power to the national grid; it can be argued that this will add to the cost. Also, for the special nature of the UAE climate which suffers from high temperatures and frequent sand storms; this will add further to the complexity of a large scale PV based power generation. PV panels have low efficiencies with most of the readily available ones come with efficiencies between 12-19%.[31] Many studies has shown that dust, humidity and heat considerably affect the performance and the efficiency of PV panels. Temperatures can reach over 50°C in the summer and over 90% humidity on the coast.[32] Along with frequent sand storms and wind carried particles, those panels can be obscured or even damaged rendering them obsolete. These conditions can result in PV panels' degradation through corrosion, delamination, defect growth and mechanical stresses. Also, the combination of dust or sand with humidity will lower the power output and efficiency of these panels

since more sunlight will be obstructed from reaching the active layers due to deposits formation on the glass surface.[33-35] Thus, in the conditions present in the UAE, these panels will require frequent cleaning, maintenance and might be replaced more frequently than the advertised performance warranty from the manufacturer.

Concentrated solar power (CSP), on the other hand, is more robust when it comes to maintaining optimal power; since mirrors are easily maintained and replaced. However, sand storms and high humidity can lower their efficiencies, and hence, lowering their cost-effectiveness. Contrary to PV, CSP can have continuous operation even in the dark. Through a joint venture between MASDAR and Spanish firm SENER, a new CSP plant was constructed in Spain. The \$320 million Gemasolar facility at Fuentes de Andalucía in Seville can provide power for 24 hours; which is considered the first solar power plant in the world capable of that.[36] The molten salt used as the heat medium can hold enough heat for many hours after sunset. Such a technology can be perfectly suited for the UAE.

Solar energy is the most obvious choice for a country like the UAE. But like any other technology, using them to provide power to the grid can be wasteful as well. This is because much of the power fed to a national grid is not used by the consumer; especially at peak periods. Also, having solar plants during sandstorms or thick fog will turn them obsolete for many hours; not to mention the possibility of damage that these factors can have on the panels or reflectors. That is why it is more beneficial for the UAE and the rest of the world to think about storing that energy when it is available into a more useful medium.

2.7 - Hydrogen

Many of the renewable energy technologies; i.e. solar, wind, tidal, etc.; are periodic and rely heavily on the natural conditions that drive them. Improving grid systems and power recovery can be useful when using such technologies. However, there is a better alternative. Hydrogen gas can be utilised as a fuel in fuel cells. Fuel cells show much better efficiencies than most of the current technologies; e.g. gas turbines and internal combustion engines. The problem is the supply and production of hydrogen and the establishment of a hydrogen infrastructure and economy. In 2002, only 4% of the hydrogen produced worldwide was obtained through electrolysis; while the rest was produced using fossil fuels.[46] Thus, in order to lower the impact on the environment and cut down on global warming, renewable sources should be used to produce hydrogen and the UAE have a very good natural source for that; the sun.

Using solar energy, hydrogen can be produced through different processes; mainly electrochemical, photochemical and thermochemical.[37,38] The first method is the most straightforward which feeds a current through an electrolysis cell where water molecules are split into hydrogen and oxygen. Photochemical processes; sometimes referred to as photocatalysis; involve water splitting by using a semiconductor material to absorb the direct sunlight; which generates an electric current to facilitate water splitting. The last process, thermochemistry, is a high temperature chemical process with multiple steps to generate the same products from water. All of these processes seem very suitable for the UAE. Most of the hydrogen production nowadays is achieved through methane steam reforming [39]; which produces CO₂ and it is mainly driven by conventional hydrocarbons based power. Water electrolysis is very attractive if

combined with green power; i.e. renewable energy sources such as solar and wind. Storing the excess energy in batteries; especially with PV technology; can be unsustainable due to the nature of most batteries, beside they add up to the overall cost.

2.8 - The Proposal

In this work, a future look is proposed for the UAE to secure its power alongside its water needs by combining different renewable technologies. Since the government has invested in solar power in great scale, as well as, establishing nuclear power to meet its future demands and the continuous build up of desalination facilities to meet high water consumption levels, fuel cell technology can be a future asset in providing much of the needed power with pure water as a by-product. Rising water consumption levels indicate higher production of waste water from the different sectors within the country; putting a heavier strain on the current power and water production facilities.

We can argue that there are alternative ways for securing both power and water for the future; while having no or low impact on the environment. Since the emirate of Abu Dhabi has many sewage treatment plants, as mentioned earlier, and many are being planned for the future; with better recycling of the produced water, a large portion of it can be readily available for hydrogen production. Most of the recycled-water produced by these plants is used for irrigation purposes. A system can be designed where solar energy can be used to power a sanitation plant; thus taking it off the grid. Afterwards, the produced water can be heated using concentrated solar energy or solar electricity in order to generate steam; which is then fed to an electrolysis system. Generating steam from waste water ensures that it does not need to be processed and/or purified even further to remove any solid contaminants that might affect the electrolysis cell performance. Also, high temperature steam electrolysis is more efficient than water

electrolysis because it consumes less power than water electrolysis and it is thermodynamically and kinetically favourable.[47] The products of electrolysis; i.e. oxygen and hydrogen gasses; can be stored or fed into existing pipelines for later uses. Storing hydrogen might be relatively easy in a major oil producing country with many storage tanks scattered around the country. There have been, also, many suggestions of storing hydrogen in depleted oil and gas fields, if this proves useful then the UAE has a great potential for having significant reserves of hydrogen. Oxygen on one hand can be used to generate an extra income by selling it to industry across the country or abroad; generating a source of income for such a project. Also, there are many indications that the fish stock in the gulf are declining as a result of the extensive desalination activities and other practices.[48] Thus, using pure oxygen for fish farming can be very useful. High oxygen level in the water is known to promote the growth of fish and improve its health and reproduction rates. Aeration systems which employ air may not raise the dissolved oxygen to significant levels in water due to the fact that there is only 21% available oxygen in air. Using air only can lead to increased consumption of power due to increased operation of such aeration systems. With the proposed waste water electrolysis using solar energy; abundant pure oxygen can be provided to a fish farming sector that will bring great benefits to the community in providing a major food resource; and if electrolysis is employed on a large scale, pure oxygen will be available at a lower cost, eventually.

Hydrogen, on the other hand, can be used in many different ways in industry in the meantime; however, the UAE has many mature oil fields, where hydrogen can be injected into them to be stored for future uses. Hydrogen is already considered as a very favourable alternative to fossil fuels for automobiles with major companies planning

ahead the production of fuel cell driven vehicles. Major testing projects; e.g. “Controlled Hydrogen Fleet and Infrastructure Demonstration and Validation Project” in the USA and the “Japan Hydrogen Fuel Cell Project (JHFC)” in Japan; were started to test the prospect of hydrogen fuel cell vehicles and the underlying infrastructure, with major car manufacturers announcing their plans to start sales of such vehicles as early as 2015.[52] Since oil prices are currently generating a high return and the UAE has the funds and means nowadays to utilise renewable energy sources; an investment in building up a significant hydrogen reserve seems applicable with low financial risks. Ultimately, the aim is to use the produced hydrogen in fuel cells generating both power and pure water from thin air; see figure 2.4. As scientific research continues to offer improvements to fuel cells in many different aspects, as well as, finding alternative materials altogether that would bring the cost of fuel cell systems down in the near future; having a significant hydrogen gas reserve will certainly prove to be very useful, especially if the hydrogen economy become very feasible in the near future. Moreover, given the huge amounts of natural gas that are being used currently to produce power and water; i.e. through desalination; in the UAE, there is a good alternative that can be utilised to improve efficiencies. This alternative is direct methane solid oxide fuel cells; which provide much higher efficiencies when compared to conventional gas turbines.[49] Methane can, also, be extracted from the waste water streams using different processes; e.g. anaerobic digestion of sludge; hence, increasing the overall efficiency of the proposed system for the UAE.[53,54] Most importantly, through proper exhaust management of the above type of fuel cell, pure water can be extracted and collected to be supplied to consumers; forming a co-generation system.

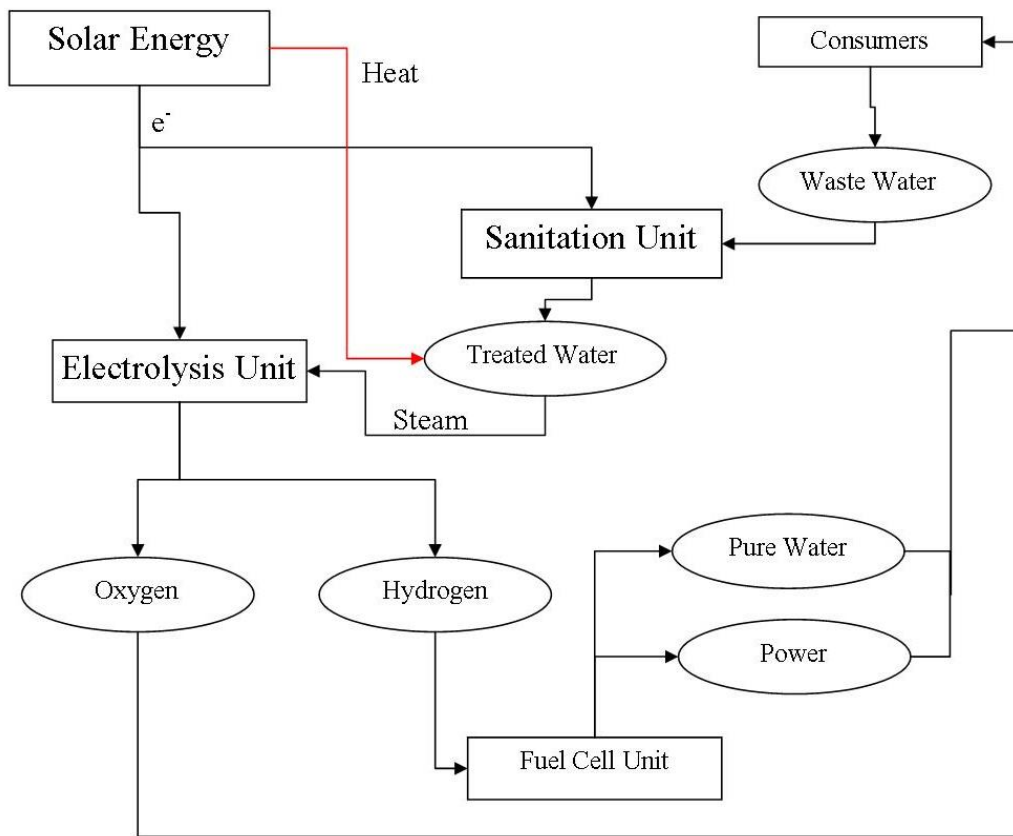


Figure 2.5: Flow chart representing the proposed hydrogen-based system for meeting future needs of the United Arab Emirates.

The higher efficiency of a co-generation methane-based system will definitely lower the harmful impact on the environment while lowering the overall cost on the government in terms of fuel, as well as, maintenance costs; i.e. conventional hydrocarbon generators and gas turbines require extensive maintenance efforts to keep them in optimal condition. Such a system is very much feasible and can prove to be very cost effective. Also, there are some suggestions that SOFC systems can be utilised to drive a gas turbine through the utilisation of the generated high temperature exhaust. Such a design is thought to give over 65% efficiency.[50] These potential applications can be considered as major drivers in the development of alternative anode materials for solid

oxide fuel cells that are fuelled by hydrocarbon based fuels; e.g. methane. Such target can see a faster implementation of fuel cell technology in different markets without the complications of establishing a hydrogen-based economy or infrastructure. Current state of the art SOFC anodes, the Ni-YSZ cermet, degrade quite significantly with sulphur and carbon containing fuels; hence, finding new materials to address those issues is vital.

What is needed now is a state funded project that will look into the feasibility of scaling up the proposed system (figure 2.5) so that it comes into par with existing technologies. Also, an involvement by the UAE government through investing in fuel cell technology can give a boost to the industry which can, in turn, bring in more governments and businesses into investing in fuel cells and the associated scientific research; thus driving the technology even further. The cost of such a plan will be immense at the beginning. However, if planned carefully, it can be seen that the initial cost of building a CSP plant, fuel cell units and electrolysis units along with the cost of an existing sanitation plant can be balanced by four new products. Hydrogen can be utilised and sold as a fuel for fuel cell based vehicles; e.g. the hydrogen bus.[40] Oxygen can be sold to different manufacturers as well to cover a bit of the initial cost if produced in large quantities and, as mentioned earlier, can be used in fish farming; which would generate a large income. When the hydrogen is used in the fuel cell unit it generates electricity which can be readily sold back to the grid. The by-product; pure water; is considered nowadays more valuable than oil and sometimes more expensive. Thus, a system like the one mentioned above can support itself with time and once all costs are covered, the system will generate huge profits since it is using free energy and wasted undrinkable water to make power and potable water at the end of the cycle. All

in all, achieving such a vision will require a long term commitment in order to bring the renewable technologies mentioned to the same level of production as the conventional technologies. Large scale fuel cells could at least provide and close the gap of electricity demand imposed by the use of air conditioning in the UAE; which will eventually lower the cost of generating electricity; e.g. about 40% of fuel could be saved; since fuel cells provide much higher efficiencies than most conventional systems.

Fuel cells and electrolysis technology are developing by the day through research and an early investment in this sector will give the UAE a unique lead away from political and financial obstacles that may exist in other parts of the world. One might consider this part of the world well off when it comes to energy costs, but the reality is far from it. To achieve such stability requires very serious and bold decisions to be made in order to protect the local environment and keep the economy in a good shape. The study in this chapter justifies the search for alternative anode materials for SOFCs, which is the main part of this thesis. As shall be seen, finding new anodes that are tolerable to many different types of fuel, especially hydrocarbon based ones, is very important for countries like the UAE. As mentioned, being one of the major oil producing countries in the world, the UAE is already consuming so much in order to meet its local power and water demands. Thus, new anodes can provide the key ingredient to give a huge boost to fuel cells development and adaptation. Alternative anode materials that are tolerable to fuel impurities and well performing under hydrocarbons, especially methane, can bring huge investment/funding for research and manufacturing efforts from countries like the UAE. Under the current global economical conditions, funding for such research programmes is in short supply. Thus, from the need of many countries in this part of the world, a large boost can be attracted

for funding research in hydrogen/hydrocarbon based fuel cells that can be used for cogeneration of power and water very efficiently. These materials advancements can save so much in the cost of power and water production. As explained in chapter 1, perovskites do show tolerance to sulphur poisoning and carbon build-up, which are the main drawbacks of the Ni-YSZ cermets when operated under hydrocarbon based fuels. Thus, the development of a new perovskite based material to be used as an alternative anode material for fuel flexible SOFCs; which may show improvements to different performance parameters; is very important to see the wide scale use of fuel cells in a market where solar energy is considered almost the only choice. A market which is almost stretched to its limits to meet the current and future demands, where water is the most important commodity and fuel cells can provide the answer to that.

2.9 - Conclusions

The climate and the nature of the United Arab Emirates led it to be one of the major energy consumers in the world, as well as, one of the top CO₂ emitters per capita. Water scarcity puts a huge strain on the power sector due to extensive desalination; which does not look to be sustainable. Solar energy is an obvious choice for the UAE; but using it to provide constant power to the grid is not the optimal use of this energy. Utilising electrolysis and fuel cell technologies can prove very beneficial for the country. Generating hydrogen from waste water using solar energy driven electrolysis and utilising the oil industry infrastructure to store this hydrogen and transport it, the UAE can be a leader producer of green hydrogen. This will help to drive the fuel cell industry and the involved research efforts. Using hydrogen in large scale fuel cells can provide sufficient power and water; which are both equally vital in this part of the world.

2.10 - References

- [1] Haseeb Haider, “*UAE explores new markets via economic, trade diversification,*” 29 March 2011, Khaleej Times Newspaper. Internet, Available from http://www.khaleejtimes.com/biz/inside.asp?xfile=/data/business/2011/March/business_March519.xml§ion=business, accessed 17 September 2012.
- [2] CIA, The World Factbook, “*United Arab Emirates.*” Internet, Available from <https://www.cia.gov/library/publications/the-world-factbook/geos/ae.html>, accessed 17 September 2012.
- [3] The UAE National Bureau of Statistics, “*Population estimates 2006-2010.*” Internet, Available from <http://www.uaestatistics.gov.ae/ReportPDF/Population%20Estimates%202006%20-%202010.pdf>, accessed 17 September 2012.
- [4] Embassy of the United Arab Emirates in Washington DC, “*The UAE: Energy in the UAE.*” Internet, Available from <http://www.uae-embassy.org/uae/energy>, accessed 17 September 2012.
- [5] International Renewable Energy Agency, “*Creation of IREN.*” Internet, available from <http://www.irena.org/menu/index.aspx?mnu=cat&PriMenuID=13&CatID=30>, accessed 17 September 2012.
- [6] RenewableEnergyWorld.Com, “*Irena Head Makes Surprise Resignation,*” 21 October 2010, News. Internet, available from <http://www.renewableenergyworld.com/rea/news/article/2010/10/irena-head-makes-surprise-resignation>, accessed 17 September 2012.
- [7] MASDAR Media Centre, “*United Arab Emirates First Middle East Country To Host A Major International Organization,*” 30 June 2009. Internet, available from http://www.masdar.ae/en/MediaArticle/NewsDescription.aspx?News_ID=124&News_Type=PR&MenuID=0&CatID=64, accessed 17 September 2012.

[8] UAE, 2012. Scale undetermined; Ahmed Aljaberi; using 'Google Maps.' <<http://maps.google.com/?ll=23.885838,48.955078&spn=45.957206,79.013672&t=p&z=4>>. (17 April 2012).

[9] Abu Dhabi Environment Agency, "*Abu Dhabi Emirate Water Resources Statistics 2006.*" Internet, available from <http://www.ead.ae/data/global/files/water%20resouces%20stat/water-statistics%202006%20english.pdf>, accessed 17 September 2012.

[10] Pacific Institute, The World's Water, Data Table 1, "Total Renewable Freshwater Supply, by Country," **2010 Update**. Internet, available from [http://www.worldwater.org/datav7/data table 1 total renewable freshwater supply by country.pdf](http://www.worldwater.org/datav7/data%20table%201%20total%20renewable%20freshwater%20supply%20by%20country.pdf), accessed 17 September 2012.

[11] UAE Ministry of Energy, "*Annual Statistical Report for Electricity and Water of the UAE,*" **2011**. Internet, available from <http://www.moenr.gov.ae/assetsmanager/files/statistics/anual%20report%202010.pdf>, accessed 17 September 2012.

[12] Food and Agriculture Organization of the UN, "*United Arab Emirates,*" **2008**. Internet, available from http://www.fao.org/nr/water/aquastat/countries_regions/unt_d_arab_em/print1.stm, accessed 17 September 2012.

[13] UAE Ministry of Energy, "*Annual Statistical Report for Electricity and Water United Arab Emirates 2003-2007,*" **2008**. Internet, available from http://www.moenr.gov.ae/assetsmanager/files/statistics/statistical_2007.pdf, accessed 17 September 2012. (In Arabic).

[14] Abu Dhabi Council For Economic Development, Government of Abu Dhabi, "*The Abu Dhabi Economic Vision 2030,*" **2009**. Internet, available from [http://www.abudhabi.ae/egovPoolPortal WAR/appmanager/ADeGP/Citizen?nfpb=true&pageLabel=p_citizen_homepage_hidenav&did=131654&lang=en](http://www.abudhabi.ae/egovPoolPortal_WAR/appmanager/ADeGP/Citizen?nfpb=true&pageLabel=p_citizen_homepage_hidenav&did=131654&lang=en), accessed 17 September 2012.

[15] Abu Dhabi Water and Electricity Authority, "*Sustainability report 2009.*"

- [16] Dubai Electricity and Water Authority, “*Electricity Statistics*,” 2010. Internet, available from <http://www.dewa.gov.ae/aboutus/electStats2010.aspx>, accessed 17 September.
- [17] April Yee, “*Icelandic clean energy solution in the desert*,” 21 Dec 2010, The National Newspaper. Internet, available from <http://www.thenational.ae/business/energy/icelandic-clean-energy-solution-in-the-desert>, accessed 17 September 2012.
- [18] S. Lattemann and T. Höpner, *Desalination*, 2008, **220**, 1-15.
- [19] Emmanuelle Landais, “*Waste dump threatens Arabian Gulf*,” 14 June 2009, GulfNews newspaper. Internet, available from <http://gulfnews.com/news/gulf/uae/environment/waste-dump-threatens-arabian-gulf-1.72058>, accessed 17 September 2012.
- [20] H. Cooley, P. H. Gleick and G. Wolff, “*DESALINATION, WITH A GRAIN OF SALT: A California Perspective*,” June 2006, Pacific Institute, California, USA. Internet, available from http://www.pacinst.org/reports/desalination/desalination_report.pdf, accessed 17 September 2012.
- [21] A. Hashim and M. Hajjaj, *Desalination*, 2005, **182**, 373-393.
- [22] M. H. I. Dore, *Desalination*, 2005, **172**, 207-214.
- [23] Caline Malik, “*Water plan needed to tackle scarcity, says GCC chief*,” 23 April 2012, The National Newspaper. Internet, available from <http://www.thenational.ae/news/uae-news/water-plan-needed-to-tackle-scarcity-says-gcc-chief>, accessed 17 September 2012.
- [24] Derek Baldwin, “*UAE one of world's top users of water, expert warns*,” 19 April 2012, Gulf News. Internet, available from <http://gulfnews.com/news/gulf/uae/environment/uae-one-of-world-s-top-users-of-water-expert-warns-1.1010372>, accessed 17 September 2012.
- [25] H. Radhi, *Build. Environ.*, 2009, **44**, 2451-2462.

- [26] H. J. AlFarra and B. Abu-Hijleh, *Energ. Policy*, 2012, **42**, 272-285.
- [27] Regional Market Opportunities, Masdar City Website. Internet, available from <http://www.masdarcity.ae/en/77/regional-market-opportunities/>, accessed 17 September 2012.
- [28] Background, About Us, Masdar Website. Internet, available from <http://www.masdar.ae/en/Menu/index.aspx?MenuID=42&CatID=12&mnu=Cat>, accessed 17 September 2012.
- [29] Nuclear Power in the United Arab Emirates, World Nuclear Association. Internet, available from http://www.world-nuclear.org/info/UAE_nuclear_power_inf123.html, accessed 17 September 2012.
- [30] Prime Contractor, ENEC's Program, Emirates Nuclear Energy Corporation. Internet, available from <http://www.enec.gov.ae/our-nuclear-energy-program/prime-contractor/>, accessed 17 September 2012.
- [31] S. Mekhilef, R. Saidur and M. Kamalisarvestani, *Renew. Sust. Energ. Rev.*, 2012, **16**, 2920-2925.
- [32] New Employee Guide, UAE University. Internet, available from http://www.uaeu.ac.ae/hr/eguide/docs/New_Emp_Guide_The_UAE_v2.pdf, accessed 17 September 2012.
- [33] C. Ferrara and D. Philipp, *Energ. Procedia*, 2012, **15**, 379-387.
- [34] B. M. A. Mohandes, L. El-Chaar and L. A. Lamont, *Appl. Solar Energy*, 2009, **45**, 242-247.
- [35] Z. Xiong, T. M. Walsh and A. G. Aberle, *Energ. Procedia*, 2011, **8**, 384-389.
- [36] Al Goodman, "Spain's round-the-clock solar power plant," 3 October 2011, CNN. Internet, available from <http://edition.cnn.com/2011/10/03/world/europe/solar-power-24-hours/index.html>, accessed 17 September 2012.
- [37] A. S. Joshi, I. Dincer and B. V. Reddy, *Int. J. Hydrogen Energ.*, 2011, **36**, 11246-11257.

- [38] L. Xiao, S. Wu and Y. Li, *Renew. Energ.*, 2012, **41**, 1-12.
- [39] L. Shao, B. T. Low, T. Chung and A. R. Greenberg, *J. Membrane Sci.*, 2009, **327**, 18-31.
- [40] Shanta Barley, "Hydrogen bus launched on London tourist route," 10 December 2010, The Guardian. Internet, available from <http://www.guardian.co.uk/environment/2010/dec/10/hydrogen-bus-london>, accessed 17 September 2012.
- [41] Masdar Institute, Our Units, Masdar Website. Internet, available from <http://www.masdar.ae/en/Menu/index.aspx?MenuID=48&CatID=26&mnu=Cat>, accessed 17 September 2012.
- [42] Vesela Todorova, "Desalination threat to the growing gulf," 31 August 2009, The National Newspaper. Internet, available from <http://www.thenational.ae/news/uae-news/environment/desalination-threat-to-the-growing-gulf#full>, accessed 17 September 2012.
- [43] Environment, ENEC's Program, Emirates Nuclear Energy Corporation website. Internet, available from <http://www.enec.gov.ae/our-nuclear-energy-program/environment/#carbon-emissions>, accessed 17 September 2012.
- [44] Gregor McClenaghan, "Sandstorms sweep across region," 13 February 2009, The National Newspaper. Internet, available from <http://www.thenational.ae/news/uae-news/sandstorms-sweep-across-region>, accessed 17 September 2012.
- [45] Vicky Kapur, "Brace up for sandstorms in UAE over weekend," 13 October 2011, Emirates 24/7 News. Internet, available from <http://www.emirates247.com/news/brace-up-for-sandstorms-in-uae-over-weekend-2011-10-13-1.423336>, accessed 17 September 2012.
- [46] R. Lan, J. T. S. Irvine and S. Tao, *Int. J. Hydrogen Energ.*, 2012, **37**, 1482-1494.
- [47] M. R. Ardigò, I. Popa, S. Chevalier, C. Desgranges and R. Bousquet, *Int. J. Hydrogen Energ.*, 2012, **37**, 8177-8184.

- [48] Rola Tassabehji, “*Water Desalination in the Gulf is Necessary, But Not at Any Cost,*” 14 March 2011, Green Prophet. Internet, available from <http://www.greenprophet.com/2011/03/desalination-saudi-arabia-solar/>, accessed 17 September 2012.
- [49] J. T. S. Irvine and A. Sauvet, *Fuel Cells*, 2001, **1**, No. 3-4.
- [50] E. C. Thomsen, G. W. Coffey, L. R. Pederson and O. A. Marina, *J. Power Sources*, 2009, **191**, 217-224.
- [51] The Encyclopedia of Earth, “*United Arab Emirates.*” Internet, available from http://www.eoearth.org/files/197401_197500/197406/dubai.a2003285.0655.500m.jpg, accessed 20 September 2012.
- [52] J. J. Hwang, *RENEW SUST ENERG REV*, 2012, **16**, 3803-3815.
- [53] I. Angelidaki, L. Ellegaard and B. K. Ahring, *Adv. Biochem. Eng. Biot.*, 2003, **82**, 1-33.
- [54] C. Bougrier, J. –P. Delgenès and H. Carrère, *Process Saf. Environ.*, 2006, **84**, 280–284.
- [55] Shams Power Company website. Internet, available from: <http://www.shampower.ae/en/>, accessed 22 March 2013.

Chapter 3

Novel A-site deficient $\text{La}_{0.2}\text{Sr}_{0.7-x}\text{Ca}_x\text{TiO}_3$

Part 1 - Structural Characterisation

Abstract

As a potential novel SOFC anode material, solid solutions of the system $\text{La}_{0.2}\text{Sr}_{0.7-x}\text{Ca}_x\text{TiO}_3$ were analysed and characterised using XRD and NPD. Symmetry changes were observed with differing calcium content and temperature. The new system strays off the ideal cubic symmetry of $\text{La}_{0.2}\text{Sr}_{0.7}\text{TiO}_3$ with calcium substitution; while maintaining the perovskite phase. Samples with low calcium content showed a tetragonal $I4/mcm$ symmetry whereas higher calcium content samples showed an orthorhombic $Pbnm$ structure. This transition was reversed at high temperatures where samples showed transitions to higher symmetries; through $Pbnm \rightarrow I4/mcm \rightarrow Pm\bar{3}m$.

3.1 - Introduction

With $\text{La}_{0.2}\text{Sr}_{0.7}\text{TiO}_3$ as the basis of the system studied in this work; the objective was to further improve the electrical conductivity by reducing the unit cell volume. Calcium was chosen to replace strontium in $\text{La}_{0.2}\text{Sr}_{0.7}\text{TiO}_3$ since it has the same valence with a smaller ionic radius; i.e. 0.135 nm for Ca^{2+} compared to 0.144 nm for Sr^{2+} for coordination number 12.[1] If the unit cell volume is to become smaller; and electrical conduction takes place between the conduction bands in the 3d orbitals of the titanium, these orbitals will be closer to each other and their overlapping will increase. This route is anticipated to enhance the electrical conductivity of this type of perovskite. Also, since lanthanum doping was found to lower the density of samples when doped into SrTiO_3 [2], calcium introduction into the structure can improve the sintering behaviour, hence the density of the solid solutions, of the prepared samples. This is helpful to obtain the desired phase at much lower temperatures. CaTiO_3 can form very stable solid solutions with many different elements; hence its use for radioactive waste storage; i.e. synthetic rock (synroc).[3] Another effect that can be anticipated, as well, is the structural instability with calcium incorporation on the lattice due to the mismatch in ionic radii between the different cations, that can lead to distorted symmetries instead of getting the ideal, cubic, perovskite structure. Three types of distortions can take place in a perovskite structure; distortions to the BO_6 octahedra, displacement of the B-site cation and the tilting of the octahedra around certain directions.[4] Thus, a structural understanding of the new material is essential to assess its suitability as anode material for SOFCs. Hence, this chapter is concerned with the structural analysis of $\text{La}_{0.2}\text{Sr}_{0.7-x}\text{Ca}_x\text{TiO}_3$ through different levels of calcium substitution. Diffraction studies were conducted to determine the crystal structure and unit cell parameters at room

temperature with different calcium content and at high temperatures for two chosen samples.

3.2 - Results and Discussion

3.2.1 - XRD Analysis

Using XRD, all solid solutions showed a single phase perovskite structure which was very similar to SrTiO_3 and $\text{La}_{0.2}\text{Sr}_{0.7}\text{TiO}_3$; i.e. $x = 0$. All the collected patterns are shown in figure 3.1.

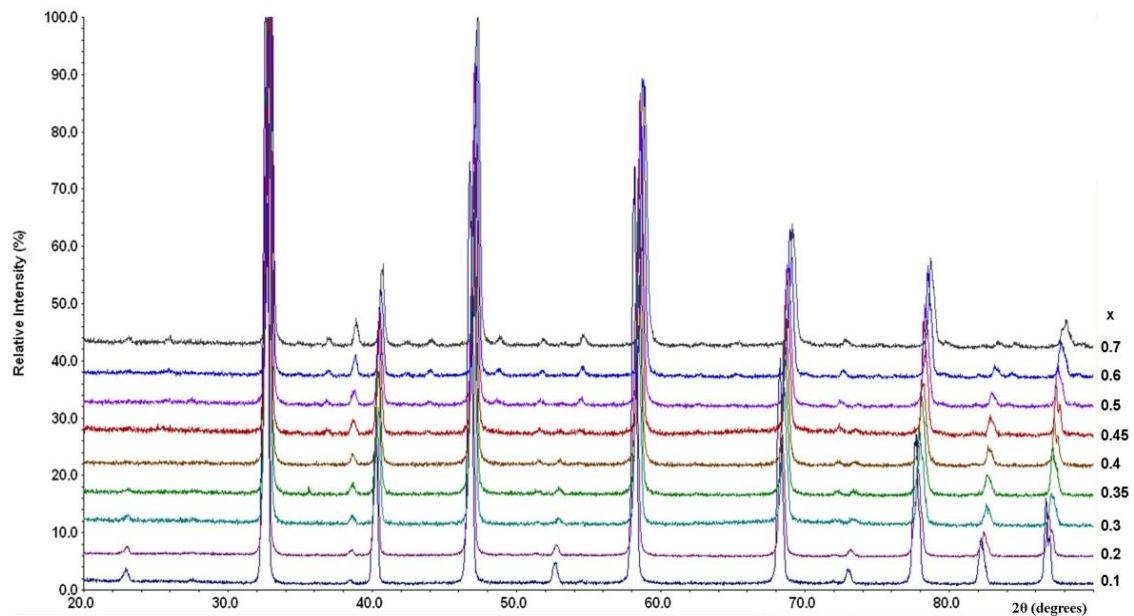


Figure 3.1: Normalised XRD patterns of all synthesised samples of $\text{La}_{0.2}\text{Sr}_{0.7-x}\text{Ca}_x\text{TiO}_3$.

Note: numbers on the side represent x for calcium.

The reduction in the unit cell volume with increasing calcium content was very obvious; i.e. from the apparent shift of the patterns toward higher angles. Taking a close look, all the main peaks of SrTiO_3 cubic unit cell is matching well with the peaks detected with the new prepared system $\text{La}_{0.2}\text{Sr}_{0.7-x}\text{Ca}_x\text{TiO}_3$; see figure 3.2. However, the ideal cubic

cell was not maintained and lower symmetries were detected. The clearest indication is the presence of a peak around $2\theta = 38.58^\circ$, right before the [1 1 1] peak of SrTiO_3 ; indicated by the arrow in figure 3.2. The new peak was an indication of a lower symmetry and impurities; e.g. rutile; were dismissed since the peak intensity increased with more calcium content and it was shifting along with the other peaks as the unit cell volume decreased, as shall be seen in the following pages.

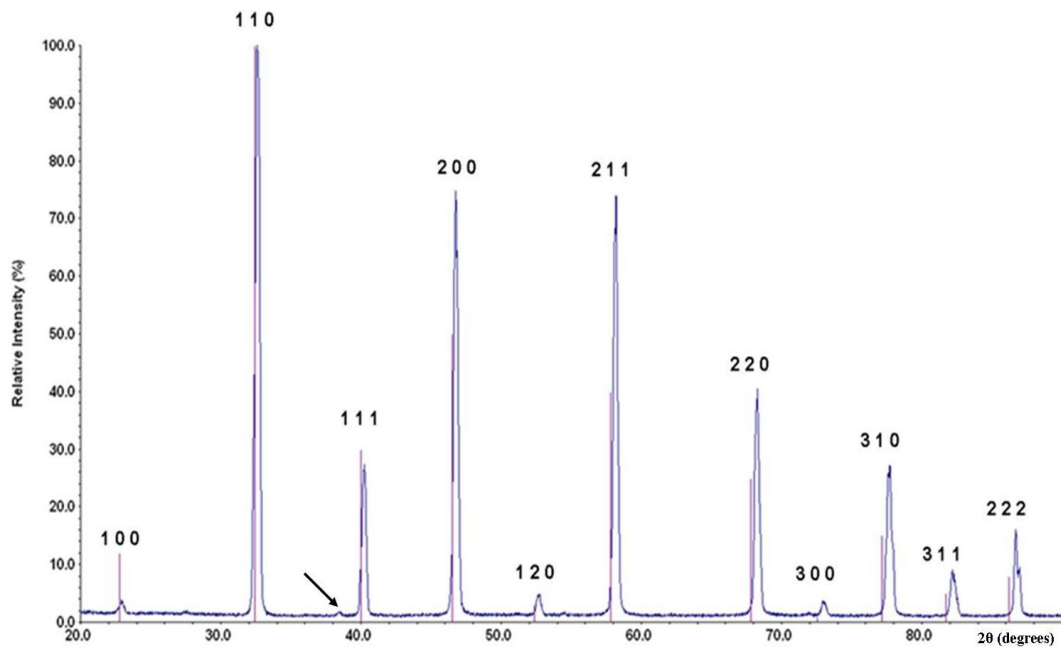


Figure 3.2: XRD pattern of $\text{La}_{0.2}\text{Sr}_{0.6}\text{Ca}_{0.1}\text{TiO}_3$ with reflections of SrTiO_3 obtained from ICDD PDF card number: 35-734. Indices are those for the SrTiO_3 phase, S.G.: Pm3-m.

Note: the arrow points at the peak representing a new symmetry.

Taking into account that the new system should have resemblances to the parent compounds, the end member of the series; i.e. $\text{La}_{0.2}\text{Ca}_{0.7}\text{TiO}_3$ ($x = 0.7$); showed more reflections and it was compared to the other parent compound, CaTiO_3 . This can be seen in figure 3.3.

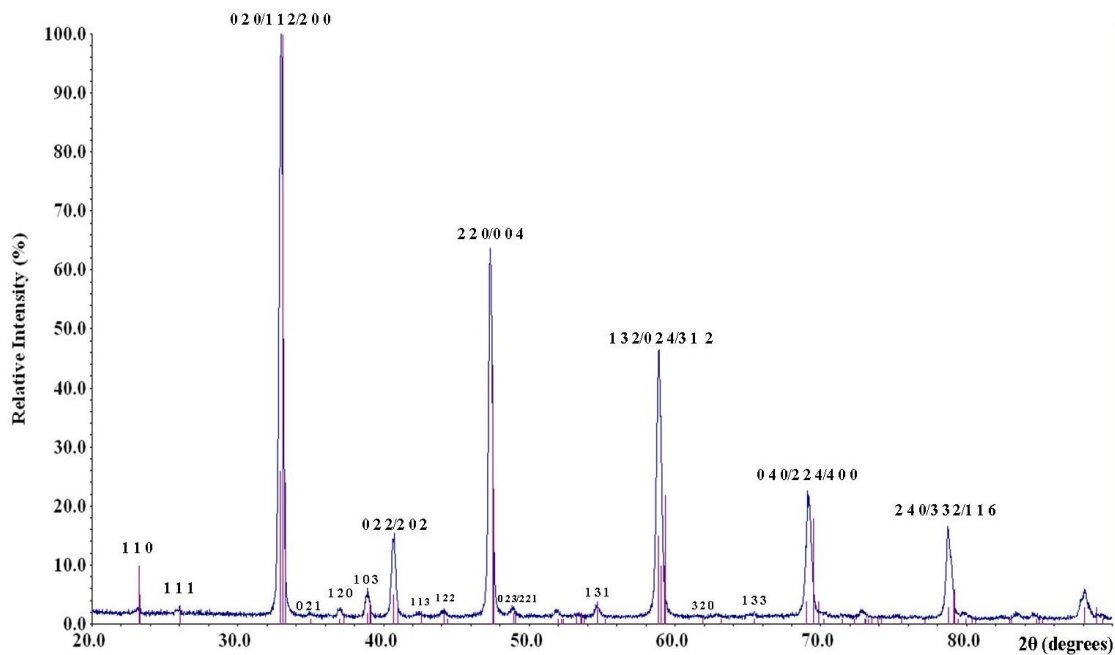


Figure 3.3: XRD pattern for $\text{La}_{0.2}\text{Ca}_{0.7}\text{TiO}_3$ with reflections of CaTiO_3 obtained from ICDD PDF card number:42-423. Indices correspond to some of the reflections of the CaTiO_3 phase.

Again, there is great resemblance between the patterns obtained in this work and the parent compounds. The starting composition $\text{La}_{0.2}\text{Sr}_{0.7}\text{TiO}_3$ showed a cubic structure with space group $\text{Pm}\bar{3}\text{-m}$ with unit cell parameter $a=3.9014(3)$. [5] A comparison was made between this compositions and the new system $\text{La}_{0.2}\text{Sr}_{0.7-x}\text{Ca}_x\text{TiO}_3$ in order to investigate the structural changes, as well as, to establish phase purity after calcium introduction into this perovskite, this is shown in figure 3.4, where few samples of the new system are included for clarity.

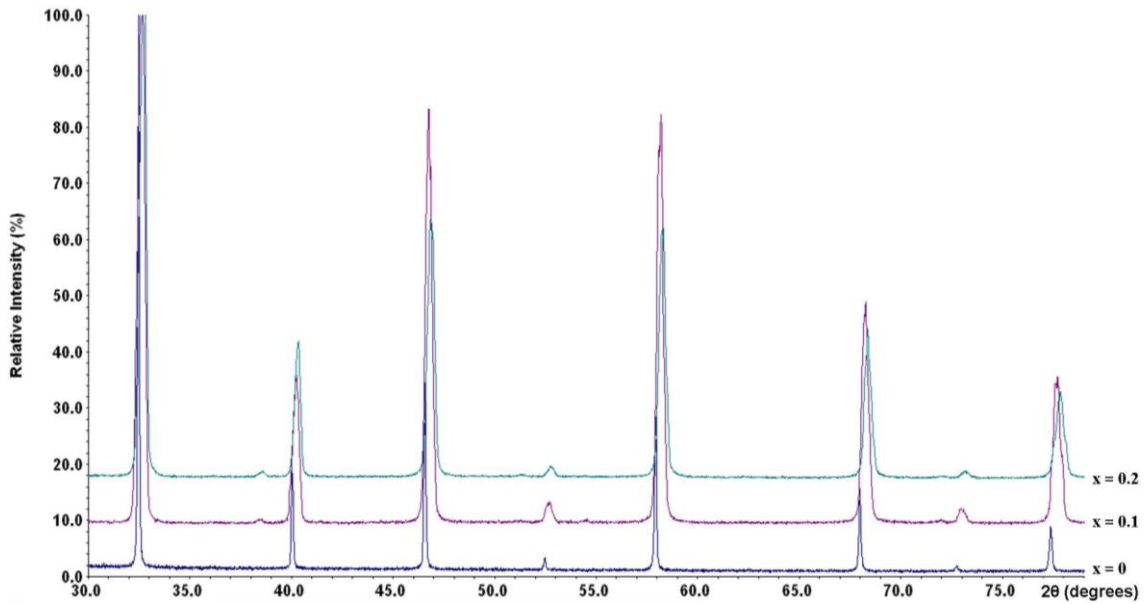


Figure 3.4: Comparing the XRD patterns of the starting material $\text{La}_{0.2}\text{Sr}_{0.7}\text{TiO}_3$ to those for some of the samples of $\text{La}_{0.2}\text{Sr}_{0.7-x}\text{Ca}_x\text{TiO}_3$.

As can be seen both sets of diffraction patterns show a great similarity between each other. The only difference that was noticed is the emergence of the peak, mentioned earlier; i.e. $2\theta = 38.58^\circ$. Also, we noticed higher intensities for many of the peaks of the new system which can be attributed to either higher crystallinity of the new system, larger grains, and instrumental conditions or due to increased distortions in certain directions which involve the oxygen anions increasing the scattering strength of X-rays. The most likely cause for the larger intensities is the increased sinterability, as shall be seen in chapter 4, which generated higher densities coming from smaller unit cells due to calcium introduction; i.e. higher electrons density. Anyway, it was obvious that the system $\text{La}_{0.2}\text{Sr}_{0.7-x}\text{Ca}_x\text{TiO}_3$ undergoes structural changes between $\text{Pm}3\text{-m}$ and Pbnm through an intermediate phase with increasing calcium. This was expected since structural changes can be affected by having different cations on the A-site; as indicated by different authors; that by having a mismatch in ionic radii of the A or B cations;

distortions of the ideal cubic structure would result; usually through the tilting of the BO_6 octahedra.[6,7,8] And there is a significant mismatch between the ionic radii of Sr^{2+} and Ca^{2+} as mentioned earlier. Also, having an A-site deficiency could lead to more distortions to the cubic unit cell in addition to the A-site cations ionic radii mismatch. As a point defect is generated in the lattice from the removal of an A-site cation; due to local relaxation around the defect; the local structure around this defect will be slightly distorted from the rest of the structure.[9] The whole structure should in theory balance this local relaxation by adopting symmetries which require less energy to maintain.

To determine the correct symmetry for the system $\text{La}_{0.2}\text{Sr}_{0.7-x}\text{Ca}_x\text{TiO}_3$ an understanding of the structures of the parent compounds was necessary. As mentioned earlier, $\text{La}_{0.2}\text{Sr}_{0.7}\text{TiO}_3$ and most related compounds; e.g. $\text{La}_x\text{Sr}_{1-x}\text{TiO}_{3-\delta}$ with $x \leq 0.4$ [2,10]; were reported to have the cubic $\text{Pm}\bar{3}\text{-m}$ symmetry. At room temperature $(1-x)\text{CaTiO}_3$ - $x\text{La}_{2/3}\text{TiO}_3$ was found to undergo structural changes from Pbnm for $0 \leq x \leq 0.5$ to $\text{Ibmm}(\text{Imma})$ for $0.5 < x < 0.7$ to I4/mcm for $0.7 < x < 0.9$ to Cmmm for $x \geq 0.9$.[11,12] The A-site deficient $\text{La}_{2(1-x)/3}\text{Ca}_x\text{TiO}_3$ was reported to be orthorhombic with Pbnm space group for $x = 0.8$ [11,13]. From this, it was anticipated that the structure of $\text{La}_{0.2}\text{Ca}_{0.7}\text{TiO}_3$ ($x = 0.7$) in our system should be orthorhombic with the space group Pbnm . On the other hand, Howard et. al.[14] reported that the system $\text{La}_x\text{Sr}_{1-3x/2}\text{TiO}_3$ has a cubic structure $\text{Pm}\bar{3}\text{-m}$ for $x \leq 0.2$, I4/mcm for $0.2 < x \leq 0.5$ and finally Cmmm for $x \geq 0.55$.

Since the XRD pattern of the first sample in the series; i.e. $\text{La}_{0.2}\text{Sr}_{0.6}\text{Ca}_{0.1}\text{TiO}_3$; did not resemble a cubic structure; this has led to an initial confusion regarding the possible symmetries, or space groups, that the different compositions in our system might adopt. There are many contradicting reports for the correct symmetries for different

compositions of $\text{Sr}_{1-x}\text{Ca}_x\text{TiO}_3$ in literature. For example, Ball et. al.[15] have shown that the system is Pnma (Pbnm) for $0.6 \leq x \leq 1$, Bmmb for $0.4 \leq x \leq 0.55$, I4/mcm for $0.1 \leq x \leq 0.35$ and Pm3-m for $x \leq 0.05$. Qin et. al.[16] have reported that the system adopts the same sequence of Pbnm-Bmmb-I4/mcm-Pm3-m with decreasing content of calcium. In a later publication[17], the same authors have reported that there was no indication of a Bmmb symmetry by using Raman spectroscopy. The correct phases were Pbnm for $0.33 < x \leq 1$, I4/mcm for $0.05 < x \leq 0.33$ and Pm3-m for $x \leq 0.05$. Ranson et. al.[18] have also confirmed that the Bmmb phase does not exist and the correct phase was Pbnm for compositions with $0.4 \leq x \leq 0.55$; however, they also indicated an Imma phase for $0.06 < x < 0.12$. Yamanaka et. al.[19] have studied single crystals of $\text{Sr}_{1-x}\text{Ca}_x\text{TiO}_3$ and concluded that the only phases were Pbnm for $0.4 \leq x \leq 1$, I4/mcm for $0.2 \leq x < 0.4$ and Pm3-m for $x < 0.2$. The Imma space group was also rejected by Howard et. al.[25] for the composition $\text{Ca}_{0.3}\text{Sr}_{0.7}\text{TiO}_3$; where the correct space group that was assigned to this composition was I4/mcm. From all the above, it was concluded that calcium content will be the factor that determines the symmetry of the solid solutions prepared in this work. An analysis by Redfern[20] indicated that the peak around $2\theta = 38.5^\circ$ corresponds to the presence of the $\{2\ 1\ 1\}$ peak of the tetragonal I4/mcm space group that CaTiO_3 adopts around 1150°C . The high temperature phases of CaTiO_3 which move to higher symmetries as temperature is increased can be analogous to the phases that the new system $\text{La}_{0.2}\text{Sr}_{0.7-x}\text{Ca}_x\text{TiO}_3$ adopts with decreased A-site ionic radii mismatch. At high temperatures, it can be argued that the perovskite unit cell is provided with enough energy to stabilise a higher symmetry regardless of the A-site ionic radius which caused the distortions associated with the lower symmetries. Hence, the same analogy was used to investigate the structural changes that resulted

from calcium introduction into $\text{La}_{0.2}\text{Sr}_{0.7}\text{TiO}_3$, where the increased A-site ionic radii mismatch is seen as a mechanism that reduces the unit cell ability to hold the ideal cubic symmetry.

Thus, using all the above inputs, it was possible to index the diffraction pattern of $\text{La}_{0.2}\text{Sr}_{0.6}\text{Ca}_{0.1}\text{TiO}_3$ with a tetragonal symmetry using the space group $I4/mcm$, as can be seen in figure 3.5. This space group was the most plausible in this case since the first composition in the series; i.e. $x = 0.1$; was expected to have a cubic symmetry similar to that of $\text{La}_{0.2}\text{Sr}_{0.7}\text{TiO}_3$. It was thought that the unit cell would not have a significant distortion to result in a lower symmetry with the addition of calcium. However, many attempts to index the pattern of the $\text{La}_{0.2}\text{Sr}_{0.6}\text{Ca}_{0.1}\text{TiO}_3$ using the $Pm\bar{3}m$ space group were not successful. Also, the new peak, indicated above; i.e. $\{211\}$; was ruled out to be a result of a secondary phase like contaminants or other oxide phases; e.g. rutile.

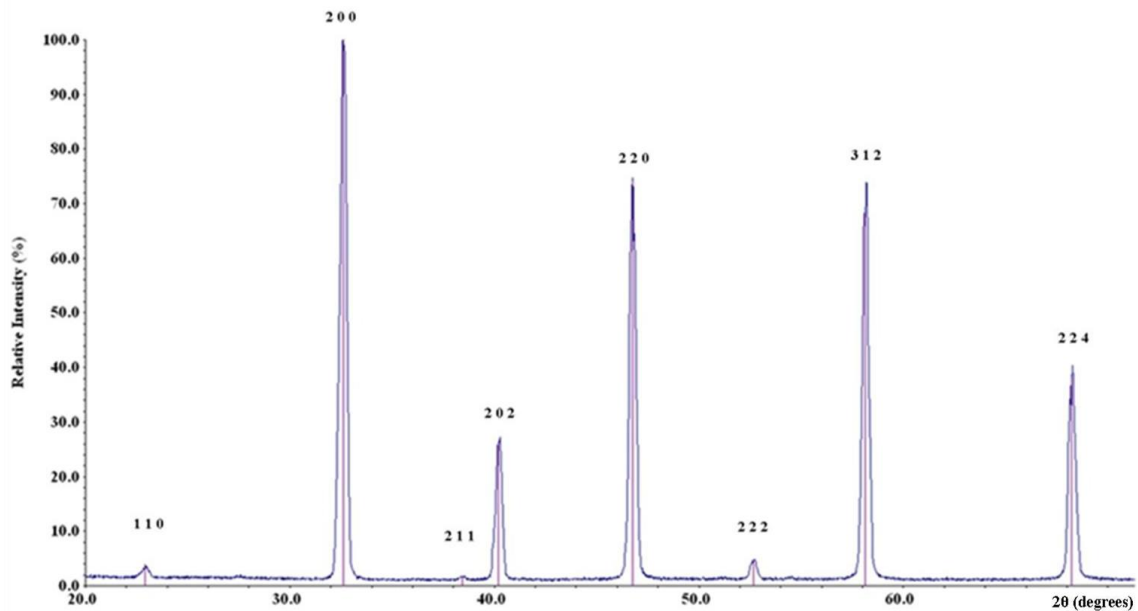


Figure 3.5: XRD pattern of $\text{La}_{0.2}\text{Sr}_{0.6}\text{Ca}_{0.1}\text{TiO}_3$ and indexed reflections using the tetragonal symmetry $I4/mcm$.

Very good fits were obtained using the above symmetry for all samples in the range $0.1 \leq x < 0.45$; however, with more calcium; i.e. $x \geq 0.45$, the system showed an extra peak which indicated an orthorhombic phase according to the analysis of Redfern; i.e. Pbnm for CaTiO_3 at lower temperatures.[20] Figure 3.6 shows the evolution of the system with increasing content of calcium.

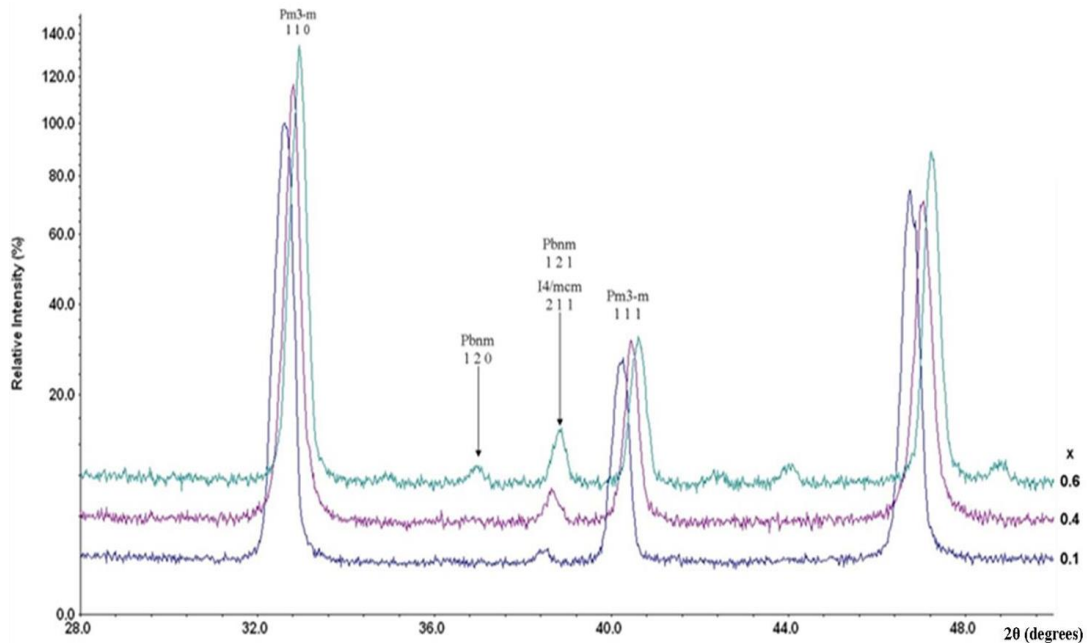


Figure 3.6: XRD patterns for samples of $\text{La}_{0.2}\text{Sr}_{0.7-x}\text{Ca}_x\text{TiO}_3$ showing the different symmetries.

The new peak; i.e. around $2\theta = 36.8^\circ$; was indexed as the $\{120\}$ reflection of the orthorhombic Pbnm space group. Figure 3.7 shows a closer picture of the behaviour of the new reflections with added calcium, where it can be seen that the intensity of the $\{211\}$, $\{120\}$ and $\{121\}$ reflections; which represent the different symmetries as indicated on figure 3.7, increased with increasing calcium content. It is known that the tetragonal I4/mcm have a tilt system $a^0a^0c^-$ in Glazer's notation which indicates anti-phase tilting around the (001) axis of the primitive cubic cell.[14]

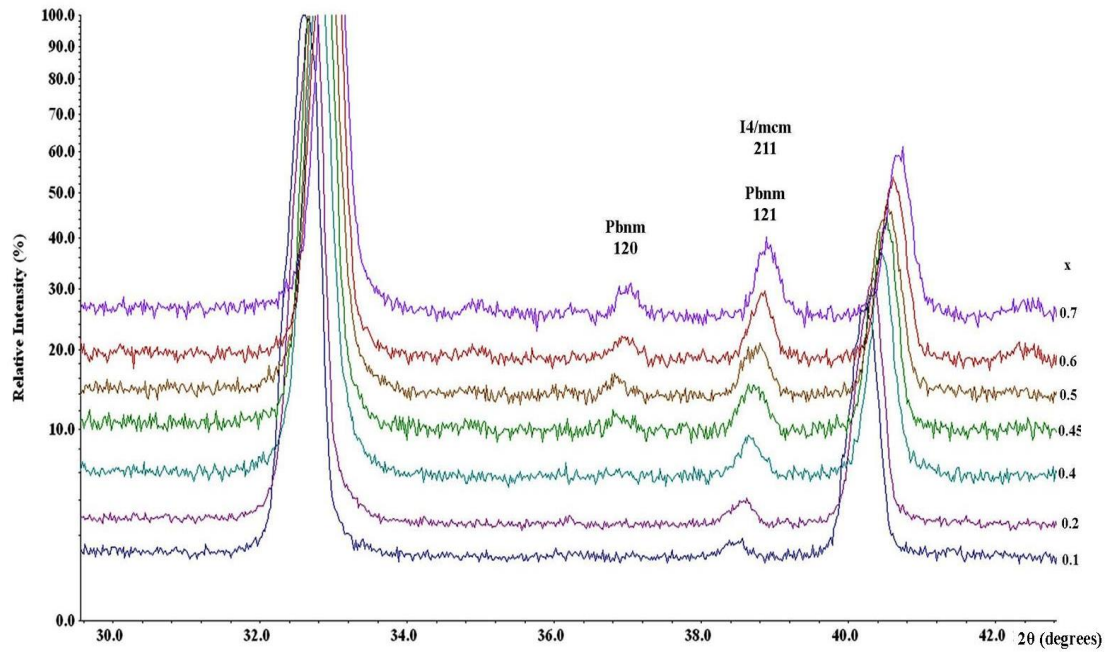


Figure 3.7: Portion of the normalised XRD patterns for samples of $\text{La}_{0.2}\text{Sr}_{0.7-x}\text{Ca}_x\text{TiO}_3$.

The Pbnm phase adopts a different tilting system with Glazer's notation of $a^-a^-c^+$. [21] These tilts are the reason behind the lower symmetry than the ideal cubic perovskite structure. The increased intensity reflects that these tilts increase in magnitude with more calcium being incorporated into the structure of our system. [20] This finding is very reasonable given that the ionic radius mismatch on the A-site increases with increasing calcium content.

Thus, from the XRD data the findings were that the system $\text{La}_{0.2}\text{Sr}_{0.7-x}\text{Ca}_x\text{TiO}_3$ showed the tetragonal I4/mcm for $0.1 \leq x \leq 0.4$ and the orthorhombic Pbnm for $0.45 \leq x \leq 0.7$. The unit cell parameters and volume, obtained using the least square method of the different compositions are shown in table 3.1.

x	S.G.	a_p (Å)	b_p (Å)	c_p (Å)	Volume(Å³)
0	Pm$\bar{3}$m	3.9014(3)	3.9014(3)	3.9014(3)	59.383(14)
0.1	I4/mcm	3.8838(12)	3.8838(12)	3.8893(2)	58.666(49)
0.2	I4/mcm	3.8697(5)	3.8697(5)	3.8788(35)	58.082(2)
0.3	I4/mcm	3.86604(9)	3.86604(9)	3.87285(8)	57.8847(39)
0.35	I4/mcm	3.86338(12)	3.86338(12)	3.86997(12)	57.7622(53)
0.4	I4/mcm	3.8595(13)	3.8595(13)	3.86548(1)	57.5792(52)
0.45	Pbnm	3.8549(2)	3.8638(7)	3.8612(2)	57.5109(31)
0.5	Pbnm	3.8468(13)	3.85791(11)	3.85923(8)	57.2734(47)
0.6	Pbnm	3.8425(21)	3.84977(13)	3.85049(8)	56.959(35)
0.7	Pbnm	3.8368(17)	3.8409(3)	3.8425(15)	56.652(66)

Table 3.1: Space groups and primitive unit cell parameters and volumes for synthesised compositions of the system $\text{La}_{0.2}\text{Sr}_{0.7-x}\text{Ca}_x\text{TiO}_3$.

Comparing the unit cell parameters provided by Zhang et. al.[12] for $\text{La}_{0.2}\text{Ca}_{0.7}\text{TiO}_3$; i.e. $a_p = 3.8385 \text{ \AA}$, $b_p = 3.8512 \text{ \AA}$ and $c_p = 3.8426 \text{ \AA}$; to the ones obtained in this work, it can be seen that there is a very good agreement. This helped in indicating that the reasoning we used in determining the different symmetries of our samples by drawing analogies from other closely related perovskites was correct. The unit cell parameters and volumes for the different compositions were plotted against calcium content in figure 3.8 where it can be seen that the unit cell volume is evolving in an almost linear fashion along with the unit cell parameters in each phase. This shows that the system is only affected by small distortions that are attributed to the tilting of the perovskite octahedra.

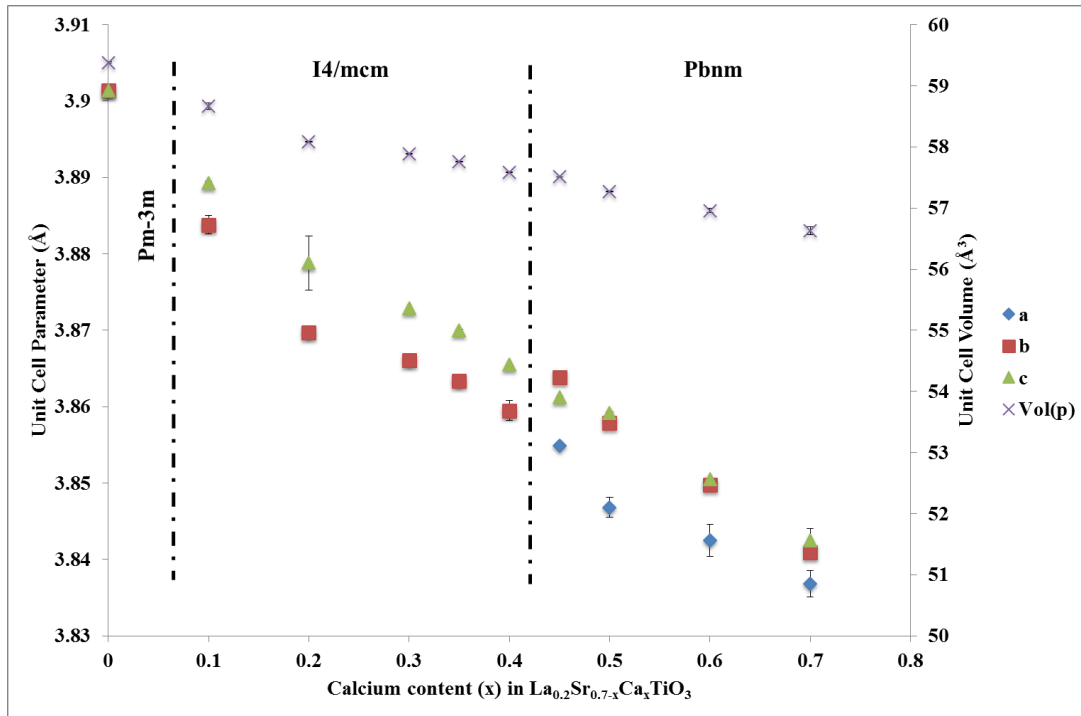


Figure 3.8: Primitive unit cell parameters and volume as a function of calcium content.

Unit cell parameters and volume of $\text{La}_{0.2}\text{Sr}_{0.7}\text{TiO}_3$ ($x = 0$) were obtained from ref.[66].

Note: some of the error bars are contained within data points' symbols.

The unit cell parameters behaviour, however, shows some departure of the same linearity seen with the unit cell volume, especially with the sample $\text{La}_{0.2}\text{Sr}_{0.5}\text{Ca}_{0.2}\text{TiO}_3$ ($x = 0.2$), where the c-parameter is showing a relatively large error. This can be attributed to a larger distortion taking place as strontium content decreases, however, the overall structure is trying to balance this offset coming from the A-site lattice points through the different planes, hence, different unit cells could have different lengths along the $[0\ 0\ 1]$ direction, making it difficult to precisely determine the c-parameter for the overall sample. The same can be seen around $x = 0.2$ with the a-parameter. Again, as the changes in symmetry that were found with this material originated from changes to the tilt angles of the BO_6 octahedra, which is affected by the A-site ionic radius

mismatch, where there is a significant difference between the ionic radius of strontium compared to lanthanum and calcium ionic radii. Thus, the nonlinearity can be explained to be a result of much more localised distortions that cannot be explained with the current results and need further investigation to ascertain the existence of a phase change taking place around the mentioned sample. No extra or distinctive peaks can be seen in the XRD pattern of this particular sample, hence, we cannot determine the exact origin of this irregularity.

The structure of this system a very good stability after reduction, see figure 3.9, with a slight increase in the unit cell volume. This increase is typical due to the reduction of titanium which gives a larger effective ionic radius for Ti^{3+} .

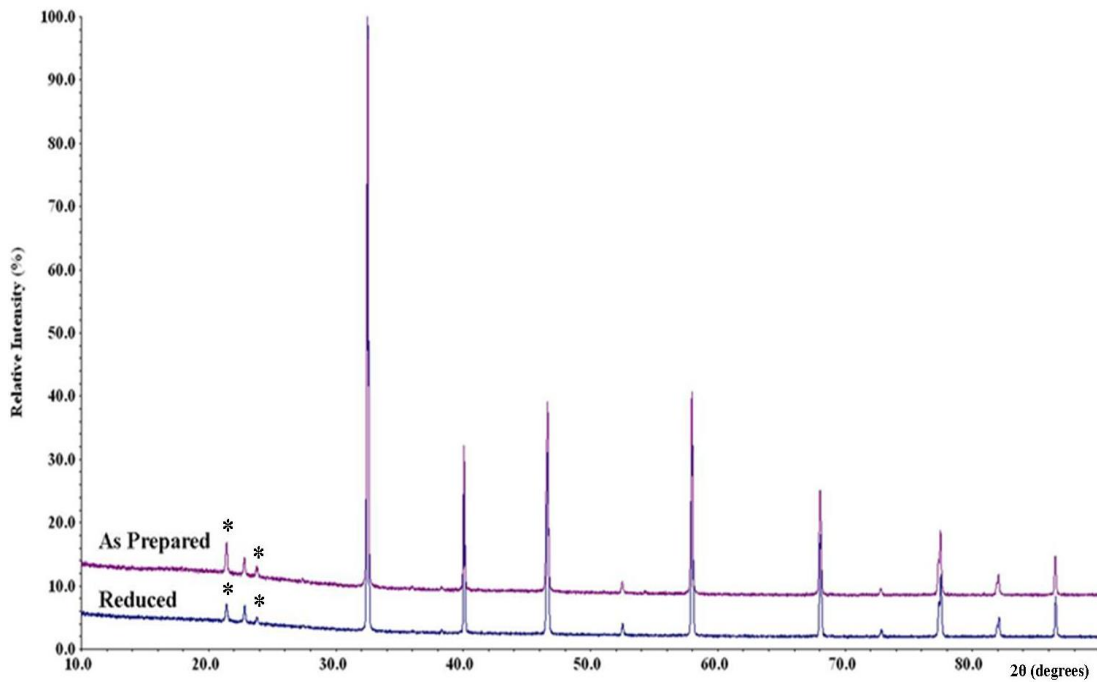


Figure 3.9: Comparison between XRD patterns of $La_{0.2}Sr_{0.6}Ca_{0.1}TiO_3$ to see the effect of reduction on the structure. Note: asterisks represent reflections of mounting grease.

Most samples were fired more than once at 1500°C to ensure phase purity and uniform solid state reaction. Calcium was chosen as dopant as it was thought to improve the sinterability of this type of perovskites. Thus, a comparison is shown in figure 3.10 to see the effect of synthesis on phase formation.

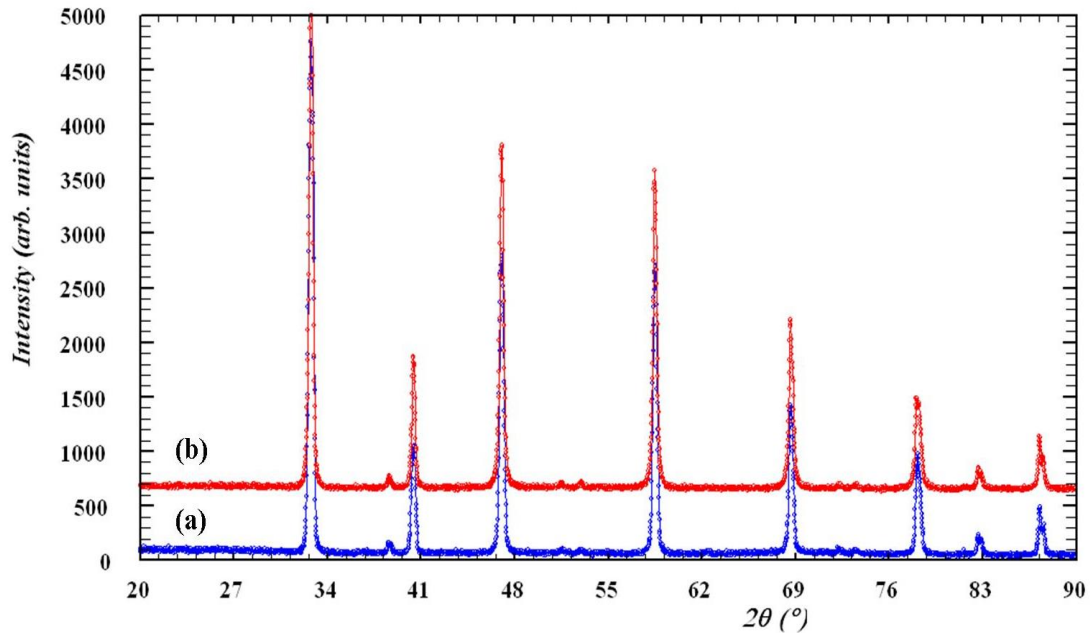


Figure 3.10: XRD patterns of two different samples of $\text{La}_{0.2}\text{Sr}_{0.3}\text{Ca}_{0.4}\text{TiO}_3$ that were (a): fired once and (b): fired twice at 1500°C for 15 hours and 8 hours, respectively.

As can be seen, both patterns show the same phase with no impurities detected suggesting that firing these samples once is sufficient to produce the correct phase. Also, a lower sintering temperature is sufficient to produce the correct phase, as can be seen from figure 3.11. Thus, it is very obvious that phase purity was achieved by firing the material at a lower temperature; which can help in reducing the cost of solid state synthesis of SOFCs anodes. This is also a good proof for the increased sinterability of the new system due to calcium introduction which reduced the temperature required to initiate the solid state reaction.

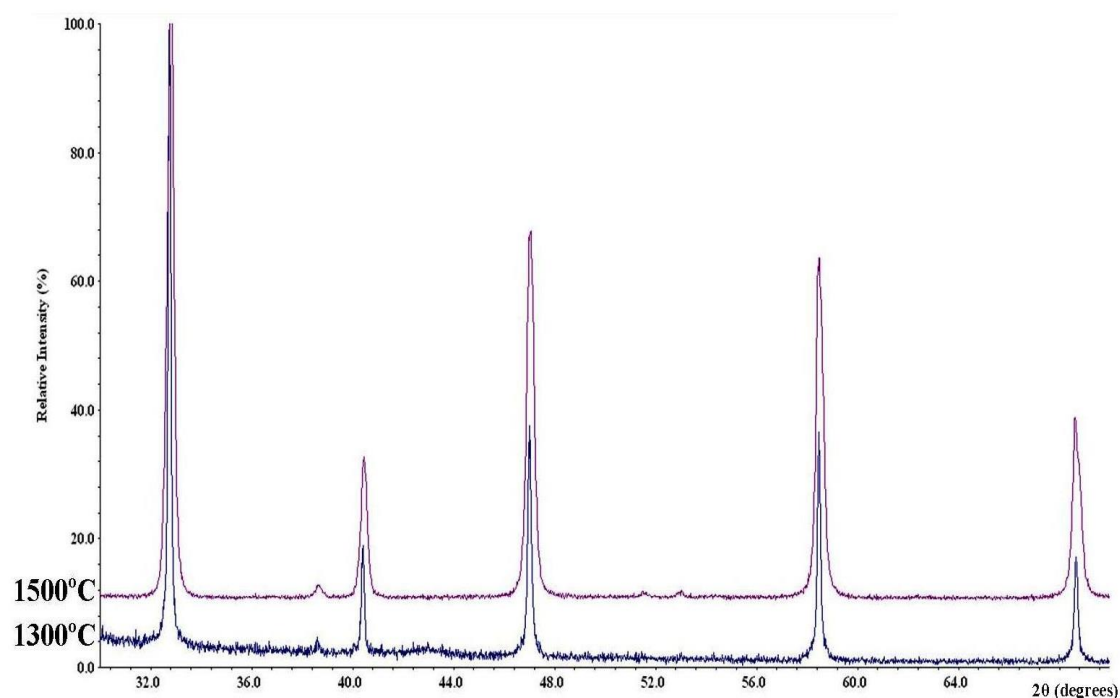


Figure 3.11: XRD patterns of two samples of $\text{La}_{0.2}\text{Sr}_{0.3}\text{Ca}_{0.4}\text{TiO}_3$ that were fired at different temperatures as shown. Note: The two patterns were obtained using different diffractometers.

Many reports indicated that an Imma phase can/must exist between the Pbnm and I4/mcm phases [11,12,18]; we used Rietveld profile matching method to determine if the Imma phase existed in our system. This method was used since it provided a much better/reliable measure for the quality of the fitted model, where the FullProf WinPlotr gives a better visualisation of the model's evolution compared to the least square method used previously. It should also be noted that the Rietveld method was used only to see which space group gave a better fit to the diffraction pattern of a single sample. Figures 3.12 and 3.13, show the XRD patterns of $\text{La}_{0.2}\text{Sr}_{0.3}\text{Ca}_{0.4}\text{TiO}_3$ ($x = 0.4$) with two fits corresponding to the I4/mcm and Imma space groups respectively.

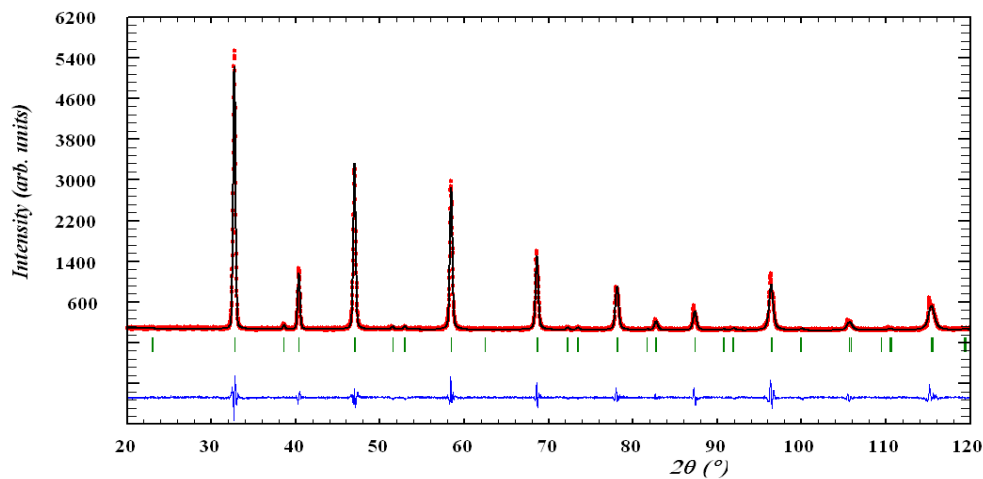


Figure 3.12: Rietveld profile matching of the XRD pattern of $\text{La}_{0.2}\text{Sr}_{0.3}\text{Ca}_{0.4}\text{TiO}_3$ with $I4/mcm$ space group with $\mathbf{a}, \mathbf{b} = 5.46155(22) \text{ \AA}$, $\mathbf{c} = 7.73590(26) \text{ \AA}$. \mathbf{R}_p : 9.70, \mathbf{R}_{wp} : 12.8, \mathbf{R}_{exp} : 8.50, χ^2 : 2.29.

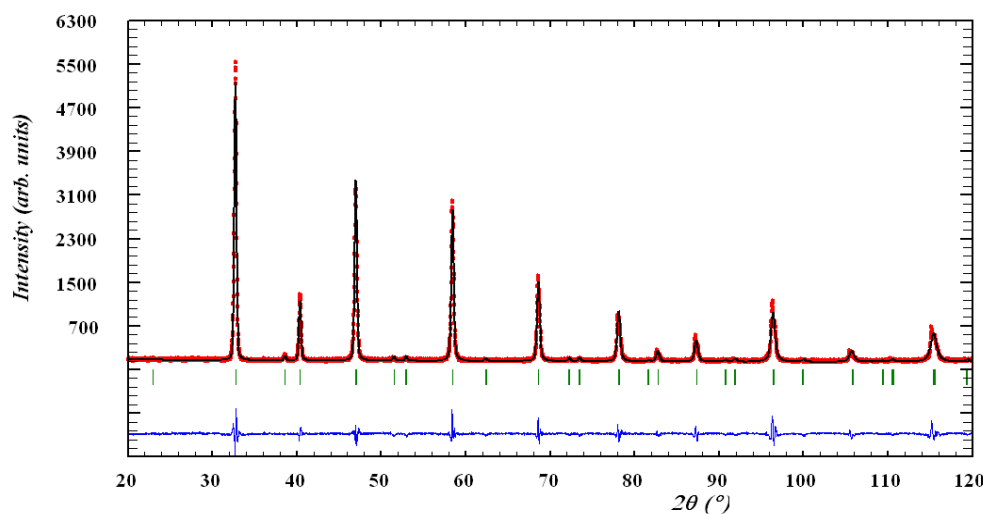


Figure 3.13: Rietveld profile matching of the XRD pattern of $\text{La}_{0.2}\text{Sr}_{0.3}\text{Ca}_{0.4}\text{TiO}_3$ with $Imma$ space group with $\mathbf{a} = 5.46765(15) \text{ \AA}$, $\mathbf{b} = 7.72377(50) \text{ \AA}$, $\mathbf{c} = 5.46369(20) \text{ \AA}$. \mathbf{R}_p : 10.5, \mathbf{R}_{wp} : 14.0, \mathbf{R}_{exp} : 8.49, χ^2 : 2.72.

From the above figures, it was clear that better fit was obtained with the $I4/mcm$ structure. The two structures; i.e. $I4/mcm$ and $Imma$; have similar reflections which

make it harder to distinguish between the two using conventional XRD techniques. The $Imma$ phase may exist in the system $Ca_xSr_{1-x}TiO_3$, as mentioned earlier, because the ionic mismatch between the A-site cations is of a considerable magnitude; given the large difference in ionic radius between strontium and calcium. However, with our system, the presence of lanthanum on the A-site is thought to balance this ionic radii mismatch giving the symmetries seen here. A phase map was made from the analysis of the XRD data obtained in this work along with data obtained from literature; this is shown in figure 3.14.

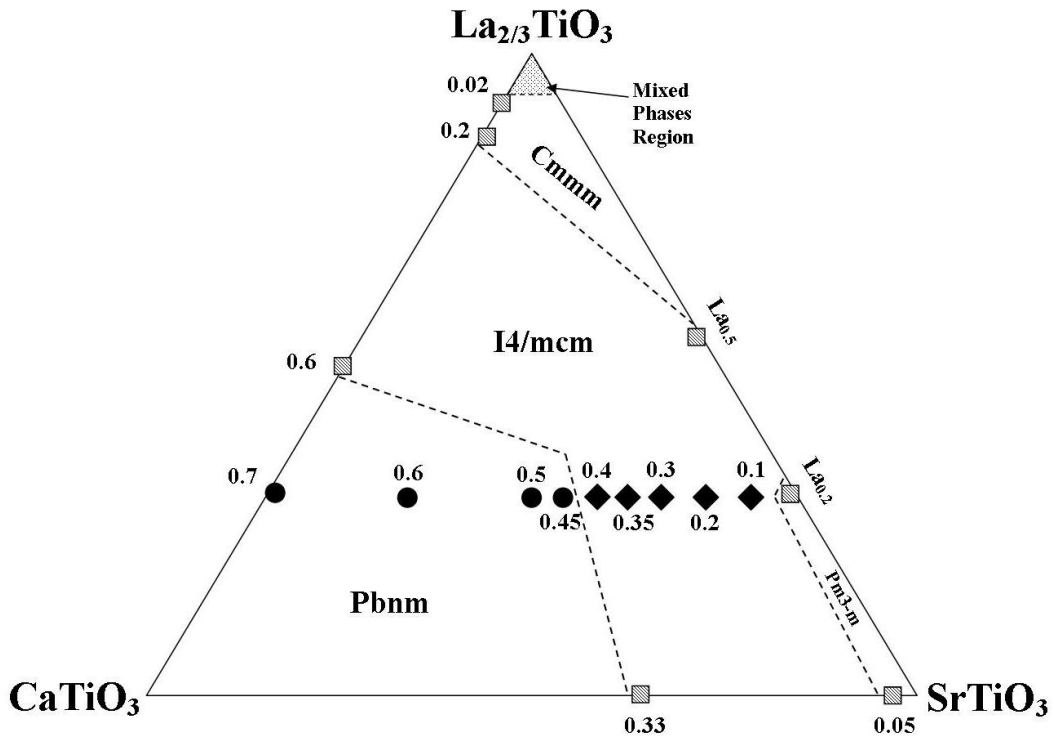


Figure 3.14: Phase diagram of the ternary system $CaTiO_3$ - $La_{2/3}TiO_3$ - $SrTiO_3$. All numbers represent calcium content. Solid symbols represent the samples studied in this work and analysed using XRD data; where shaded ones represent compositions obtained from literature.[11,12,17,14,19] ◆ refers to the tetragonal samples and ● refers to the orthorhombic samples.

It should be noted that in the phase map above the $Imma$ space group reported on the line $CaTiO_3$ - $La_{2/3}TiO_3$ [11,12] was excluded. Since the $Imma$ structure gives a very similar diffraction pattern as an $I4/mcm$ structure and there was no sufficient evidence of this phase in our data, thus its removal was in order to show the spread of the $I4/mcm$ phase across the map; which leads us to believe that this can be the more accurate space group in this ternary system. Also, there is stronger evidence in the literature that the $Imma$ phase does not exist on the line between $CaTiO_3$ - $SrTiO_3$ which can indicate that this phase may be localised only at the line between $CaTiO_3$ and $La_{2/3}TiO_3$. Castillo-Martinez et. al.[22] indicated the same behaviour when calcium was introduced into the perovskite $SrCrO_3$. With more calcium it was found that the structure adopts lower symmetries than the ideal cubic cell with phase transitions from $Pm3-m$ to $I4/mcm$ to $Pbnm$, where these observations were confirmed by ED and HRTEM.[22] Thus, from the analysis presented here the structures in the system $La_{0.2}Sr_{0.7-x}Ca_xTiO_3$ with different calcium content are $Pm3-m$ for $x = 0$, $I4/mcm$ for $0.1 \leq x \leq 0.4$ and $Pbnm$ for $0.45 \leq x \leq 0.7$. All solid solutions showed phase purity and stability with different sintering temperatures and with reduction.

3.2.2 - NPD Analysis

Neutron diffraction was used to better determine that structure of the different samples of $\text{La}_{0.2}\text{Sr}_{0.7-x}\text{Ca}_x\text{TiO}_3$. Since the symmetry changes were attributed to the tilting of the octahedra; and this involves the atomic positions of the oxygen anions in the structure; neutron diffraction is understood to give a better picture due to the relatively large scattering length of oxygen.[23] NPD data showed that the phase transition between $I4/mcm$ and $Pbnm$ was not at $\text{La}_{0.2}\text{Sr}_{0.25}\text{Ca}_{0.45}\text{TiO}_3$ ($x=0.45$) as was determined from XRD studies, but at $\text{La}_{0.2}\text{Sr}_{0.3}\text{Ca}_{0.4}\text{TiO}_3$ ($x=0.4$). Table 3.2 shows the results of the Rietveld refinement of the different samples at room temperature. Our initial analysis of adopting the tetragonal symmetry $I4/mcm$ and orthorhombic $Pbnm$ showed good fits with the data from neutron diffraction. Also, there were no indications of any secondary phases throughout the different compositions studied here; which confirms the initial conclusions from the XRD results. Starting with the structural parameters given by Yashima and Ali[24] for the tetragonal $I4/mcm$ phases of CaTiO_3 at high temperatures; the compositions of the system $\text{La}_{0.2}\text{Sr}_{0.7-x}\text{Ca}_x\text{TiO}_3$ for $0.1 \leq x \leq 0.35$ very good fits were obtained; as can be seen from figure 3.15. It should be noted, at this point, that the occupancies of the different atomic sites were kept constant throughout the refinement procedure; since attempting to refine those did not result in any improvements to the fits nor it significantly changed the initial stoichiometry values that were used. Another important aspect here is that it was almost straightforward to refine the NPD patterns using the unit cell parameters and space groups that resulted from the XRD studies explained in the first section of this chapter.

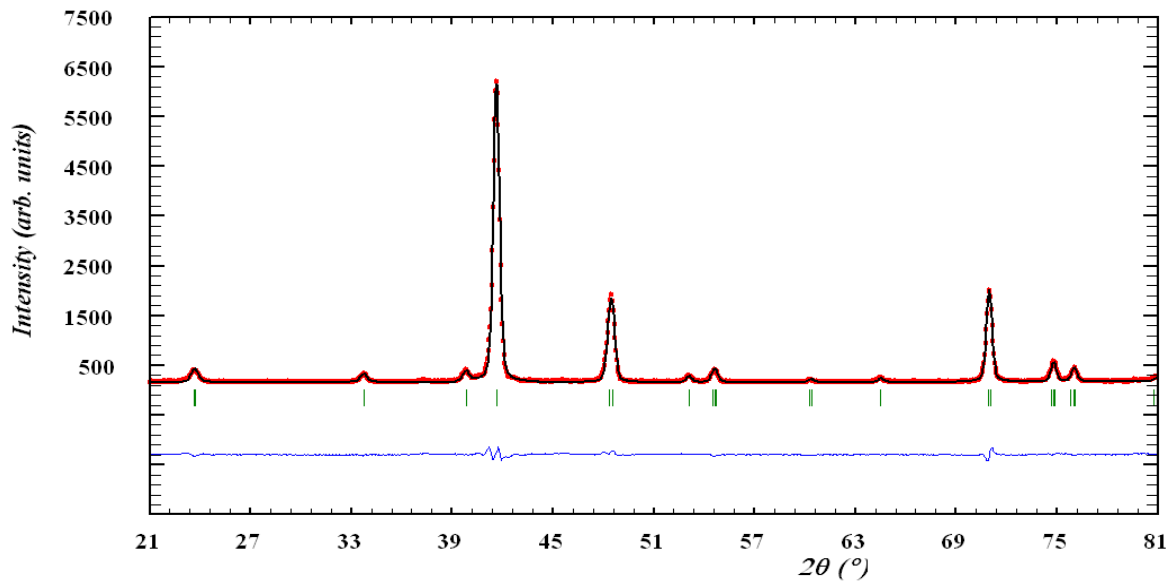


Figure 3.15: Observed (Red), calculated (Black) NPD pattern and the difference line (in Blue) for $\text{La}_{0.2}\text{Sr}_{0.5}\text{Ca}_{0.2}\text{TiO}_3$ using $I4/mcm$ space group.

For the orthorhombic phases, the structural parameters given by Kennedy et. al.[7] were used to refine compositions in the range $0.4 \leq x \leq 0.7$. The unit cell volume of the different samples studied here is shown in figure 3.16 plotted against calcium content.

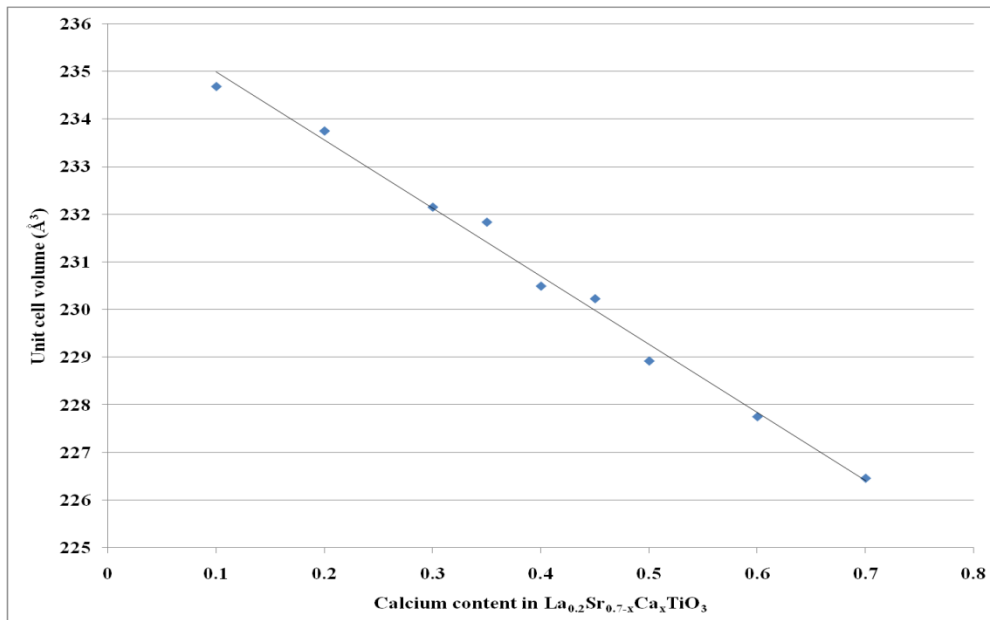


Figure 3.16: Unit cell volume of the studied samples of $\text{La}_{0.2}\text{Sr}_{0.7-x}\text{Ca}_x\text{TiO}_3$ from NPD analysis. Note: error bars contained within the data points symbols.

x in La_{0.2}Sr_{0.7-x}Ca_xTiO₃		0.1	0.2	0.3	0.35	0.4	0.45	0.5	0.6	0.7
Space Group		I4/mcm	I4/mcm	I4/mcm	I4/mcm	Pbnm	Pbnm	Pbnm	Pbnm	Pbnm
Unit Cell Parameters										
a (Å)		5.49188(7)	5.48200(10)	5.47153(9)	5.46967(15)	5.46525(11)	5.46211(7)	5.45053(23)	5.43749(27)	5.42213(17)
b (Å)		5.49188(7)	5.48200(10)	5.47153(9)	5.46967(15)	5.46699(11)	5.46338(7)	5.45351(22)	5.44635(21)	5.44102(14)
c (Å)		7.78107(18)	7.77807(20)	7.75443(23)	7.74916(32)	7.71426(27)	7.71399(21)	7.70132(25)	7.69044(42)	7.67594(29)
V (Å³)		234.683(7)	233.749(9)	232.149(9)	231.834(13)	230.490(10)	230.198(8)	228.918(15)	227.748(19)	226.455(13)
Atomic Positions										
La,Sr,Ca	x	0	0	0	0	-0.00814(93)	-0.00436(147)	0.00259(221)	0.00461(154)	0.00824(88)
	y	0.5	0.5	0.5	0.5	0.49718(132)	0.50711(78)	0.51071(66)	0.51493(55)	0.52036(42)
	z	0.25	0.25	0.25	0.25	0.25	0.25	0.25	0.25	0.25
	B_{iso}(Å²)	0.341(24)	0.521(29)	0.424(28)	0.334(31)	0.161(28)	0.462(25)	0.507(26)	0.422(31)	0.495(32)
Ti	x	0	0	0	0	0	0	0	0	0
	y	0	0	0	0	0	0	0	0	0
	z	0	0	0	0	0	0	0	0	0
	B_{iso}(Å²)	1.051(49)	0.791(51)	0.445(43)	0.790(55)	1.119(51)	0.625(37)	0.488(37)	0.763(45)	0.266(38)
O1	x	0	0	0	0	-0.05155(35)	-0.05372(48)	-0.05277(68)	-0.05676(79)	-0.0613(6)
	y	0	0	0	0	0.00142(195)	-0.00585(99)	-0.00799(87)	-0.00830(61)	-0.0098(4)
	z	0.25	0.25	0.25	0.25	0.25	0.25	0.25	0.25	0.25
	B_{iso}(Å²)	0.486(48)	0.961(62)	1.496(50)	1.369(66)	1.189(61)	0.878(48)	0.879(55)	0.392(63)	0.639(83)
O2	x	0.23134(13)	0.22613(17)	0.22061(18)	0.21849(13)	0.23814(112)	0.23289(75)	0.22909(65)	0.22304(47)	0.21839(38)
	y	0.73133(13)	0.72613(17)	0.72061(18)	0.71849(13)	0.26255(106)	0.26907(67)	0.27251(56)	0.27813(45)	0.28177(36)
	z	0	0	0	0	0.02270(15)	0.02392(22)	0.02683(28)	0.02959(31)	0.03169(23)
	B_{iso}(Å²)	0.981(31)	1.056(33)	1.073(27)	0.872(29)	1.070(38)	1.149(33)	1.157(36)	1.246(46)	0.988(48)
R-factors	R_p	3.48	3.68	3.63	3.75	3.68	3.35	2.77	3.42	3.13
	R_{wp}	4.76	4.98	5.01	5.09	4.96	4.44	3.59	4.52	4.13
	R_{exp}	1.95	1.96	2.02	1.93	1.86	1.77	2.01	1.77	1.92
	χ²	5.98	6.42	6.17	6.95	7.07	6.33	3.19	6.48	4.64

Table 3.2: Summary of the Rietveld refinement results of NPD data for different samples of La_{0.2}Sr_{0.7-x}Ca_xTiO₃ at room temperature.

The unit cell volume of the whole system shows a continuous decrease with increasing content of calcium; with no irregularities observed. This can suggest a good stability of the perovskite phase. The unit cell parameters are shown in figure 3.17 for all the samples prepared in this work.

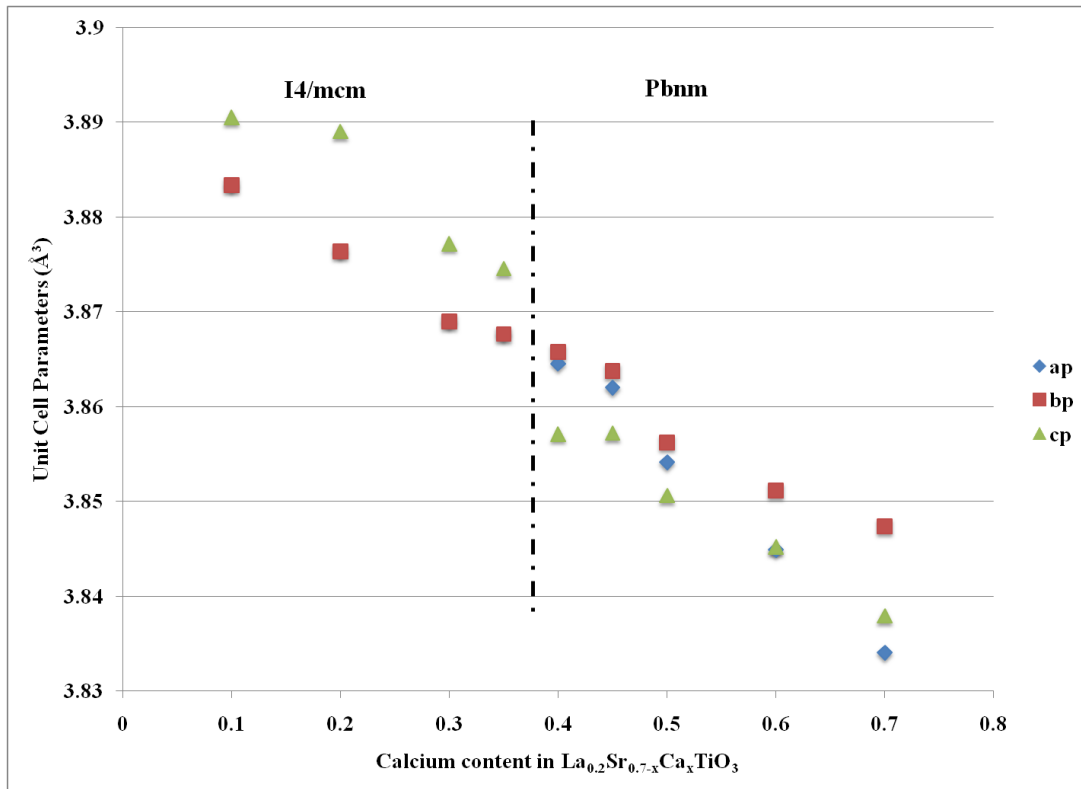


Figure 3.17: The primitive unit cell parameters of the studied samples obtained from NPD analysis. Note: error bars are contained within the data points symbols.

It can be seen that the unit cell parameters a and b within the orthorhombic phase close in on each other with less calcium content which indicate a transformation into a tetragonal phase. The same can be seen with the “a”, “b” and “c” parameters within the tetragonal phase suggesting that the structure is moving toward a higher symmetry. The “a” and “b” parameters seem to follow a straight line throughout the system where the “c” parameter shows a discontinuous change at the Pbnm-I4/mcm phase boundary.

With neutron diffraction, a better determination of the unit cell space group was possible. This was apparent especially with the compositions close to the phase boundary; i.e. $x = 0.4$ and 0.45 . With XRD analysis, it was found that $x = 0.4$ adopted the tetragonal $I4/mcm$ symmetry since there was no indication of the $\{1\ 2\ 0\}$ reflection of the $Pbnm$ phase. However, with NPD analysis, it was revealed that this composition is not quite tetragonal. It can be seen that the “a” and “b” unit cell parameters are almost overlapping. Fitting the data of this composition with the tetragonal symmetry did not result in a good fit. In the XRD studies, an irregular behaviour regarding the “c” parameter was found with calcium content; i.e. figure 3.8 in the XRD section; where it showed a large relative error compared to the other parameter at the composition with $x = 0.2$. The same thing can be seen here, where the “c” parameter for the same composition obtained from NPD diffraction is slightly off than the rest values. Also, the same can be seen for the compositions with $x = 0.4$ and 0.45 , where the “c” parameter is showing a strange behaviour between the two samples. The only plausible explanation which might need further investigation in the future is that as the unit cell is going through a phase transition from $Pbnm$ to $I4/mcm$ symmetries, it experiences significant strains on the $[0\ 0\ 1]$ direction due to all the distortions and changes to the tilt angles of the BO_6 octahedra. As explained previously, the ionic radius mismatch is the major player here in determining the symmetry of the unit cells of these perovskites. Hence, the strain on the $[0\ 0\ 1]$ direction does not follow a very linear or regular fashion as the strontium/calcium content is varying. The exact origins of this behaviour can be the topic of future investigations that, at the current stage, extend beyond the main scope of this work. Nonetheless, the findings here which are very similar to the XRD findings are very important indeed in giving another confirmation on the symmetries of the

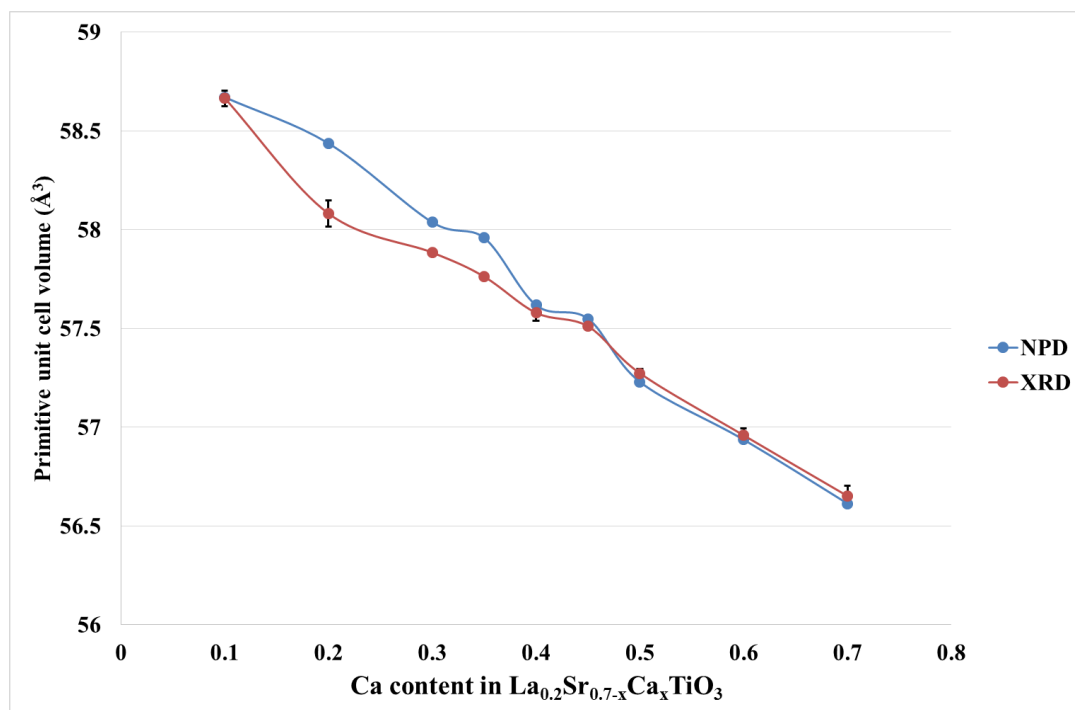


Figure 3.19: Comparing the primitive unit cell volumes obtained from XRD and NPD; using the least square and Rietveld methods, respectively. Note: some error bars are contained within the data points symbols.

The above figure shows a good agreement between the two sets of data for many of the samples studied. The errors are indicative that neutron diffraction is more suitable to study such distorted perovskites; i.e. much less compared to the XRD errors. The mismatch between the two sets of data in the range $0.2 \leq x \leq 0.35$ can be explained from the fact that with X-rays, the reflections due to oxygen are less resolved when compared to neutrons. Overall, both sets show a uniform decrease with more calcium and no major discrepancies throughout the series. The unit cell volume has shown a 0.2% increase after reduction for $\text{La}_{0.2}\text{Sr}_{0.25}\text{Ca}_{0.45}\text{TiO}_3$ which is very close to the obtained value of 0.3% using XRD data for the same composition. This shows a good stability of the structure in reducing conditions. Using the atomic coordinates obtained from the NPD analysis of the different compounds it was possible to confirm the initial deduction

that the intensity of the $\{2\ 1\ 1\}$ reflection reflects the amplitude of the anti-phase tilt along the $[001]$ direction. This is represented in figure 3.20.

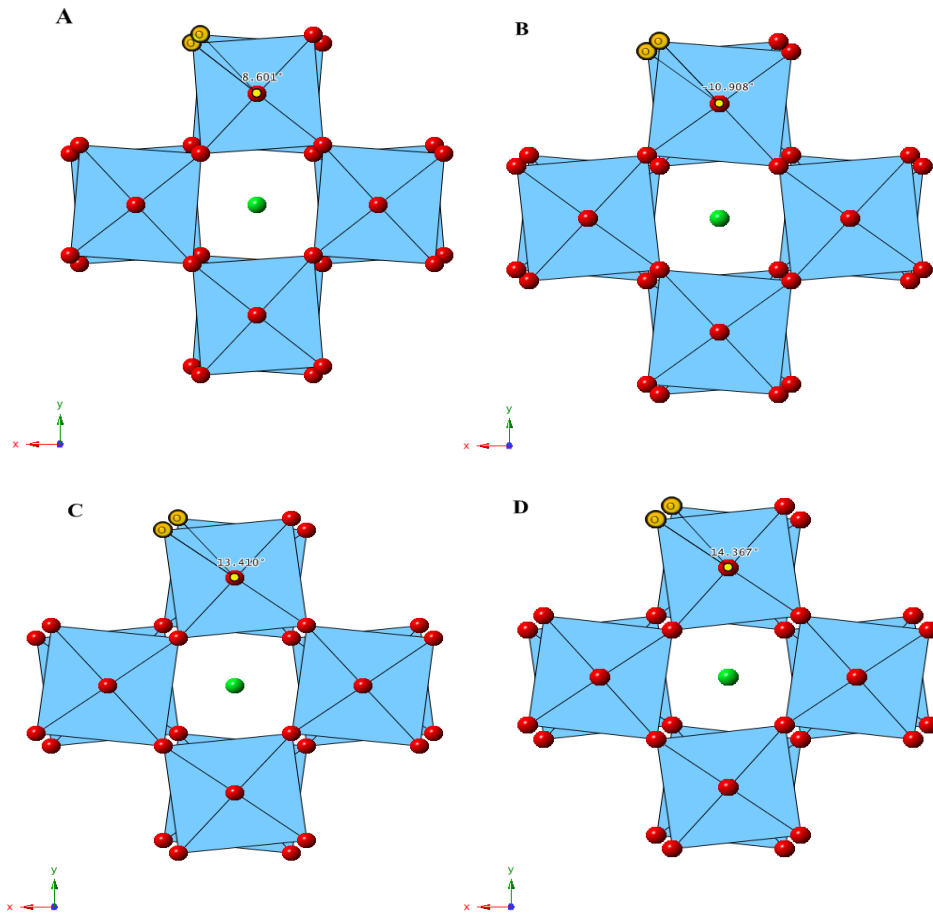


Figure 3.20: Structure view along the $[00\bar{1}]$ of the tetragonal samples of $\text{La}_{0.2}\text{Sr}_{0.7-x}\text{Ca}_x\text{TiO}_3$ where A: 0.1, B: 0.2, C: 0.3 and D: 0.35 for x . The out of phase tilt angles associated with the $I4/mcm$ symmetry are shown; i.e. obtained using CrystalMaker[®].

The intensity of the $\{2\ 1\ 1\}$ reflection increased with calcium content as can be seen from the NPD patterns in figure 3.21, which is indicative of the increase in the anti-phase tilt angles.

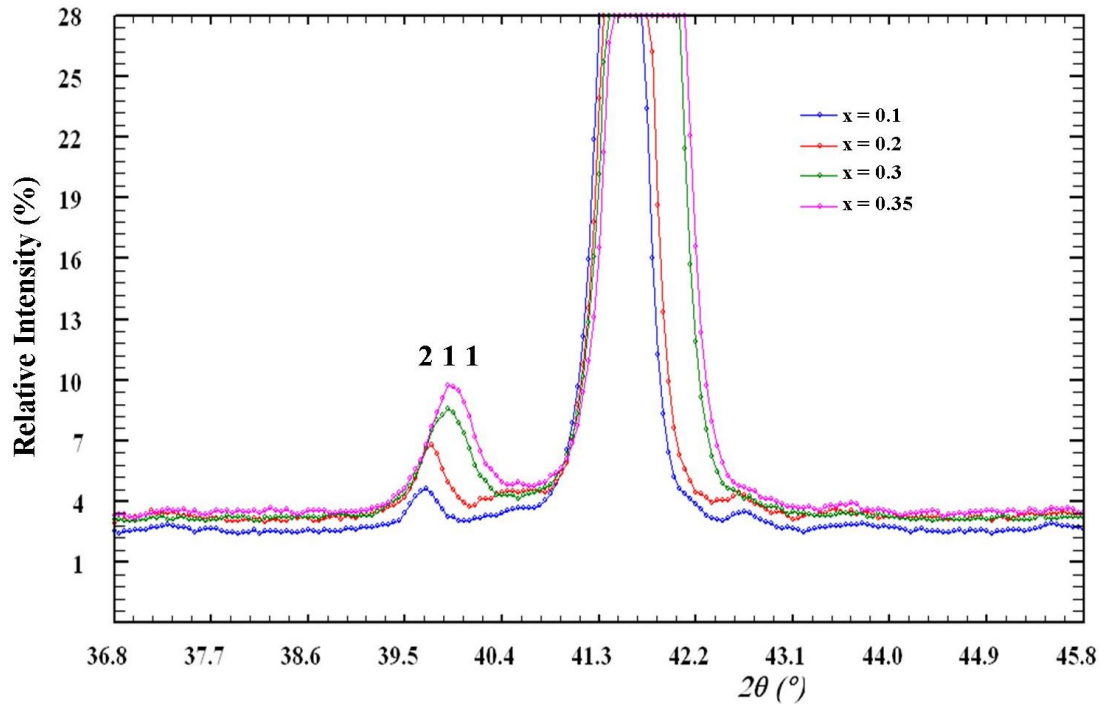


Figure 3.21: Portion of the NPD patterns for samples of $\text{La}_{0.2}\text{Sr}_{0.7-x}\text{Ca}_x\text{TiO}_3$ which show a tetragonal symmetry; $0.1 \leq x \leq 0.35$; showing the $\{2\ 1\ 1\}$ reflection.

This confirms that the system adopts a lower symmetry as a result of the octahedra tilt which increases with calcium content. The figure above shows some traces of small peaks around the main peaks which can be resulting from contamination within the vanadium containers used in collecting the NPD patterns; i.e. these containers were difficult to clean. This is more apparent for the first two samples; i.e. $x = 0.1$ and $x = 0.2$; which their patterns were collected at higher resolution compared to the others. For the orthorhombic phases, the anti-phase tilting occurred along the $[100]$ and $[010]$ directions along with an in-phase tilting along the $[001]$ direction. The tilt systems along the $[001]$ direction for the $I4/mcm$ and $Pbnm$ symmetries are shown in figure 3.22.

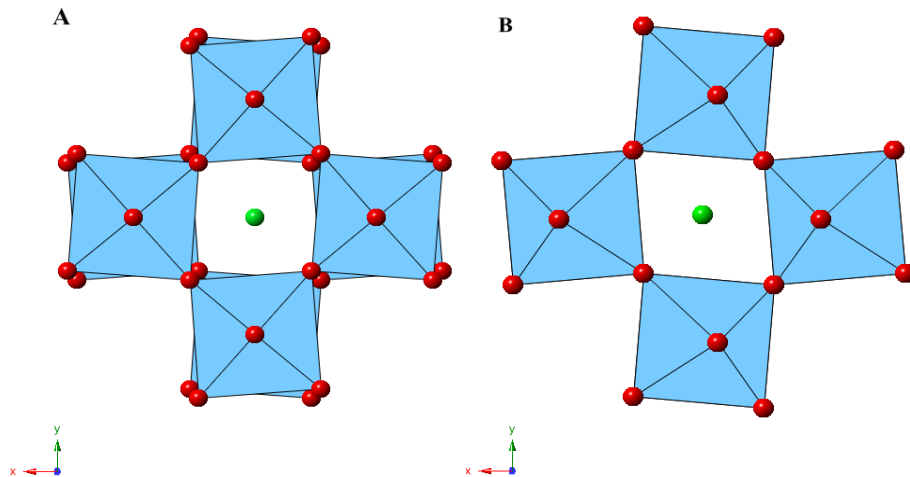


Figure 3.22: Structure views along the $[00\bar{1}]$ showing the (A) anti-phase and (B) the in-phase tilting of the TiO_6 octahedra for the $I4/mcm$ and $Pbnm$ phases, respectively.

The anti-phase tilting systems along the $[100]$ and $[010]$ directions are shown in figure 3.23.

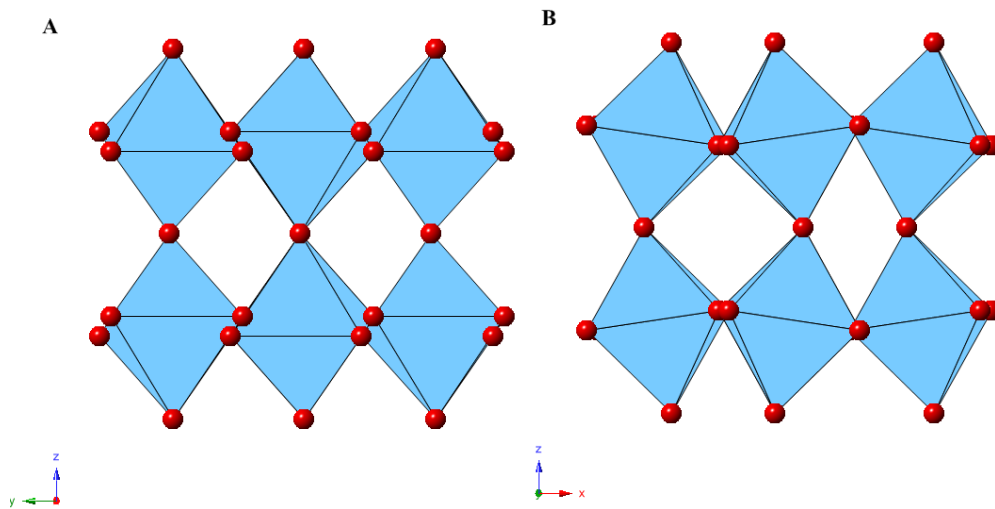


Figure 3.23: Structure views along the (A) $[100]$ and (B) $[010]$ direction of the orthorhombic unit cell of $\text{La}_{0.2}\text{Sr}_{0.2}\text{Ca}_{0.5}\text{TiO}_3$; demonstrating the anti-phase tilting of the octahedra.

The out-of-phase tilt angles in the different samples were calculated using the atomic coordinates for the O2 atom from the results of Rietveld refinement. The magnitude of

the angles was calculated using the method provided by Yashima and Ali[23] and Qin et. al.[17]. Taking the O2 atom coordinates as $\left(\frac{1}{4} - u, \frac{1}{4} + v, w\right)$ the out-of-phase tilt angle along the [001] direction in the I4/mcm phase is equal to $\varphi = \tan^{-1} 4u$. The out-of-phase tilt angles along the [100] and [010] directions in the Pbnm phase were equal to $\varphi = \tan^{-1} 4\sqrt{2}u$. These calculated tilt angles were plotted against calcium content as shown in figure 3.24.

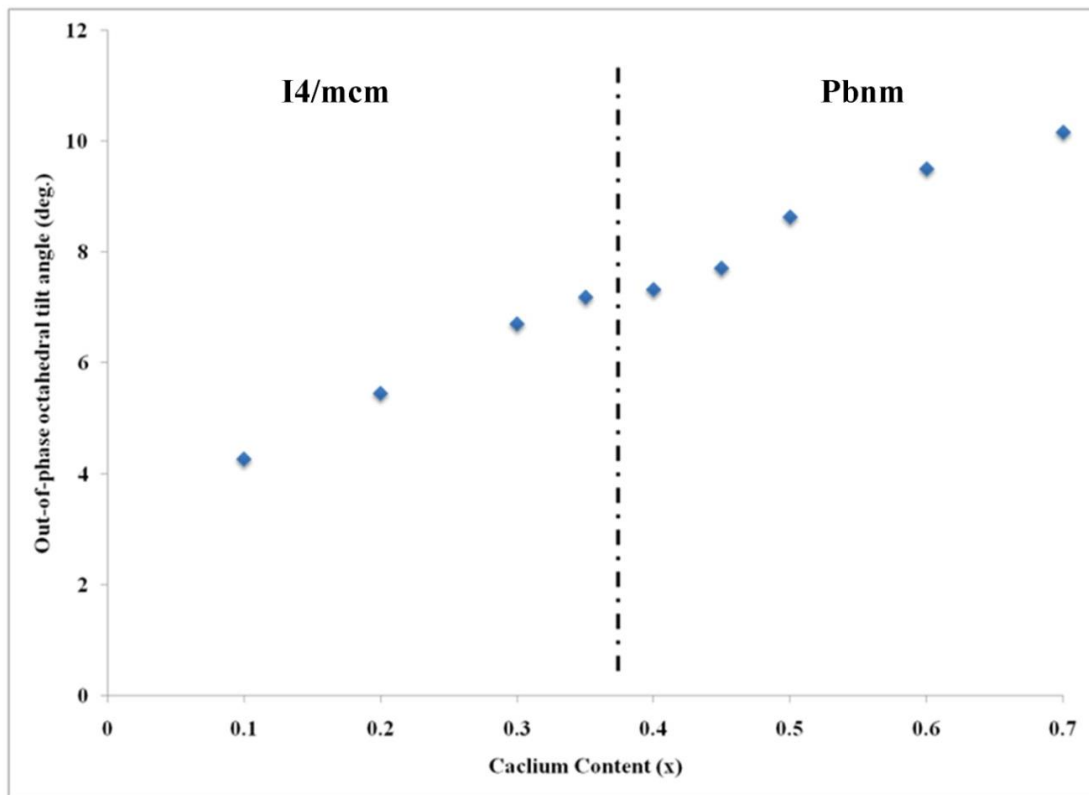


Figure 3.24: The out-of-phase tilt angle values for the different compositions of $\text{La}_{0.2}\text{Sr}_{0.7-x}\text{Ca}_x\text{TiO}_3$ at room temperature. Note: error bars are contained within the data points symbols.

From the figure above, it is clear that the magnitude of the tilt angles is decreasing with decreasing calcium content which indicates a transition toward a higher symmetry.

Also, around the phase boundary the change looks continuous. This result is similar to the findings of Qin et. al.[17] for the system $\text{Sr}_{1-x}\text{Ca}_x\text{TiO}_3$; however, for CaTiO_3 the out-of-phase tilt angle was shown to be $\approx 12^\circ$. This value is higher than the obtained value for $\text{La}_{0.2}\text{Ca}_{0.7}\text{TiO}_3$ which was 10.2° . This can indicate that our system is less distorted than CaTiO_3 . The atomic coordinates were also used to investigate the bond lengths between the different cations and oxygen in the different samples. The first was the bond between titanium and oxygen to determine if the BO_6 octahedra were rigid; i.e. not distorted; with different calcium content. This is shown in figure 3.25.

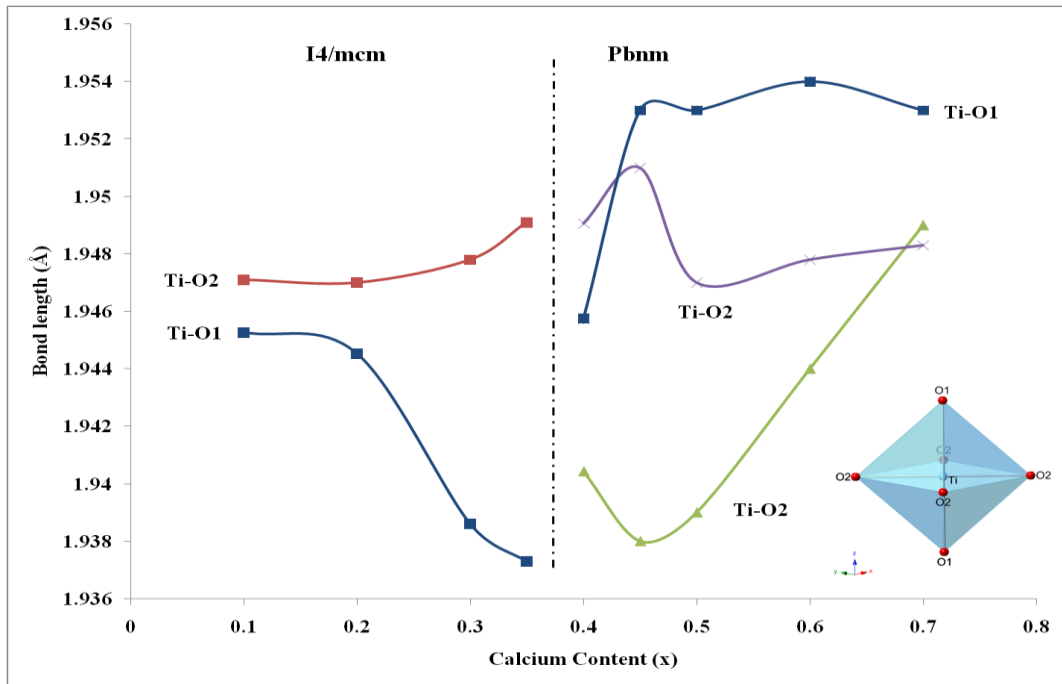


Figure 3.25: Bond lengths between titanium and the neighbouring oxygen anions forming the BO_6 octahedral for the different samples of $\text{La}_{0.2}\text{Sr}_{0.7-x}\text{Ca}_x\text{TiO}_3$. Lines are guides to the eye. Note: error bars are contained within the data points symbols.

As explained, elsewhere, the perovskite B cation is sitting in the void at the centre of the octahedron made up by 6 oxygen atoms. Usually, these octahedra are rigid and any

changes to the structure are manifested in changes in the tilt angles of these octahedra. From the behaviour of the bond lengths between the titanium (B-site) and the oxygen anions, it can be seen that at the phase boundary; i.e. $x=0.4$; and there is an obvious distortion that occurs to the octahedra themselves along with the accompanying tilts. Within the tetragonal phase it can be seen that while the Ti-O2 bond length is slightly increasing, the Ti-O1 bond length decreases with increasing calcium content. Within the orthorhombic phase; e.g. $x > 0.45$; the Ti-O1 bond is relatively constant as calcium content is increased; whereas the distortion to the octahedra is localised along the Ti-O2 bonds. It can be seen from the lengths of the latter bonds that the distortion is maximised around the phase boundary between the $I4/mcm$ and $Pbnm$ symmetries; which is very apparent from the difference between the two Ti-O2 bonds. This difference indicates that the each octahedron becomes elongated along one axis while the other bond becomes smaller around the phase boundary. These two Ti-O2 bonds are brought closer together at higher calcium content; i.e. $x > 0.5$; to end up with very similar values at $x = 0.7$; which indicates a less distorted octahedra. This confirms that as the ionic radius mismatch on the A-site increases with increasing calcium content, the system adopts a lower symmetry not only through the change in the tilt of the octahedra; but also through distortions to the octahedra themselves; which are quite significant around the phase boundary. In other words, the system starts with a relatively rigid octahedra up to $x = 0.2$ after which distortions take place only to stabilise with slightly larger octahedra with $x \geq 0.5$. Within the intermediate compositions; i.e. $0.3 \leq x \leq 0.5$, the ionic radius mismatch is greater. The origin of the octahedra distortions may be a result of the A-site deficiency in the system $La_{0.2}Sr_{0.7-x}Ca_xTiO_3$. As discussed earlier, with the reported symmetries of the stoichiometric

compounds of the system $\text{Ca}_{1-x}\text{Sr}_x\text{TiO}_3$; most of the reports seldom mention distortions to the TiO_6 octahedra and only discuss the different changes to the tilt angles corresponding to the lower symmetry space groups. The octahedra distortions in our system indicate less rigid TiO_6 octahedra; which was indicated by the relatively higher isothermal parameters of the titanium atomic position; i.e. table 3.2; when compared to the A-site isothermal parameter in most of the different samples. Thus, this shows that in the system $\text{La}_{0.2}\text{Sr}_{0.7-x}\text{Ca}_x\text{TiO}_3$, the structure is influenced by an interplay between the A-site ionic radius mismatch and the defects created by the A-site deficiency. The bond lengths between the A-site cations and oxygen anions are plotted in figure 3.26.

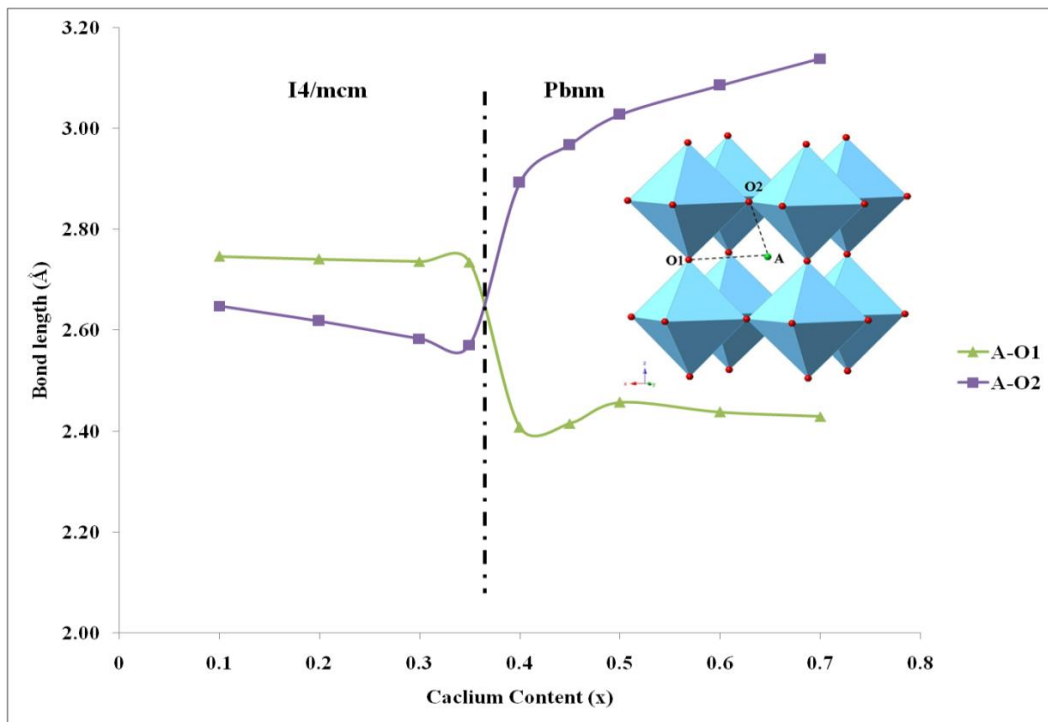


Figure 3.26: Bond lengths between the A-site cation and oxygen in the perovskite unit cell for the different samples of $\text{La}_{0.2}\text{Sr}_{0.7-x}\text{Ca}_x\text{TiO}_3$. The lines are guides to the eye.

The behaviour of the A-O bonds are more subtle when compared to the Ti-O bonds, as was shown above. First, it can be seen that the A-O1 bond length is almost constant

since there are no tilts involved in the x and y directions within the tetragonal phase. The A-O2 bond length, however, shows a decrease which can be linked to the out-of-phase tilt angle along the z-axis ([001] direction), as well as, the reduction in unit cell volume. Second, in the orthorhombic phase, the A-O1 is almost constant again while the A-O2 bond length increases with increasing calcium content; which indicates increased distortions to the octahedra originating from more tilt angles being present. The A-O1 bond length change with calcium content is very small compared to the unit cell volume; which indicate that the unit cell volume is mainly controlled by the distortions of the octahedra. In other words, as the system adopts the orthorhombic phase, the unit cell volume is largely affected by the tilts of the octahedra.

CaTiO₃ was found to undergo two phase transitions which were reversible; Pbnm to I4/mcm and I4/mcm to Pm $\bar{3}$ m at 1498K and 1634K respectively.[23] The same behaviour was reported by Kennedy et. al.[7] where the Pbnm-I4/mcm transition occurred near 1500K and the I4/mcm-Pm $\bar{3}$ m transition occurred above 1580K. Redfern[20] also indicated the same using XRD analysis where he reported the Pbnm-I4/mcm transition to occur around 1423K and the I4/mcm-Pm $\bar{3}$ m at 1523K.

Two samples of La_{0.2}Sr_{0.7-x}Ca_xTiO₃; i.e. x = 0.45 and 0.5; were analyzed at high temperatures to determine the structural changes that occur. These two were chosen to see the structural differences between them since they are close to the phase boundary and showed a change in the electrical conductivity that was increasing with calcium content up to x = 0.45 and then started decreasing for samples with x \geq 0.5.

Figure 3.27 shows NPD patterns collected at different temperatures for La_{0.2}Sr_{0.2}Ca_{0.5}TiO₃ where different symmetries were observed.

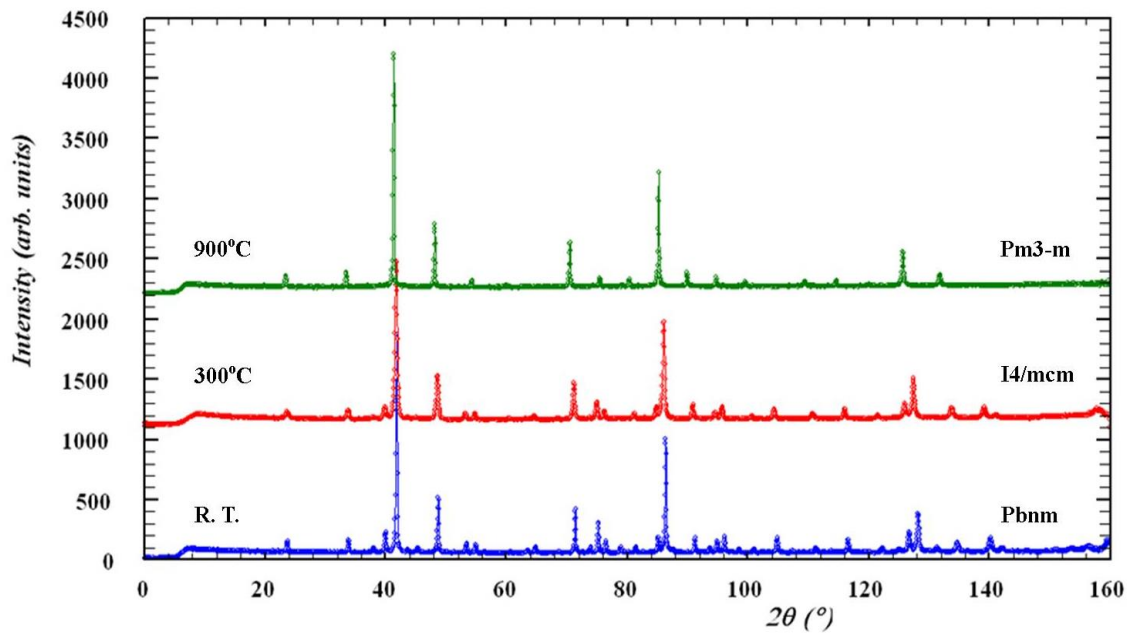


Figure 3.27: NPD patterns for $\text{La}_{0.2}\text{Sr}_{0.2}\text{Ca}_{0.5}\text{TiO}_3$ showing the phase transitions at high temperatures.

From the patterns above, it is very obvious that the system is moving to higher symmetry as it was heated; which were very well fitted as shown in figure 3.28. This result shows that the system investigated in this work adopts higher symmetries at much lower temperatures than CaTiO_3 ; which indicates much lower distortions to the perovskite structure. The structural parameters obtained from Rietveld refinement of a reduced sample of $\text{La}_{0.2}\text{Sr}_{0.25}\text{Ca}_{0.45}\text{TiO}_3$ are summarised in table 3.3 and the unit cell parameters and volumes are plotted against temperature in figure 3.29.

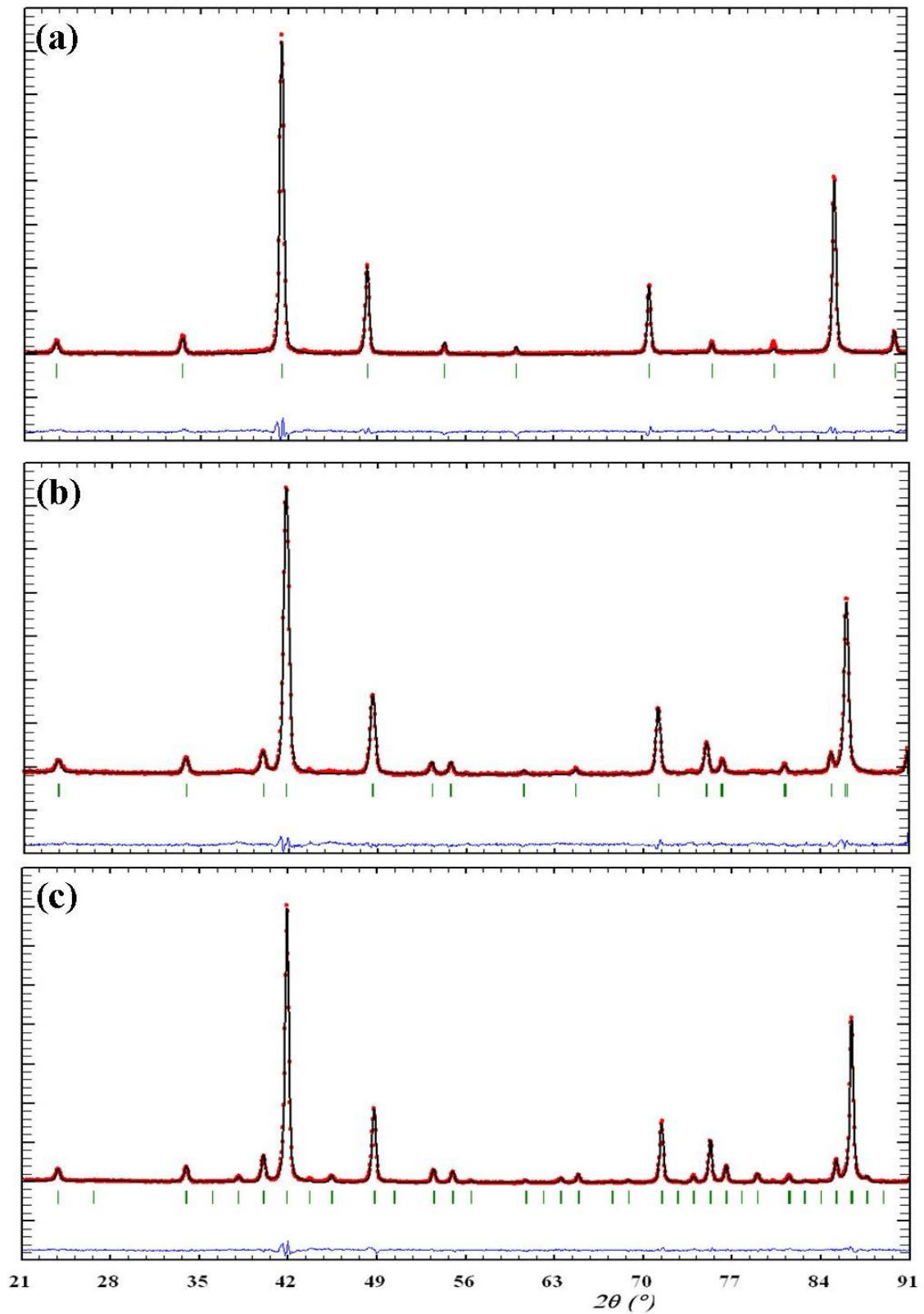


Figure 3.28: Rietveld refinement results of NPD patterns for $\text{La}_{0.2}\text{Sr}_{0.2}\text{Ca}_{0.5}\text{TiO}_3$ at (a) 900°C, (b) 300°C and (c) at room temperature.

Temperature	R.T.	100°C	200°C	300°C	500°C	600°C	700°C	800°C	900°C	
Space Group	Pbnm	Pbnm	Pbnm	I4/mcm	I4/mcm	I4/mcm	I4/mcm	I4/mcm	Pm $\bar{3}$ m	
Unit Cell Parameters										
a (Å)	5.46555(11)	5.47200(43)	5.48256(16)	5.47519(15)	5.48476(13)	5.49600(11)	5.50334(15)	5.51489(78)	3.90390(4)	
b (Å)	5.46636(11)	5.47429(40)	5.48302(16)	5.47519(15)	5.48476(13)	5.49600(11)	5.50334(15)	5.51489(78)	3.90390(4)	
c (Å)	7.72028(32)	7.72631(34)	7.74109(46)	7.75914(39)	7.77881(35)	7.79341(31)	7.80009(42)	7.80208(216)	3.90390(4)	
V (Å³)	230.656(12)	231.444(27)	232.705(17)	232.601(15)	234.007(13)	235.408(12)	236.239(16)	237.293(81)	59.497(1)	
Atomic Positions										
La,Sr,Ca	x	-0.0071(27)	-0.0054(23)	-0.0073(18)	0	0	0	0	0.5	
	y	0.5068(10)	0.5056(13)	0.5007(22)	0.5	0.5	0.5	0.5	0.5	
	z	0.25	0.25	0.25	0.25	0.25	0.25	0.25	0.25	
	B_{iso}(Å²)	0.557(29)	0.741(34)	0.918(35)	0.987(41)	1.366(41)	1.612(58)	1.868(59)	2.093(65)	2.139(60)
Ti	x	0	0	0	0	0	0	0	0	
	y	0	0	0	0	0	0	0	0	
	z	0	0	0	0	0	0	0	0	
	B_{iso}(Å²)	0.603(41)	0.748(48)	0.682(48)	1.040(57)	1.200(59)	1.403(73)	1.705(77)	1.790(90)	1.485(59)
O1	x	-0.05226(73)	-0.05465(74)	-0.0460(10)	0	0	0	0	0.5	
	y	-0.0075(13)	-0.0108(14)	0.0026(29)	0	0	0	0	0	
	z	0.25	0.25	0.25	0.25	0.25	0.25	0.25	0.25	
	B_{iso}(Å²)	1.377(81)	1.426(81)	1.99(12)	2.266(72)	1.972(74)	1.65(11)	1.48(11)	1.45(13)	3.286(38)
O2	x	0.23052(83)	0.2322(11)	0.2323 (16)	0.21743(17)	0.22214(20)	0.22510(23)	0.22902(26)	0.23533(44)	-
	y	0.27011(79)	0.2705(10)	0.2617(11)	0.71743(17)	0.72214(20)	0.72150(23)	0.72902(26)	0.73533(44)	-
	z	0.02594(29)	0.02378(34)	0.02367(40)	0	0	0	0	0	-
	B_{iso}(Å²)	0.949(45)	1.061(46)	1.374(63)	1.743(36)	2.456(46)	2.840(71)	3.346(78)	3.881(99)	
R-factors	R_p	2.90	3.68	4.16	3.91	3.85	3.68	3.44	3.93	3.35
	R_{wp}	3.70	4.67	5.38	4.97	4.97	4.71	4.39	5.05	4.51
	R_{exp}	1.98	3.54	3.67	3.57	3.66	3.46	3.42	3.40	2.00
	χ²	3.48	1.74	2.14	1.94	1.84	1.86	1.65	2.20	5.09

Table 3.3: Summary of the Rietveld refinement results of NPD data for a reduced sample of La_{0.2}Sr_{0.25}Ca_{0.45}TiO₃ at different temperatures.

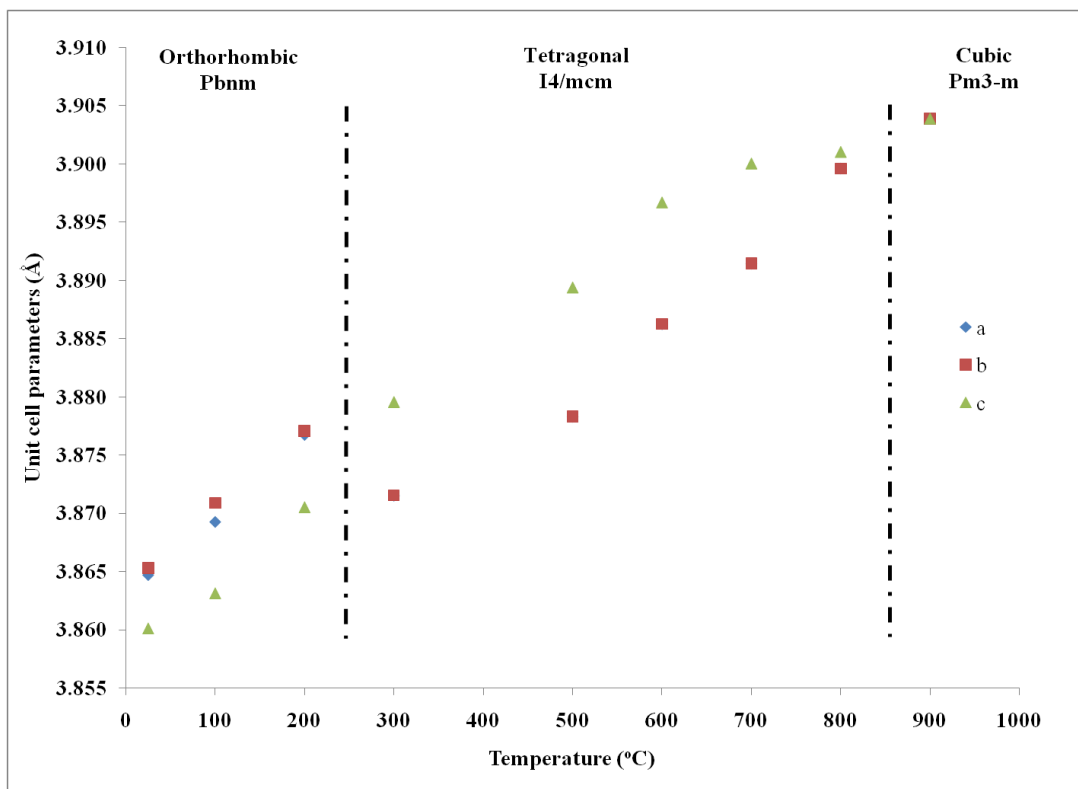


Figure 3.29: Unit cell parameters for a reduced sample of $\text{La}_{0.2}\text{Sr}_{0.25}\text{Ca}_{0.45}\text{TiO}_3$ as a function of temperature. Note: error bars are contained within the data points symbols.

It can be seen that the “a” and “b” unit cell parameters were very close to each other as was the case with the as-prepared $\text{La}_{0.2}\text{Sr}_{0.25}\text{Ca}_{0.45}\text{TiO}_3$ at room temperature. As the temperature was raised, thermal expansion separated the two parameters slightly where at 300°C they moved closer to each other indicating a higher symmetry. The discontinuous change in the “c” parameter however indicates a first order transition between the Pbnm and I4/mcm. The transition from the I4/mcm to the Pm3-m phase can be seen to be of a second or higher order from the continuous trend of the unit cell parameters; as was the case with CaTiO_3 at high temperatures.[23] The primitive unit cell volume of the reduced $\text{La}_{0.2}\text{Sr}_{0.25}\text{Ca}_{0.45}\text{TiO}_3$ at different temperatures is shown in figure 3.30; where it can be seen that the volume increased with temperature without

any major irregularities; which indicates a very good stability of the structure with temperature.

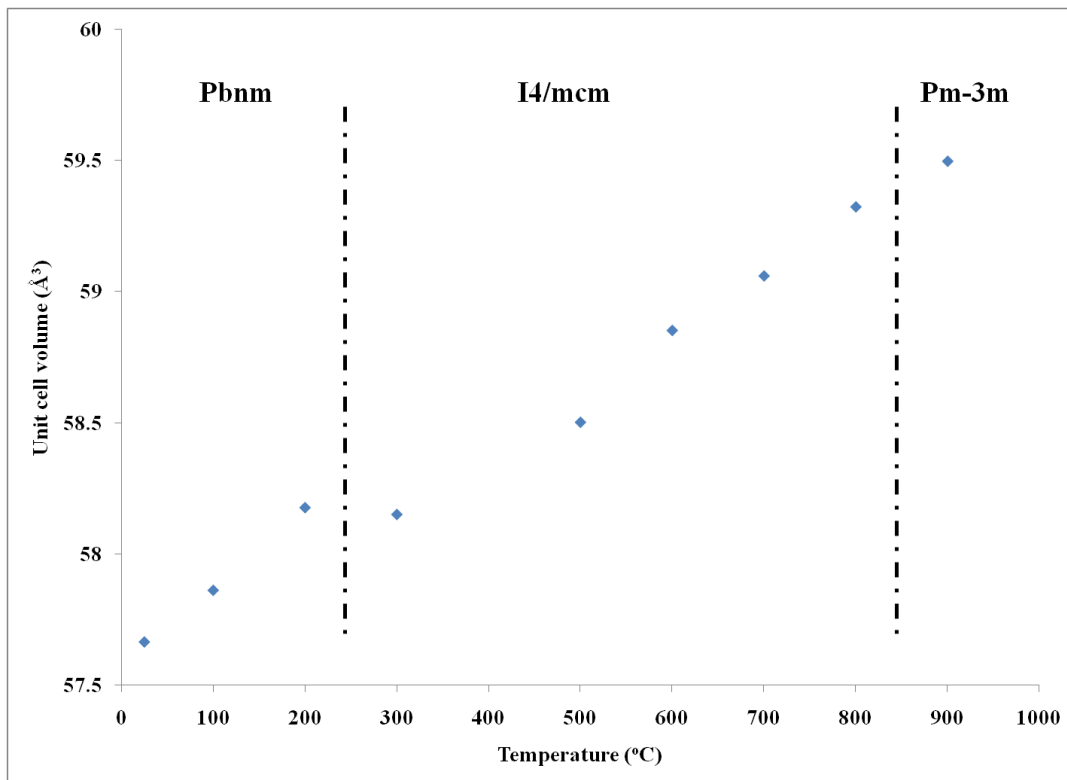


Figure 3.30: Primitive unit cell volume of the reduced $\text{La}_{0.2}\text{Sr}_{0.25}\text{Ca}_{0.45}\text{TiO}_3$ plotted against temperature. Note: error bars are contained within the data points symbols.

$\text{La}_{0.2}\text{Sr}_{0.2}\text{Ca}_{0.5}\text{TiO}_3$ ($x = 0.5$) has also shown the same high temperature transitions as $\text{La}_{0.2}\text{Sr}_{0.25}\text{Ca}_{0.45}\text{TiO}_3$ ($x = 0.45$). The unit cell parameters are plotted against temperature in figure 3.31. The refined structural parameters for $\text{La}_{0.2}\text{Sr}_{0.2}\text{Ca}_{0.5}\text{TiO}_3$ are summarised in table 3.4.

Temperature		R.T.	300°C	500°C	600°C	700°C	900°C
Space Group		P6mm	I4/mcm	I4/mcm	I4/mcm	I4/mcm	Pm3m
Unit Cell Parameters							
a (Å)		5.45053(23)	5.46744(19)	5.47925(19)	5.48742(13)	5.49423(14)	3.89750(4)
b (Å)		5.45351(22)	5.46744(19)	5.47925(19)	5.48742(13)	5.49423(14)	3.89750(4)
c (Å)		7.70132(25)	7.74474(39)	7.76746(40)	7.77707(33)	7.78345(39)	3.89750(4)
V (Å ³)		228.918(15)	231.513(16)	233.196(16)	234.182(13)	234.955(15)	59.205(1)
Atomic Positions							
La,Sr,Ca	x	0.0026(22)	0	0	0	0	0.5
	y	0.51071(66)	0.5	0.5	0.5	0.5	0.5
	z	0.25	0.25	0.25	0.25	0.25	0.5
	B _{iso} (Å ²)	0.507(26)	1.290(62)	1.616(62)	1.724(62)	1.938(62)	2.270(79)
Ti	x	0	0	0	0	0	0
	y	0	0	0	0	0	0
	z	0	0	0	0	0	0
	B _{iso} (Å ²)	0.488(37)	1.270(78)	1.481(74)	1.508(76)	1.710(77)	1.699(90)
O1	x	-0.05277(68)	0	0	0	0	0.5
	y	-0.00799(87)	0	0	0	0	0
	z	0.25	0.25	0.25	0.25	0.25	0
	B _{iso} (Å ²)	0.879(55)	2.27(15)	1.69(10)	1.60(10)	1.57(11)	3.382(45)
O2	x	0.22909(65)	0.21729(19)	0.22164(23)	0.22361(24)	0.22696(27)	-
	y	0.27251(56)	0.71729(19)	0.72164(23)	0.72361(24)	0.72696(27)	-
	z	0.02683(28)	0	0	0	0	-
	B _{iso} (Å ²)	1.157(36)	1.628(59)	2.521(64)	2.812(69)	3.235(76)	-
R-factors	R _p	2.77	3.63	3.66	3.61	3.39	3.22
	R _{wp}	3.59	4.72	4.64	4.67	4.39	4.50
	R _{exp}	2.01	3.48	3.46	3.45	3.44	1.92
	χ ²	3.19	1.84	1.80	1.83	1.62	5.48

Table 3.4: Summary of the Rietveld refinement results of NPD data of La_{0.2}Sr_{0.2}Ca_{0.5}TiO₃ at different temperatures.

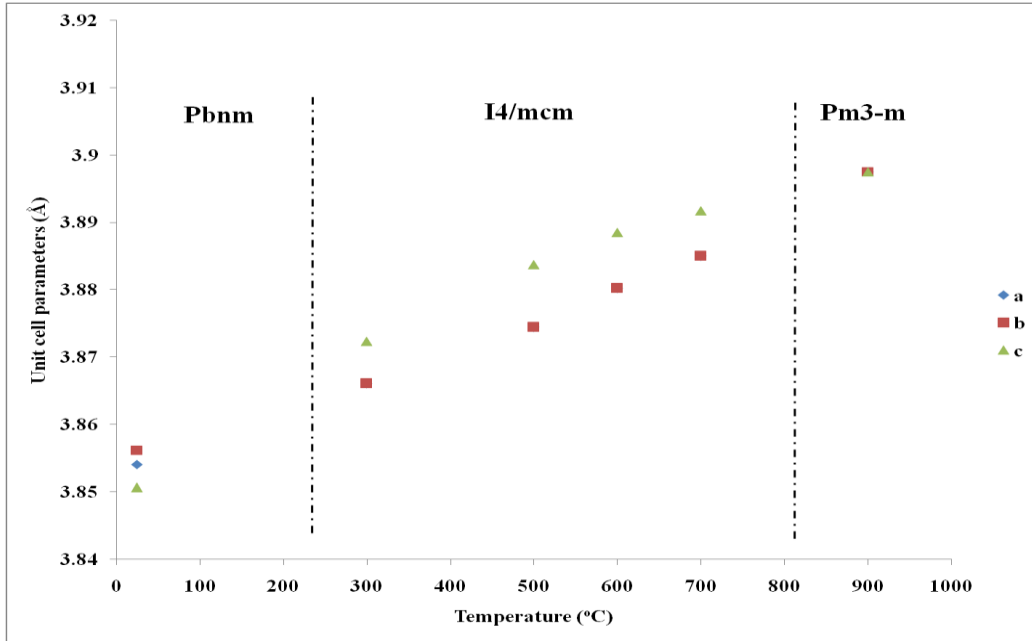


Figure 3.31: Unit cell parameters for $\text{La}_{0.2}\text{Sr}_{0.2}\text{Ca}_{0.5}\text{TiO}_3$ as a function of temperature.

Note: error bars are contained within the data points symbols.

The above result, again, show good stability for the second sample that was tested at higher temperatures; where the unit cell parameters are changing in the same manner as those for the reduced $\text{La}_{0.2}\text{Sr}_{0.25}\text{Ca}_{0.45}\text{TiO}_3$. The unit cell volume is shown in figure 3.32.

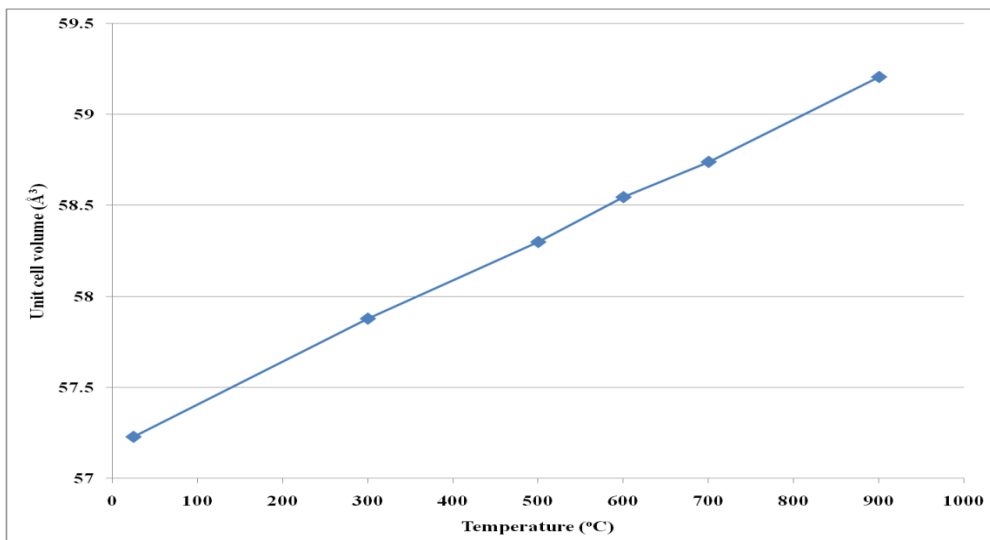


Figure 3.32: Primitive unit cell volume of $\text{La}_{0.2}\text{Sr}_{0.2}\text{Ca}_{0.5}\text{TiO}_3$ as a function of temperature. Note: error bars are contained within the data points symbols.

From the plots of the unit cell volume as a function of temperature it was found that for both samples; i.e. $x = 0.45$ and $x = 0.5$; the unit cell volume increased with a rate of $0.002 \text{ \AA}^3/\text{°C}$; indicating a very similar thermal expansion of the unit cell for these two closely related compositions.

Since distortions to the octahedra were found earlier; especially for compositions close to the phase boundary; this distortion was assumed to be removed at higher temperatures. Figure 3.33 shows the bond lengths between titanium and oxygen anions for $\text{La}_{0.2}\text{Sr}_{0.2}\text{Ca}_{0.5}\text{TiO}_3$ as a function of temperature.

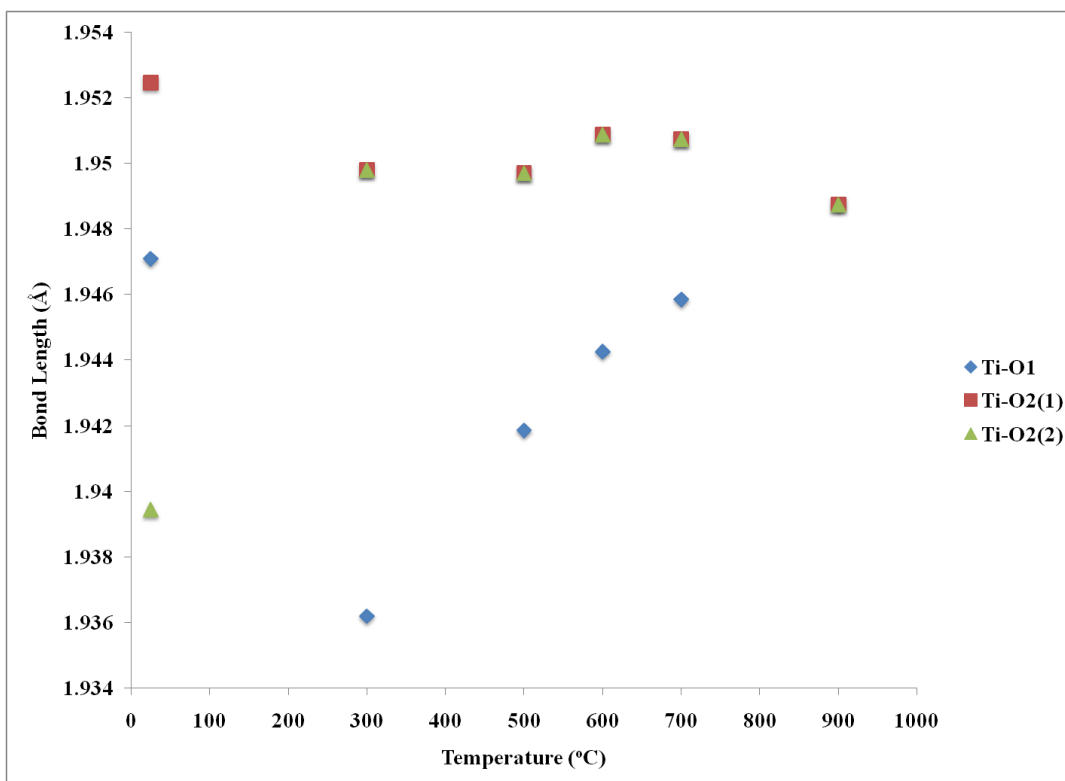


Figure 3.33: Bond lengths between titanium and oxygen for $\text{La}_{0.2}\text{Sr}_{0.2}\text{Ca}_{0.5}\text{TiO}_3$ at high temperatures. Note: error bars are contained within the data points symbols.

The result above confirms that the distortion is lowered with increasing temperature; which indicates a higher symmetry of this type of perovskite. The phase transitions with

temperature were found to be reversible as shown in figure 3.34; which shows the NPD patterns for $\text{La}_{0.2}\text{Sr}_{0.2}\text{Ca}_{0.5}\text{TiO}_3$ obtained at 500°C during heating and cooling.

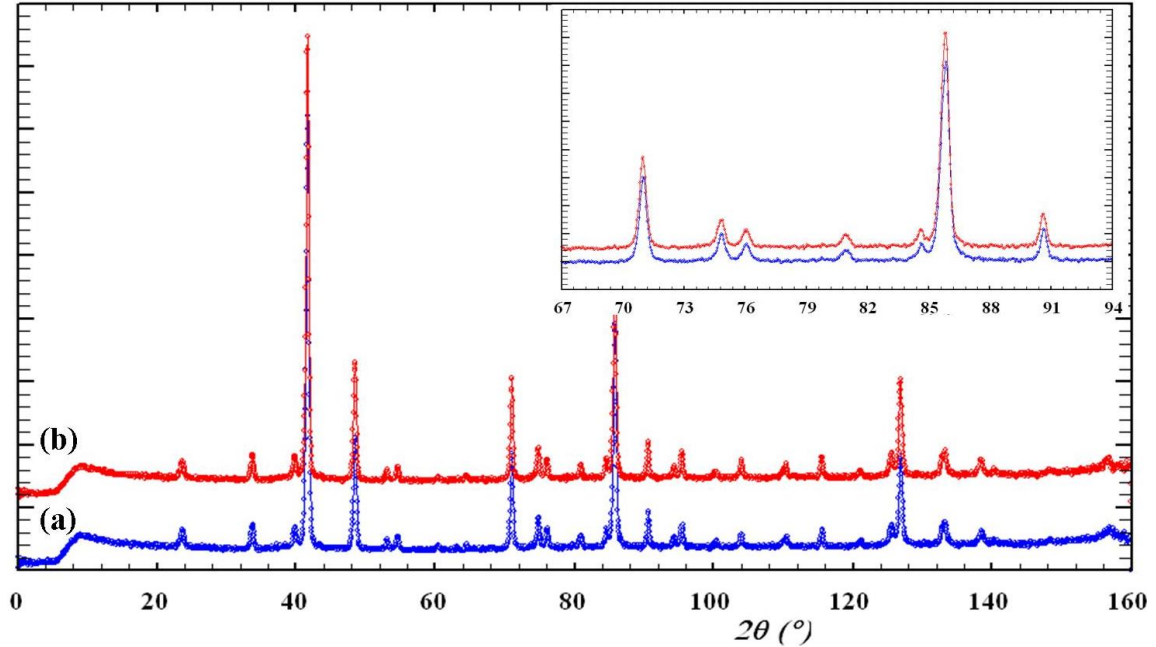


Figure 3.34: NPD patterns of $\text{La}_{0.2}\text{Sr}_{0.2}\text{Ca}_{0.5}\text{TiO}_3$ at 500°C collected during (a) heating and (b) cooling. The inset shows a closer look into a portion of the same patterns.

The symmetry of the unit cell of the above sample changed from $I4/m\bar{c}m$ to $\text{Pm}\bar{3}m$ at 900°C . Thus, the result above shows the same $I4/m\bar{c}m$ unit cell as the sample was cooled down to 500°C again. This indicates that the phase transitions present in the samples studied here are reversible and the structures are dependent on temperature. Also, it shows that the studied system has a very good structural stability with thermal cycling. The results outlined in this chapter indicate that in the system $\text{La}_{0.2}\text{Sr}_{0.7-x}\text{Ca}_x\text{TiO}_3$, two types of distortion are present; i.e. the tilting of the octahedra along with distortions to the octahedra themselves. All these distortions seem to become smaller with less calcium present in the structure as well as at higher temperatures. This was expected; since increasing the A-site cation radius for a given B cation can give a higher

symmetry as well as raising the temperature.[4] With a bigger effective A-site size, the perovskite unit cell is well supported and the distortions are removed; where at higher temperatures, due to atomic vibrations, the effective A-site size increases as well; which result in higher symmetries as was seen earlier. Most important is that the distortions in the system $\text{La}_{0.2}\text{Sr}_{0.7-x}\text{Ca}_x\text{TiO}_3$ turned out to be much less than the parent compound CaTiO_3 which helped the system adopting the ideal cubic symmetry at much lower temperatures.

3.3 - Conclusions

XRD and NPD studies have showed that all the prepared samples of $\text{La}_{0.2}\text{Sr}_{0.7-x}\text{Ca}_x\text{TiO}_3$ have shown stable perovskite structures with all the solid solutions being phase pure. The structures here have moved from the ideal cubic symmetry of $\text{La}_{0.2}\text{Sr}_{0.7}\text{TiO}_3$ to lower symmetries with calcium introduction into the system. This change is driven by the ionic radii mismatch of the A-site cations; which resulted in slight distortions to the BO_6 octahedra which manifested into in-phase and out-of-phase tilts. The distortions were not very severe as with the system $\text{Ca}_{1-x}\text{Sr}_x\text{TiO}_3$ where there are disagreements in the literature of the correct space groups. The ionic radius mismatch was less pronounced due to the presence of the same level of lanthanum in the A-site throughout the range of samples investigated here. The system showed a tetragonal $I4/mcm$ symmetry for $0.1 \leq x \leq 0.35$ and an orthorhombic $Pbnm$ symmetry for $0.4 \leq x \leq 0.7$. Samples showed structural stability with different sintering temperatures and repetitions as well as with reduction. High temperature NPD studies showed a systematic evolution of the samples to higher symmetries following the sequence $Pbnm \rightarrow I4/mcm \rightarrow Pm\bar{3}m$ with increasing temperature. The unit cell

parameters and volumes shows very good stability with temperature with no major irregularities. From all the structural investigations presented here, it can be deduced that the system $\text{La}_{0.2}\text{Sr}_{0.7-x}\text{Ca}_x\text{TiO}_3$ shows impressive stability of the perovskite phase which makes it a very competitive anode material for SOFCs. This especially true for $\text{La}_{0.2}\text{Sr}_{0.25}\text{Ca}_{0.45}\text{TiO}_3$ which showed the highest electrical conductivity; i.e. as discussed in chapter 4; among the different samples and showed a stable structure at different temperatures and after reduction making it a very good candidate as anode material for SOFC that shows a very good thermal and chemical stability.

3.4 - References

- [1] T. D. McColm and J. T. S. Irvine, *Ionics*, 2001, **7**, 116-121.
- [2] X. Li, H. Zhao, N. Xu, X. Zhou, C. Zhang and N. Chen, *Int. J. Hydrogen Energ.*, 2009, **34**, 6407-6414.
- [3] N. U. Navi, R. Z. Shneck, T. Y. Shvareva, G. Kimmel, J. Zabicky, M. H. Mintz and A. Navrotsky, *J. Am. Ceram. Soc.*, 2012, **95**, 1717-1726.
- [4] L. Li, B. J. Kennedy, Y. Kubota, K. Kato and R. F. Garrett, *J. Mater. Chem.*, 2004, **14**, 263-273.
- [5] P. R. Slater, D. P. Fagg and J. T. S. Irvine, *J. Mater. Chem.*, 1997, **7(12)**, 2495-2498.
- [6] S. M. Plint, P. A. Connor, S. Tao and J. T. S. Irvine, *Solid State Ionics*, 2006, **177**, 2005-2008.
- [7] B. Kennedy, C. J. Howard and B. C. Chakoumakos, *J. Phys.: Condens. Matter*, 1999, **11**, 1479-1488.
- [8] G. J. Thorogood, M. Avdeev, M. L. Carter, B. J. Kennedy, J. Ting and K. S. Wallwork, *Dalton T.*, 2011, **40**, 7228-7233.
- [9] J. Maier, "*Physical Chemistry of Ionic Materials: Ions and Electrons in Solids*", John Wiley & sons Ltd., England, **2004**.
- [10] O. A. Marina, N. L. Canfield and J. W. Stevenson, *Solid State Ionics*, 2002, **149**, 21-28.
- [11] V. Vashook, L. Vasylechko, N. Trofimenko, M. Kuznecov, P. Otchik, J. Zosel and U. Guth, *J. Alloy. Compd.*, 2006, **419**, 271-280.
- [12] Z. Zhang, G. R. Lumpkin, C. J. Howard, K. S. Knight, K. R. Whittle and K. Osaka, *J. Solid State Chem.*, 2007, **180**, 1083-1092.
- [13] V. Vashook, L. Vasylechko, M. Knapp, H. Ullmann and U. Guth, *J. Alloy. Compd.*, 2003, **354**, 13-23.

- [14] C. J. Howard, G. R. Lumpkin, R. I. Smith and Z. Zhang, *J. Solid State Chem.*, 2004, **177**, 2726-2732.
- [15] C. J. Ball, B. D. Begg, D. J. Cookson, G. J. Thorogood and E. R. Vance, *J. Solid State Chem.*, 1998, **139**, 238-247.
- [16] S. Qin, A. I. Becerro, F. Seifert, J. Gottsmann and J. Jiang, *J. Mater. Chem.*, 2000, **10**, 1609-1615.
- [17] S. Qin, X. Wu, F. Seifert and A. I. Becerro, *J. Chem. Soc., Dalton T.*, 2002, **19**, 3751-3755.
- [18] P. Ranson, R. Ouillon, J. -P. Pinan-Lucarre, Ph. Pruzan, S. K. Mishra, R. Ranjan and D. Pandey, *J. Raman Spectrosc.*, 2005, **36**, 898-911.
- [19] T. Yamanaka, N. Hirai and Y. Komatsu, *Am. Mineral.*, 2002, **87**, 1183-1189.
- [20] S. A. T. Redfern, *J. Phys.: Condens. Matter*, 1996, **8**, 8267-8275.
- [21] R. Ranjan, D. Pandey, V. Siruguri, P. S. R. Krishna and S. K. Paranjpe, *J. Phys.: Condens. Matter*, 1999, **11**, 2233-2246.
- [22] E. Castillo-Matinez, A. Duran and M. A. Alario-Franco, *J. Solid State Chem.*, 2008, **181**, 895-904.
- [23] R. Ali and M. Yashima, *J. Solid State Chem.*, 2005, **178**, 2867-2872.
- [24] M. Yashima, R. Ali, *Solid State Ionics*, 2009, **180**, 120-126.
- [25] C. J. Howard, R. L. Withers, Z. Zhang, K. Osaka, K. Kato and M. Takata, *J. Phys.: Condens. Matter*, 2005, **17**, L459-465.

Chapter 4

Novel A-site Deficient $\text{La}_{0.2}\text{Sr}_{0.7-x}\text{Ca}_x\text{TiO}_3$

Part 2 – Further Analysis

Abstract

Samples of $\text{La}_{0.2}\text{Sr}_{0.7-x}\text{Ca}_x\text{TiO}_3$ were analysed in terms of electrical conductivity, thermal and chemical properties through dilatometry and thermogravimetric analysis and finally studies of the morphology of the material. The system showed very encouraging properties to be regarded as a very good candidate as an anode material for SOFCs. Thermal studies showed close thermal expansion coefficient to YSZ and very similar shrinkage behaviour. Also, TGA measurements showed that the maximum electrical conductivity that was achieved with the composition $\text{La}_{0.2}\text{Sr}_{0.25}\text{Ca}_{0.45}\text{TiO}_{3-\delta}$; i.e. $\sigma = 27.5 \text{ S/cm}$; was a result of an oxygen deficiency of $\delta = 0.034$. DTA analysis showed no evidence of significant phase transitions; signifying very small distortions. DC conductivity measurements showed an increasing conductivity as calcium content increased up to $x = 0.45$; after which it started to decrease with increased calcium content. SEM studies showed very good sinterability of the solid solutions prepared and no significant effects on the morphology due to different thermal treatments and/or reduction.

4.1 - Introduction

As explained in previous chapters, $\text{La}_{0.2}\text{Sr}_{0.7-x}\text{Ca}_x\text{TiO}_3$ was chosen as a system to investigate its suitability as anode material for SOFCs. In chapter 3, the system showed very good stability of the perovskite phase throughout the series as well as with reduction and temperature. The symmetry changes were due to octahedral tilting and distortions which were less severe than the parent compound CaTiO_3 . However, in many occasions, small distortions can have profound effects on many different properties of the material, especially its electrical conductivity.

In this chapter, different analysis techniques were used in order to understand this material behaviour and suitability as anode material for SOFCs. First, the thermal expansion coefficient was measured for different samples using dilatometry, as well as, samples shrinkage/sintering behaviour was compared to that of YSZ. This is one of the main challenges in the design of new materials of SOFC anodes. Next, changes to samples stoichiometry through reduction and oxidation at different temperatures were determined using TGA. The electrical conductivity of these titanates depends on the ease of reducing Ti^{4+} which introduces electrons into the conduction bands. The third part dealt with the samples electrical conductivity at different temperatures and oxygen partial pressures. All samples were initially studied as prepared and were reduced in-situ at 900°C , however, as the main objective of this work was to find which sample from the series $\text{La}_{0.2}\text{Sr}_{0.7-x}\text{Ca}_x\text{TiO}_3$ showed the highest electrical conductivity, all samples were prepared and pre-reduced prior to conductivity measurements to ensure reliability of comparison of the different samples. And finally, the morphology of the different samples was studied using SEM, to see how much calcium introduction can affect the microstructure of the solid solutions of this system.

4.2 – Thermal Analysis

4.2.1 – Thermal Expansion

Any new material that would be utilised as a component in SOFCs should be compatible with the other components both mechanically and chemically. The thermal expansion coefficient (TEC) is an important quantitative measure to determine the suitability of materials to be used along/with other materials in any high temperature system. The TEC was measured for different samples of $\text{La}_{0.2}\text{Sr}_{0.7-x}\text{Ca}_x\text{TiO}_3$ and compared to that of the state-of-art electrolyte YSZ. Also, the shrinkage/sintering behaviour of samples was observed during sintering and compared to YSZ as well.

Results and Discussion

The TEC of the first sample in the series; i.e. $x = 0.1$; is shown in figure 4.1, where the sample was thermally cycled between ambient temperature and 1000°C in $5\% \text{H}_2/95\% \text{Ar}$ atmosphere.

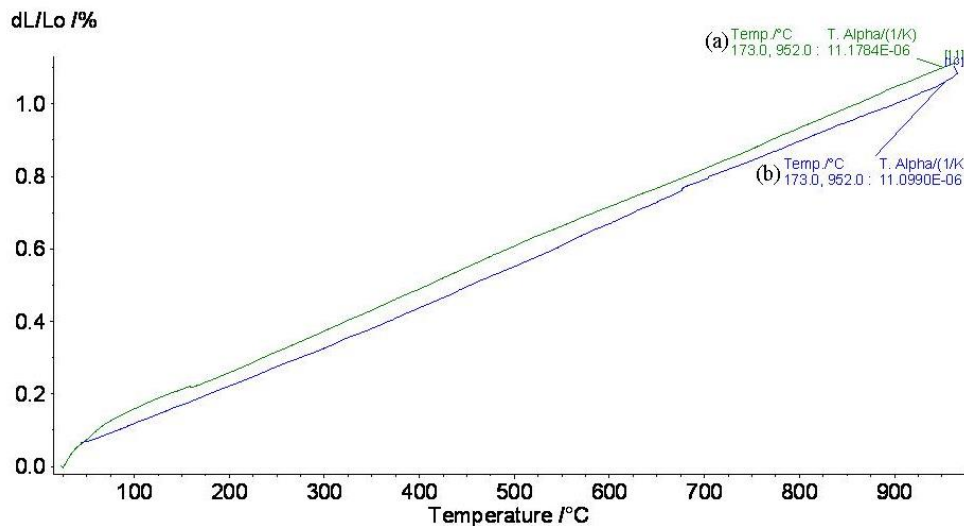


Figure 4.1: Thermal expansion curves of $\text{La}_{0.2}\text{Sr}_{0.6}\text{Ca}_{0.1}\text{TiO}_3$ measured in $5\% \text{H}_2$ showing TEC during heating (a) and cooling (b).

The TEC values shown in the above figure indicate slightly higher values to the TEC of YSZ; i.e. $10.2\text{--}10.8\times 10^{-6}\text{ K}^{-1}$ [1,2]. The TEC values for the different samples studied in this work are shown in table 4.1.

x	TEC (K⁻¹)	Atmosphere
0.1	11.217×10^{-6}	5%H ₂
0.2	6.608×10^{-6}	5%H ₂
0.35	7.456×10^{-6}	5%H ₂
0.4	10.419×10^{-6}	5%H ₂
0.45	7.972×10^{-6}	5%H ₂
0.45	8.968×10^{-6}	Air
0.5	10.179×10^{-6}	Air
0.7	10.160×10^{-6}	5%H ₂

Table 4.1: Thermal expansion coefficients of different samples of $\text{La}_{0.2}\text{Sr}_{0.7-x}\text{Ca}_x\text{TiO}_3$ as measured between ambient temperature and 1000°C.

The obtained TECs for the samples studied here are less than the ones reported for $\text{La}_x\text{Sr}_{1-x}\text{TiO}_3$, where the TEC values varied between $11 - 12 \times 10^{-6}\text{ K}^{-1}$ for compositions of $x = 0.1 - 0.4$. [3] The results here show no consistent dependence of the TEC on calcium content. The highest TEC was measured for the strontium rich composition $\text{La}_{0.2}\text{Sr}_{0.6}\text{Ca}_{0.1}\text{TiO}_3$; which can be explained by the larger size of the strontium cation, giving, initially a higher thermal expansion. The sample $x = 0.4$; which showed the transition to the Pbnm space group, at room temperature, with increasing calcium

content; was the one that showed the closest TEC value to that of YSZ. The TEC behaviour of the different samples can be affected by the thermal history.[4] The sample $\text{La}_{0.2}\text{Sr}_{0.25}\text{Ca}_{0.45}\text{TiO}_3$ has shown the highest electrical conductivity among the different samples; its TEC curves are shown in figure 4.2.

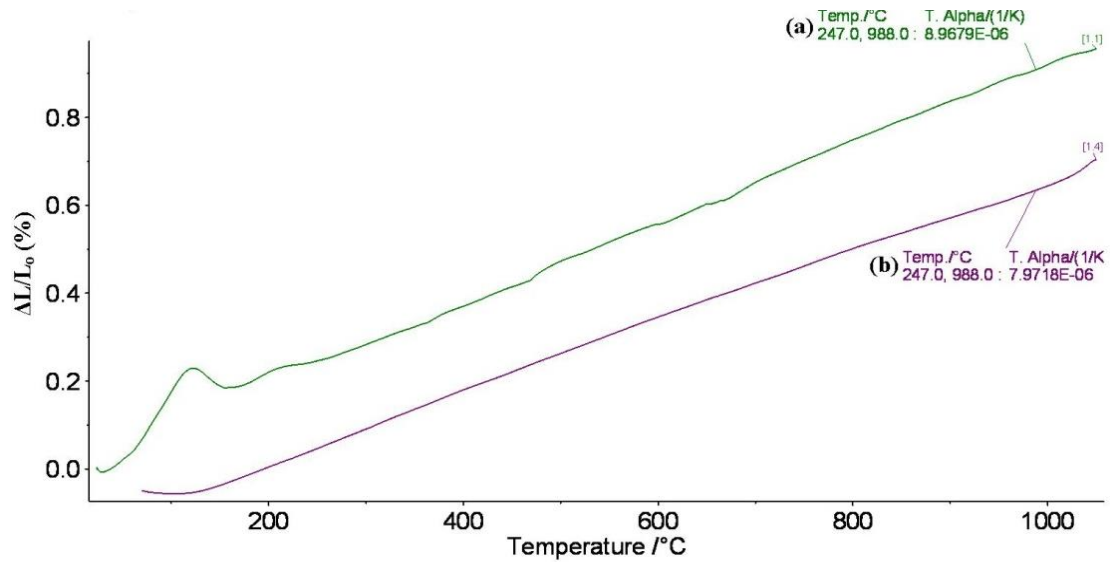


Figure 4.2: Thermal expansion curves of $\text{La}_{0.2}\text{Sr}_{0.25}\text{Ca}_{0.45}\text{TiO}_3$ measured while (a) heating in air and (b) cooling in 5% H_2 :95% Ar.

This sample TEC was found to be higher; i.e. closer to the TEC of YSZ; when it is heated in air compared to being heated in 5% H_2 . This result was the opposite to the behaviour of $\text{La}_{0.2}\text{Sr}_{0.7}\text{TiO}_3$ which showed higher TEC when measured under 5% H_2 than that in air.[4] This can be explained to the distorted unit cell of $\text{La}_{0.2}\text{Sr}_{0.7-x}\text{Ca}_x\text{TiO}_3$ compared to the cubic $\text{La}_{0.2}\text{Sr}_{0.7}\text{TiO}_3$, which might affect the thermal expansion of the material. Also, as Lee and Manthiram[5] indicated, the results here can indicate a response to reduction in the material under study here; i.e. oxygen ion vacancies presence lowers the thermal expansion coefficient of a given oxide. Thus, the different TEC values that are shown in table 4.1 can be explained by differences in oxygen

deficiency/vacancies between the different samples and the different atmospheres that the experiments were conducted at. This is more clear with the result shown in figure 4.2, above, when the sample was held in an atmosphere of 5%H₂ at 1050°C for at least 10 hours; giving a much lower TEC compared with the other 5%H₂ runs shown in table 4.2, which were reduced at 1000°C. The behaviour of the thermal expansion curves for the samples studied here all indicate very good stability and apparent linear response to temperature. The TEC of the samples here can be brought to close values to that of the YSZ through careful considerations of the synthesis method and through control of the microstructure that can tailor the reduction mechanism in these perovskites in order to minimise any unwanted stresses between the anode and electrolyte during operation of a solid oxide fuel cell. In the development of new anode materials for SOFCs, compatibility with other components is very important. In synthesis, the different components, usually synthesised in-situ, should all shrink/expand in a similar manner. Thus, different samples of La_{0.2}Sr_{0.7-x}Ca_xTiO₃ were studied for their shrinkage behaviour during sintering in air.

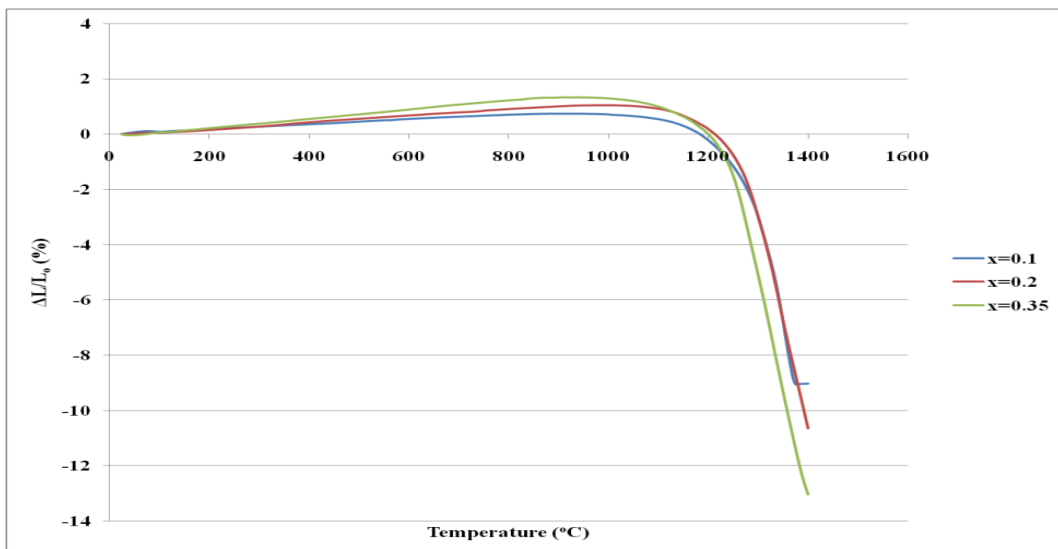


Figure 4.3: Sintering behaviour of various samples of La_{0.2}Sr_{0.7-x}Ca_xTiO₃ in air.

It can be seen from figure 4.3 that the solid state reaction in the new compositions starts at temperatures around 1200°C; which indicates that calcium introduction did lower the melting point and improved the densification of the solid solutions obtained in this work. Again, there is no relevant dependence on calcium content. The shrinkage of the composition $x=0.45$ compared to that of YSZ is shown in figure 4.5, where a very good match with YSZ can be seen. As this sample showed the highest electrical conductivity, its sintering behaviour is very close to that of YSZ, which makes it a very strong candidate/alternative as an anode material in SOFCs.

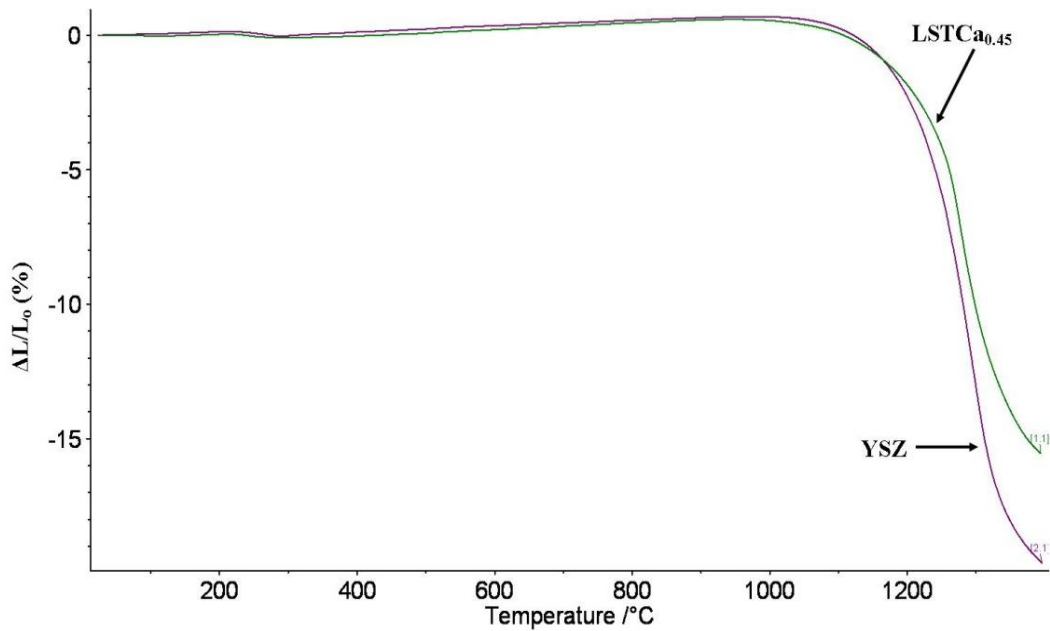


Figure 4.4: Sintering behaviour of $\text{La}_{0.2}\text{Sr}_{0.25}\text{Ca}_{0.45}\text{TiO}_3$ in air compared to that of YSZ.

The above result was used to determine the temperature at which $\text{La}_{0.2}\text{Sr}_{0.25}\text{Ca}_{0.45}\text{TiO}_3$ sintering begins by taking the differential of the above curves. As shown in figure 4.5, the sample behaviour is very close to the YSZ.

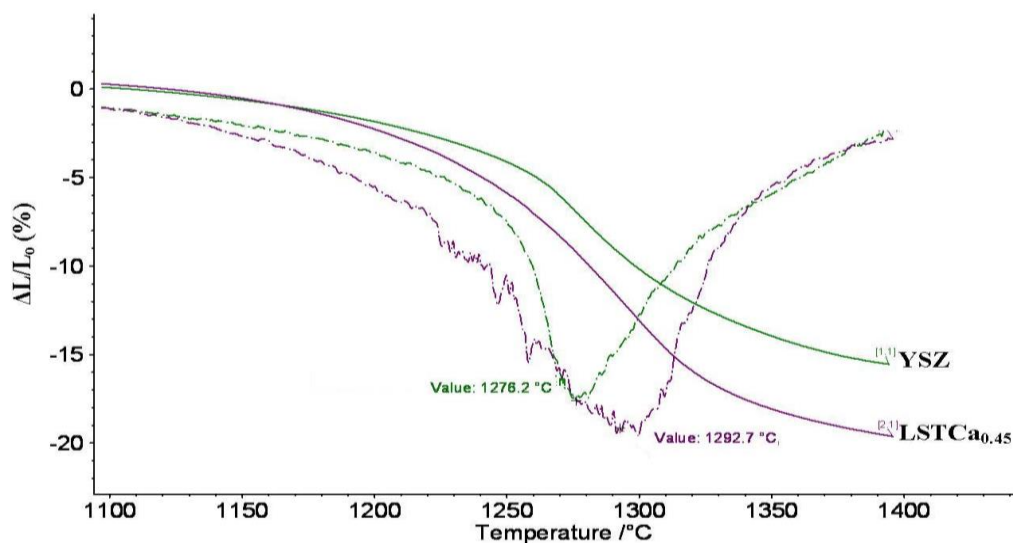


Figure 4.5: Plot showing the temperatures at which both materials start the sintering process.

Both materials start sintering at very close temperatures; the minima of the differential curves differ by only 16°C; which is relatively comparable at these high temperatures. The results above show that the system $\text{La}_{0.2}\text{Sr}_{0.7-x}\text{Ca}_x\text{TiO}_3$ is showing very encouraging thermal expansion behaviour which is very close to the widely used SOFC electrolyte YSZ. TEC values indicated that the closest composition to the YSZ TEC was the one with $x = 0.4$ which was heated in 5% H_2 . The TECs reported here were not that different from the ones reported by Savaniu and Irvine for dense samples of $\text{La}_{0.2}\text{Sr}_{0.7}\text{TiO}_3$; i.e. $9.45 \times 10^{-6} \text{ K}^{-1}$ in 5% H_2 and $8.55 \times 10^{-6} \text{ K}^{-1}$ in air.[4] There are strong indications that the thermal expansion coefficient of these samples depends or greatly affected by oxygen vacancies concentration as well as by the ionic radius mismatch that exists in the studied samples. Also, strontium can lead to irregular thermal expansion coefficients and significant dimensional changes on redox cycling.[7] Hence, this is a major driver for the work conducted in this thesis, where lower strontium content can bring a better match of the thermal expansion coefficient of the new anode material to that of the electrolyte material.

4.2.2 - TGA/DTA Analysis

The electrical conductivity of $\text{La}_{0.2}\text{Sr}_{0.7-x}\text{Ca}_x\text{TiO}_3$ depends on the oxygen stoichiometry where it was found, from DC conductivity measurements, that the higher the reduction level was the higher the resultant electrical conductivity. TG analysis is useful in determining how large the oxygen deficiency in a compound once it undergoes a redox reaction. Also, differential thermal analysis is useful in detecting any phase changes that can take place within a structure. This section shows some different thermal analysis conducted on some samples in this work.

Results and Discussion

Prior to DC conductivity measurement most samples were pre-reduced at 1050°C for 72 hours to achieve a considerable ratio of oxygen vacancies. The TGA curve of $\text{La}_{0.2}\text{Sr}_{0.25}\text{Ca}_{0.45}\text{TiO}_3$ is shown in figure 4.6.

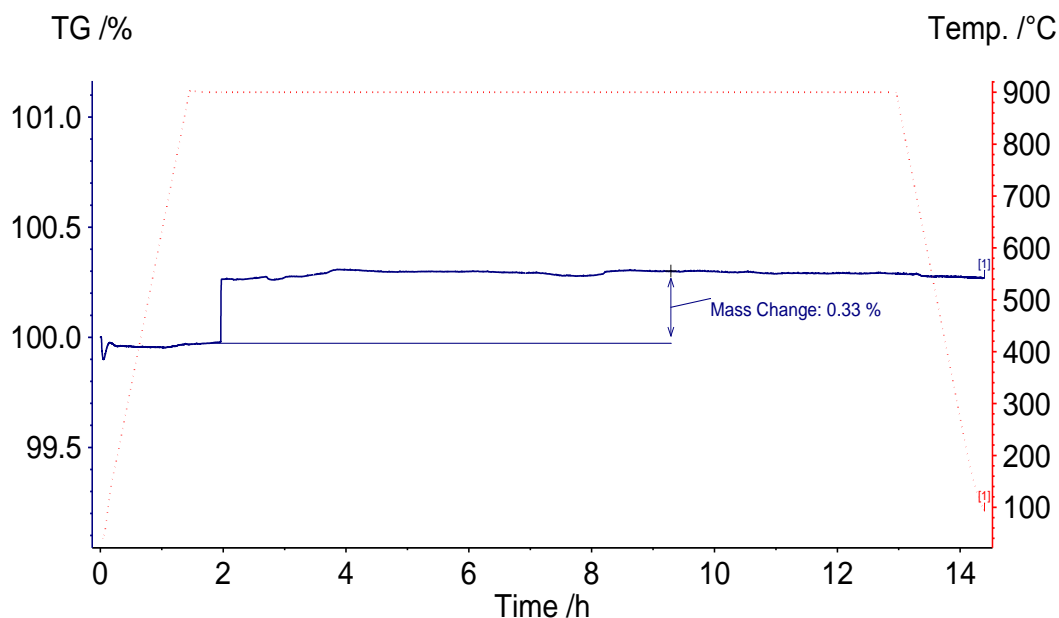


Figure 4.6: TGA curve of a pre-reduced sample of $\text{La}_{0.2}\text{Sr}_{0.25}\text{Ca}_{0.45}\text{TiO}_3$ during oxidation at 900°C .

This mass change indicate that a pre-reduced sample at 1050°C for 72 hours had an oxygen deficiency of about $\delta \approx 0.03$; giving a stoichiometry of $\text{La}_{0.2}\text{Sr}_{0.25}\text{Ca}_{0.45}\text{TiO}_{2.97}$.

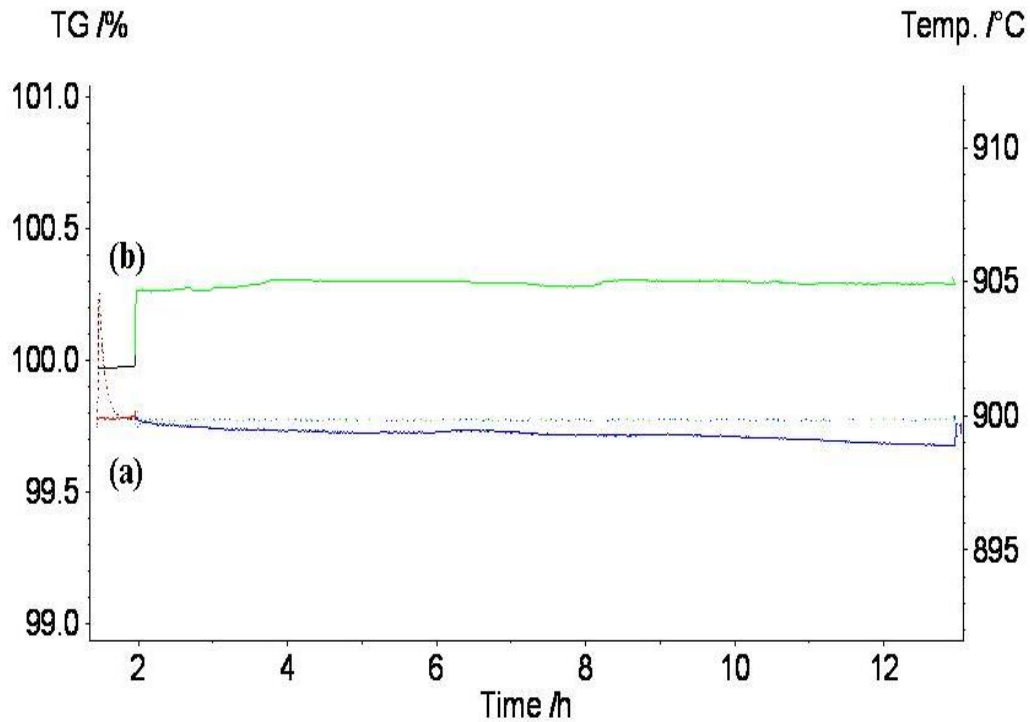


Figure 4.7: TGA curves for (a) in-situ reduction and (b) oxidation of pre-reduced samples at 900°C for samples of $\text{La}_{0.2}\text{Sr}_{0.25}\text{Ca}_{0.45}\text{TiO}_3$.

From figure 4.7, it is clear how reducing this type of titanate is much harder than oxidising them. Also, it is obvious that a higher oxygen deficiency can be obtained by using a higher temperature for reduction. Reducing an as-prepared sample of $\text{La}_{0.2}\text{Sr}_{0.25}\text{Ca}_{0.45}\text{TiO}_3$ at 900°C resulted in an oxygen deficiency of only $\delta \approx 0.01$; which is much less compared to the value obtained with reduction at 1050°C. The oxygen deficiency with different calcium content was almost the same as shown in figure 4.8.

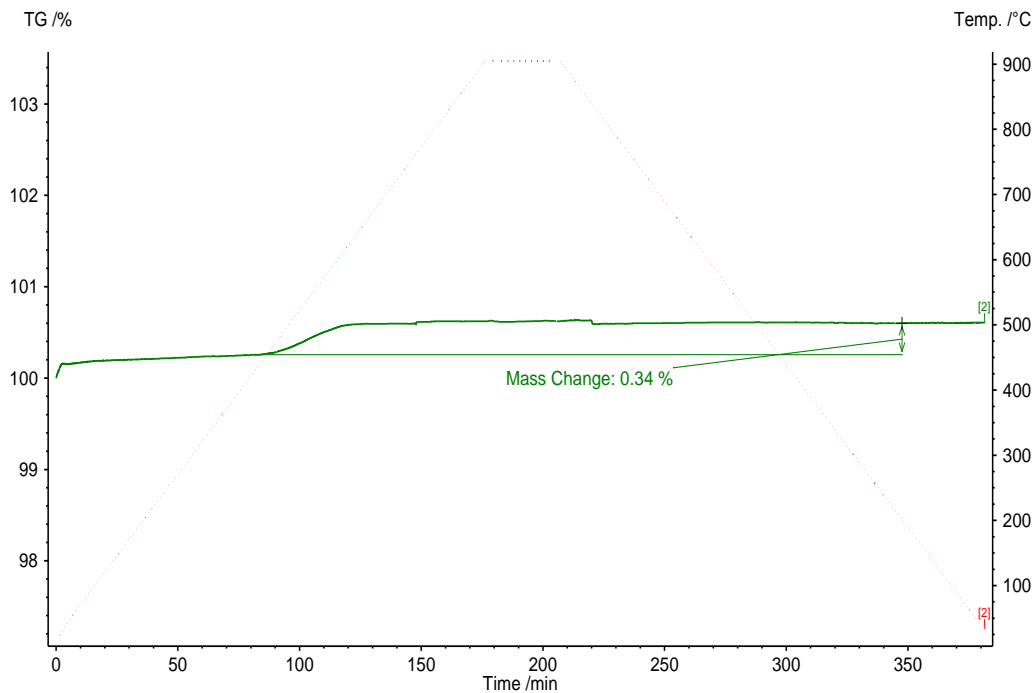


Figure 4.8: TGA curve showing the oxidation of a pre-reduced $\text{La}_{0.2}\text{Sr}_{0.2}\text{Ca}_{0.5}\text{TiO}_3$ at 900°C .

The oxygen deficiency from the above mass change was calculated to be $\delta \approx 0.03$; giving a nominal stoichiometry of $\text{La}_{0.2}\text{Sr}_{0.2}\text{Ca}_{0.5}\text{TiO}_{2.97}$ was pre-reduced at the same conditions for the $\text{La}_{0.2}\text{Sr}_{0.25}\text{Ca}_{0.45}\text{TiO}_3$ sample; where both samples show, to a certain degree, the same mass% change indicating a very similar oxygen deficiency that was obtained at similar reduction conditions; i.e. 1050°C for 72 hours.

Another aspect that was tested is thermal phase changes that may take place in the system $\text{La}_{0.2}\text{Sr}_{0.7-x}\text{Ca}_x\text{TiO}_3$. A DTA measurement result is shown in figure 4.9 for $\text{La}_{0.2}\text{Sr}_{0.25}\text{Ca}_{0.45}\text{TiO}_3$, where no phase changes were detected.

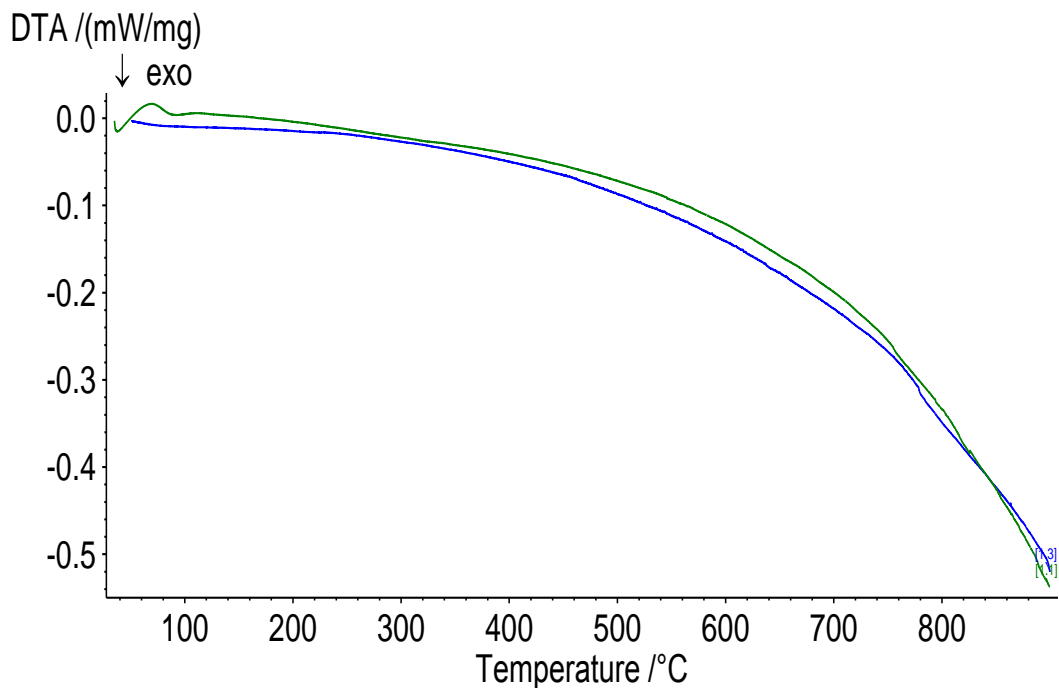


Figure 4.9: DTA curves for $\text{La}_{0.2}\text{Sr}_{0.25}\text{Ca}_{0.45}\text{TiO}_3$ during thermal cycling in air.

The DTA curves above show no phase changes that took place in $\text{La}_{0.2}\text{Sr}_{0.25}\text{Ca}_{0.45}\text{TiO}_3$ which indicated a very good stability of the phase of this material. With high temperature NPD studies of this composition, there were two phase transitions; i.e. Pbnm-I4/mcm and $\text{I4/mcm-Pm}\bar{3}\text{m}$; as the temperature was raised to 900°C . The different symmetries resulted from different tilts to the BO_6 octahedra of these perovskites. The DTA result presented here could not detect these phase transitions; which can indicate that the changes to the unit cell were very small to be detected; a notion which was deduced in chapter 3. Overall, the system showed very good stability during thermal and redox cycling.

4.3 - DC Conductivity Measurement

Introducing calcium in $\text{La}_{0.2}\text{Sr}_{0.7}\text{TiO}_3$ is thought to improve the electronic conductivity of this type of perovskites. We've already seen that the unit cell volume had decreased with increasing calcium content and that symmetry changed as well. At 900°C tested samples showed a cubic perovskite structure with the unit cell volume of the higher calcium content sample being smaller. These structural observations are linked here to the electrical conductivity of the different samples in the system $\text{La}_{0.2}\text{Sr}_{0.7-x}\text{Ca}_x\text{TiO}_3$.

Results and Discussion

The first test was to measure the conductivity of the first sample of the series; i.e. $\text{La}_{0.2}\text{Sr}_{0.6}\text{Ca}_{0.1}\text{TiO}_3$ which was heated (as-prepared) to 900°C under air. Once at isotherm the atmosphere was switched to 5% H_2 /95% Ar gas mixture. The conductivity behaviour is shown in figure 4.10.

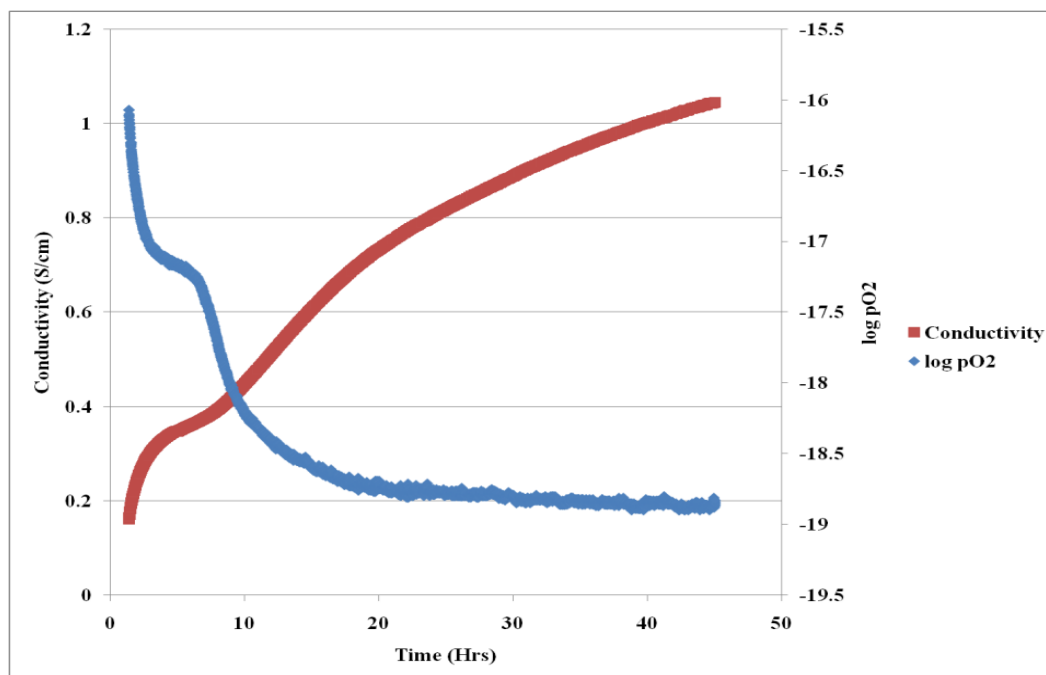


Figure 4.10: Conductivity and $\log p\text{O}_2$ as function of time for $\text{La}_{0.2}\text{Sr}_{0.6}\text{Ca}_{0.1}\text{TiO}_3$ at 900°C .

It can be seen from the result above that the response of the material at a fixed temperature depends largely on the oxygen partial pressure. Once the oxygen partial pressure reached a stable value, the conductivity was found to increase very slowly in a linear fashion with a rate of 8mS/hour. Figure 4.11 shows a plot of the conductivity of $\text{La}_{0.2}\text{Sr}_{0.6}\text{Ca}_{0.1}\text{TiO}_3$ as a function of $\log p\text{O}_2$ at 900°C .

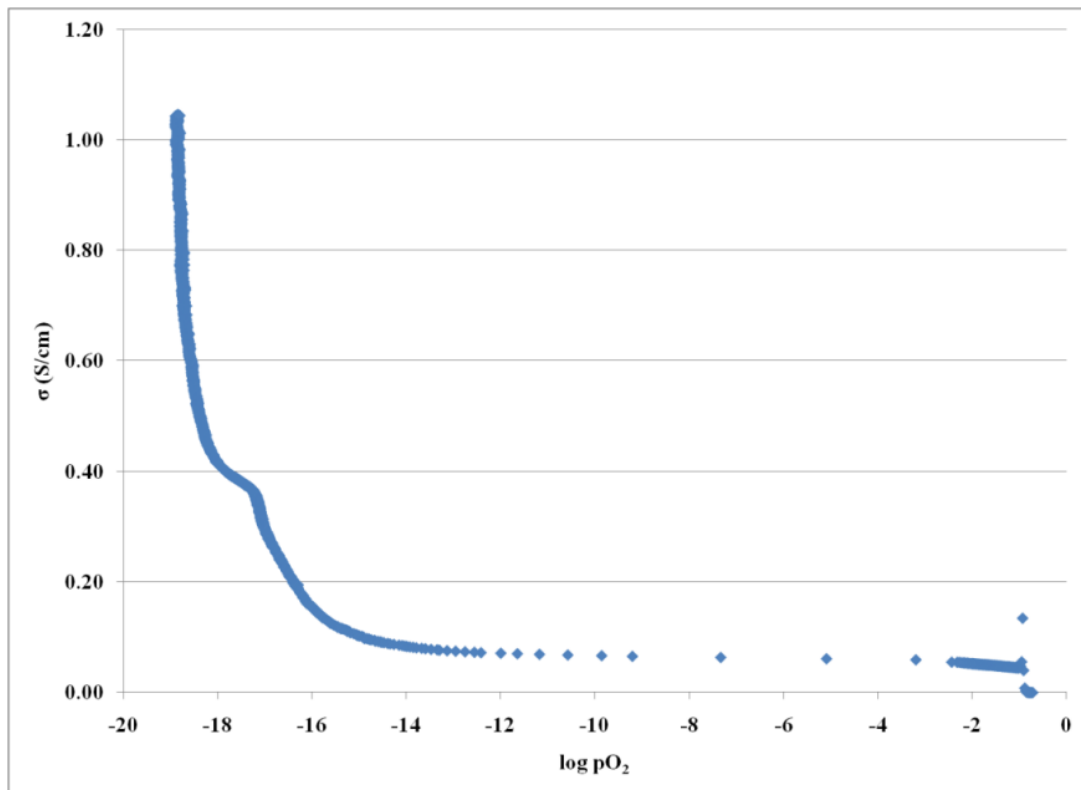


Figure 4.11: The conductivity of $\text{La}_{0.2}\text{Sr}_{0.6}\text{Ca}_{0.1}\text{TiO}_3$ as a function of $\log p\text{O}_2$ at 900°C .

It is clear from the result above that the material starts reducing at a very low oxygen partial pressure; i.e. $p\text{O}_2 < 10^{-14}$ atm; where it is clear that the conductivity starts increasing in a very fast rate which can be indicative of the surface reduction; which is then followed by the slower reduction of the bulk of the sample.

The sample was then taken through a thermal cycle in a fixed oxygen partial pressure; the result is shown in figure 4.12.

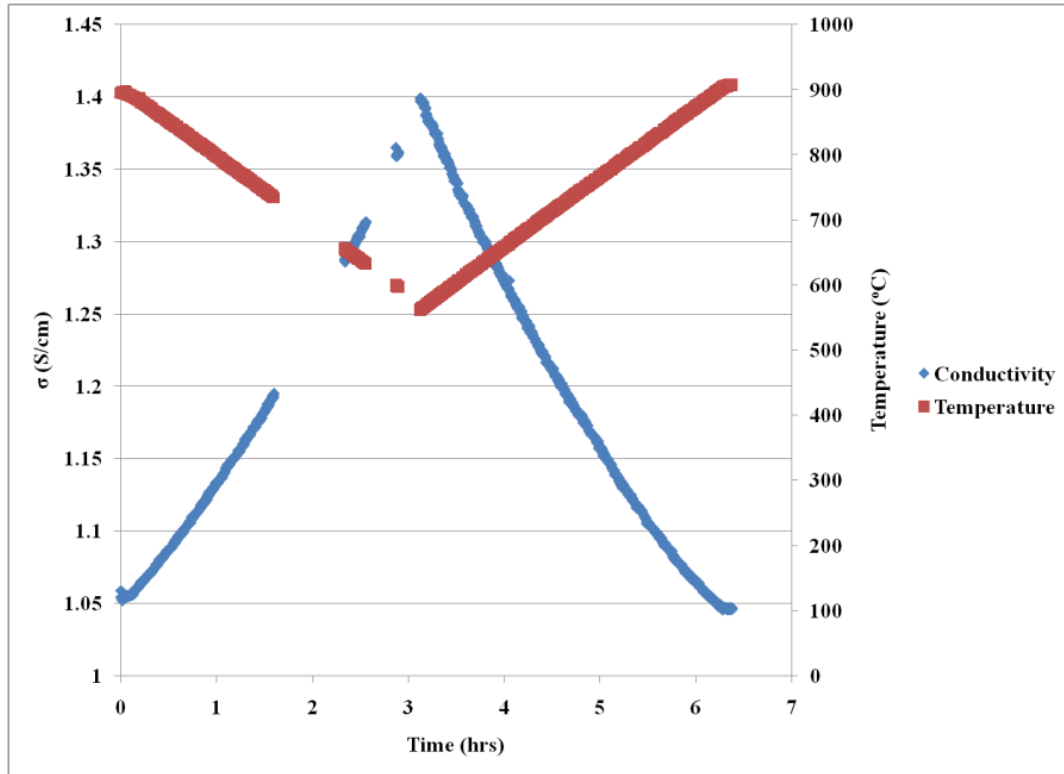


Figure 4.12: Thermal cycling of $\text{La}_{0.2}\text{Sr}_{0.6}\text{Ca}_{0.1}\text{TiO}_3$ at a $p\text{O}_2$ of 10^{-19} atm.

Once the sample was reduced, its conductivity showed a temperature dependence that resembled a metallic behaviour. $\text{La}_{0.2}\text{Sr}_{0.6}\text{Ca}_{0.1}\text{TiO}_3$ showed a very low electrical conductivity, this was thought to originate from the high relative density of the pellet used to obtain the earlier results; which made it more difficult to reduce a significant proportion of Ti^{4+} into Ti^{3+} in situ. Thus, a porous pellet was made from the same composition which had a relative density of 70.92%. Also, since the reduction rate was very poor in the first experiment, the porous pellet was pre-reduced at 900°C for 72 hours. A considerable increase in the conductivity was observed as shown in figure 4.13.

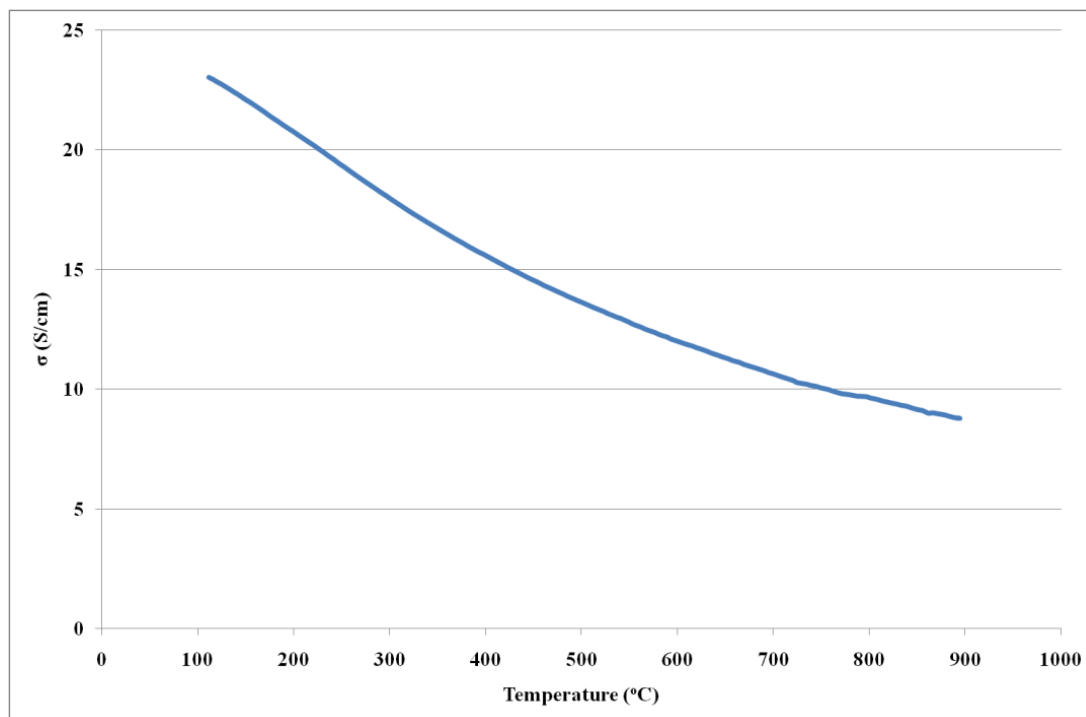


Figure 4.13: Conductivity as a function of temperature for a pre-reduced porous pellet of $\text{La}_{0.2}\text{Sr}_{0.6}\text{Ca}_{0.1}\text{TiO}_3$ in reducing conditions.

With pre-reduction and the increased porosity, the conductivity increased by almost 9 times compared to the dense sample. This result is significant because it shows that having a significant proportion of Ti^{4+} reduced to Ti^{3+} which adds up to the electrical conductivity requires either longer times or higher temperatures. Even with pre-reduction, the pellet conductivity was increasing as it was kept in an isotherm of 900°C ; indicating further reduction; which can be seen in figure 4.14, which is a continuation of the run shown in figure 4.13.

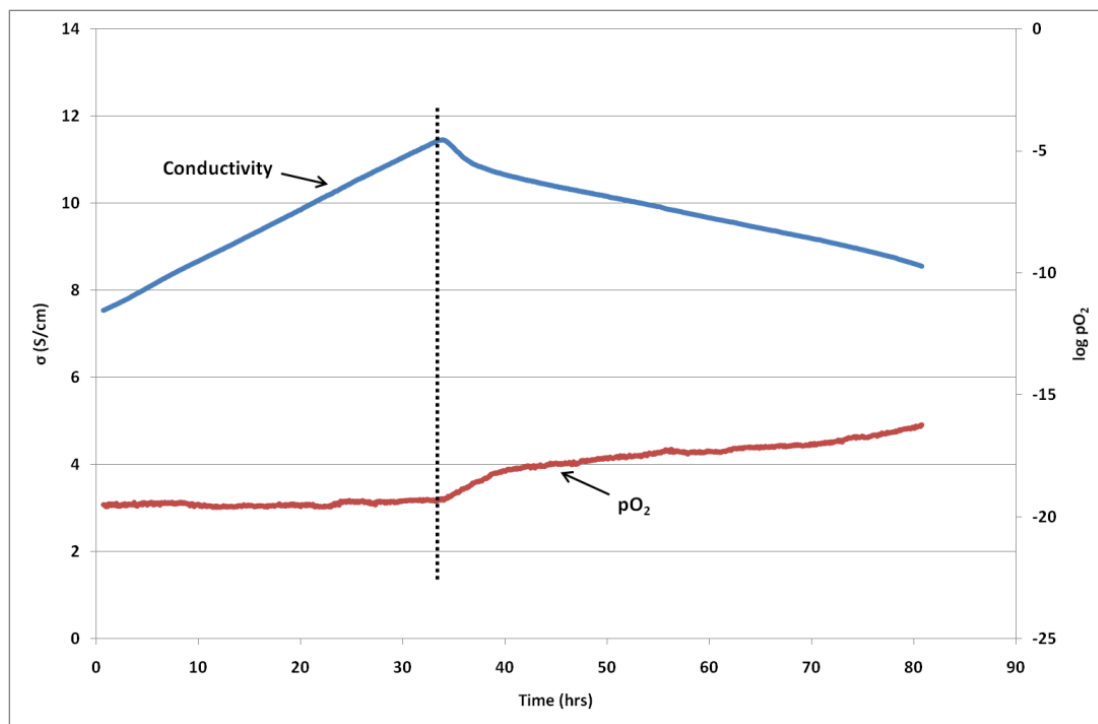


Figure 4.14: Response of the conductivity of the porous pellet of $\text{La}_{0.2}\text{Sr}_{0.6}\text{Ca}_{0.1}\text{TiO}_3$ at 900°C to changes to oxygen partial pressure. The line shows the point where the purging of $5\%\text{H}_2$ stopped and air was allowed to enter the furnace.

As can be seen, the conductivity was increasing even after leaving the sample in a fixed $p\text{O}_2$ for almost 30 hours. A slight increase in oxygen partial pressure was sufficient to trigger a loss in conductivity at a relatively constant rate. This again signifies that in order to achieve a very considerable electrical conductivity in this material, it is very necessary to insure significant reducing conditions. This, in part, led to consider pre-reducing all samples, as it was explained in chapter 1. The response of the conductivity to changes in oxygen partial pressure for the porous sample was compared to that of the dense one in figure 4.15.

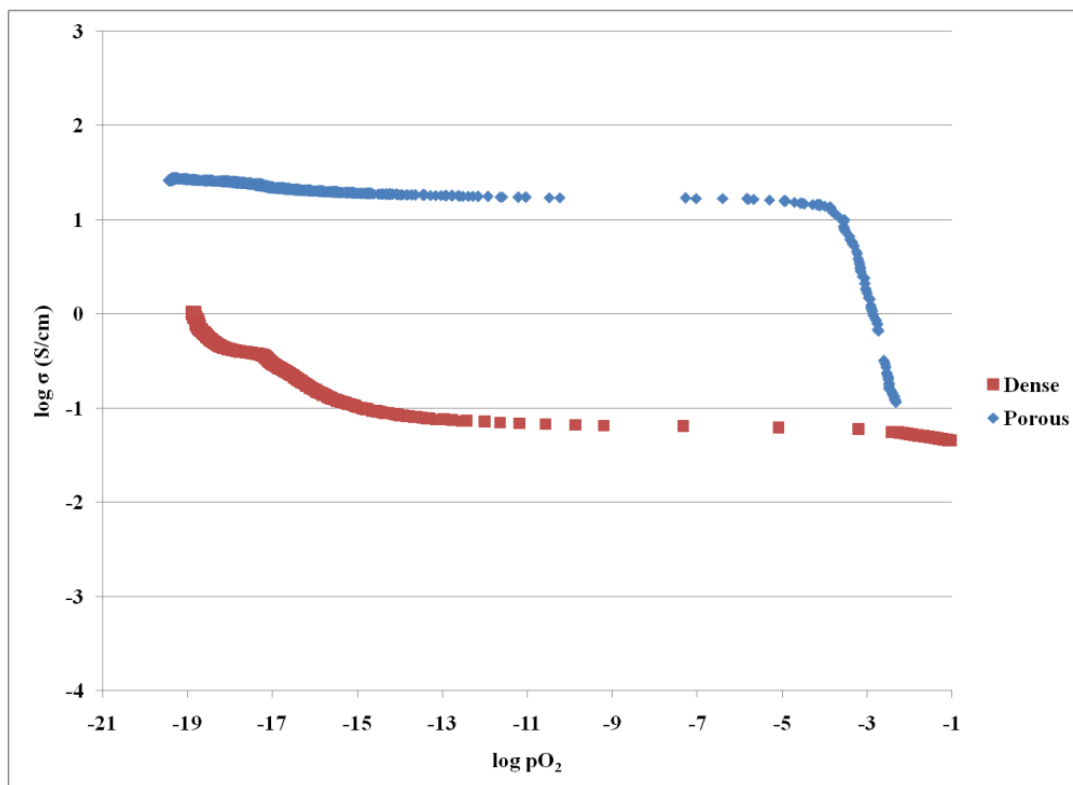


Figure 4.15: plot of $\log(\sigma)$ vs. $\log(pO_2)$ comparing the conductivity response to pO_2 between the dense and the porous samples of $La_{0.2}Sr_{0.6}Ca_{0.1}TiO_3$ at $900^\circ C$.

From both traces, it can be seen that the conductivity is mainly n-type. The porous sample showed a much faster response where the reduction started at much higher pO_2 compared to the dense one; this indicated a much higher gas diffusion rate into the sample which increased the reduction rate considerably; i.e. this is much clearer at very low pO_2 . The defect chemistry of this material could not be determined since it was not possible to achieve equilibrium with oxygen partial pressure; even with the porous sample. This shows that this material is fairly stable in a wide range of oxygen partial pressure; which is ideal for anodic operation. However, at $10^{-4} \leq pO_2 \leq 10^{-15}$ atm, it can be seen that the conductivity is possibly due to oxygen vacancies migration, but the slope of the lines is not representative of a particular type of defect, hence, it can be

argued that these perovskites are mostly dominated by the electronic conductivity. The A-site deficiency was implemented into the structure in order to help create oxygen vacancies after reduction which should facilitates or introduce ionic conductivity. The reduction rate of the system $\text{La}_{0.2}\text{Sr}_{0.7-x}\text{Ca}_x\text{TiO}_3$ was not affected by the content of calcium; as can be seen in figure 4.16.

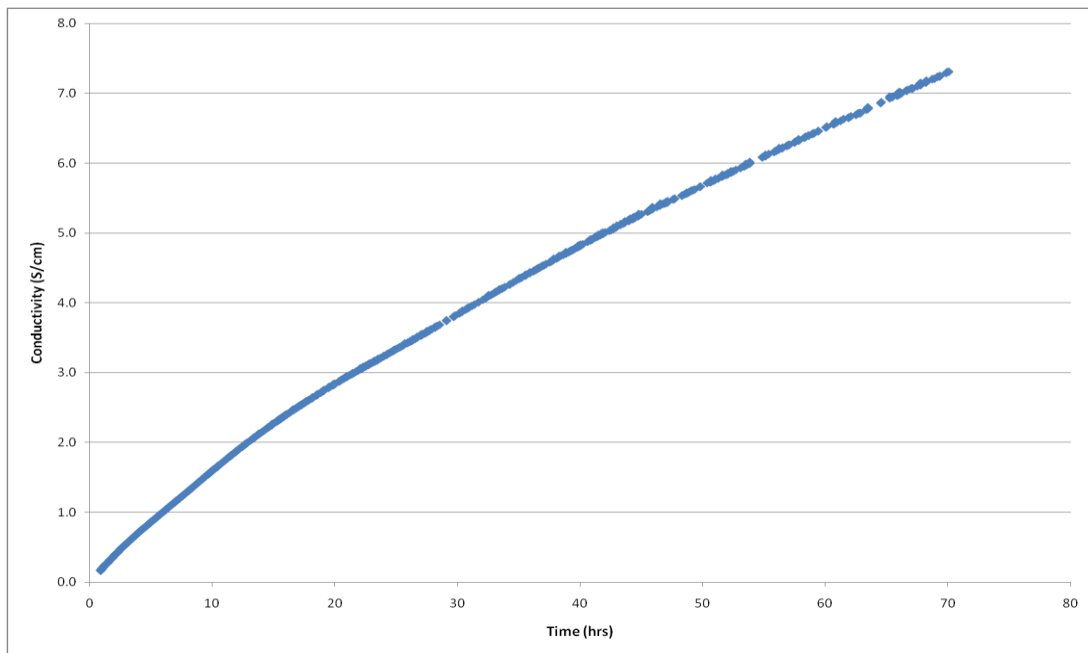


Figure 4.16: Plot of the electrical conductivity as a function of time for a dense pellet of $\text{La}_{0.2}\text{Sr}_{0.5}\text{Ca}_{0.2}\text{TiO}_3$ being reduced in-situ at 900°C and $p\text{O}_2 = 10^{-18}$ atm.

With added calcium content, as the unit cell volume decreased, the electrical conductivity increased significantly. This showed that the starting method chosen in this work, a smaller unit cell volume, proved to be successful in improving the conductivity of this type of titanates. As the conduction orbitals are brought closer to each other; i.e. the titanium octahedra; the perovskite structure becomes a better conductor. However, in-situ reduction at 900°C took more than 70 hours, as explained

earlier. Nevertheless, the system showed a very good redox performance as can be seen from figures 4.17 and 4.18.

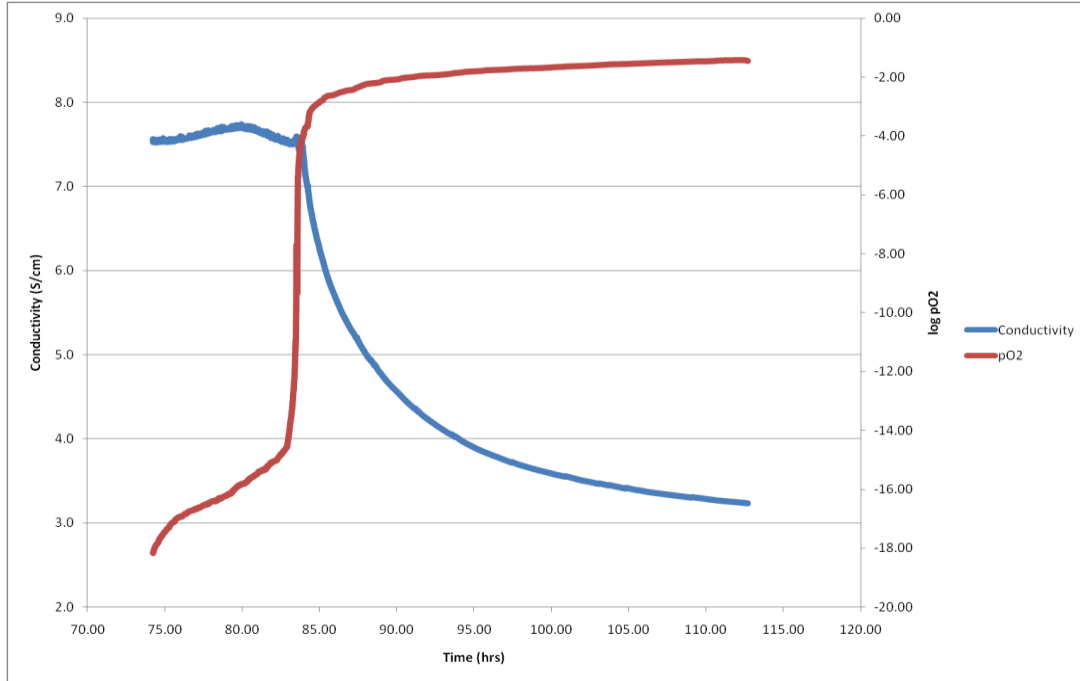


Figure 4.17: Oxidation of a dense sample of $\text{La}_{0.2}\text{Sr}_{0.5}\text{Ca}_{0.2}\text{TiO}_3$ at 900°C .

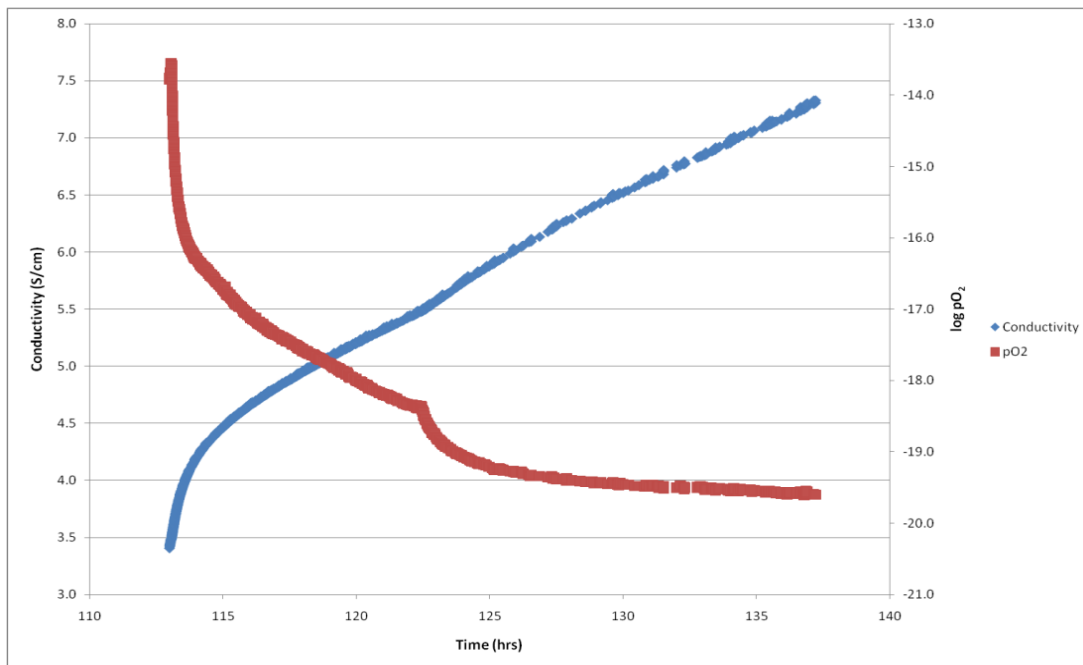


Figure 4.18: Reduction of a dense sample of $\text{La}_{0.2}\text{Sr}_{0.5}\text{Ca}_{0.2}\text{TiO}_3$ at 900°C .

The results above show that the sample electrical conductivity is very dependent on oxygen partial pressure at a fixed temperature. The two plots above, also, show that the material is redox stable; i.e. the same conductivity values can be obtained after redox cycling. Given the high relative density for this sample; i.e. > 92%; a full reduction or oxidation of the whole pellet could not be achieved. Comparing the times between oxidation and re-reduction, it can be seen that the sample was not fully oxidised due to the high density. However, the important aspect is that the sample regained the original conductivity value it had prior to oxidation. The results above led to all later samples to be pre-reduced at 1050°C; in order to save time on the testing jig. By now, the focus turned towards the thermal behaviour of the electrical conductivity and finding the composition with the maximum electrical conductivity. Figure 4.19 shows the electrical conductivity as a function of temperature for the first two samples that were shown earlier and two later samples which were pre-reduced as mentioned earlier.

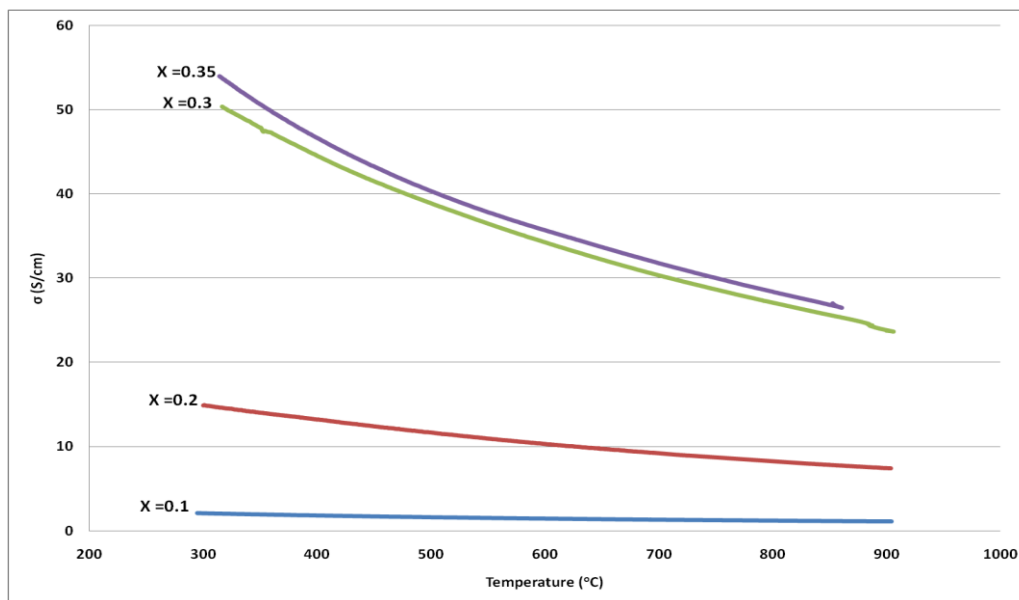


Figure 4.19: Temperature dependence of the electrical conductivity of different samples of $\text{La}_{0.2}\text{Sr}_{0.7-x}\text{Ca}_x\text{TiO}_3$ in reducing conditions. Note: samples $x = 0.3$ and 0.35 were pre-reduced at 1050°C and the electrical conductivity was measured using the van der Pauw technique.

As it was expected with titanates, the electrical conductivity at a fixed temperature and oxygen partial pressure is very dependent on how much Ti^{3+} exist in the system. With pre-reduction at 1050°C for 72 hours; the electrical conductivity of $x = 0.3$ and 0.35 increased considerably when compared to the previous samples; i.e. $x = 0.1$ and 0.2 . Also, the electronic conductivity of these perovskites kept on improving with more calcium content, where it was maximised in the composition with $x = 0.45$; i.e. figure 4.20 shows this composition electrical conductivity as a function of temperature in a reducing atmosphere.

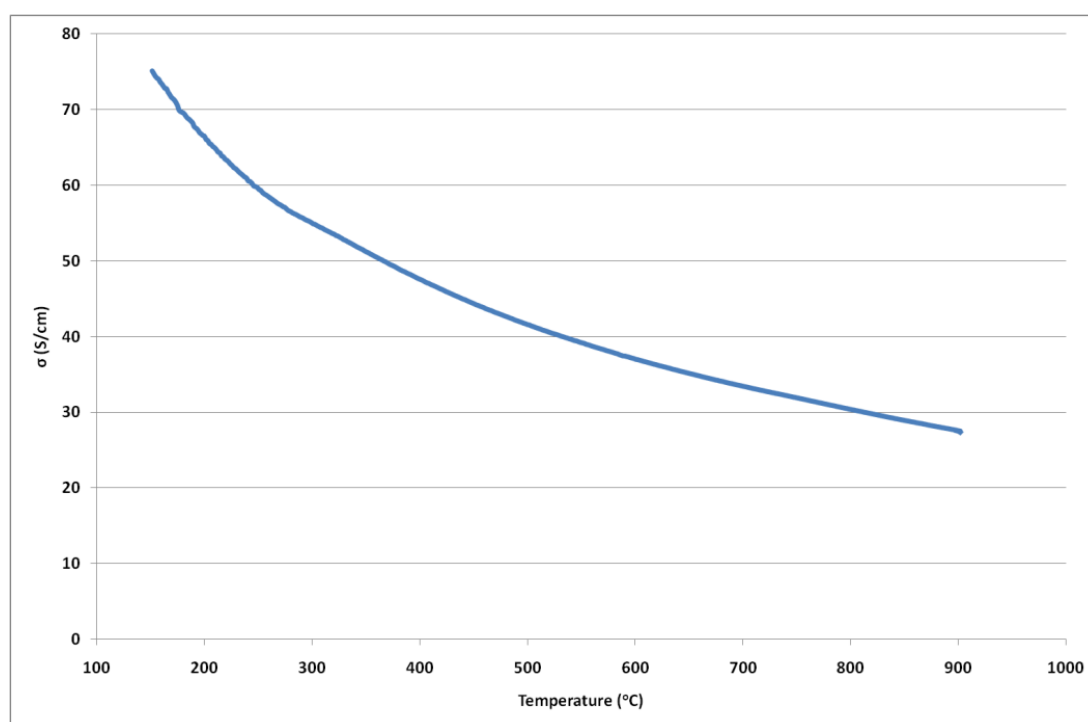


Figure 4.20: Temperature dependence of the electrical conductivity of a dense pre-reduced pellet of $\text{La}_{0.2}\text{Sr}_{0.25}\text{Ca}_{0.45}\text{TiO}_3$ under $5\% \text{H}_2/95\% \text{Ar}$, $p\text{O}_2 \approx 10^{-19}$ atm.

With an electrical conductivity of 27.5 S/cm at 900°C and $p\text{O}_2$ of 10^{-19} atm; $\text{La}_{0.2}\text{Sr}_{0.25}\text{Ca}_{0.45}\text{TiO}_3$ showed the highest conductivity among the different samples that

were pre-reduced at 1050°C. The conductivity was stable during thermal cycling with a metallic behaviour as can be seen from figure 4.21.

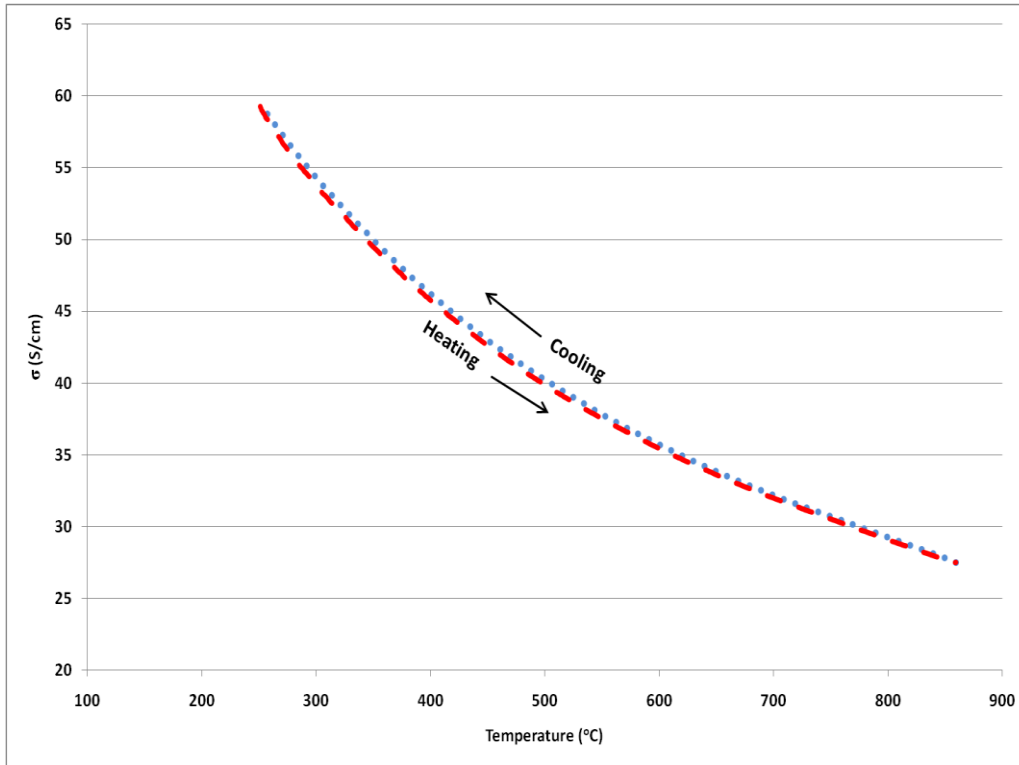


Figure 4.21: Temperature dependence of the electrical conductivity of $\text{La}_{0.2}\text{Sr}_{0.25}\text{Ca}_{0.45}\text{TiO}_3$ during thermal cycling in 5% H_2 .

As can be seen from figure 4.21, the sample holds the n-type conductivity feature very well during thermal cycling, even at very low temperatures, which indicates no loss of the density of Ti^{3+} within the structure; or in other words, the structure is stable in terms of its oxygen deficiency which enhances the electrical conductivity. This clearly suggests that this material is showing encouraging features to be used as an alternative anode material for SOFCs; where the stable performance is very important. The increasing electrical conductivity with increasing calcium content, hence a smaller unit

cell volume, did not hold. Figure 4.22 shows the electrical conductivity of high calcium content samples that was measured in the same conditions previously.

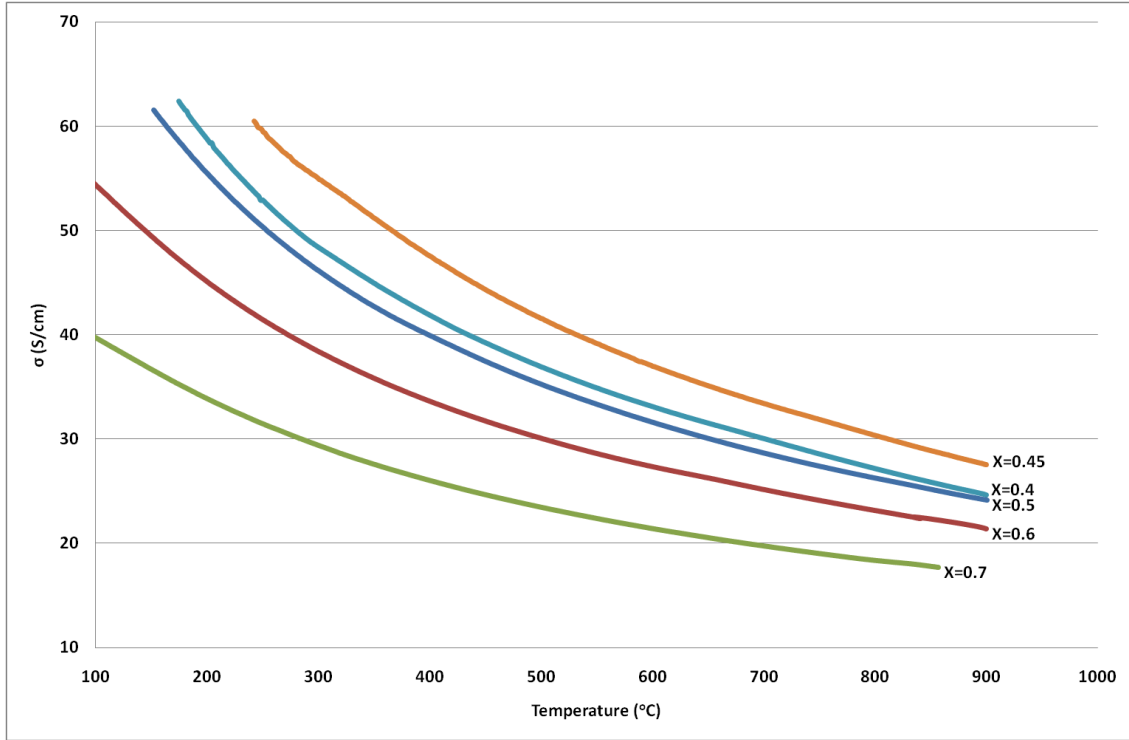


Figure 4.22: Temperature dependence of the electrical conductivity for pre-reduced samples of $\text{La}_{0.2}\text{Sr}_{0.7-x}\text{Ca}_x\text{TiO}_3$ in reducing atmosphere.

As can be seen above, after achieving the highest electrical conductivity at 900°C with the sample with nominal $x = 0.45$, the electrical conductivity started to drop with increasing calcium content. Another intriguing finding is that the dependence on calcium content is very clear throughout the temperature range, even at low temperatures the electrical conductivity shows the same behaviour to calcium content at 900°C. This indicates a very good stability of the material's conductivity regardless of the structural changes that occur at different temperatures, as found in chapter 3.

Figure 4.23 shows the maximum conductivity of all the samples of $\text{La}_{0.2}\text{Sr}_{0.7-x}\text{Ca}_x\text{TiO}_3$ that was measured at 900°C in reducing conditions.

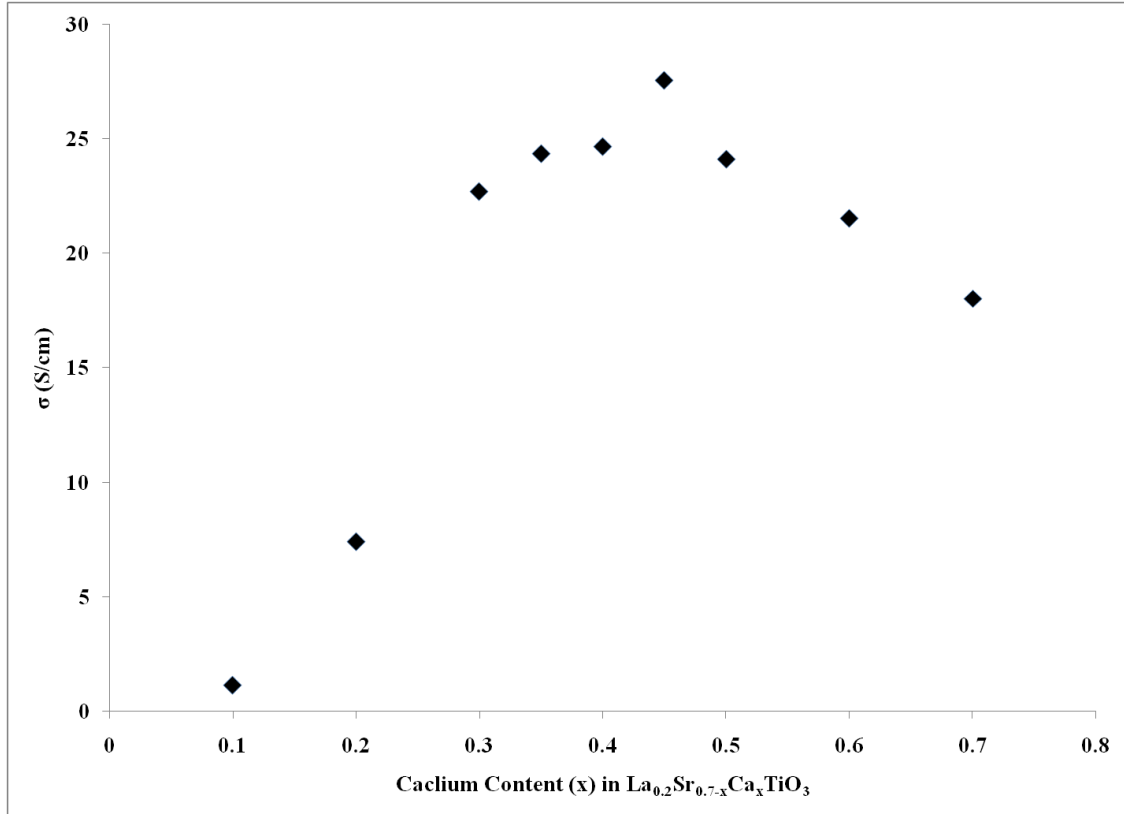


Figure 4.23: Comparison of the maximum conductivity at 900°C and $p\text{O}_2 \approx 10^{-19}$ atm for all pre-reduced dense samples of $\text{La}_{0.2}\text{Sr}_{0.7-x}\text{Ca}_x\text{TiO}_3$. Note: errors contained within data points symbols.

In the figure above, the electrical conductivity increases with more calcium to reach a maximum at $x = 0.45$, where it then starts dropping. Comparing the structure of $x = 0.45$ to that of $x = 0.5$ the two are very similar; i.e. cubic $\text{Pm}\bar{3}\text{m}$ at 900°C ; as the results in chapter 3 revealed. The unit cell volume of $x=0.5$ is smaller than that of $x = 0.45$. Both pre-reduced compositions showed a very similar oxygen deficiency as was determined from TGA earlier; i.e. $\delta \approx 0.03$. All these parameters indicate that the conductivity of $x = 0.5$ should be higher following the trend seen above. However, even after repeating

the measurement for $x = 0.5$ several times, the same value was obtained each time. Going back to the structural analysis using NPD at 900°C for both compositions, it can be seen that the difference between the two lies in the isotropic atomic displacement parameters. Table 4.2 lists the isotropic atomic displacement parameters for the different atomic sites within the cubic unit cell of the two compositions in question at 900°C.

La_{0.2}Sr_{0.25}Ca_{0.45}TiO₃		La_{0.2}Sr_{0.2}Ca_{0.5}TiO₃	
Site	B_{iso}	Site	B_{iso}
Ti	1.485	Ti	1.699
La,Sr,Ca	2.139	La,Sr,Ca	2.270
O	3.286	O	3.383

Table 4.2: Isotropic atomic displacement parameters of La_{0.2}Sr_{0.25}Ca_{0.45}TiO₃ and La_{0.2}Sr_{0.2}Ca_{0.5}TiO₃ at 900°C.

From the values above, it is clear that the composition La_{0.2}Sr_{0.2}Ca_{0.5}TiO₃ ($x = 0.5$) is more distorted at 900°C. From the higher B_{iso} for the different sites, especially the titanium and oxygen, it is clear that the conduction orbitals overlap will be affected by the thermal displacement of the ions involved; thus increasing the resistance of the material. Thus, it was obvious that the unit cell volume decrease improves the electronic conductivity of this type of titanates. However, as the unit cell volume crosses a certain threshold; the distortions in the unit cell increase and dominate at high temperatures; which result in lowering the orbitals overlap, hence, reducing the electrical conductivity. If one pictures the unit cell at high temperatures; the thermal vibrations of the different

atomic sites must be affected by the ionic radius mismatch of the A-site; where a large A-site should, in theory, stabilise the unit cell, rendering a stable orbital overlap. Thus, we see that the electrical conductivity of the compositions $x = 0.5, 0.6$ and 0.7 decreases with increasing calcium content; contrary to the initial behaviour that was seen. Going back to the findings of Savaniu and Irvine [4] who found that pre-reducing their samples of $\text{La}_{0.2}\text{Sr}_{0.7}\text{TiO}_3$ produced higher conductivity values, the results, here, indicate that there is a limit to calcium doping; i.e. $x = 0.45$ in $\text{La}_{0.2}\text{Sr}_{0.7-x}\text{Ca}_x\text{TiO}_3$; after which the distortions on the unit cell due to the A-site cations radii mismatch are higher, thus the total conductivity is lower with high calcium content samples in the studied series. Although, it is very important to take much care when comparing conductivity values between different materials reported in literature. The reason behind this notion is that it was suggested that several heat treatments of such materials can generate different types of defects that do affect the electrical behaviour of a given sample.[6] Most importantly, the results here do show that the electrical conductivity can be enhanced through careful implementation of doping and processing techniques. Also, improvements to the conductivity of $\text{La}_{0.2}\text{Sr}_{0.25}\text{Ca}_{0.45}\text{TiO}_3$ can be obtained through control of the porosity and/or impregnation with catalytic active materials; e.g. ceria; which will be the focus of future works with this system. In a recent study working on commercially relevant cells, SOFC anode formulations based on the sample $x = 0.45$ developed in this work have yielded very promising performances.[8] Hence, perovskite based materials are, indeed, offering a great framework to study and improve on materials properties for many different applications.

4.4 - SEM Studies

The morphology of the different samples prepared in this work was studied through SEM. As we shall see there were no significant effects on the morphology and grain growth with different calcium levels of substitution as was the case with structural changes.

Results and Discussion

As there were different samples of $\text{La}_{0.2}\text{Sr}_{0.7-x}\text{Ca}_x\text{TiO}_3$ with different calcium content, SEM was used to see if there were any effects on the morphology of these samples as the calcium content was varied. Figure 4.24 shows different SEM micrographs of a number of samples.

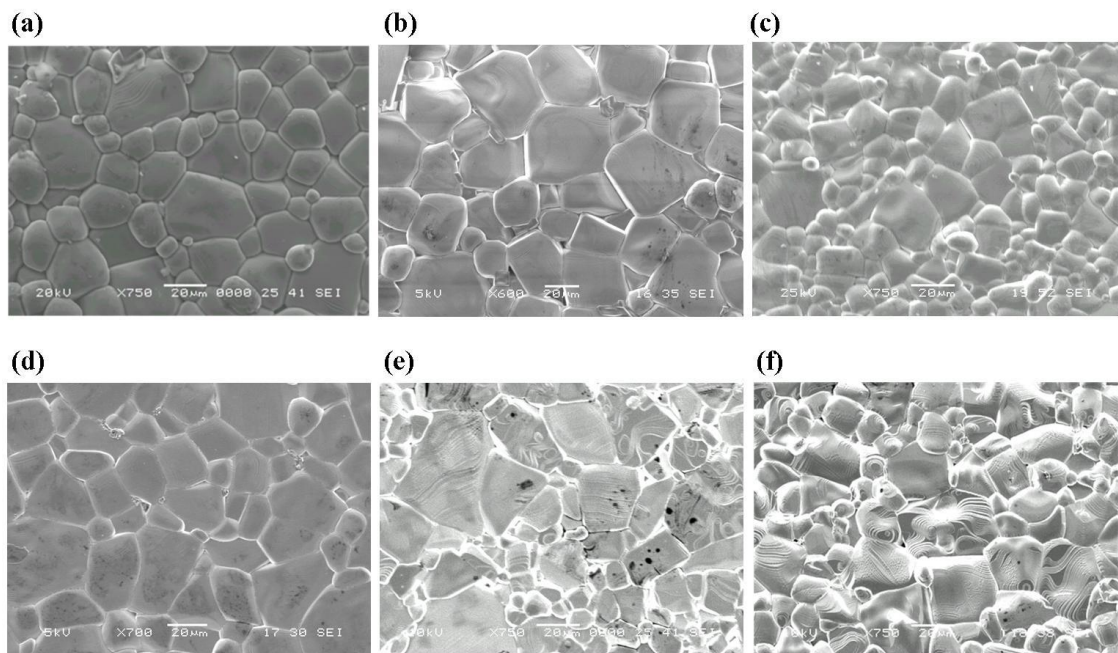


Figure 4.24: SEM micrographs of different samples of $\text{La}_{0.2}\text{Sr}_{0.7-x}\text{Ca}_x\text{TiO}_3$ sintered in air where (a): 0.1, (b): 0.35, (c): 0.4, (d): 0.45, (e): 0.6 and (f): 0.7 for x.

From the micrographs above, the shape and size of the grains is very similar across the series; with no strong effect that can be linked directly to increasing calcium content. The samples close to the phase boundary; i.e. $x = 0.4$ and 0.45 from structural analysis; also show no clear difference in morphology with the other samples. The only effect that can be seen is the increased sinterability of the samples with increasing calcium content which was very obvious when some pellets were sintered with 20wt% of a pore-former mixture, this is shown in figure 4.25.

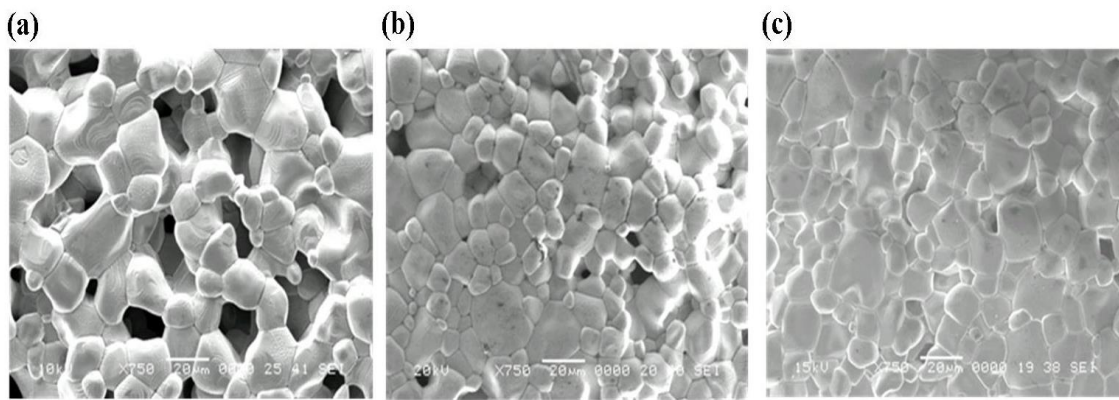


Figure 4.25: SEM micrographs showing samples of $\text{La}_{0.2}\text{Sr}_{0.7-x}\text{Ca}_x\text{TiO}_3$ sintered in air at 1400°C with 20wt% pore-former mixture; where (a): $x = 0.1$, (b): $x = 0.2$, (c): $x = 0.35$.

It is clear that the pores had closed up with increasing calcium content. The relative density measured for these samples also showed an increase with increasing calcium content; the values are shown in table 4.3.

x	Relative Density
0.1	70.9%
0.2	81.4%
0.35	82.6%

Table 4.3: Relative density of samples of $\text{La}_{0.2}\text{Sr}_{0.7-x}\text{Ca}_x\text{TiO}_3$; which were sintered with 20wt% pore-former.

This confirms that the calcium improved the densification process of this type of titanates counteracting the effect of lanthanum introduction as explained in chapter 1. Since this system is intended to be used as an anode material for SOFCs, the stability under reducing atmospheres is important. The structure was shown to be stable after reduction as was found from structural analysis in the previous chapter. The effect of reduction on the morphology is shown in figure 4.26.

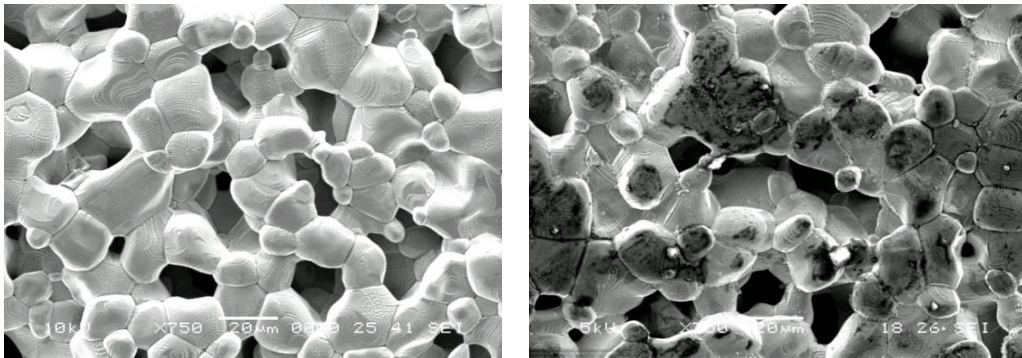


Figure 4.26: SEM micrographs of a porous $\text{La}_{0.2}\text{Sr}_{0.6}\text{Ca}_{0.1}\text{TiO}_3$ before (left) and after (right) reduction.

There were no indications of any secondary phases forming on the surface or any major differences in the morphology of the samples after reduction; which indicates a very good stability of this material in reducing atmospheres. Most samples were pressed uniaxially under loads of 4-5 tonnes prior to sintering; a comparison was made to see the effect of lower loads, which is shown in figure 4.27.

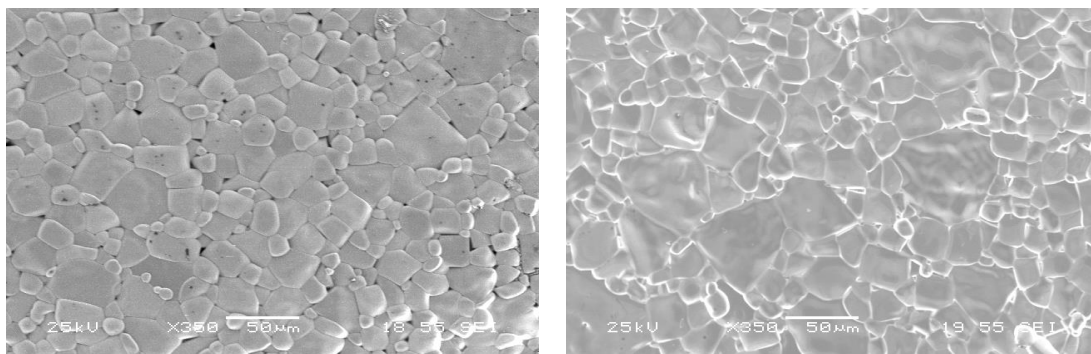


Figure 4.27: SEM micrographs for two pellets of $\text{La}_{0.2}\text{Sr}_{0.25}\text{Ca}_{0.45}\text{TiO}_3$ pressed at 1 ton (left) and 4 tonnes (right).

Both samples above were sintered together at 1500°C for 15 hours in air from the same starting powders. The effect of increasing the press load can be seen to increase the relative density of the sintered pellets, where pores can be seen on the pellet that was pressed with a load of 1 ton. The shape and relative sizes of the grains are very similar in both cases which are understandable from the fact that grain growth depends on the sintering conditions, which were the same in this case. The effect of multiple sintering processes was investigated as figure 4.28 shows a comparison between two samples that were sintered at the same temperature with different repetitions.

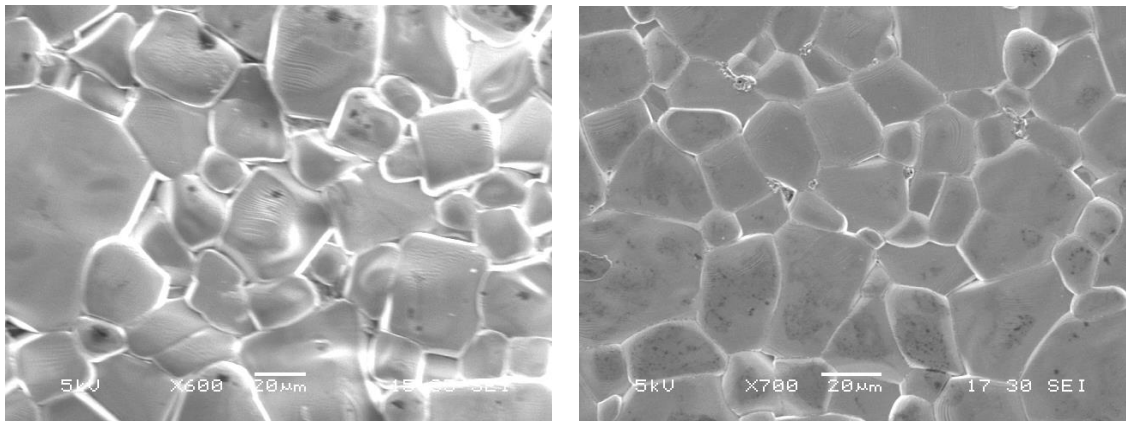


Figure 4.28: SEM micrographs showing two samples of $\text{La}_{0.2}\text{Sr}_{0.25}\text{Ca}_{0.45}\text{TiO}_3$ that were sintered once (left) and four times (right) at 1500°C.

From the figure above it can be seen that the grains are not affected and very similar to each other in terms of the shape, size and distribution. This again confirms that calcium improves the sinterability of this type of titanates considerably. All in all, the system shows very impressive stability with the morphology more or less the same across the different samples studied here.

4.5 - Conclusions:

One of the main tasks of this work was to pinpoint how much the electrical conductivity of the system $\text{La}_{0.2}\text{Sr}_{0.7-x}\text{Ca}_x\text{TiO}_3$ could be improved as the calcium content in the system was varied. This showed that the electrical conductivity could be mainly affected by two mechanisms, the degree by which the conduction orbitals overlap and by the concentration of electrons. The first is affected by calcium content, up to a certain point; i.e. $x=0.45$; after which the unit cell distortions and thermal vibrations negatively affected the electrical conductivity as the unit cell volume decreased with increasing calcium content. Distortions and tilts can be viewed as disturbances to the conduction orbitals stability. The second is mainly controlled by the proportion of the reduced Ti^{4+} that adds up to the electrons concentration in the conduction band of the titanium 3d orbitals. Reducing this system at higher temperatures generated more electrons and higher oxygen deficiency. The oxygen deficiency that was obtained during the pre-reduction process did not show much of a dependence on the composition. This can be further improved via experimenting with different microstructures and the introduction of different catalyst materials to the studied substrate. The highest conductivity was found for the pre-reduced composition $\text{La}_{0.2}\text{Sr}_{0.25}\text{Ca}_{0.45}\text{TiO}_{2.97}$ with a value of 27.5 S/cm at 900°C and $p\text{O}_2 = 10^{-19}$ atm. Calcium introductions, to reduce the unit cell volume, did prove to be useful in improving the electrical conductivity to a certain point. The electrical conductivity showed a dependency on the oxygen partial pressure, although this was more pronounced at high reducing and oxidising conditions; i.e. high relative density of produced samples; indicating a dependence on oxygen vacancies concentration. The system also showed that its sintering behaviour was very similar to the most common SOFC electrolyte

material YSZ, with some of the samples showing very close TEC values to that of the YSZ. The TEC of the different samples did not show much dependence on calcium content/crystal structure but did show some dependence on oxygen deficiency. The morphology of the material was not affected, significantly, by calcium content but by the synthesis methods that were employed. These affected the density of the samples, where it was obvious that increasing calcium content lowered the melting point of the different samples. Overall, all samples showed very impressive thermal and chemical stability when operated under anodic conditions which really shows a very encouraging potential for this system to be a very good candidate as an alternative anode material for SOFCs.

4.6 - References

- [1] R. J. Gorte and J. M. Vohs, *Curr. Opin. Colloid In.*, 2009, **14**, 236-244.
- [2] M. Mori, Y. Hiei and T. Yamamoto, *J. Am. Ceram. Soc.*, 2001, **84**, 781-786.
- [3] O. A. Marina, N. L. Canfield and J. W. Stevenson, *Solid State Ionics*, 2002, **149**, 21-28.
- [4] C. D. Savaniu and J. T. S. Irvine, *J. Mater. Chem.*, 2009, **19**, 8119-8128.
- [5] K. T. Lee and A. Manthiram, *Solid State Ionics*, 2007, **178**, 995-1000.
- [6] J. W. Fergus, *Solid State Ionics*, 2006, **177**, 1529-1541.
- [7] A. Atkinson, S. Barnett, R. J. Gorte, J. T. S. Irvine, A. J. McEvoy, M. Mogensen, S. C. Singhal and J. Vohs, *Nat. Mater.*, 2004, **3**, 17-27.
- [8] M.C. Verbraeken, B. Iwanschitz, A. Mai, and J.T.S. Irvine, *J. Electrochem. Soc.*, 2012, **159**, F757-F762.

Chapter 5

Investigation of Possible Ferroelectricity

in the A-site Deficient Perovskite

$\text{La}_{0.2}\text{Sr}_{0.7-x}\text{Ca}_x\text{TiO}_3$ using AC Impedance

Abstract:

Different samples of the A-site deficient perovskite $\text{La}_{0.2}\text{Sr}_{0.7-x}\text{Ca}_x\text{TiO}_3$ were tested for at different temperatures using AC impedance spectroscopy. Samples showed high capacitance that decreased with increasing temperatures. This led to investigating the existence of any ferroelectric behaviour of the samples in this series. As samples in this series showed symmetry changes with temperature, these changes did not show any ferroelectric behaviour at many different temperatures. Hence, this confirms that all the different symmetries are centrosymmetric and the structural analysis of the system was correct. It also confirmed that there is no B-site displacement taking place on the Ti cations in the distortions associated with the lower symmetries found in chapter 3.

5.1 - Introduction

The system $\text{La}_{0.2}\text{Sr}_{0.7-x}\text{Ca}_x\text{TiO}_3$ showed phase transitions between $\text{Pm}\bar{3}\text{m}$ - I4/mcm - Pbnm with different calcium content, as well as, at different temperatures; where the structures adopted higher symmetries. These findings were based on results from XRD and NPD studies; i.e. Chapter 3. Investigating whether this system can possess a ferroelectric nature or not came to mind; since $\text{Sr}_{1-x}\text{Ca}_x\text{TiO}_3$ samples in the range $0.002 \leq x \leq 0.12$; which showed the I4/mcm symmetry at room temperature, exhibited a ferroelectric behaviour at temperatures below 35K; the reported phase had a point group $\text{mm}2$ without a space group being specified at these temperatures.[1,2] Also, earlier impedance measurements indicated, as shall be illustrated in the next section, that the capacitance of some samples of the system $\text{La}_{0.2}\text{Sr}_{0.7-x}\text{Ca}_x\text{TiO}_3$ was changing with temperature. The studies conducted on $\text{La}_{0.2}\text{Sr}_{0.7-x}\text{Ca}_x\text{TiO}_3$, in the previous chapters, were involved with the high temperature properties; since the system was designed to be a potential anode material for SOFCs. BaTiO_3 , one of the well known ferroelectric perovskites, is tetragonal with space group P4mm under 130°C ; where above this temperature it transforms into a paraelectric cubic structure with space group $\text{Pm}\bar{3}\text{m}$.[3,4] The ferroelectricity originates from the displacement of titanium from its centrosymmetric position creating an electric dipole.[3] Thus, as distortions to the BO_6 octahedra of $\text{La}_{0.2}\text{Sr}_{0.7-x}\text{Ca}_x\text{TiO}_3$ were observed, the study in this chapter can give a better insight into the structural changes of this system and the potential of this material beyond the realm of fuel cells components.

5.2 - Results and Discussion

Since the results at chapter 3 showed that many phase or symmetry changes do take place in different compositions of the system $\text{La}_{0.2}\text{Sr}_{0.7-x}\text{Ca}_x\text{TiO}_3$, studying these materials for ferroelectric behaviour can be very useful in understanding the structural changes these materials undergo. The early measurements in this work indicated a change in the capacity of tested pellets with temperature; which indicated changes to the dielectric properties. The first sample that was tested was $\text{La}_{0.2}\text{Sr}_{0.25}\text{Ca}_{0.45}\text{TiO}_3$; which was very resistive at room temperature; when fully oxygenated.

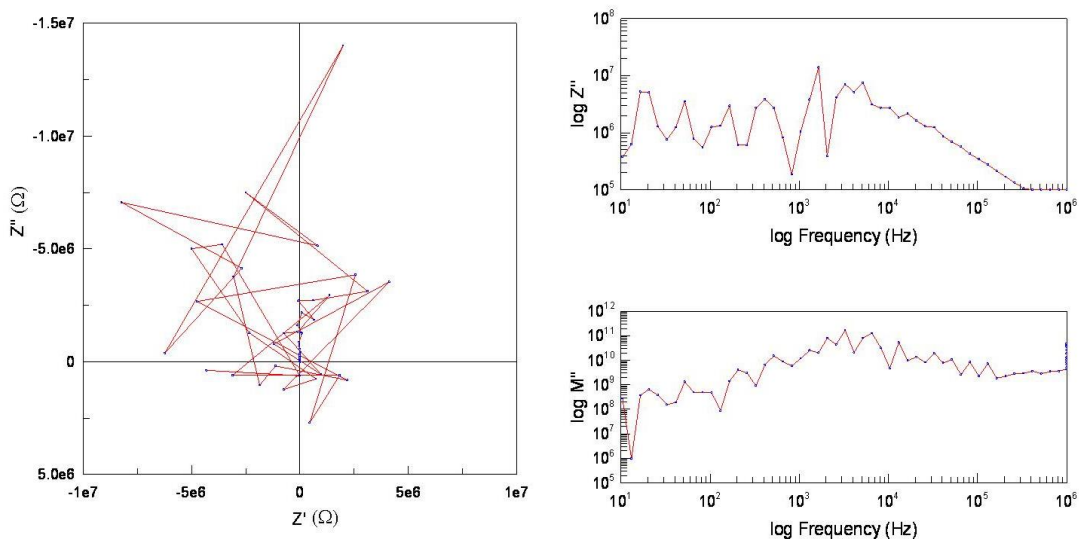


Figure 5.1: Impedance plots of $\text{La}_{0.2}\text{Sr}_{0.25}\text{Ca}_{0.45}\text{TiO}_3$ at 300°C showing the results at the low frequency range.

This bulk of this sample has shown the very high resistance even at higher temperatures until typical impedance arcs were obtained at temperatures higher than 500°C as shown in figure 5.2.

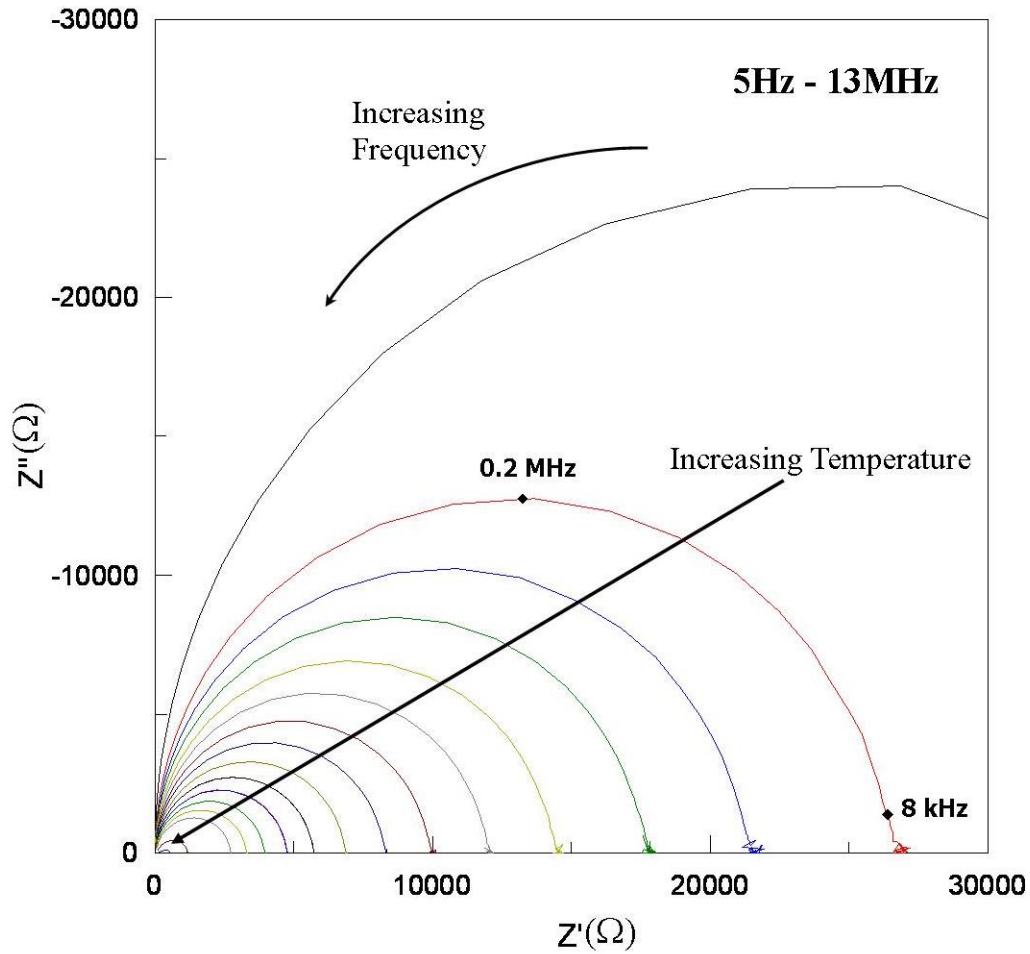


Figure 5.2: Impedance spectra of $\text{La}_{0.2}\text{Sr}_{0.25}\text{Ca}_{0.45}\text{TiO}_3$ at temperatures between 550° and 900°C in air.

It was clear that this material was exhibiting a semiconducting behaviour as its resistance was decreasing with increasing temperature. As this sample was tested as-prepared; i.e. fully oxidised; no free charge carriers are expected to exist within the material. Also, it was clear that the material behaviour is being dominated by the bulk; since low frequency region of the impedance spectra was very noisy and did not represent typical impedance patterns.

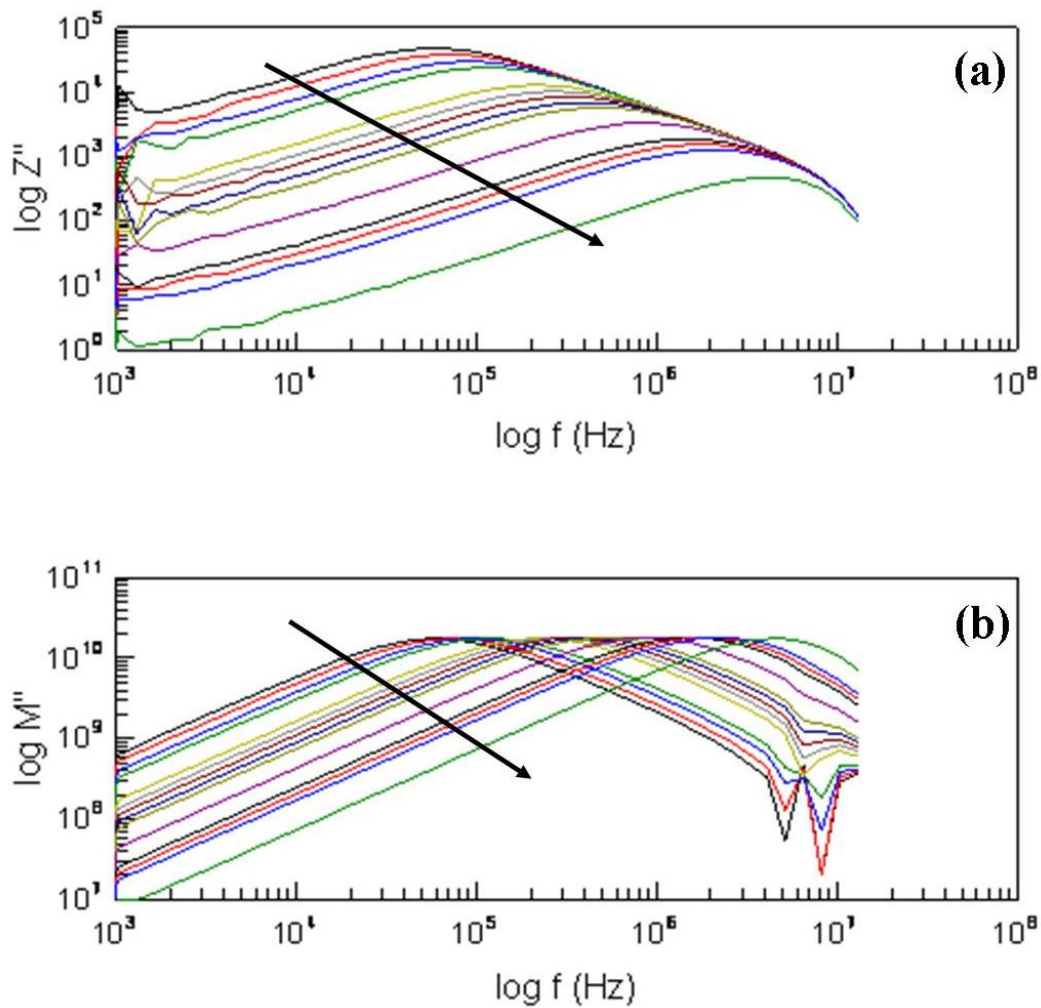


Figure 5.3: Frequency plots of Z'' and M'' for $\text{La}_{0.2}\text{Sr}_{0.25}\text{Ca}_{0.45}\text{TiO}_3$ at temperatures between 550° and 900°C . Note: arrows indicate the direction of increasing temperature.

It is known that as the maxima in the $\log Z''$ and $\log M''$ plots fall at the same frequency; this represents an ideal RC element.[11] This led to the estimation of the resistivity and capacitance of the material tested here through the least square fitting of an equivalent circuit (see figure 5.4) to the arcs shown in figure 5.2. The equivalent circuit consisted of a resistor and a capacitor connected in parallel; this represented one contribution from the material microstructure.

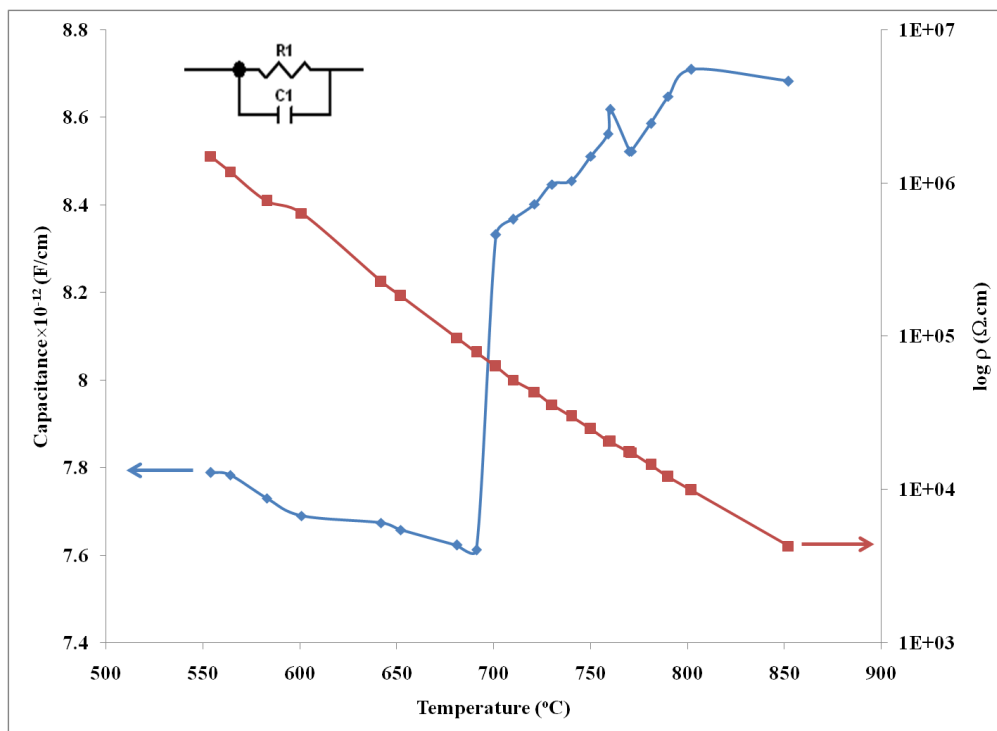


Figure 5.4: Plot of the capacitance and resistivity at different temperatures of $\text{La}_{0.2}\text{Sr}_{0.25}\text{Ca}_{0.45}\text{TiO}_3$ obtained using least square fitting of impedance data to a simple RC element (shown). Note: lines are guides to the eye.

The figure above shows a very small increase in the capacitance; i.e. around 730°C. The values of the capacitance ($1 \times 10^{-12} \text{ F} \cdot \text{cm}^{-1}$), as well as, the result of a single arc in the impedance plots, show that this material behaviour is dominated by the bulk and that any other contributions are insignificant; e.g. grain boundary. This, in turn, can indicate a relatively homogeneous semiconducting material; especially since the resistance is decreasing significantly and consistently with increasing temperature. The change in capacitance in figure 5.4 around 730°C was the main drive that led us to believe that there might exist a phase at certain temperature with distortions that might lead to a non-centrosymmetric space group with the titanium cation shifted off its central position within the BO_6 octahedra of these perovskites. Thus, it was necessary to use different

setups (see chapter 1) to better estimate the dielectric behaviour of the different samples with better control on temperature and impedance reliability.

As previously stated, strontium rich compositions in the system $\text{Ca}_x\text{Sr}_{1-x}\text{TiO}_3$ have shown ferroelectric behaviour at very low temperatures; thus, a test was done on the first sample of the system $\text{La}_{0.2}\text{Sr}_{0.7-x}\text{Ca}_x\text{TiO}_3$; i.e. the composition with nominal $x = 0.1$. The capacitance of this sample is shown in figure 5.5 as it was cooled down to 50K.

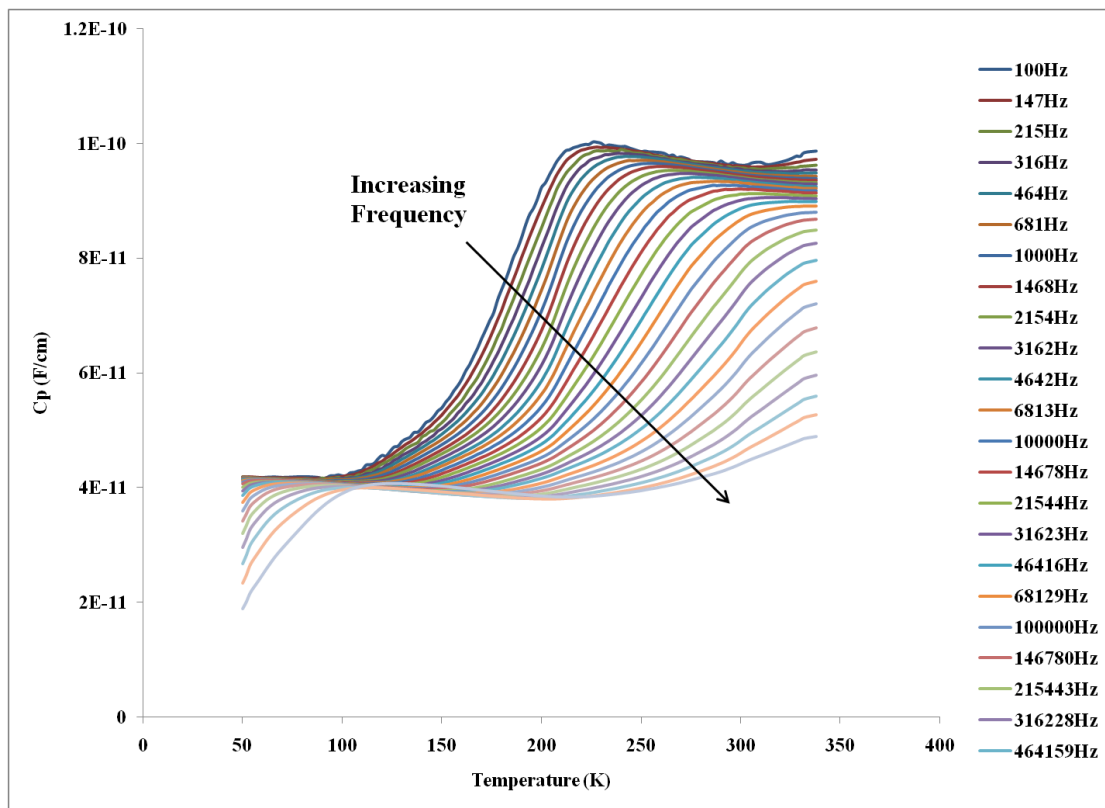


Figure 5.5: Temperature dependence of specific C_p at different frequencies for $\text{La}_{0.2}\text{Sr}_{0.6}\text{Ca}_{0.1}\text{TiO}_3$ at sub-ambient temperatures.

As can be seen from the result above, there was no distinctive maximum in the response of the capacitance of the sample that would indicate a ferroelectric - paraelectric transition point; i.e. a Curie point. The capacitance can be seen to decrease at lower

temperatures, indicating a decreasing dielectric constant. The calculated dielectric constant is plotted against temperature in figure 5.6.

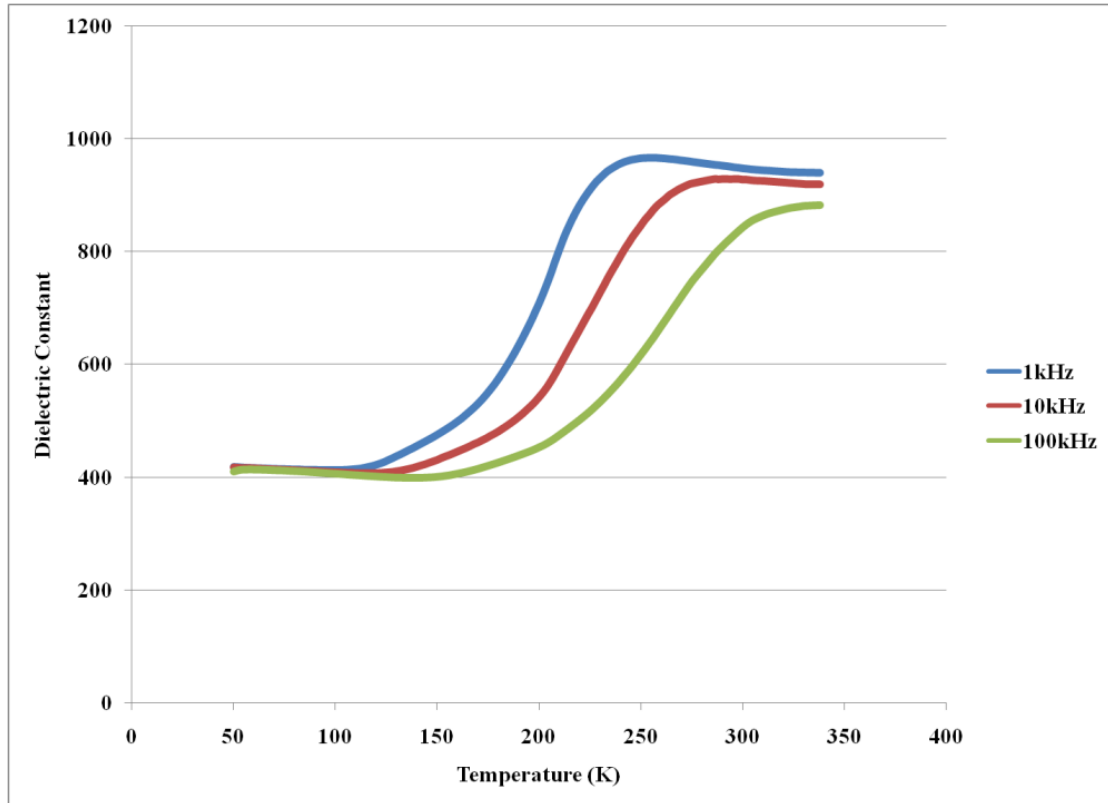


Figure 5.6: Dielectric constant of $\text{La}_{0.2}\text{Sr}_{0.6}\text{Ca}_{0.1}\text{TiO}_3$ as a function of temperature at selected frequencies.

The dielectric constant of $\text{La}_{0.2}\text{Sr}_{0.6}\text{Ca}_{0.1}\text{TiO}_3$ is observed to increase with increasing temperature in a non-linear fashion. Two plateaus can be seen which can indicate a possible phase; i.e. symmetry; change which is very possible at these low temperatures. However, the change in the values of the dielectric constant is not that significant. The dielectric loss ($\tan\delta$) for the same sample above is plotted against temperature in figure 5.7.

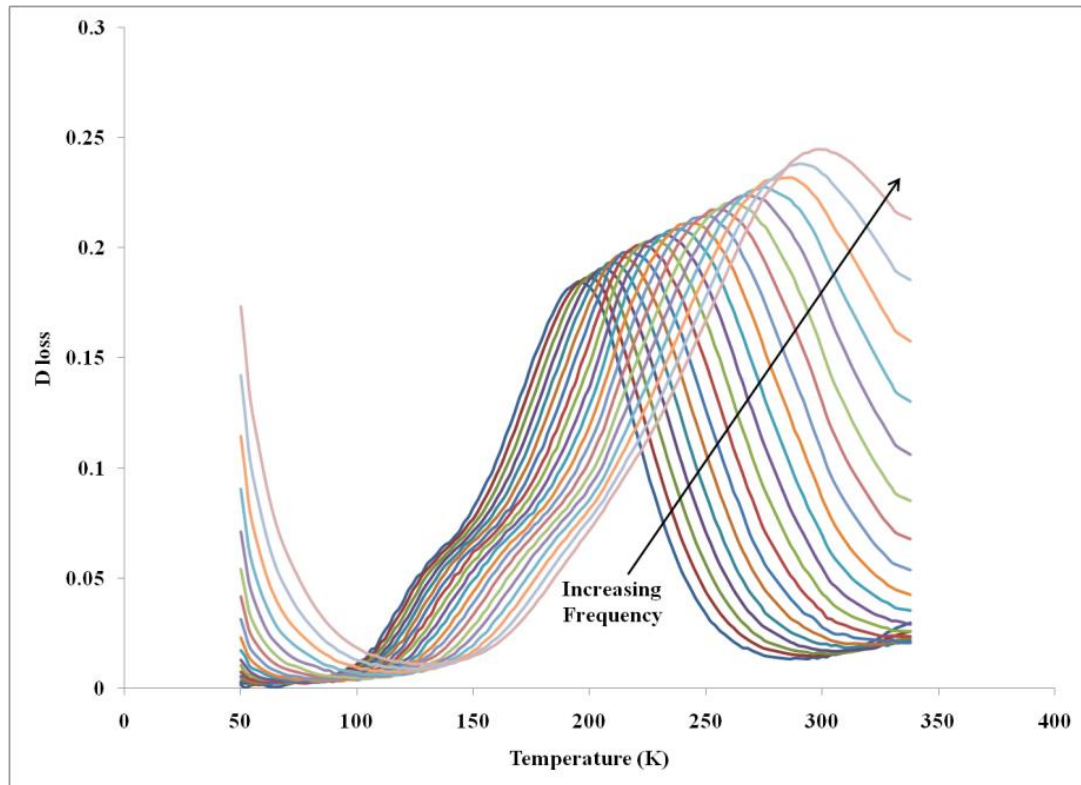


Figure 5.7: Dielectric loss of $\text{La}_{0.2}\text{Sr}_{0.6}\text{Ca}_{0.1}\text{TiO}_3$ at different frequencies as a function of temperature.

The dielectric loss peaks shifted to higher temperatures with increasing frequency. This behaviour is very similar to the behaviour of $\text{CaCu}_3\text{Ti}_4\text{O}_{12}$ (CCTO).[5] However, CCTO has shown a much larger increase in the dielectric constant; i.e. from 100 to over 10000. This can indicate that the dielectric behaviour of the different samples studied here is mainly affected by slight distortions to the octahedra, instead of a shift in the titanium position which can give rise to a ferroelectric nature. At high temperatures $\text{La}_{0.2}\text{Sr}_{0.6}\text{Ca}_{0.1}\text{TiO}_3$ also showed a non-ferroelectric behaviour as can be seen from figure 5.8.

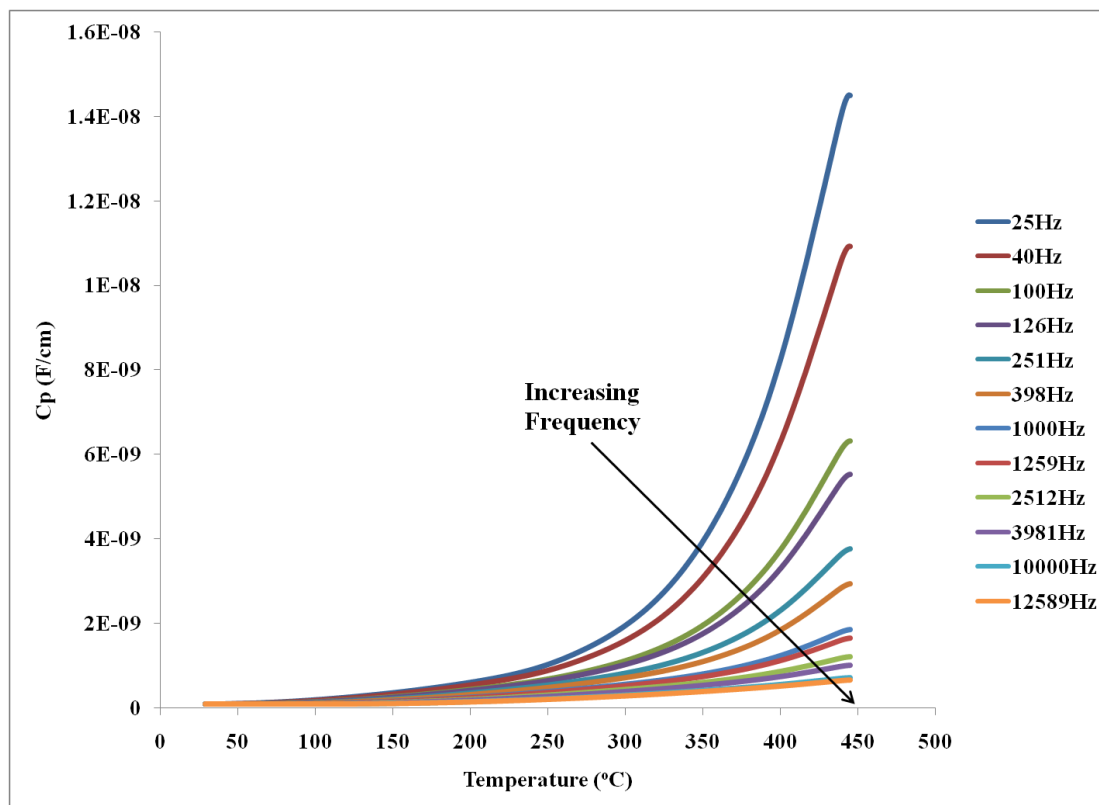


Figure 5.8: Temperature dependence of specific C_p at different frequencies for $\text{La}_{0.2}\text{Sr}_{0.6}\text{Ca}_{0.1}\text{TiO}_3$ at high temperatures.

It can be seen that the capacitance; and the dielectric constant; at high temperatures is much higher than the one at sub-ambient temperatures. At certain temperature ranges, the dielectric seems to be insensitive to the change in temperature; e.g. $30^\circ < T < 80^\circ\text{C}$. The dielectric constant is found to be more sensitive to changes in temperature at low frequencies. The dielectric loss is plotted against temperature for the high temperature measurement in figure 5.9; where no peaks were detected as was seen in the low temperature measurement. Also, the scale of the dielectric loss is higher above room temperature.

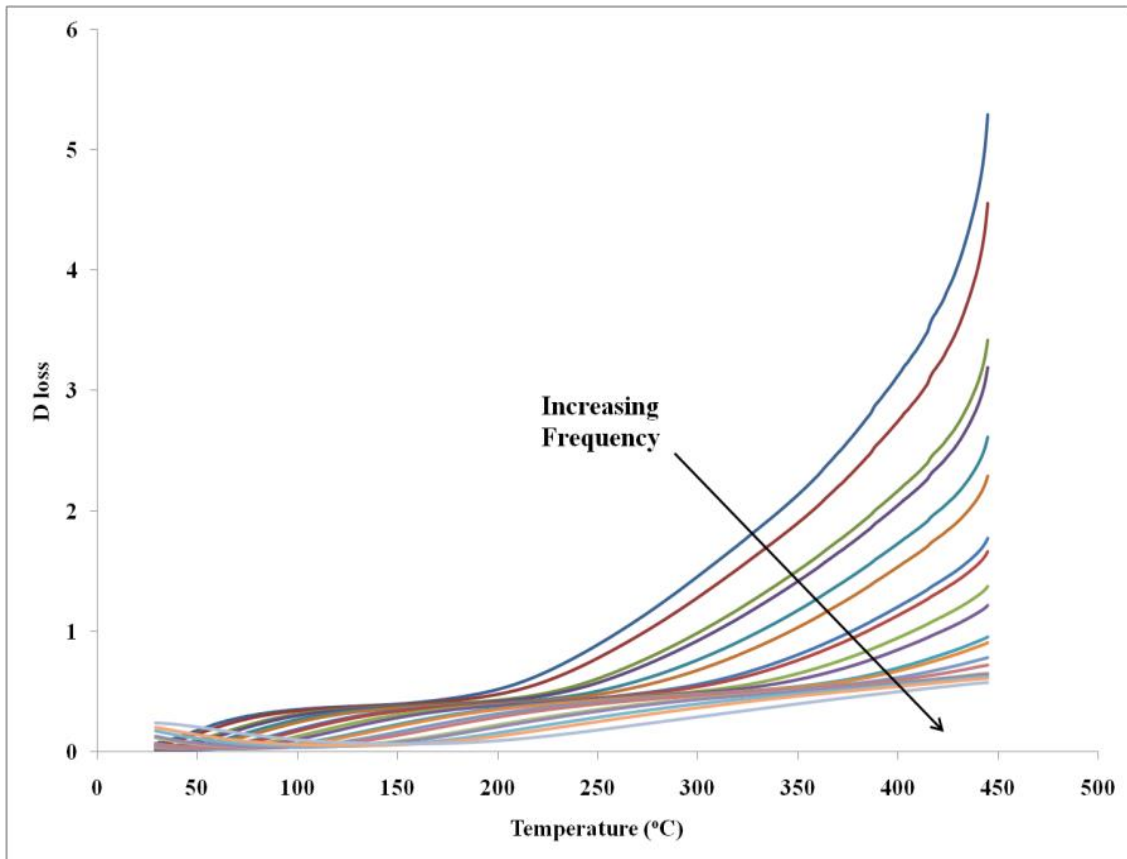


Figure 5.9: Dielectric loss of $\text{La}_{0.2}\text{Sr}_{0.6}\text{Ca}_{0.1}\text{TiO}_3$ at different frequencies as a function of temperature.

It is suggested that the higher dielectric constant values at lower frequencies are attributed to space charges which in this case are manifested in charge vacancies (defects) due to the A-site deficiency of the system studied here.[6,7] However, these samples did show a very high resistance which makes it very difficult to investigate the exact mechanisms involved to give such behaviour. Nonetheless, no phase changes were detected with this sample through thermal cycling as shown in figure 5.10.

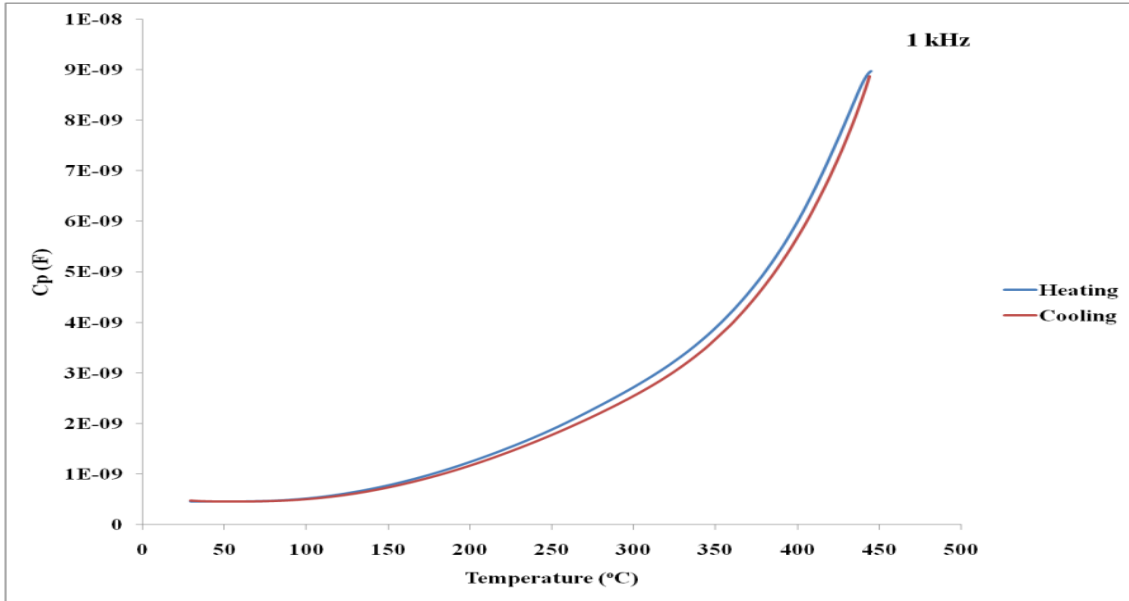


Figure 5.10: C_p as a function of temperature for $\text{La}_{0.2}\text{Sr}_{0.6}\text{Ca}_{0.1}\text{TiO}_3$ at 1 kHz during thermal cycling.

The behaviour of the capacitance of $\text{La}_{0.2}\text{Sr}_{0.6}\text{Ca}_{0.1}\text{TiO}_3$ as a function of frequency is shown in figure 5.11.

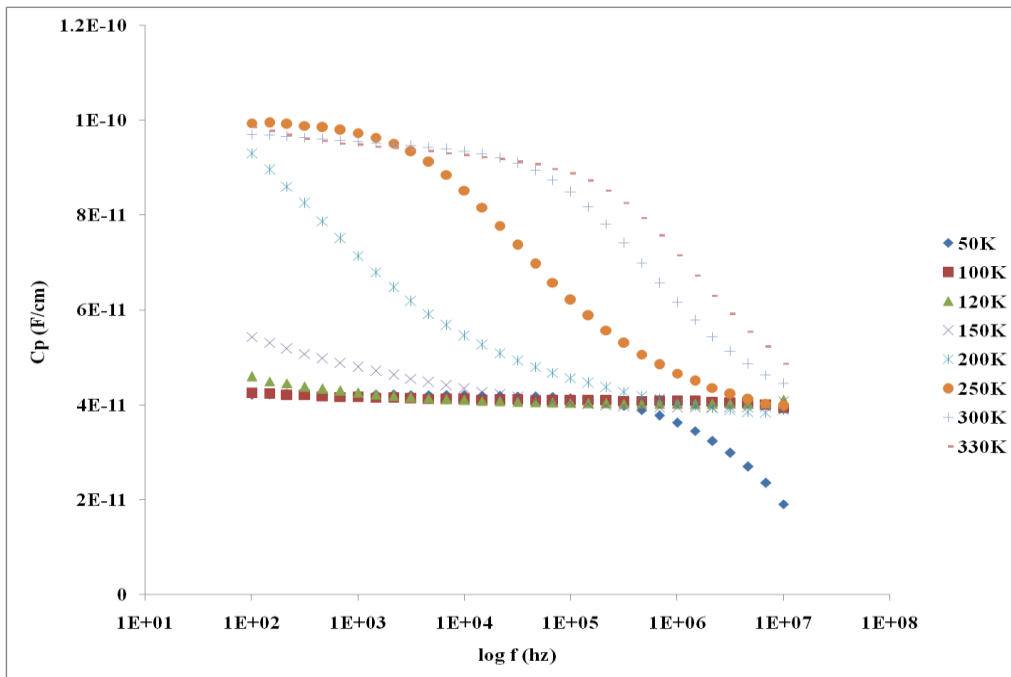


Figure 5.11: C_p vs. Frequency at different temperatures of $\text{La}_{0.2}\text{Sr}_{0.6}\text{Ca}_{0.1}\text{TiO}_3$.

It can be seen that the capacitance of the sample, above, show very small variation; i.e. same order of magnitude; especially at low temperatures. A depression is more pronounced as the sample is heated, with the inflection point shifting to higher frequencies as the temperature is increased. According to West et. al. [12], in $\text{CaCu}_3\text{Ti}_4\text{O}_{12}$ (CCTO) a high capacitance, low frequency plateau results from grain boundaries and a low capacitance, high frequency plateau indicates a semiconducting bulk. The behaviour of our material cannot be compared to that of CCTO; since the latter capacitance changes by two orders of magnitude at the same frequency range; i.e. 10^{-9} to 10^{-11} [12]; whereas the capacitance in our composition is relatively low and stable within the same order of magnitude. This can indicate a relatively homogenous phase throughout this sample. At higher temperatures, the capacity of the same sample, above, is shown in figure 5.12.

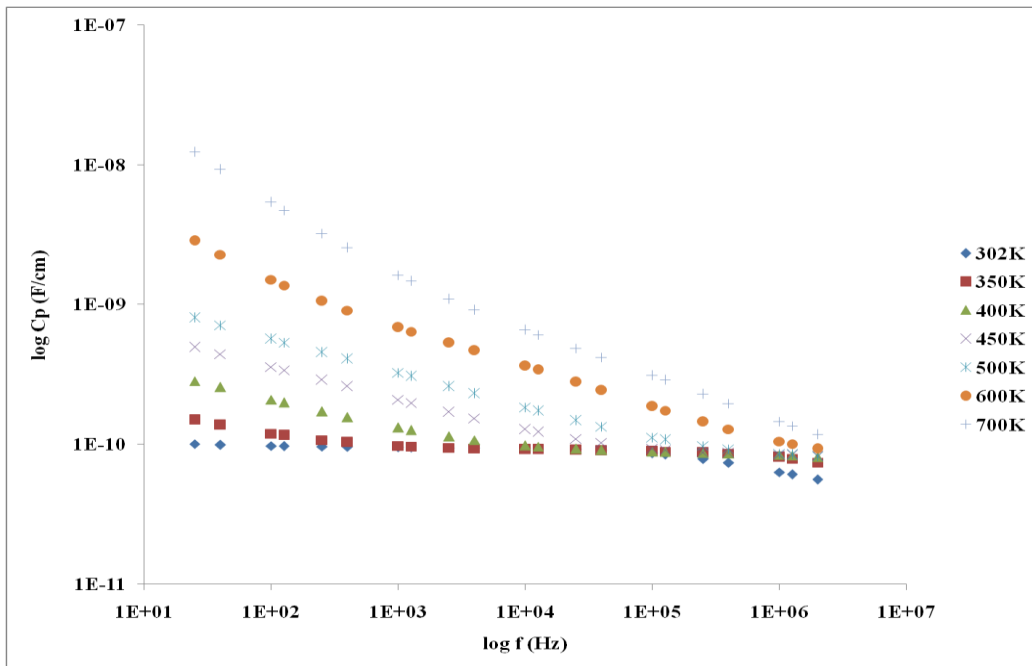


Figure 5.12: C_p vs. Frequency at different temperatures of $\text{La}_{0.2}\text{Sr}_{0.6}\text{Ca}_{0.1}\text{TiO}_3$ at high temperatures.

At high temperatures, the plateaus seen earlier are not present here. As the figure above indicates, it is obvious that the grain boundaries are dominating the behaviour of this material; at high temperatures; as it can be seen that the low frequency part of the capacitance is changing significantly with temperature. This may be related to the high relative density of these materials; e.g. > 92%; which limit all processes to the grain boundaries at the temperatures explored here. The increase in the capacitance with temperature can also be linked to the decreased resistance of the bulk of the material giving rise to the domination of grain boundaries. Also, as we've seen in chapter 3, it is very likely that these compositions adopt the ideal cubic perovskite structure at different temperatures corresponding to different calcium content. The samples with low calcium content, as the one above, were found to have very small distortion; i.e. small octahedral tilts. However, it seems like the processes involved here are of an electrical nature.

The conclusion that the grain boundaries are dominating the behaviour of this type of titanates is consistent with the measurements of the DC conductivity and the nature of the electronic conductivity of this system. In the results of chapter 4, it was found that in order to access more Ti^{4+} within the bulk of the material, higher reduction temperatures were needed; since it was assumed that a maximum conductivity for a in-situ re-reduced sample was not matching the conductivity of the pre-reduced at 1050°C because as the grains surface is reduced it becomes harder to reduce the bulk if the material was oxidised.

The temperature dependence of the capacitance of the second sample with $x = 0.2$ is shown in figure 5.13; to see the effect of increasing calcium content.

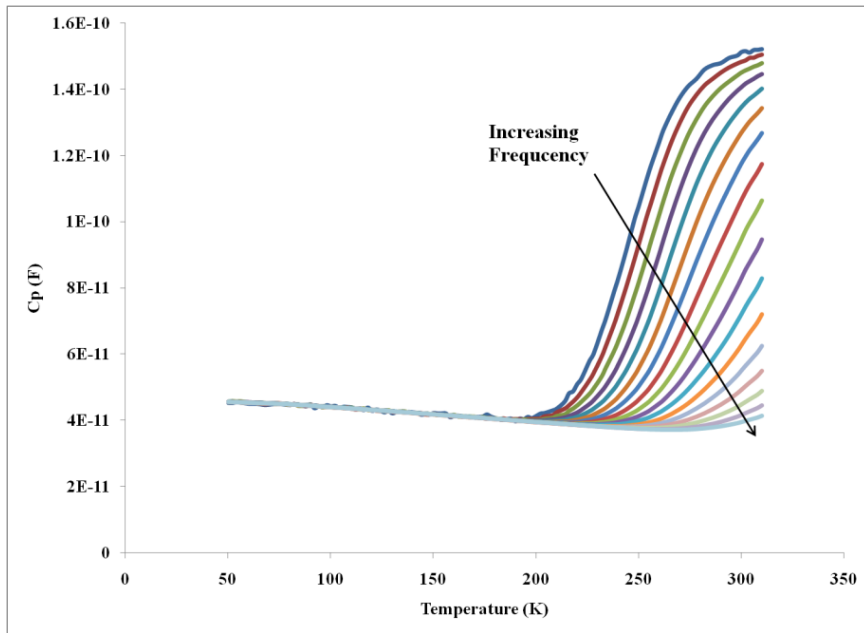


Figure 5.13: Temperature dependence of C_p at different frequencies for $\text{La}_{0.2}\text{Sr}_{0.5}\text{Ca}_{0.2}\text{TiO}_3$ at sub-ambient temperatures.

The dielectric loss of $\text{La}_{0.2}\text{Sr}_{0.5}\text{Ca}_{0.2}\text{TiO}_3$ is shown in figure 5.14 as a function of temperature.

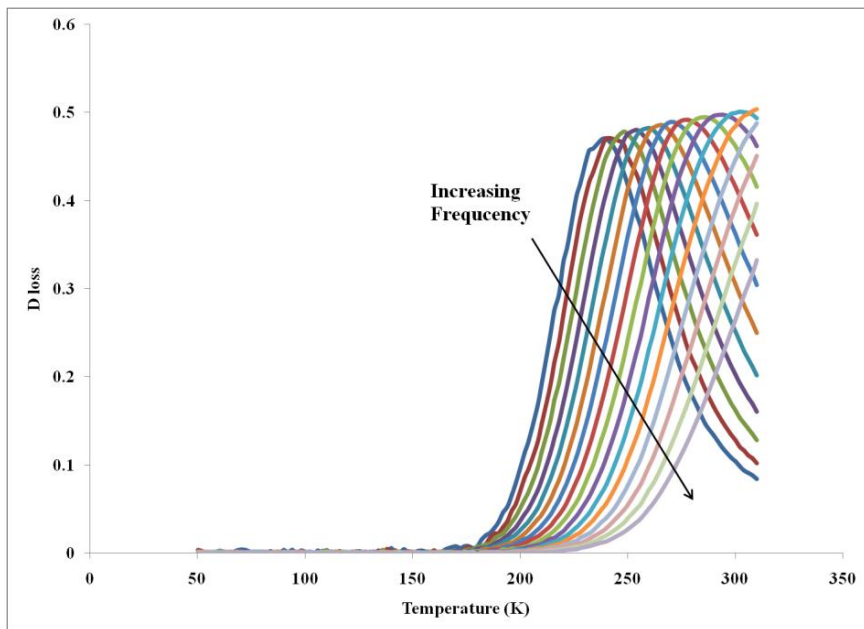


Figure 5.14: Dielectric loss of $\text{La}_{0.2}\text{Sr}_{0.5}\text{Ca}_{0.2}\text{TiO}_3$ at different frequencies as a function of temperature.

The response of the capacitance and the dielectric loss in $\text{La}_{0.2}\text{Sr}_{0.5}\text{Ca}_{0.2}\text{TiO}_3$ are similar to the previous compositions but the responses seem to start at higher temperatures. Another aspect that was noticed is with more calcium, the capacitance decreased; indicating a smaller dielectric constant. The decrease in capacitance was more pronounced with the composition $\text{La}_{0.2}\text{Sr}_{0.4}\text{Ca}_{0.3}\text{TiO}_3$ ($x=0.3$); the obtained C_p is plotted against temperature in figure 5.15.

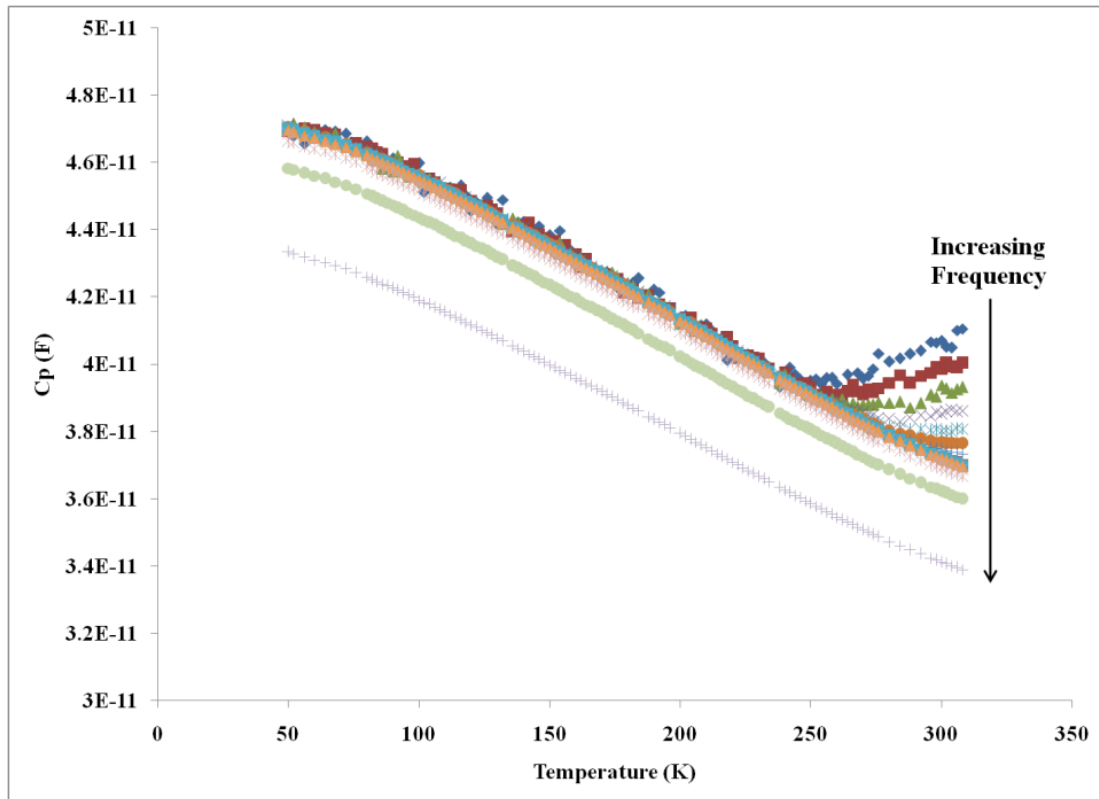


Figure 5.15: Temperature dependence of capacity (C_p) at different frequencies for $\text{La}_{0.2}\text{Sr}_{0.4}\text{Ca}_{0.3}\text{TiO}_3$ at sub-ambient temperatures.

In figure 5.15, it can be seen that for most of the sub-ambient temperature range of the measurement the capacitance show very small frequency and temperature dependence; indicating a very stable phase. Figure 5.16 and 5.17 show the capacitance of the three different samples measured at low and high temperature respectively.

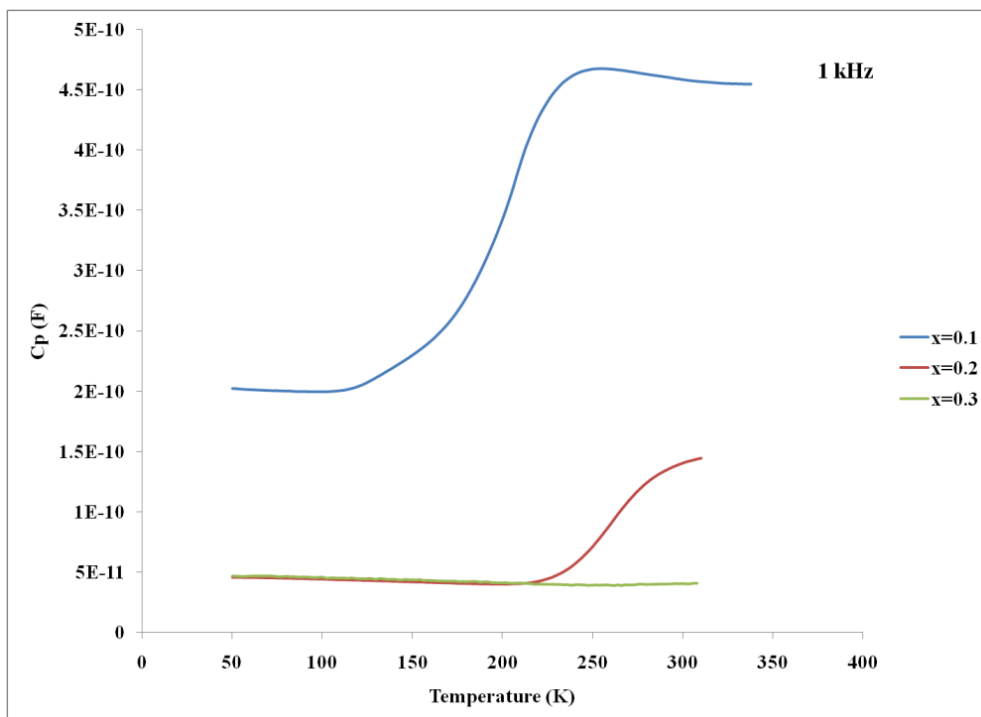


Figure 5.16: Measured capacity of samples of $\text{La}_{0.2}\text{Sr}_{0.7-x}\text{Ca}_x\text{TiO}_3$ at sub-ambient temperatures at 1 kHz.

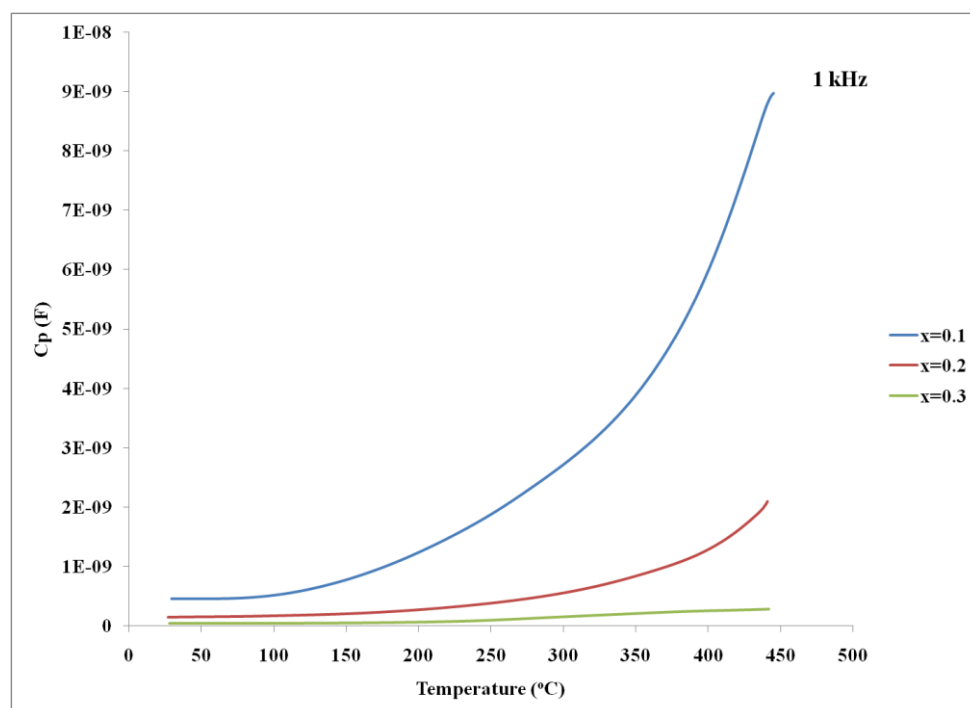


Figure 5.17: Capacity of samples of $\text{La}_{0.2}\text{Sr}_{0.7-x}\text{Ca}_x\text{TiO}_3$ at high temperatures at 1 kHz.

From the previous two figures, it can be seen that with more calcium content, the capacitance decreases in magnitude at different temperatures. The dielectric constant of some samples studied in this work is plotted as a function of temperature in figure 5.18.

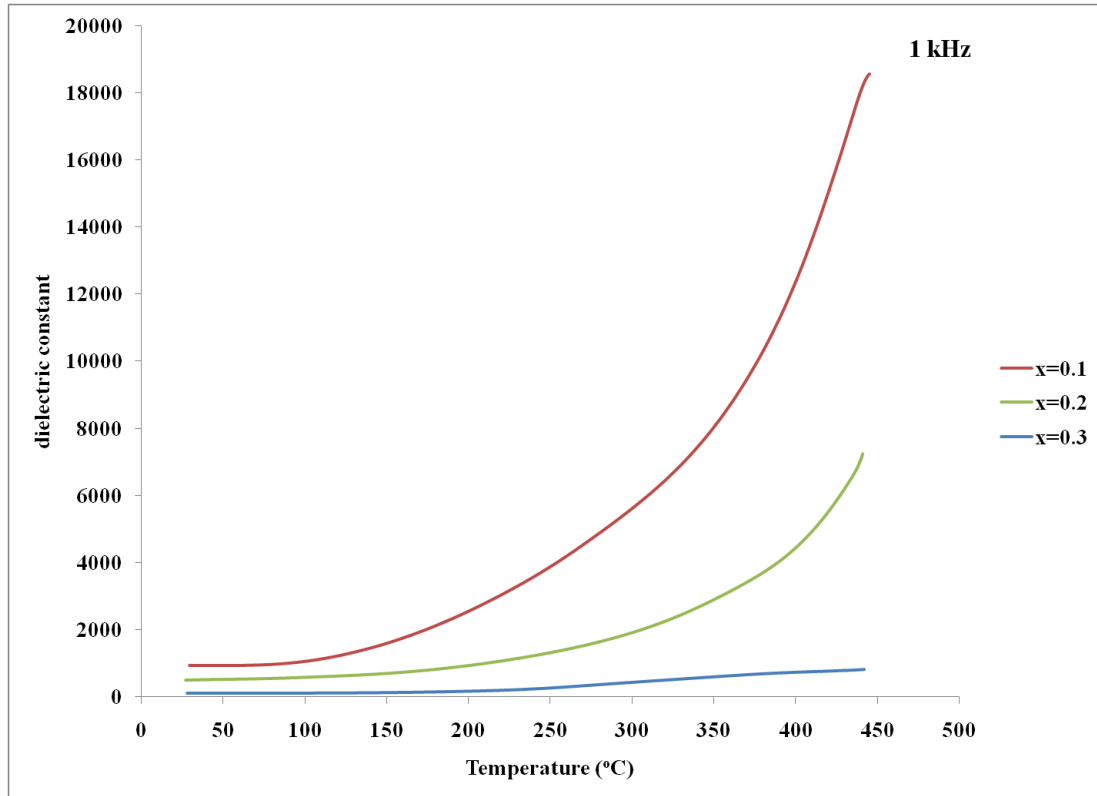


Figure 5.18: Dielectric constant of different samples of the system $\text{La}_{0.2}\text{Sr}_{0.7-x}\text{Ca}_x\text{TiO}_3$ measured at 1 kHz.

The dielectric constant of the composition with nominal $x = 0.1$ showed the highest response to temperature and the highest value. All samples showed a non-linear increase of the dielectric constant with temperature. The results above also indicate no phase changes that take place upon heating to temperatures below 450°C. The high temperature studies in chapter 3; revealed that the calcium rich compositions of $\text{La}_{0.2}\text{Sr}_{0.7-x}\text{Ca}_x\text{TiO}_3$ showed a transition to the ideal cubic symmetry at 900°C; well below the range of the measurements conducted here. This led to the expectation that

the I4/mcm symmetry; of the strontium rich compositions; is stable up to 450°C and the transition to the cubic phase may take place at temperatures below 900°C. The response and the magnitude of the dielectric constant decreased significantly with increasing calcium content; which can be related to changes in the electrical nature of the samples. At sub-ambient temperatures, the behaviour of the dielectric loss for $\text{La}_{0.2}\text{Sr}_{0.6}\text{Ca}_{0.1}\text{TiO}_3$, as mentioned before, is similar to CCTO which represented a Maxwell-Wagner relaxation.[5,8] Figure 5.19 shows the behaviour of both the dielectric constant and the loss for $\text{La}_{0.2}\text{Sr}_{0.6}\text{Ca}_{0.1}\text{TiO}_3$ on the same plot.

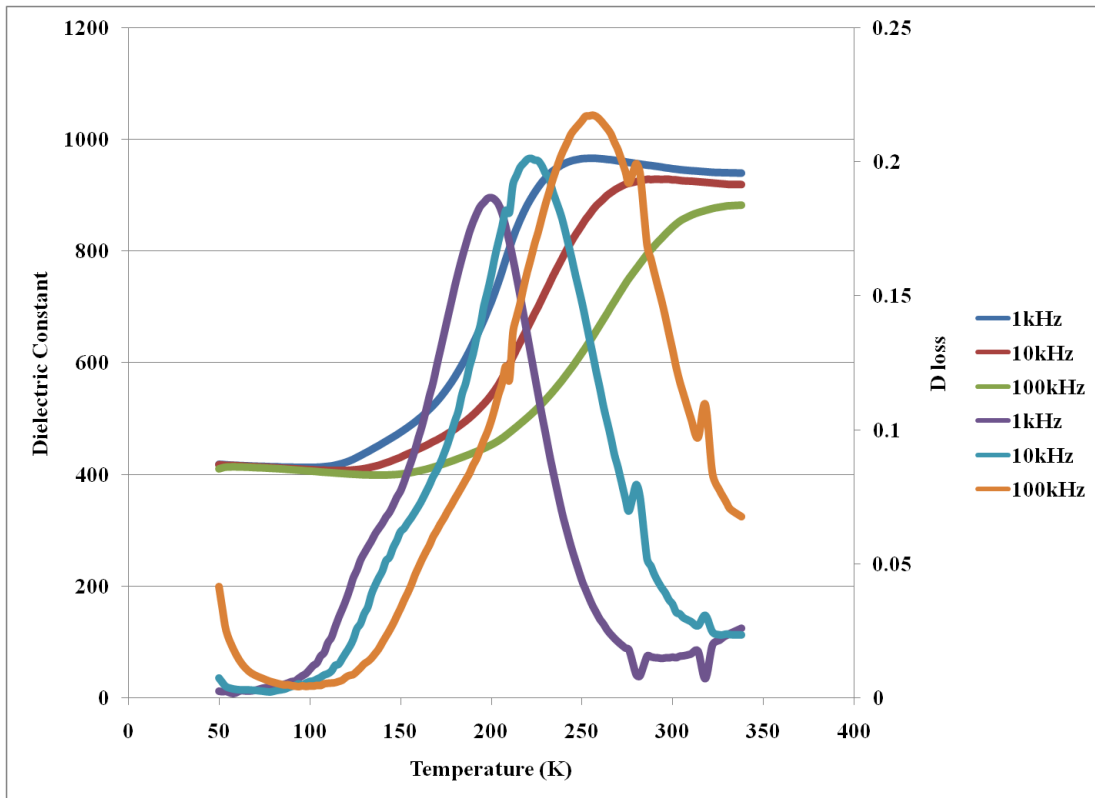


Figure 5.19: Dielectric constant and dielectric loss plotted against temperature for



A Maxwell-Wagner model suggests that the samples are electrically inhomogeneous[9]; which is understandable when the system $\text{La}_{0.2}\text{Sr}_{0.7-x}\text{Ca}_x\text{TiO}_3$ is slightly

reduced/oxidised which generates different layers that show either n-type or p-type behaviour, respectively. The A-site deficiency and calcium introduction are methods employed here to improve the electrical conductivity of this material. This was obvious in this chapter; since the capacitance decreased with more calcium content at different temperatures. The samples here showed an opposite behaviour to CaTiO_3 and SrTiO_3 ; where the dielectric constant increased at lower temperatures, indicating an incipient ferroelectricity or a quantum paraelectricity.[10] Overall, the results here confirmed the structural analysis conducted earlier on different samples of the system $\text{La}_{0.2}\text{Sr}_{0.7-x}\text{Ca}_x\text{TiO}_3$ and showed phase stability at high temperatures.

5.3 - Conclusions

The results presented in this chapter clearly show that the studied samples of the system $\text{La}_{0.2}\text{Sr}_{0.7-x}\text{Ca}_x\text{TiO}_3$ did not show any ferroelectric characteristics through a wide range of temperatures. This proves that the system does not adopt any non-centrosymmetric structures which are associated with ferroelectric behaviour. The results present here also show that there are only two types of distortions as was concluded in chapter 3; i.e. distortions and tilting of the octahedra; and there is no atomic displacement of the B-site titanium. A Maxwell-Wagner relaxation resemblance was noticed for some of the samples studied here, with the highest dielectric constant measured for the sample with $x = 0.1$. The dielectric constant decreased with increasing calcium content; indicating increasing concentrations of charge carriers.

5.4 - References

- [1] M. A. Carpenter, S. Rios, P. Sondergeld, W. Crichton and P. Bouvier, *J. Solid State Chem.*, 2007, **180**, 360-369.
- [2] J. Manchado, F. J. Romero, M. C. Gallardo, J. del Cerro, T. W. Darling, P. A. Taylor, A. Buckley and M. A. Carpenter, *J. Phys-Condens. Mat.*, 2009, **21**, 295903.
- [3] M. B. Smith, K. Page, T. Siegrist, P. L. Redmond, E. C. Walter, R. Seshadri, L. E. Brus and M. L. Steigerwald, *J. Am. Chem. Soc.*, 2008, **130**, 6955-6963.
- [4] F. D. Morrison, D. C. Sinclair and A. R. West, *J. Am. Ceram. Soc.*, 2001, **84**, 531-538.
- [5] A. P. Ramirez, M. A. Subramanian, M. Gardel, G. Blumberg, D. Li, T. Vogt and S. M. Shapiro, *Solid State Commun.*, 2000, **115**, 217-220.
- [6] R. Zuo, S. Su, Y. Wu, J. Fu, M. Wang and L. Li, *Mater. Chem. Phys.*, 2008, **110**, 311-315.
- [7] C. Elissalde and J. Ravez, *J. Mater. Chem.*, 2001, **11**, 1957-1967.
- [8] M. A. Subramanian, D. Li, N. Duan, B. A. Reisner and A. W. Sleight, *J. Solid State Chem.*, 2000, **151**, 323-325.
- [9] J. Liu, C. Duan, W. Yin, W. N. Mei, R. W. Smith and J. R. Hardy, *Phys. Rev. B*, 2004, **70**, 144106.
- [10] V. V. Lemanov, A. V. Sotnikov, E. P. Smirnova, M. Weihnacht and R. Kunze, *Solid State Commun.*, 1999, **110**, 611-614.
- [11] A. R. West, D. C. Sinclair and N. Hirose, *J. Electroceram.*, 1997, **1**, 65-71.
- [12] A. R. West, T. B. Adams, F. D. Morrison and D. C. Sinclair, *J. Euro. Ceram. Soc.*, 2004, **24**, 1439-1448.

Chapter 6

Development and Implementation of a Novel Simultaneous TGA/DC Conductivity Analysis Instrument

Abstract

An existing TGA instrument was transformed in order to provide DC conductivity measurement in controlled atmosphere and temperature environment. The original sample pan of the TA Instruments SDT2960 was transformed to accommodate a pellet of the chosen sample to measure its weight change and conductivity simultaneously. Measurements were made on different samples of $\text{La}_{0.2}\text{Sr}_{0.25}\text{Ca}_{0.45}\text{TiO}_3$ that proved the concept and successfully showed an overlap between weight change and conductivity response upon reduction and oxidation at a fixed temperature. It was also possible to measure the oxygen diffusion coefficient using the conductivity relaxation method and the mass change rates which showed a very good agreement. The diffusion coefficient was higher for porous samples.

6.1 - Introduction

Many of the advances in modern technologies are traced back to the outcomes of material research. By understanding the different physical and chemical properties of different compounds; scientists can produce materials that end up advancing and improving many different aspects of our daily lives. Advances in semiconductors, for example, that led to improving data processing, telecommunications, electronics and many other applications all have originated from the better understanding of how matter behaves and what affect its different properties. Through material science or material research, scientists are continuously finding better techniques in making alternative materials that ultimately make things more efficient, reliable, robust and finally to reduce the cost of the end product. Thus, by linking how the structure of a material affects its properties and how this structure can be controlled through different synthesis and processing methods; this scientific discipline is quite important and indeed beneficial on a large scale.

There are many techniques that material scientists rely on that to expand their understanding of materials from the atomic and molecular stage to the macroscopic behaviour and properties. X-ray and neutron diffraction are widely used to characterise the atomic arrangement of different materials as well as to check the purity of synthesised samples. Other techniques include scanning and transmission electron microscopy, electron diffraction, spectroscopy and thermal analysis.

Thermal analysis is a wide discipline in material science that covers a wide range of techniques. They include differential scanning calorimetry(DSC), differential thermal analysis (DTA), dielectric thermal analysis (DETA), dilatometry, dynamic

mechanical analysis (DMA), Thermogravimetric analysis (TGA) and many more.[1,2] Of the many techniques, TGA is an important method when it comes to studying materials behaviour and changes with temperature.

One of the most technologies that rely on thermal analysis is the search for alternative materials for solid oxide fuel cells (SOFCs). Since these cells are usually operated at temperatures higher than 600°C, this puts a huge strain on the components of a typical fuel cell.[3] Elevated temperatures can affect the lifetime of a fuel cell through degradation of its components as well as chemical and physical instability. A ceramic based anode material must be electrically conductive at high temperatures and many of these undergo structural and chemical changes that affect their conductivity. TGA can give a better insight into the physical and chemical stability of an anode material at high temperatures as well as to the electrochemical processes that govern its conductivity and overall catalytic activity. Thus it is obvious that both properties; i.e. the mass change and electrical conductivity; are important in determining the suitability of a material to be a component of a fuel cell. In most cases, TGA and electrical conductivity results are reported separately. Almost all TGA studies are conducted on samples in powder form within a crucible. On the other hand, electrical conductivity of different materials is usually measured on bars or pellets of the same material. To some extent this is tolerable depending on the level of care in conducting the experiments and the analysis of the different data to correlate them.

Many researchers are targeting materials that show both ionic and electronic conductivity; i.e. mixed ionic electronic conductor (MIEC); to employ them usually as electrodes to extend the triple phase boundary (TPB) of the electrochemical reaction in a fuel cell. It is usually difficult to determine the contribution of the ionic conductivity

to the total conductivity.[4,23] A very important parameter is used to compare between different MIEC materials, this parameter is the chemical diffusion coefficient.[5,6,7] It provides a quantitative measure of the type of defects that control both types of conductivity and their mobility and concentrations. There are many methods that can be used to measure the oxygen diffusion namely oxygen permeation, oxygen ionic relaxation, isotope exchange using secondary ion mass spectrometry (SIMS), electronic blocking electrodes and electrical conductivity relaxation.[8,9] The electrical conductivity relaxation method is widely used to measure the diffusion coefficient of oxygen which determines the ionic conductivity and other parameters as explained in the theory section of this chapter. Usually this technique is accompanied by a TGA analysis to determine the oxygen stoichiometry in MIEC materials. Thus it is very obvious that there is a great potential of combining conductivity relaxation measurement with a simultaneous thermogravimetric analysis (TGA) in one setup to better understand the electrochemistry of such materials.

Hence, we are presenting a novel analysis technique that combines TGA with a simultaneous measurement of DC conductivity of solid materials in controlled temperature and oxygen partial pressure settings.

6.2 - Theory

6.2.1 - Thermogravimetric Analysis

Among the many techniques employed by chemists to quantify materials properties is the thermogravimetric analysis (TGA). It is defined as the monitoring of mass change of a substance measured as a function of temperature at a controlled temperature programme.[10] A typical TGA device records the mass change of a sample as a function of temperature as the sample is heated or cooled in a controlled atmosphere usually provided with certain gas purging. Also, mass changes can occur when the environment surrounding the sample is changed; i.e. by switching between different purge gasses at a fixed temperature; and mass is recorded as a function of time. TGA is very useful in studying the volatility, stability, water content, oxidation and lifetime of different materials.

6.2.2 DC Conductivity Measurement

Measuring the conductivity of a material is very important in many scientific and industrial fields. The resistance of a sample (R) is given by Ohm's law:

$$R = \frac{V}{I} \quad (6.1)$$

Where V is the voltage measured when the sample is subjected to a current I. While the resistance of a sample can be easily measured, it does not present a specific property for the material under test. The resistivity of a material is on the other hand specific and depends on the structure and composition of a sample. Resistivity can be obtained from the resistance of a sample under a constant current; however it requires a correction factor for the geometry of the sample.

The resistivity of a wire for example is given by:

$$\rho = \frac{RA}{l} \quad (6.2)$$

Where A is the cross section area of the wire and l is its length as shown in figure 6.1.

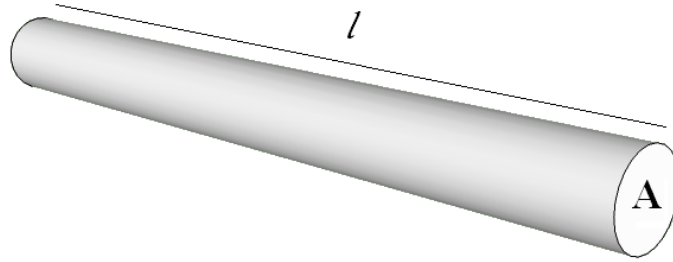


Figure 6.1: The geometry of a wire.

Conductivity is simply the inverse of the resistivity of a substance:

$$\sigma = \frac{1}{\rho} \quad (6.3)$$

The most common techniques that are used to measure the conductivity of solids are the 4-point probe technique and the van der Pauw technique which are explained in the next few pages.

6.2.2.1 - The 4-point Probe DC Conductivity Technique

This technique is based on using four finite probes to measure the resistance across the surface of a sample. The typical arrangement of the technique is shown in figure 6.2. Four probes are equally separated from each other, where two probes supply the current and the other two are used to measure the voltage generated across the sample.

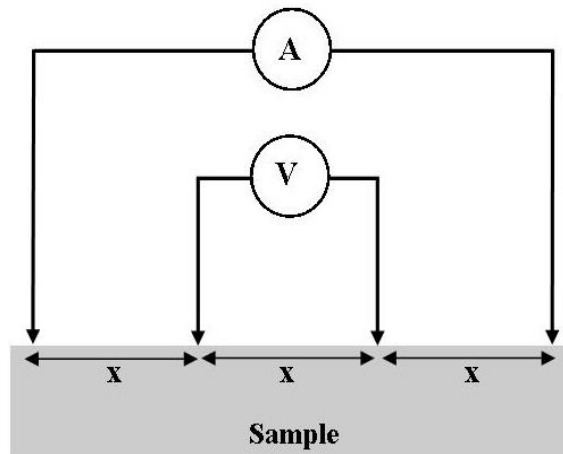


Figure 6.2: Typical arrangement of the 4-point DC conductivity measurement technique.

The resistivity of the material can be found by using:

$$\rho = 2\pi x F \frac{V}{I} \quad (6.4)$$

The F factor is a correction factor that includes multiple correction factors for probe location, sample thickness, sample diameter, probe separation and the sample temperature.[11] A discussion of the different correction factors can be found in reference [12].

6.2.2.2 - The van der Pauw (vdP) Technique

Measuring the conductivity of a solid sample usually imposes high degree of symmetry and precision in the shape of the sample. This is not ideal in many cases since it is very difficult to provide such geometries. The vdP technique makes it possible to measure the resistivity; hence the conductivity; of arbitrary shaped samples.[13,14]

L. J. van der Pauw has shown that a correction factor for the geometry of a sample is not necessary to measure the resistivity. An arbitrary shaped sample resistivity can be

measured given that the contacts are sufficiently small and are on the circumference of the sample. Also, the sample is homogeneous in thickness and the surface is singly connected; i.e. a homogenous material.[15]

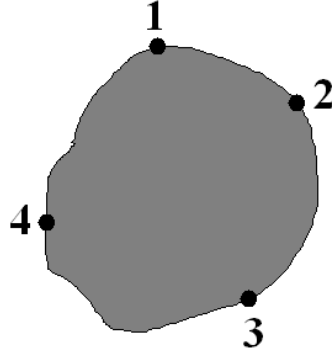


Figure 6.3: Contacts arrangement for an arbitrary shaped sample.

For an arbitrary shaped sample as the one shown in figure 6.3; the resistivity can be deduced from:

$$\rho = \frac{\pi d}{\ln 2} \left(\frac{R_1 + R_2}{2} \right) f \left(\frac{R_1}{R_2} \right) \quad (6.5)$$

With

$$R_1 = \frac{V_{3,4}}{I_{1,2}} \quad \text{and} \quad R_2 = \frac{V_{1,4}}{I_{2,3}}$$

The subscripts of V and I represents the corresponding contact numbers in figure 3. The function $f \left(\frac{R_1}{R_2} \right)$ should satisfy the relation:

$$\cosh \left(\left[\frac{\frac{R_1}{R_2} - 1}{\frac{R_1}{R_2} + 1} \right] \frac{\ln 2}{f} \right) = \frac{1}{2} e^{\frac{\ln 2}{f}} \quad (6)$$

For a uniform disk with four contacts at 90° intervals on the circumference and $R_1 = R_2$, equation 5 reduces to:

$$\rho = \frac{\pi d}{\ln 2} R \quad (6.7)$$

Where d is the thickness of the disk.[13] This shows that the conductivity can be easily deduced from a single resistance measurement for a uniform disk/pellet of thickness d . Also, no switching is needed as proven by Kasl and Hoch[13]; who also showed that by having the contacts across the edges of a thick pellet, the accuracy of the van der Pauw technique increases.

Thus, the van der Pauw technique is much simpler to use since it is much easier to make pellets from solid state reactions and the placement of contacts will be simpler than with the 4-point technique.

6.2.3 - Oxygen Sensor

In order to determine the partial pressure of oxygen for the surroundings of samples, a YSZ based oxygen sensor was used. A general representation of such a sensor is shown in figure 6.4.

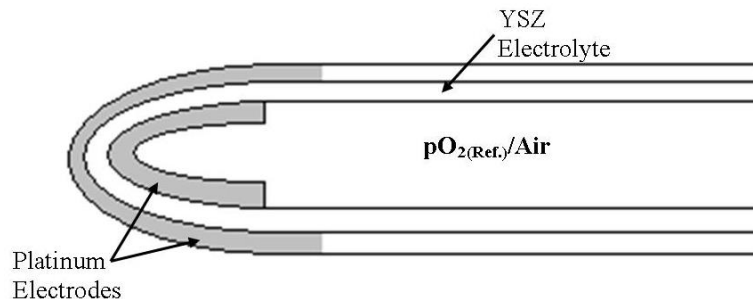


Figure 6.4: Typical YSZ based oxygen sensor.

The oxygen partial pressure of an enclosure can be determined using Nernst equation:

$$V = \frac{RT}{4F} \ln \left(\frac{pO_2}{pO_{2ref}} \right) \quad (6.8)$$

Where R is the gas constant, T is the temperature in Kelvin and F is Faraday's constant.[16] In most cases the inside of such a sensor is exposed to the ambient air where the oxygen partial pressure is $pO_{2ref} = 21\%$.

6.2.4 - Oxygen Chemical Diffusion Coefficient

The ionic conductivity of an oxide is mainly governed by the concentration of two type of defects; i.e. oxygen vacancies and interstitial oxygen ions.[17] The ionic conductivity can be calculated using the Nernst-Einstein equation:

$$\sigma = \frac{z^2 F^2 D_O^* C_O}{RT} \quad (6.9)$$

Where zF is the electrical charge of an oxygen mole, D_o^* is the tracer self-diffusion coefficient, C_O is the concentration of oxygen, R is the gas constant and T is the absolute temperature.[7] If the ionic conductivity of an oxide increases with increasing oxygen partial pressure then the controlling defect will be the interstitial oxygen instead of oxygen vacancies; since the latter concentration will be smaller. The measurement of the ionic conductivity is not simple. Thus, many rely on measuring the oxygen tracer diffusion coefficient using the isotope exchange technique.[18,19] The tracer self diffusion coefficient D^* is related to the chemical diffusion coefficient D through the relation:

$$D \approx \gamma \times D^* \quad (6.10)$$

Where γ is a thermodynamic factor that can be obtained using TGA according to the relation:

$$\gamma = \frac{1}{2RT} \times \frac{\partial(\mu_{O_2})}{\partial \ln C_O} = \frac{1}{2} \times \frac{\partial \ln p_{O_2}}{\partial \ln C_O} \quad (6.11)$$

Where μ_{O_2} is oxygen chemical potential and p_{O_2} is the oxygen partial pressure.[7]

Many researchers indicated that the chemical diffusion coefficient can be obtained using the electric conductivity relaxation method. This method involves changing the oxygen partial pressure abruptly in the surroundings of a sample; while monitoring the change in the conductivity.[17,19] It is known that the sensitivity of conductivity to changes in oxygen partial pressure is much higher than other properties; e.g. weight.[17]

The chemical diffusion coefficient is best described by Fick's second law of diffusion:

$$\frac{\partial C}{\partial t} = -D \frac{\partial^2 C}{\partial x^2} \quad (6.12)$$

Where C is the concentration of the diffusing element and D is the chemical diffusion coefficient. In the case of oxygen, the chemical diffusion coefficient gives a measure of the flux of oxygen ions in or out of a unit surface area of a sample in unit time; i.e. $\text{cm}^2 \cdot \text{s}^{-1}$. A solution to Fick's second law was provided by Crank[7,17,20], which relates the mass change to the diffusion coefficient. With appropriate boundary conditions the solution is

$$\frac{M_t}{M_\infty} = 1 - \sum_{n=0}^{\infty} \frac{8}{(2n+1)^2 \pi^2} \times \exp \left\{ - \frac{(2n+1)^2 \pi^2 D t}{L^2} \right\} \quad (6.13)$$

Here, M_t and M_∞ are the mass at time t and the mass at infinity after a relaxation transition. A similar analogy was made for the change in conductivity where the

normalized conductivity measured through the relaxation step is related to the above equation through:

$$\frac{\sigma_t - \sigma_1}{\sigma_\infty - \sigma_1} = 1 - \sum_{n=0}^{\infty} \frac{8}{(2n+1)^2 \pi^2} \times \exp \left\{ - \frac{(2n+1)^2 \pi^2 D t}{L^2} \right\} \quad (6.14)$$

Here σ_t is the apparent conductivity at time t , σ_1 is the initial conductivity and σ_∞ is the conductivity after reaching equilibrium.[7] Through least square fitting of the normalized conductivity, the diffusion coefficient can be deduced. Two different approximations were given by Maier[20] to better estimate the oxygen chemical diffusion coefficient during conductivity relaxation measurements. For small relaxation times, equation 6.14 reduces to the following:

$$\frac{\sigma_t - \sigma_1}{\sigma_\infty - \sigma_1} \approx \frac{4}{\pi^{3/2}} \sqrt{\frac{t}{\tau}} \quad (6.15)$$

Where for long relaxation times, a different normalisation gives the relation:

$$\frac{\sigma_t - \sigma_\infty}{\sigma_1 - \sigma_\infty} \approx \frac{8}{\pi^2} e^{-t/\tau} \quad (6.16)$$

Where in both cases:

$$\tau = \frac{L^2}{\pi^2 D} \quad (6.17)$$

Where τ can be estimated from the slope of the normalised conductivities during relaxation and L is the sample thickness in cm.[20] Using the above relations, for the first time a measure of the ionic conductivity of materials in one setting is possible through the use of the new setup developed in this work. Relaxation method and TGA can be performed simultaneously to give a precise determination of the oxygen

chemical diffusion coefficient, which then can be used to determine the tracer self diffusion coefficient using the thermodynamic factor obtained within the same run from the TGA side of the new system. This should give a better insight into the type of defects that control the total conductivity of different oxides and the overall electrochemical properties.

6.3 - The Instrument

6.3.1 - Introduction

The first step for developing a device that combines TGA and DC conductivity was to utilise an existing TGA instrument. The SDT2960, shown in figure 6.5, was a very good choice since its design for the balance arms and pans offered great degree of freedom for adding the needed contacts to measure the conductivity of samples.



Figure 6.5: Photograph of the SDT2960 used in this work.

Also, since the arms are oriented horizontally, see figure 6.6, within the furnace unit with extensions on the back to place counter weights, this proved useful in compensating for the added weight after using pellets with DC conductivity contacts; i.e. compared to powder samples. The SDT2960 is a unique TGA instrument which offers great features from a wide temperature range; i.e. room temperature to 1500°C; to a balance sensitivity of 0.1µg. Also, the design of this instrument's furnace gives better control in terms of temperature and atmosphere where the purge gas flows horizontally over the sample thus minimising the chimney effect.[21]

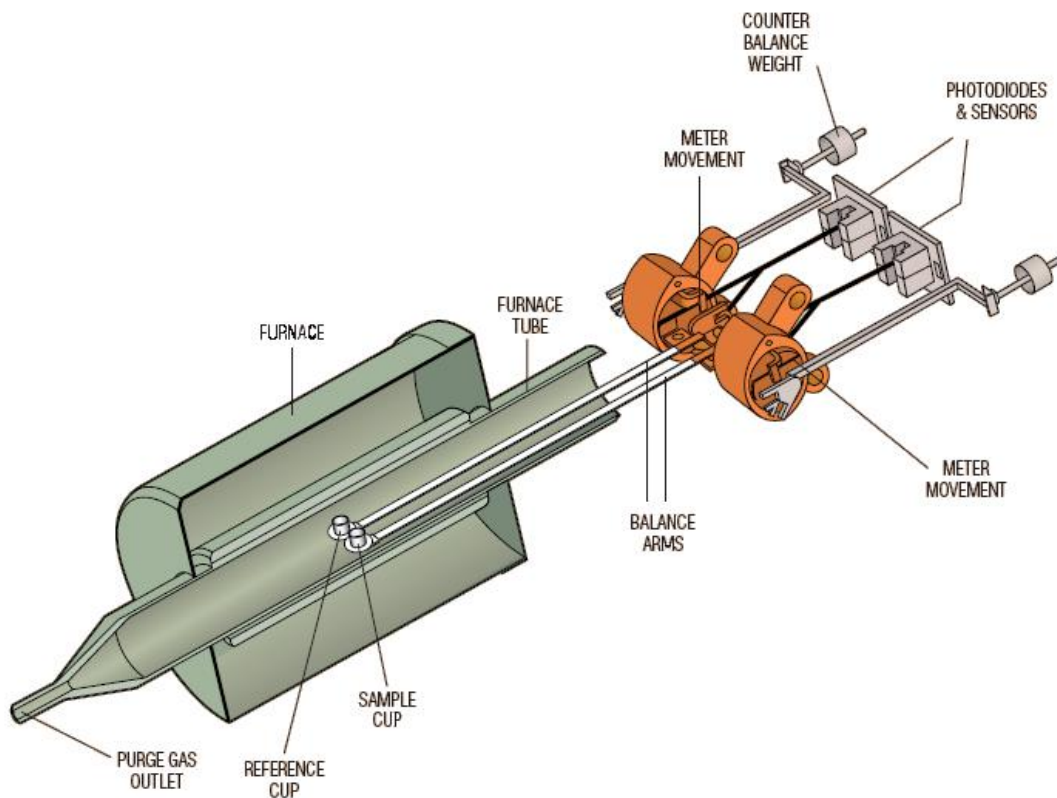


Figure 6.6: Schematic of the SDT2960 different components.[21]

Some of the SDT2960 specifications given by the manufacturer are listed in table 6.1, of which is the very good balance sensitivity which is important to study defect changes in materials; i.e. oxygen vacancies formation in this study.

Property	Specification
Temperature range	Ambient – 1500°C
Sample Capacity	200 mg
Balance sensitivity	0.1 µg
Maximum gas purge rate	1 litre/min
Data Collection Rate	0.5 to 1000 sec/point

Table 6.1: Specifications of the SDT2960.[21]

6.3.2 - Initial Issues with the SDT2960

The first step was to identify the fault that the SDT2960 was suffering from. The instrument kept generating an error signal due to unstable reference weight signal that originated from the second arm. Thus, as a first step, we tried to stabilise the reference arm by restricting its movement mechanically. This was done by placing two metal slabs above and below the metallic beam that extended towards the optical sensors on the back of the module; see figure 6.7.

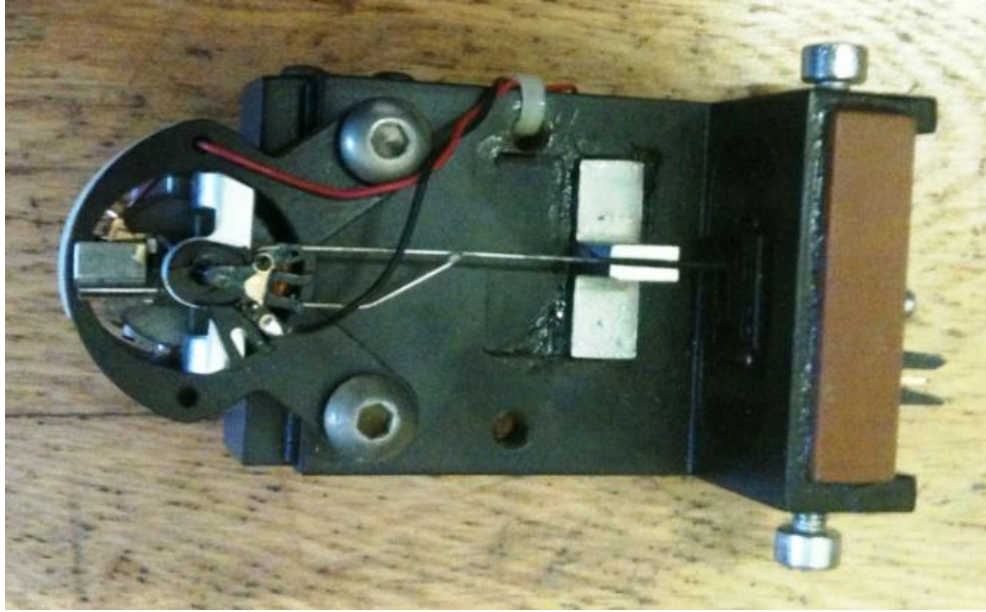


Figure 6.7: Weight meter module.

Using this approach proved to be ineffective in fixing the error. As a result, another approach was needed by looking into the internal electronics. After going through the different circuit diagrams it was concluded that the faulty signal from the reference arm was originating from the arithmetic electronics within the machine. The change in mass is monitored by the SDT2960 by measuring how much current is needed to bring back the arm to the zero position after a change had occurred. This current is fed to the coil surrounding a magnet. Thus, it was necessary to by-pass the whole reference circuit since it was very difficult to pinpoint the exact point that generated the wrong calculations. This was done by cutting the link between the reference arm and the data acquisition circuits which read the signal coming through as the reference weight. After physically cutting the link, see figure 6.8, and feeding it with the signal coming through from the sample arm; it was possible to start the machine without any errors generated.

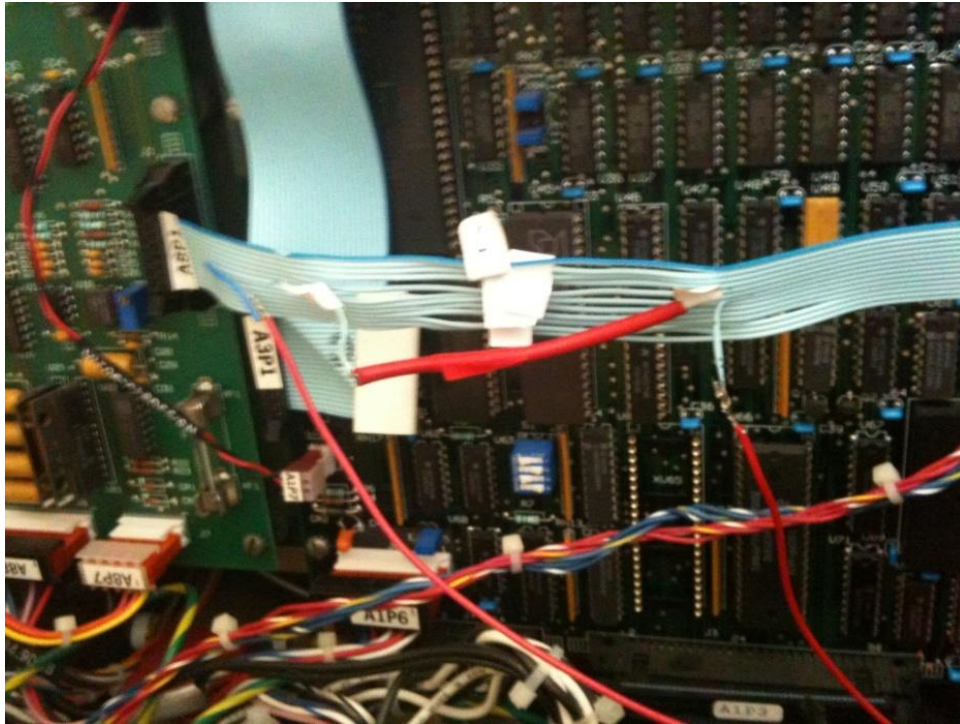


Figure 6.8: Image showing the by-passing of the reference weight signal.

This measure was found to be unsuitable since both ends, the sample and reference, were reading the same weight. Since the SDT2960 is continuously using the reference arm signal to correct for the sample weight; having both reading the same signal led to no weight change being detected. This was apparent after few runs where all plots had a straight line for the weight with temperature or time. Going back to the drawing board, it was necessary to determine the type of signal that was fed to the output terminal of the reference arm. By using an oscilloscope, it was found that the signal was in the form of a square wave and the weight value was set according to the frequency of this signal. A wave generator was then used to feed a fake signal to the SDT2960 in place of the original reference weight signal. By now, the instrument is reading a constant weight signal for the reference arm. This was a necessary measure to take in order to be able to operate the instrument and the furnace. By taking the reference arm out, an automated

correction mechanism was sacrificed and as a result the weight change of any sample will not be an absolute value. It was concluded that monitoring weight change in an isotherm that result from chemical changes to the material will be sufficient enough. Mainly, the machine will be used to monitor any weight changes that result during oxidation and/or reduction of the sample and correlate that to changes in electrical conductivity on a time scale at a fixed temperature.

Physically removing the reference weight module from the SDT2960 led to another fault that restricted the machine from operating normally. This was corrected by short circuiting two terminals on the plug which was connected to the module; as shown in figure 6.9. These two terminals are responsible for generating a signal that confirmed that the reference module was connected.



Figure 6.9: The plug of the reference module with the first two terminals short-circuited.

With all the previous steps, the SDT2960 was fixed and it was possible to start the furnace. Many runs were performed to test for the furnace operation and the whole

instrument prior to any measurements. By using an external thermocouple it was possible to check that the furnace controls were operating correctly in terms of ramp rates and set temperatures.

6.3.3 - Alterations to the SDT2960

In order to combine DC conductivity measurement with TGA, certain changes were necessary to the original instrument. Firstly, four new contacts were needed for supplying current and measuring the voltage generated across the sample. This meant that four new wires were needed around the sample pan. To minimise any disturbances to the weight measurement, the wires were inserted through a new multi-pore alumina tube. The tube had a diameter close to the original beam of the SDT2960. Also, the original sample pan was altered by removing the edges and cutting four grooves around the circumference to accommodate the new wires. The pan has a hole in the centre for a thermocouple which was suitable to give close measurement of the sample's temperature.

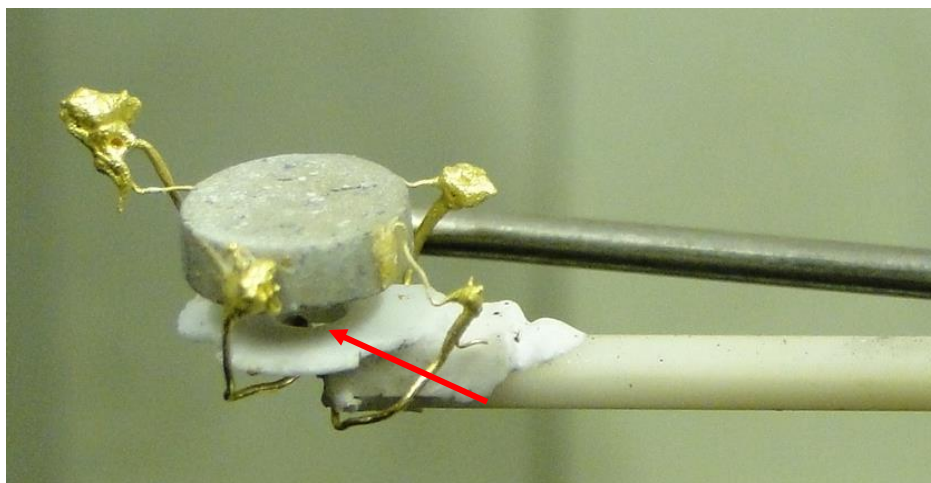


Figure 6.10: The new sample pan with a pellet connected and lifted to show the thermocouple location; as indicated by the red arrow.

All wires were fixed in place by using a ceramic based cement to make the whole assembly rigid and close up the holes within the new tube at both ends. Gold was used as the material of choice for the new wires; since platinum can be affected by hydrogen at high temperatures. On the other end, the wires were connected to different terminals on the connections board using very thin copper wires. This was adopted from the original setup which used thin wires to connect the thermocouples to the middle terminals. The use of thin wires is necessary to lower any tensions that can affect the weight sensitivity and accuracy.

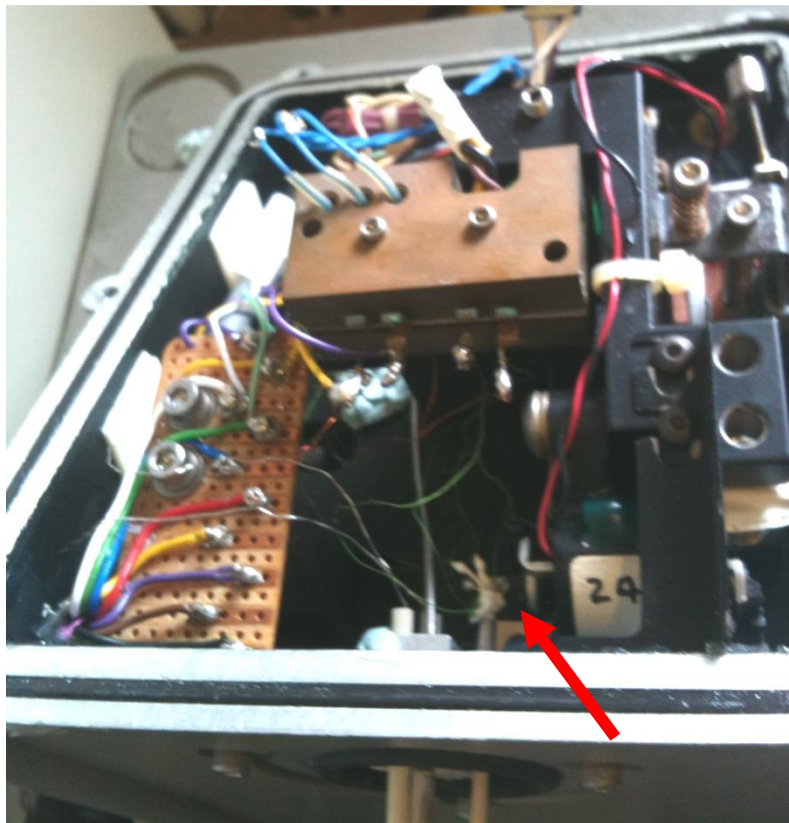


Figure 6.11: Image showing the inside of the meter housing. The arrow points at the tip of the sample arm connected with fine wires.

The added weight of the new sample arm was compensated by custom made stainless steel counter weights which were designed in the same manner as the original ones.

Multiple weights were made since the end user is expected to have different samples; e.g. pellets, bars, films...etc; thus different weights might be needed.

DC conductivity is a very useful technique and it is more useful if combined with a measure of oxygen partial pressure (pO_2). Thus, it was necessary to provide an oxygen sensor for the new jig. Since there was little space to work with, a small diameter thin YSZ tube was employed to be used as an oxygen sensor. The tube was painted with two electrodes on one tip by using platinum paste. The paste was fired at 900°C for at least 1 hour to burn any organic solvents and solidify the platinum electrodes. Thin platinum wires were attached to the electrodes, using more platinum paste and this was followed by firing at the same conditions.



Figure 6.12: The YSZ tube used (bottom) and the improvised pO_2 sensor (top).

Since the SDT2960 should be kept well sealed, and for the lack of space within the meters housing, the inside of the YSZ tube had to be kept at a constant oxygen partial pressure. This was done by using a buffer made out of a mixture of two different manganese oxides. Using a buffer is thought to maintain a fixed oxygen partial pressure within the zirconia tube.

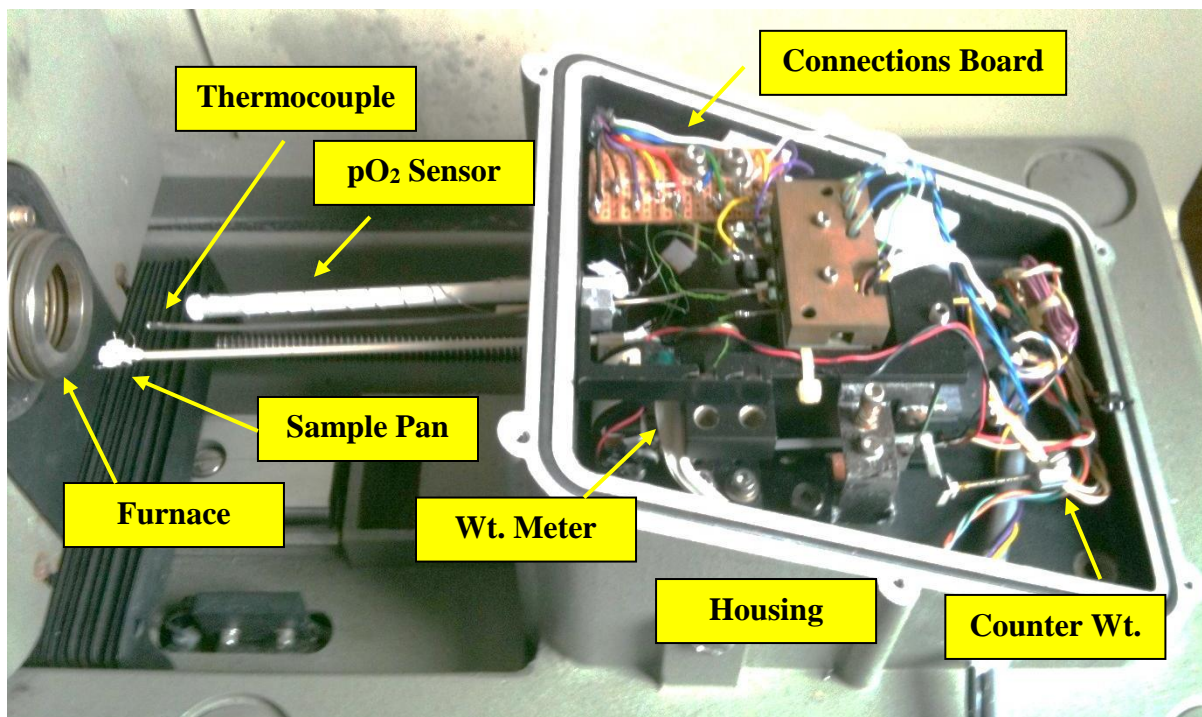


Figure 6.13: The new setup for the SDT2960.

The overall new setup is shown in figure 6.13. All fine wires were connected to the connection board that was fixed in the same harness that carried the old reference weight meter module. With 4 terminals for the conductivity of the sample measurement, 2 terminals for the pO_2 sensor and 4 others for the two thermocouples used in the setup; all signals were collected within a single cable that was taken out through a hole on the side of the housing.

A source meter (Keithley 2400) was used for the measurement of the conductivity, a digital multimeter (Schlumberger 7150 plus) for measuring the voltage across the pO_2 sensor electrodes and a multi-channel thermocouple data logger (PICO USB TC-08). Also, a wave generator (Global Specialties, 2001 Function Generator) was used to supply a fixed reference weight signal to the SDT2960.

6.3.4 - Control and Logging Programmes (Software)

Since the object of this work is to combine two techniques into one and due to restrictions imposed by copyrights it was necessary to design and use two separate programmes to control and monitor the new jig. The first software was the Thermal Advantage (Version 1.1A) by TA Instruments which is used to control the SDT2960 and log the weight signal of the sample. The second software was an in-house designed logging programme using the National Instruments LabVIEW developer suite (ver. 2010) software; which is in use by current conductivity measurement jigs; i.e. those were used to get the conductivity data outlined in chapter 4. For this work, the software used for the work shown in this chapter was called logTGA.

6.3.4.1 - Thermal Advantage

The main objectives of this software, shown in figure 6.14, are to control and programme the furnace of the SDT2960 and to log the weight and temperature of the sample as measured by the sample arm. As with any analytical instrument used in laboratories around the world, certain copyright restrictions prohibit the end user from being able to alter the controlling software or to communicate with the instrument externally using custom made software. We have tried to communicate and extract the relevant code externally. However, this attempt was not successful. Also, since the original manufacturer stopped supporting the SDT2960; given its old age compared to new instruments that are available; obtaining the original controls code was not possible. Thus, for the lack for any alternatives, a new version of the manufacturer control software was obtained which did work with the SDT2960.

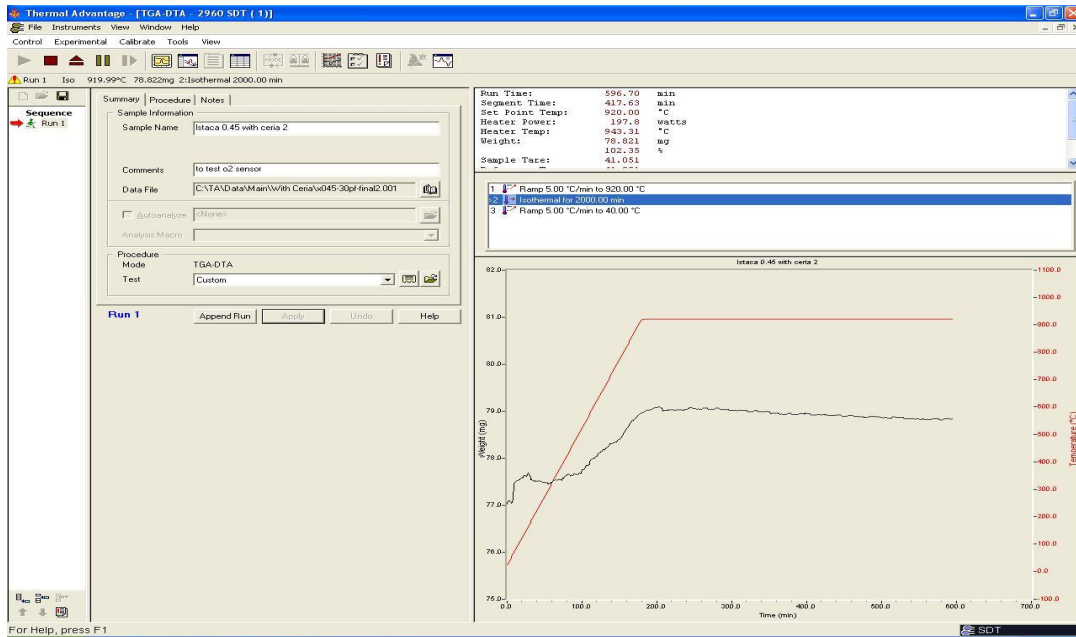


Figure 6.14: A screen capture of the main window of the Thermal Advantage programme.

6.3.4.2 - LogTGA

This programme is used to log all the signals that are relevant to measuring the conductivity of samples with respect to temperature, oxygen partial pressure and time.



Figure 6.15: A screen capture of the LogTGA programme.

The different parameters that were logged using the logTGA programme are shown in figure 6.16.

	A	B	C	D	E	F	G	H	I	J	K	L
1	time (sec)	current (A)	voltage (V)	conductivity (S/cm)	cond_factor	VpO2 (V)	CalcpO2	Log(pO2)	ref_pO2	pO2_temp (C)	sample_temp (C)	notes
2	0	4.61E-11	-0.000088	-4.55E-07	0.191	0.093661	7.29E-04	-3.137156	0.1525	540.747864	572.533081	5%H2
3	1	1.00E-05	-0.000092	-9.45E-02	0.191	0.093678	7.29E-04	-3.137347	0.1525	540.828491	572.57312	5%H2
4	3	1.00E-04	-0.000071	-1.22E+00	0.191	0.093693	7.29E-04	-3.13753	0.1525	540.894897	572.626343	5%H2
5	4	1.00E-03	0.000146	5.94E+00	0.191	0.093707	7.28E-04	-3.137647	0.1525	540.975342	572.69281	5%H2
6	6	1.00E-02	0.002326	3.72E+00	0.191	0.093727	7.28E-04	-3.137943	0.1525	541.045349	572.719482	5%H2
7	7	1.00E-01	0.024109	3.59E+00	0.191	0.093744	7.28E-04	-3.138125	0.1525	541.129089	572.825867	5%H2
8	8	1.00E-01	0.024157	3.58E+00	0.191	0.093757	7.27E-04	-3.138217	0.1525	541.209717	572.892395	5%H2
9	10	1.00E-01	0.024225	3.57E+00	0.191	0.093777	7.27E-04	-3.138493	0.1525	541.286682	572.97229	5%H2
10	11	1.00E-01	0.024288	3.56E+00	0.191	0.093804	7.26E-04	-3.138932	0.1525	541.367126	573.052124	5%H2
11	12	1.00E-01	0.024337	3.56E+00	0.191	0.093833	7.25E-04	-3.13943	0.1525	541.444214	573.118652	5%H2
12	14	1.00E-01	0.024369	3.55E+00	0.191	0.093862	7.25E-04	-3.139948	0.1525	541.51416	573.198547	5%H2
13	15	1.00E-01	0.024392	3.55E+00	0.191	0.093889	7.24E-04	-3.140397	0.1525	541.591125	573.304993	5%H2
14	17	1.00E-01	0.024407	3.55E+00	0.191	0.093917	7.23E-04	-3.14085	0.1525	541.675049	573.384766	5%H2
15	18	1.00E-01	0.024418	3.55E+00	0.191	0.093944	7.22E-04	-3.141289	0.1525	541.755493	573.504578	5%H2
16	19	1.00E-01	0.024424	3.54E+00	0.191	0.093971	7.22E-04	-3.141757	0.1525	541.8255	573.584351	5%H2
17	21	1.00E-01	0.024429	3.54E+00	0.191	0.094001	7.21E-04	-3.14227	0.1525	541.905945	573.664185	5%H2
18	22	1.00E-01	0.024434	3.54E+00	0.191	0.094029	7.20E-04	-3.142754	0.1525	541.979248	573.757202	5%H2
19	24	1.00E-01	0.024437	3.54E+00	0.191	0.094055	7.19E-04	-3.143167	0.1525	542.059692	573.850342	5%H2
20	25	1.00E-01	0.02444	3.54E+00	0.191	0.094081	7.18E-04	-3.14361	0.1525	542.129761	573.956848	5%H2
21	26	1.00E-01	0.024444	3.54E+00	0.191	0.094106	7.18E-04	-3.144069	0.1525	542.18573	574.036743	5%H2
22	28	1.00E-01	0.024445	3.54E+00	0.191	0.094128	7.17E-04	-3.144413	0.1525	542.255737	574.116577	5%H2
23	29	1.00E-01	0.024445	3.54E+00	0.191	0.094153	7.16E-04	-3.144801	0.1525	542.336365	574.236389	5%H2
24	30	1.00E-01	0.024447	3.54E+00	0.191	0.094171	7.16E-04	-3.145086	0.1525	542.392334	574.302917	5%H2
25	32	1.00E-01	0.02445	3.54E+00	0.191	0.094181	7.16E-04	-3.145163	0.1525	542.451843	574.395996	5%H2

Figure 6.16: Spreadsheet showing the different parameters logged by the LogTGA programme.

The LogTGA programme was designed in order to facilitate the measurement of DC conductivity using the two different techniques explained earlier; i.e. 4-point and vdP; which is mainly done by using a switch on the main screen while providing a correction factor or a thickness of the sample, respectively. The programme carries out the necessary calculations to give the final conductivity of the sample. Also, since the oxygen partial pressure inside the used pO₂ sensor is not known, an input field was set for inserting a reference pO₂ value by the user. Different controls are also included to control the experiment. The user can control the logging speed and set when the experiment should stop by giving a time frame in hours or minutes and if the temperature is below a certain value.

6.3.5 - Testing Phase

The first test that was performed for the new jig was that of the furnace. By using two thermocouples; i.e. the SDT2960 S-type and an R-type; it was possible to confirm that the furnace was in a good operational order. The furnace was given a step programme with a ramp rate of 5°C/min with different set isotherms.

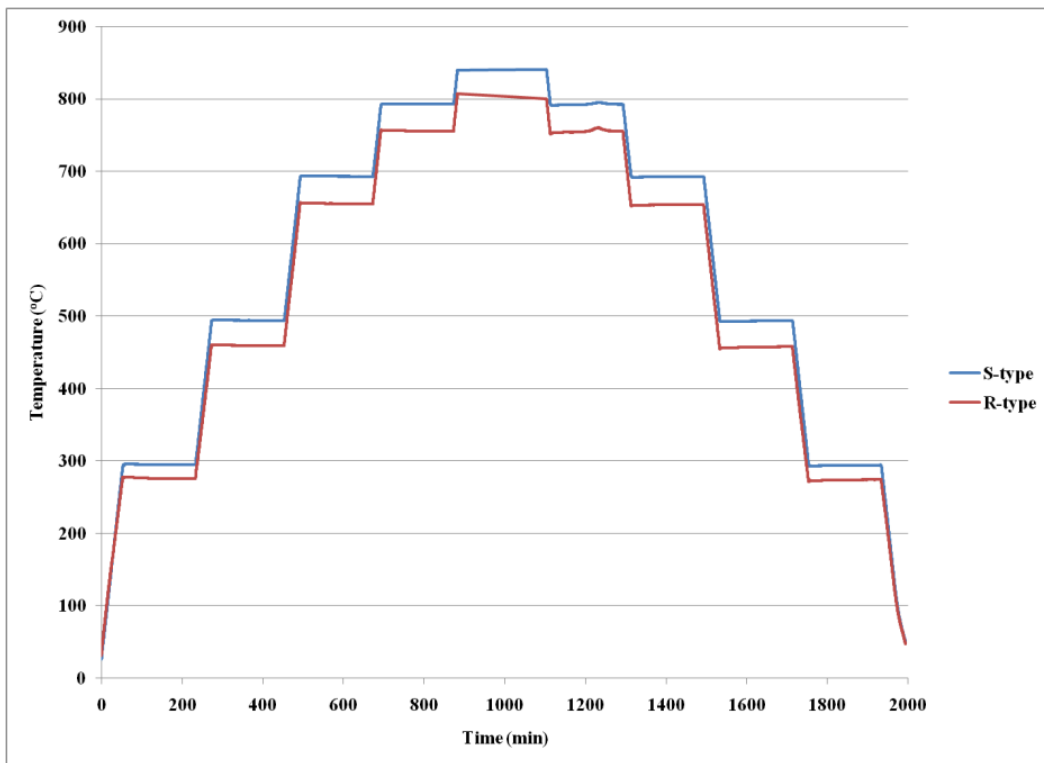


Figure 6.17: Profile of the temperature programme as measured by two different thermocouples.

The first result, shown in figure 6.17, proved that the SDT2960 furnace followed the given programme. Both readings were logged using the logTGA programme using the external circuit. The R-type reading is lower because it was placed slightly away from where the sample pan was positioned within the furnace. Most importantly, the ramp rate was followed exactly as was given and the isotherms were kept for the given

periods of time. A comparison between the temperature read by the SDT2960 and the R-type thermocouple through the external circuit is shown in figure 6.18.

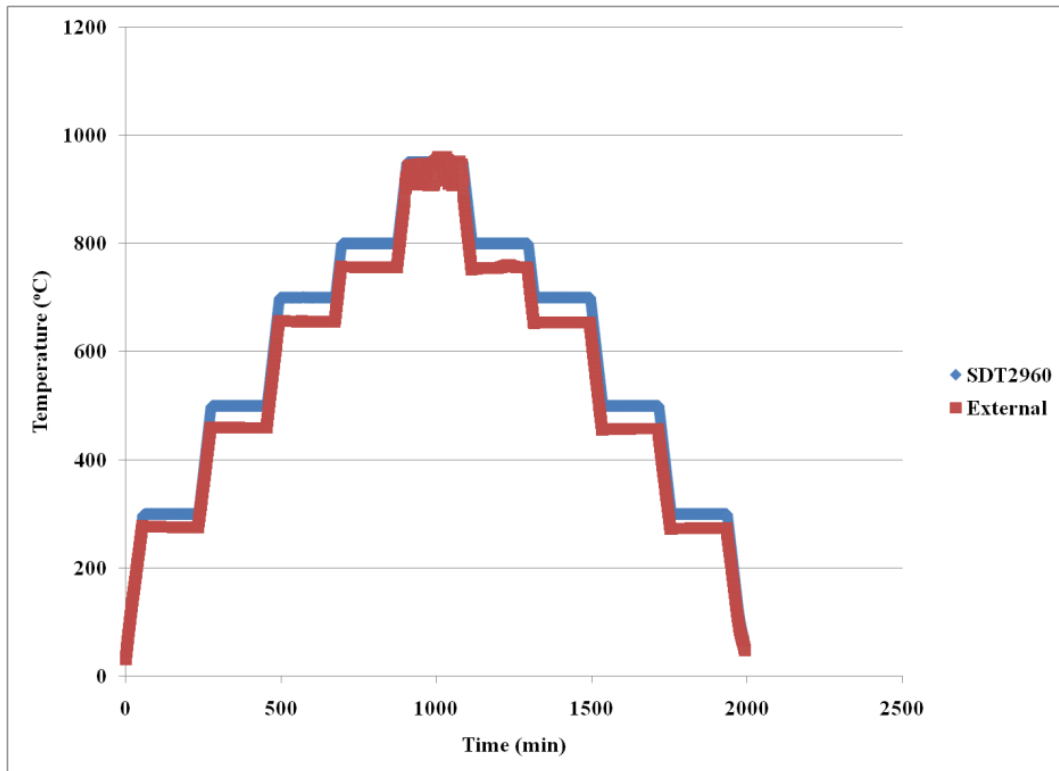


Figure 6.18: Temperature programme as measured by the SDT2960 and the R-type thermocouple.

Again, this shows great agreement in terms of the ramp rate and lengths of the isotherms. Moreover, a comparison was done for the same temperature programme between the SDT2960 and the external circuit using the shared S-type thermocouple. This is shown in figure 6.19.

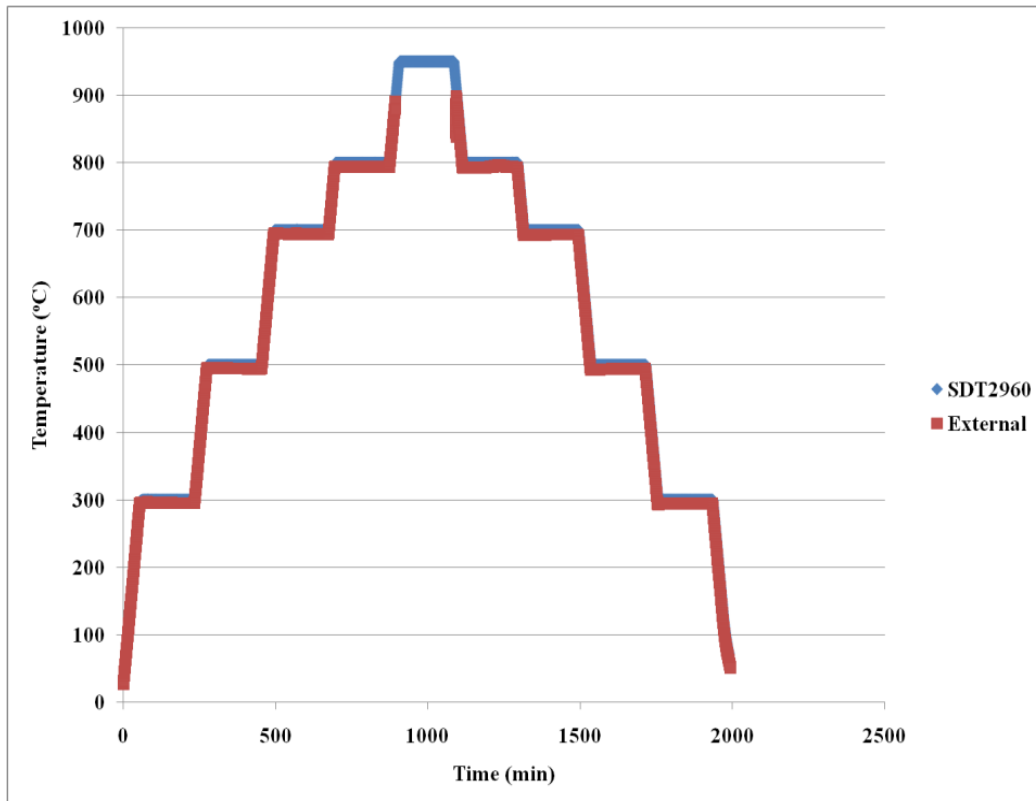


Figure 6.19: Temperature measured using the same S-type thermocouple showing a great overlap between the two systems. Note: some data were omitted due to an error.

This step was very important to ascertain that the new control software; i.e. Thermal Advantage; was controlling the SDT2960 correctly in feeding the correct power to the furnace for a given set temperature.

The second part of testing was for the new setup to measure the conductivity. A pellet of $\text{La}_{0.2}\text{Sr}_{0.25}\text{Ca}_{0.45}\text{TiO}_3$ was pre-reduced at 1050°C in $5\%\text{H}_2/\text{Ar}$ for 72 hours. The pellet was connected to the gold wires on the sample pan and heated to 900°C at $5^\circ\text{C}/\text{min}$.

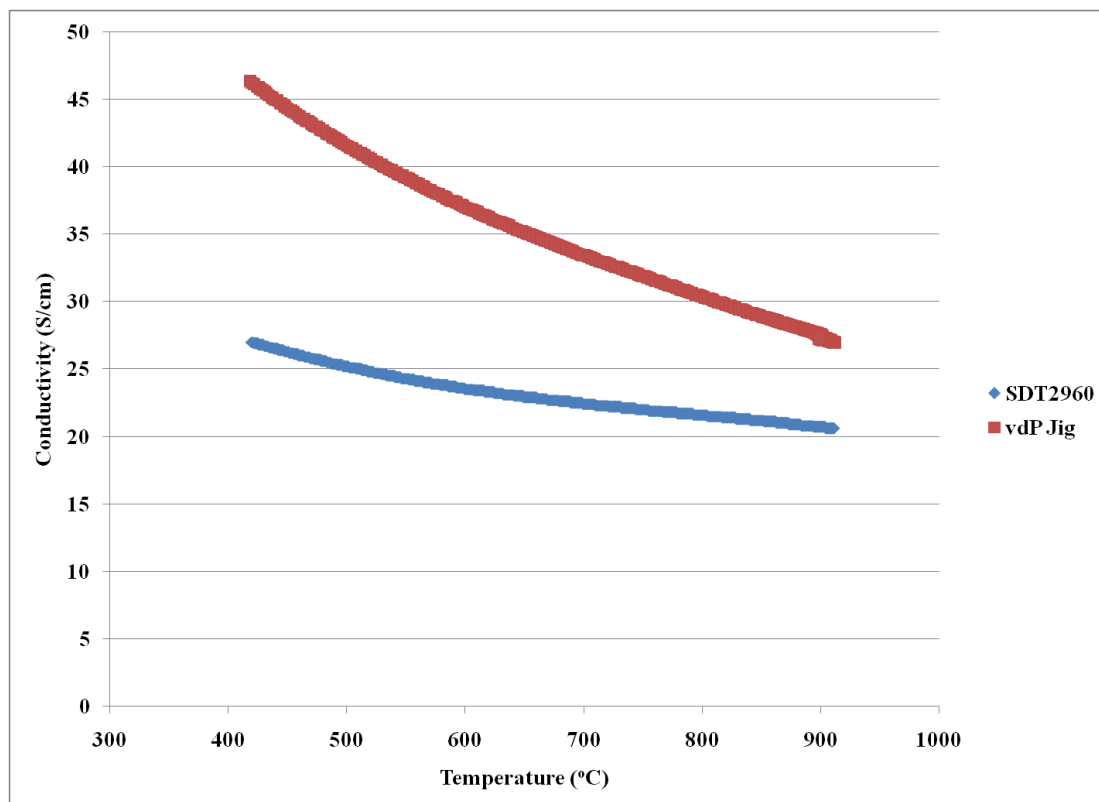


Figure 6.20: The conductivity of dense $\text{La}_{0.2}\text{Sr}_{0.25}\text{Ca}_{0.45}\text{TiO}_3$ as a function of temperature measured in two different jigs under reducing conditions.

As the conductivity of $\text{La}_{0.2}\text{Sr}_{0.25}\text{Ca}_{0.45}\text{TiO}_3$ was measured using a stand-alone vdp jig and then using the new setup of the SDT2960; it is very obvious that both are showing very good resemblance. Measuring the conductivity of the same material in the new setup showed a loss in the maximum conductivity at 900°C by about 7 S/cm. Since the sample used within the new setup underwent further thermal treatments in order to reduce its diameter to fit for the new sample pan; it was concluded that this loss might be due to this since these materials performance is affected by the thermal history of the sample. However, it was proven that both runs look very similar in shape; i.e. metallic n-type conductivity; that it confirmed that the conductivity setup is working well.

Many tests were conducted to test the pO_2 sensor used. Mainly these tests were carried out to determine the oxygen partial pressure within the tube to get a reference value to be used in future experiments. Tests have revealed that the pO_2 sensor was too long to have a uniform temperature thus the voltage generated was not precise enough to give a reliable measure of the oxygen partial pressure. Having a compact horizontal furnace leads to having a temperature gradient along its main axis. This was evident from the temperature difference measured between the two thermocouples used. Thus it was decided to alter the pO_2 sensor to make it shorter and have a smaller exposure area to the ambient environment. This is shown in figure 6.21. The YSZ tube was held in place by using an alumina tube with both ends sealed using ceramic based cement.



Figure 6.21: New pO_2 sensor in place next to the sample arm in the SDT2960.

Testing the new sensor showed a better thermal response; see figure 6.22; thus confirming the need for this change. A smaller confinement will yield a faster approach to equilibrium for the inner part of the YSZ tube, which is necessary to give a precise measure of the oxygen partial pressure of the surrounding atmosphere much more readily.

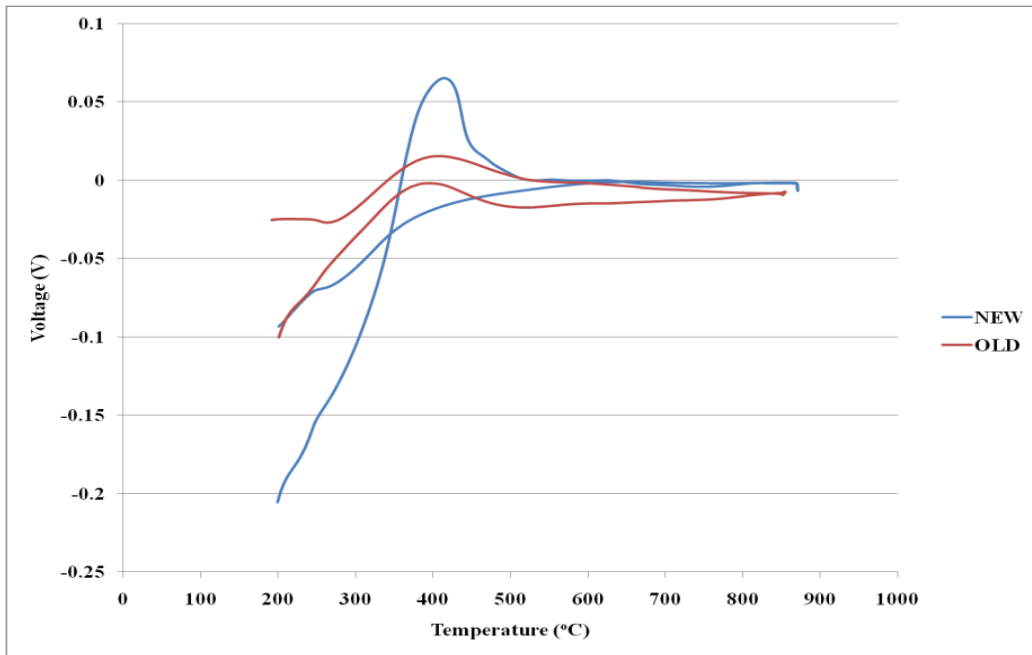


Figure 6.22: Voltage generated across the new and old pO₂ sensors as a function of temperature in air.

The thermal response of the new oxygen sensor has improved with more high temperature runs as shown in figure 6.23.

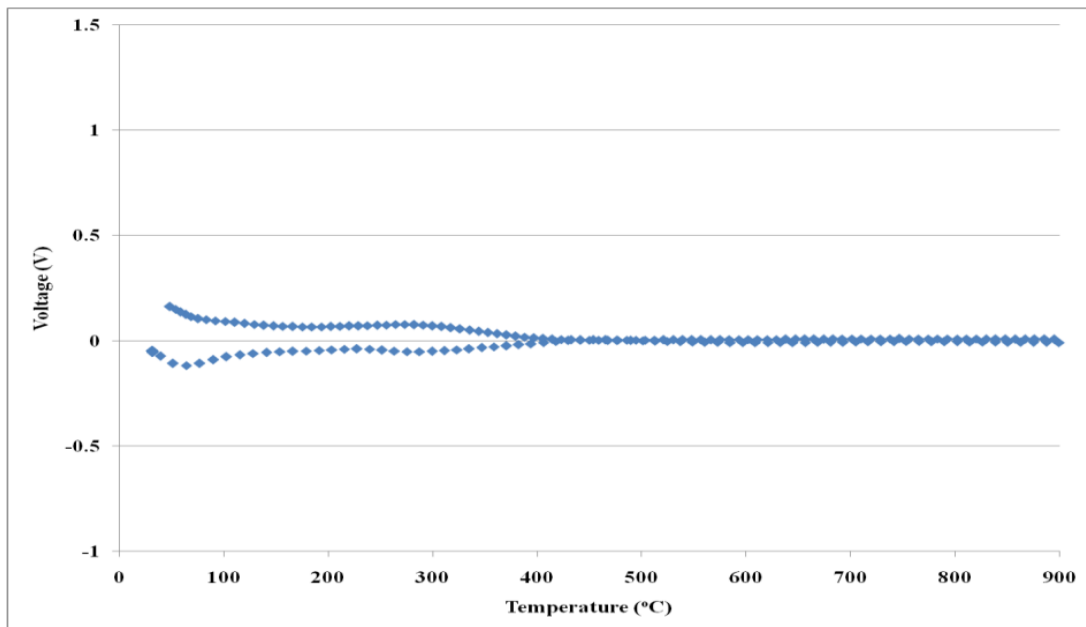


Figure 6.23: Voltage generated by the new sensor as a function of temperature in air; after further runs.

Although the performance of the new sensor has improved with more runs; which might be due to improved contact of the platinum electrodes; an accurate measure of oxygen partial pressure was not achieved due to leaks. Various attempts to improve the sealing of the YSZ tube were taken with little success. Figure 6.24 illustrates the performance of the new sensor as it was heated to 932°C in air and then taken through a redox cycle.

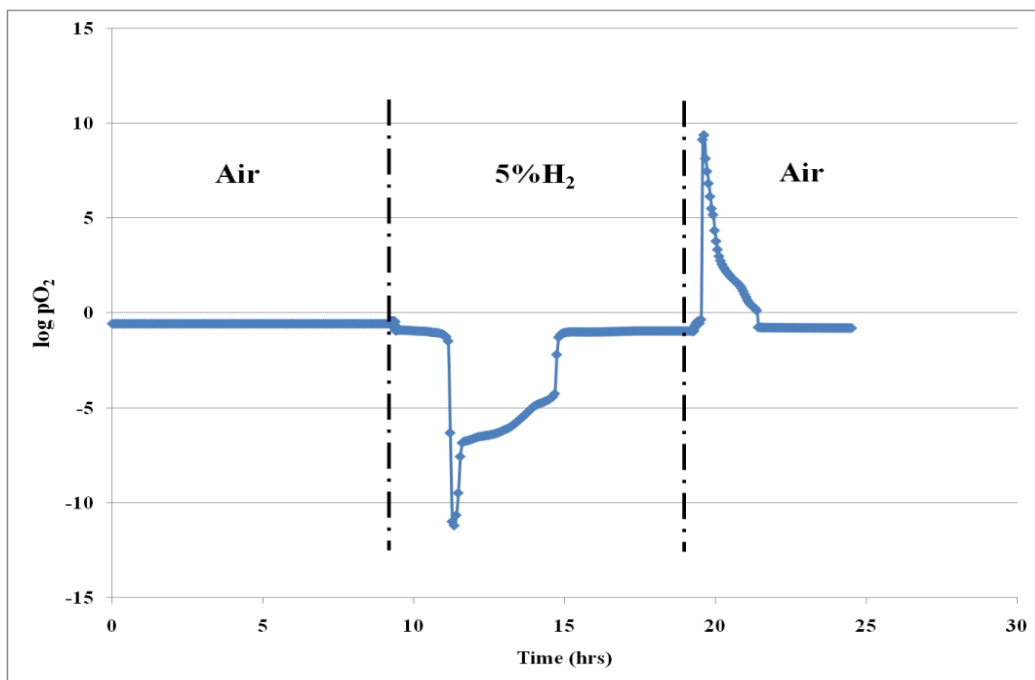


Figure 6.24: oxygen partial pressure as measured by the new sensor at 932°C as the purging gas was switched as shown above.

It was clear that the sensor is working as intended since log pO₂ decreased significantly when subjected to hydrogen. However, it was clear that there is a leak even after multiple applications of extra sealant.

Despite this, the new jig showed a very satisfying performance through the testing phase, where we went for testing the new concept of simultaneously measuring the weight change and dc conductivity of samples.

6.4 - Experimental

Pellets were synthesised from a batch of $\text{La}_{0.2}\text{Sr}_{0.25}\text{Ca}_{0.45}\text{TiO}_3$ powder that was previously synthesised and ball milled into fine powder. Powder was pressed into a 7 mm diameter pellet using a uniaxial press. Pellets were fired between 1300-1400°C for 8-12 hours at a heating/cooling rate of 5°C/min. Porous samples were sintered with a 50:50% mixture of glassy carbon and graphite. A dense pellet with relative density of 90.11% was produced. Also, two pellets were sintered with 30wt% and 50wt% of the pore former; giving relative densities of 74.28% (sample A) and 69.51% (sample B) respectively. The dense pellet was pre-reduced at 1050°C for 72 hours with 5% H_2 . Since ceria is known to improve the catalytic activity of many oxide based materials towards the oxidation of fuel (chapter 1), especially hydrocarbons, sample A was tested as prepared and then it was impregnated with ceria using a solution of 0.3 moles/litre of cerium nitrate in ethanol. Droplets of the solution were dropped on the pellet and then it was fired at 250°C for an hour. This process was repeated to reach a 2.81 wt% of ceria, following improvement works conducted on other materials within our research group. Also, excess weight percentage of ceria can dominate the electronic conductivity of the prepared samples.

Gold contacts and fine wires were placed on the pellets using gold paste painted around the circumference of each pellet at 90° intervals. These were fired at 900°C for an hour to burn any organic solvents. Also, gold paste was used to connect the wires on the pellet circumference to the wires on the sample arm and burned eventually. All contacts were checked prior to the start of any measurement.

Samples were tested in the new jig while kept at an isotherm around 900°C and switching the purge gas between air and 5%H₂:95%Ar to monitor any changes to weight and conductivity. Both gasses were supplied directly from gas cylinders.

6.5 - Results and Discussion

Testing the new jig by using the dense pellet of La_{0.2}Sr_{0.25}Ca_{0.45}TiO₃ showed good correlation between weight change and the change in electrical conductivity. Figure 6.25 shows the pellet taken through a redox cycle at 912°C.

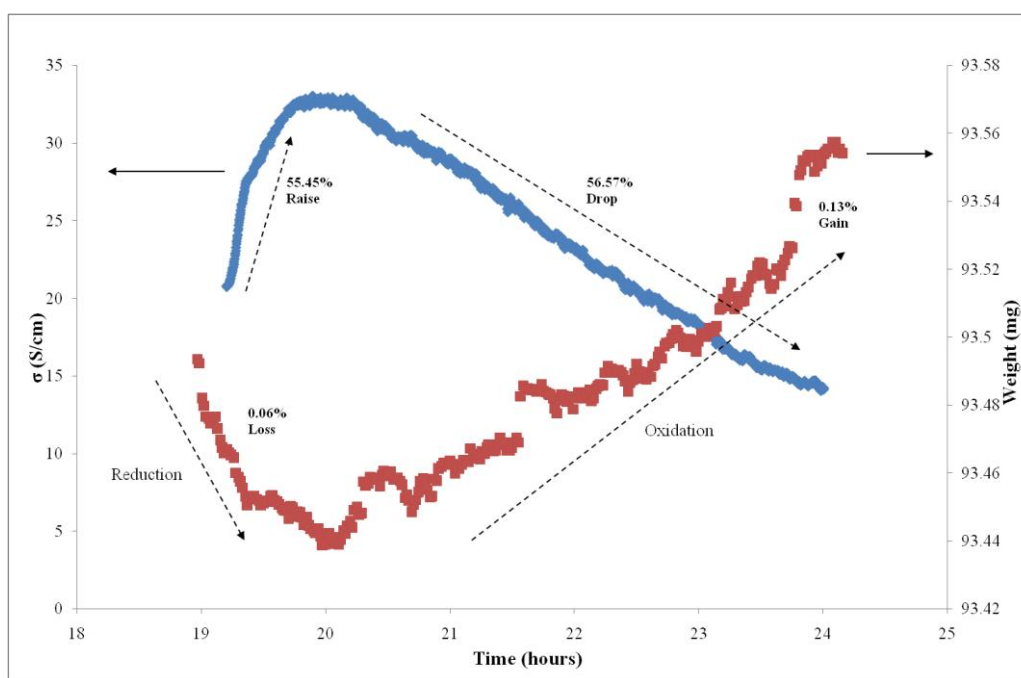


Figure 6.25: Electrical conductivity and the corresponding weight change of dense La_{0.2}Sr_{0.25}Ca_{0.45}TiO₃ through a redox cycle at 912°C.

Although the weight signal was noisy, it is clear from the figure above that there is a strong dependence of the electrical conductivity on the oxygen content of the sample. It should also be noted that the sample did not reach equilibrium under air; since the shown result in figure 6.25 indicates a 0.13% weight gain; compared to 0.32% weight

gain obtained for the same composition in a standalone TGA instrument for a fully oxidised sample. Both signals; i.e. conductivity and weight; show a very similar behaviour to each other, see figure 6.26.

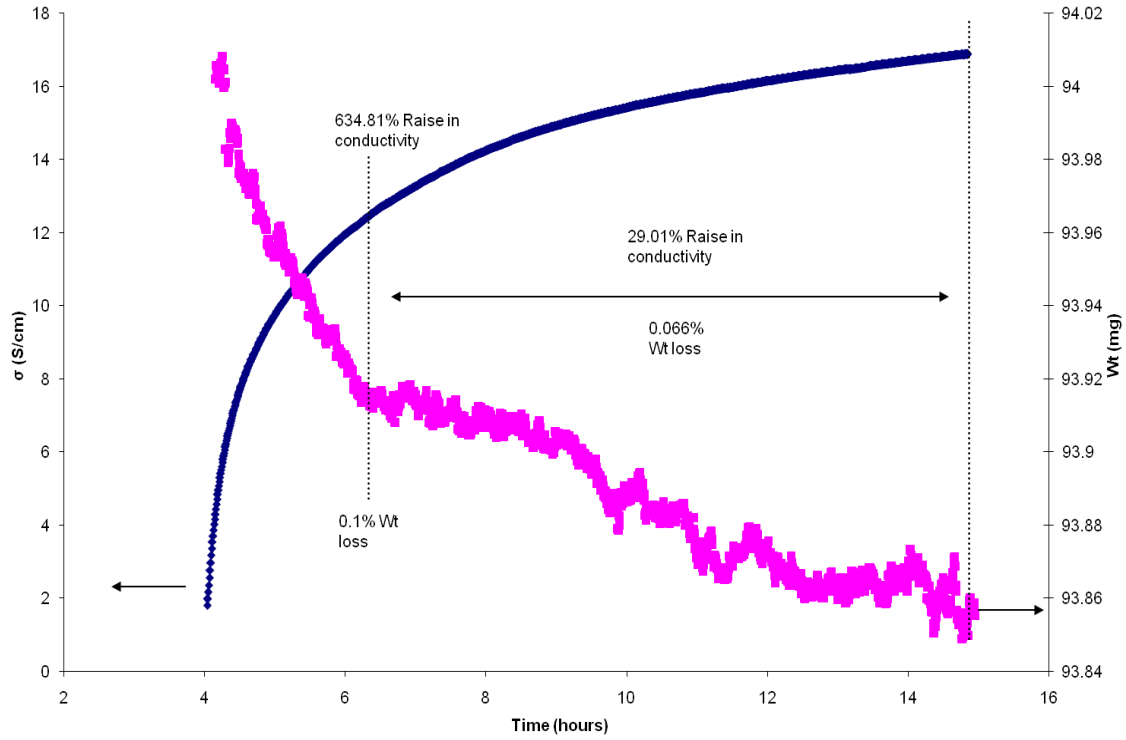


Figure 6.26: Electrical conductivity and the corresponding weight change of dense $\text{La}_{0.2}\text{Sr}_{0.25}\text{Ca}_{0.45}\text{TiO}_3$ through a second redox cycle at 912°C .

After reducing the sample; an oxygen deficiency of about 0.017 was calculated, giving a nominal stoichiometry of $\text{La}_{0.2}\text{Sr}_{0.25}\text{Ca}_{0.45}\text{TiO}_{2.983}$. Also, since this pellet was slightly oxidised during the firing of the gold contacts; i.e. an hour under air at 900°C ; the conductivity increased slightly initially as shown in figure 6.25. After oxidising the pellet for at least 24 hours, the maximum conductivity obtained decreased significantly; from 32.8 S/cm to 16.9 S/cm ; which suggests that increasing the oxygen deficiency of this material requires higher reduction temperatures and/or very long times. Re-

reduction of the dense pellet revealed that there were two steps involved; where it can be seen that different rates of reduction are involved. This can suggest that reducing the surface of a specimen takes place first; and the electrical conductivity takes place mainly through the surface grains. This is followed by a much slower reduction rate which can reflect the activity of the bulk of the sample.

Porous samples of $\text{La}_{0.2}\text{Sr}_{0.25}\text{Ca}_{0.45}\text{TiO}_3$ that were reduced in-situ were tested to see the response of the conductivity to a lower relative density.

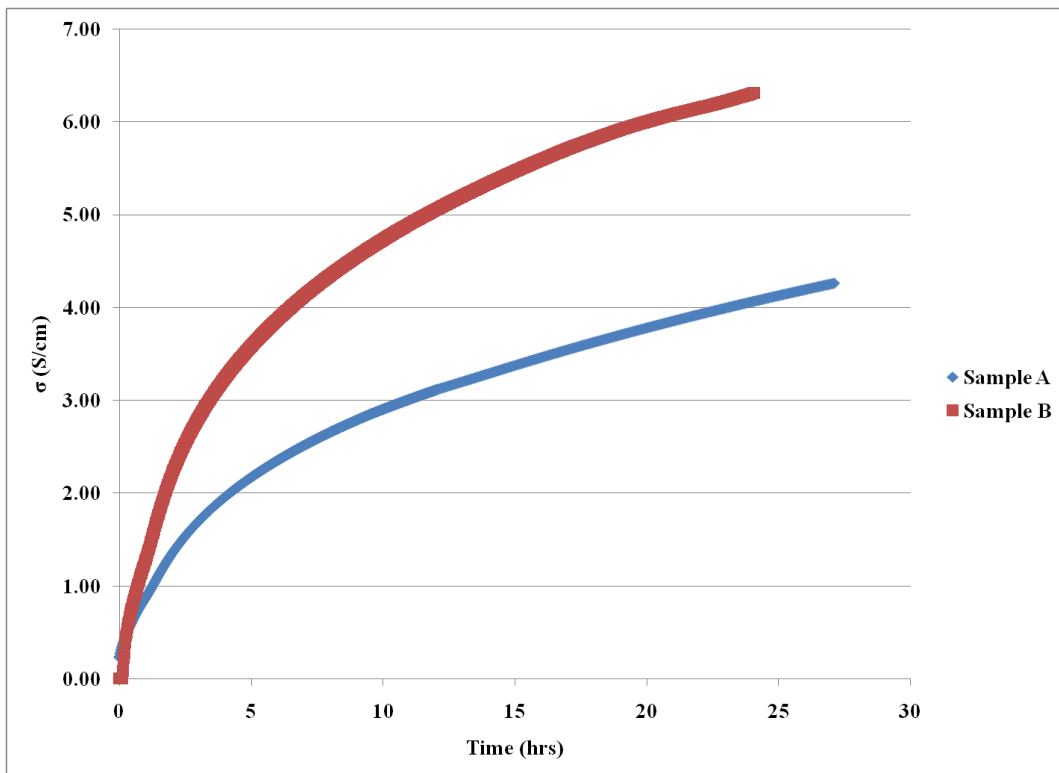


Figure 6.27: Response of conductivity of the porous samples of $\text{La}_{0.2}\text{Sr}_{0.25}\text{Ca}_{0.45}\text{TiO}_3$ during reduction at 907°C .

As can be seen from figure 6.27, the response of sample B is faster than that of Sample A and the conductivity was higher indicating more Ti^{4+} was reduced. As both were exposed to $5\% \text{H}_2$, the catalytic activity of sample B is higher because of the lower

relative density; hence, the higher diffusion rate of oxygen. Weight signal for this part could not be measured accurately due to ambient noise that was picked up by the instrument leading to significant errors in weight measurement. The most probable source of the noise might be to heavy traffic in the surrounding area due to the location of the instrument near the delivery entrance of the laboratory. Also, there were extensive renovation works taking place in the room next door. During the course of testing and experimenting with this new setup, as mentioned elsewhere, it was found that extra care must be insured in order to establish vibration free surroundings to obtain reliable weight change readings. Since we have discarded the reference arm; due to the fault mentioned earlier; it was noticed that if the instrument; i.e. the weight arm more specifically; has picked up some noise, the weight signal changes correspondingly. And for this signal to return to the correct weight value, it takes quite a significant time; e.g. 1-3 hours; in the absence of the noise that generated this error.

It should be noted that the conductivity of both samples were corrected for the difference in density according to equation 18.[4]

$$\frac{\sigma_m}{\sigma_c} = 2 \times \left(\frac{\rho_{rel}}{100} - 0.5 \right) \quad (6.18)$$

Where σ_m , σ_c and ρ_{rel} are the measured conductivity, corrected conductivity and relative density, respectively.

The ceria impregnated pellet was taken through a redox cycle, figure 6.28, to see the effect on the catalytic activity of the material.

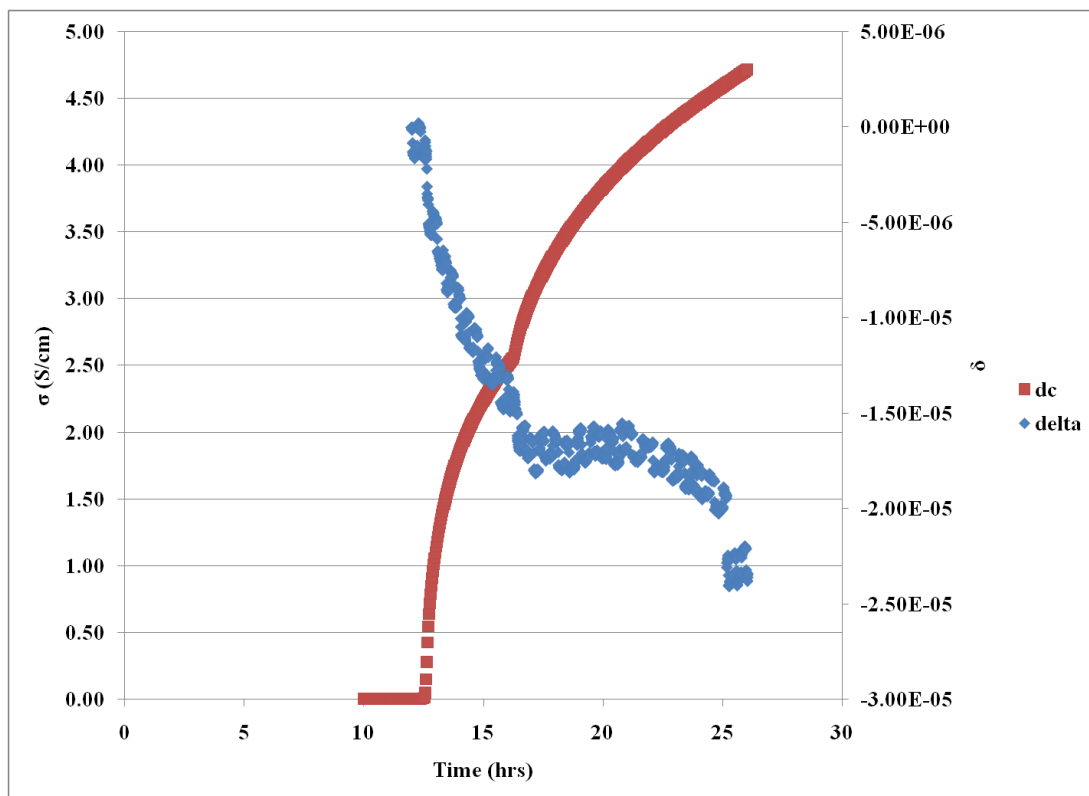


Figure 6.28: Conductivity and oxygen deficiency change of the ceria impregnated pellet reduction at 918°C. Note: Sample was left to equilibrate at the set temperature and to get a stable weight signal from the SDT2960 for 10 hours.

Ceria has shown an improvement to the catalytic activity of sample A significantly; where it is clear that the conductivity increased in a faster pace than before once the pellet was exposed to hydrogen. A very distinct feature of ceria impregnation was that the conductivity and weight behaviour in the reduction stage showed two different rates. This was understood to originate from the catalytic activity of ceria which facilitated a faster reduction to the surface of the sample which was followed by the normal reduction of the bulk which can be seen from the weight signal. Another observation from the above result is the small oxygen deficiency created within the re-reduced pellet at 900°C. This goes back again to the finding that higher oxygen deficiency is easily

obtained at higher temperatures; e.g. 1050°C; where the conductivity of the same material was much higher.

The oxygen chemical diffusion coefficient was measured using the conductivity relaxation method explained earlier. Relaxation data for the oxidation step of the porous samples of $\text{La}_{0.2}\text{Sr}_{0.25}\text{Ca}_{0.45}\text{TiO}_3$ showed a much faster change which is typical with titanates; thus for more reliable estimate of the diffusion coefficient the reduction steps were used instead for these samples. The first result was to estimate the diffusion coefficient of the dense sample. Figure 6.29 shows the natural log of the normalised conductivity M which was calculated using the left hand side of equation 16.

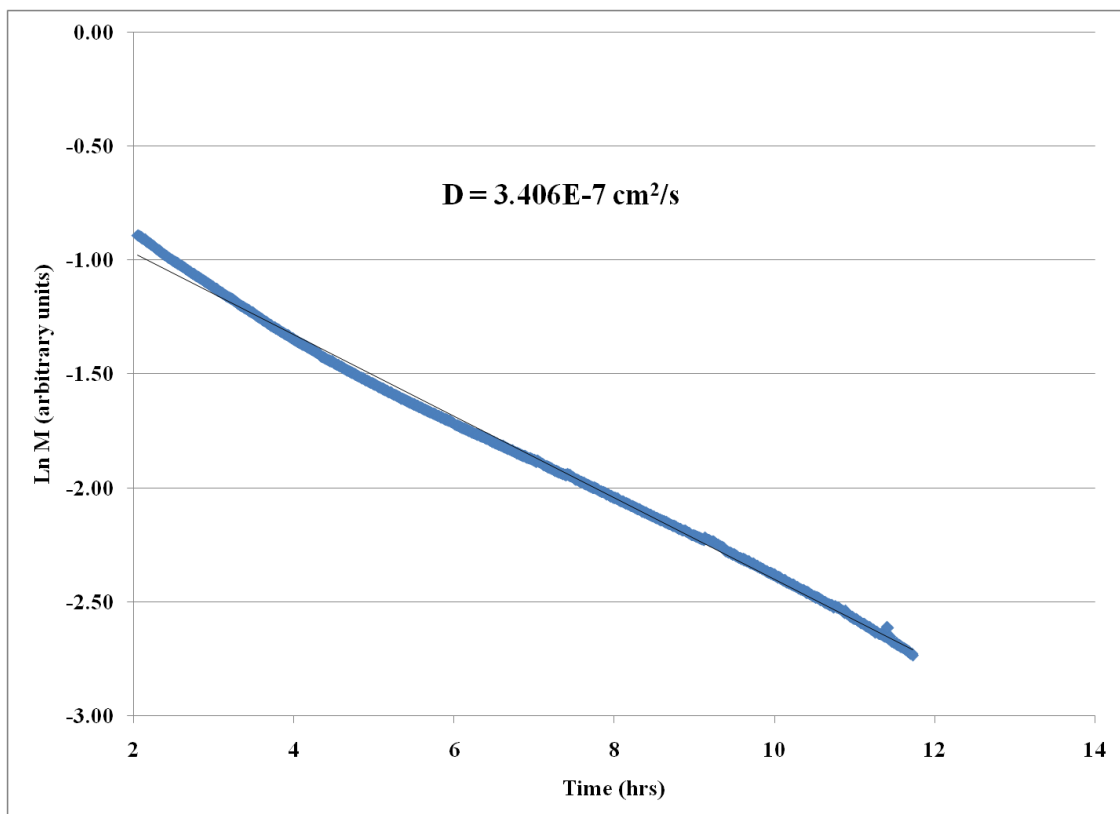


Figure 6.29: Normalised relaxation conductivity for the reduction of dense $\text{La}_{0.2}\text{Sr}_{0.25}\text{Ca}_{0.45}\text{TiO}_3$ at 900°C with the calculated oxygen chemical diffusion coefficient shown.

For the dense sample the oxygen chemical diffusion coefficient measured during oxidation was very similar; i.e. $4.373 \times 10^{-7} \text{ cm}^2/\text{s}$; which confirms the success of the method used in this work. This oxygen diffusion coefficient is in the same order of magnitude to that of YSZ and CGO as reported in literature.[18,22] This result was compared to that for the porous sample A; the diffusion coefficient is shown in figure 6.30..

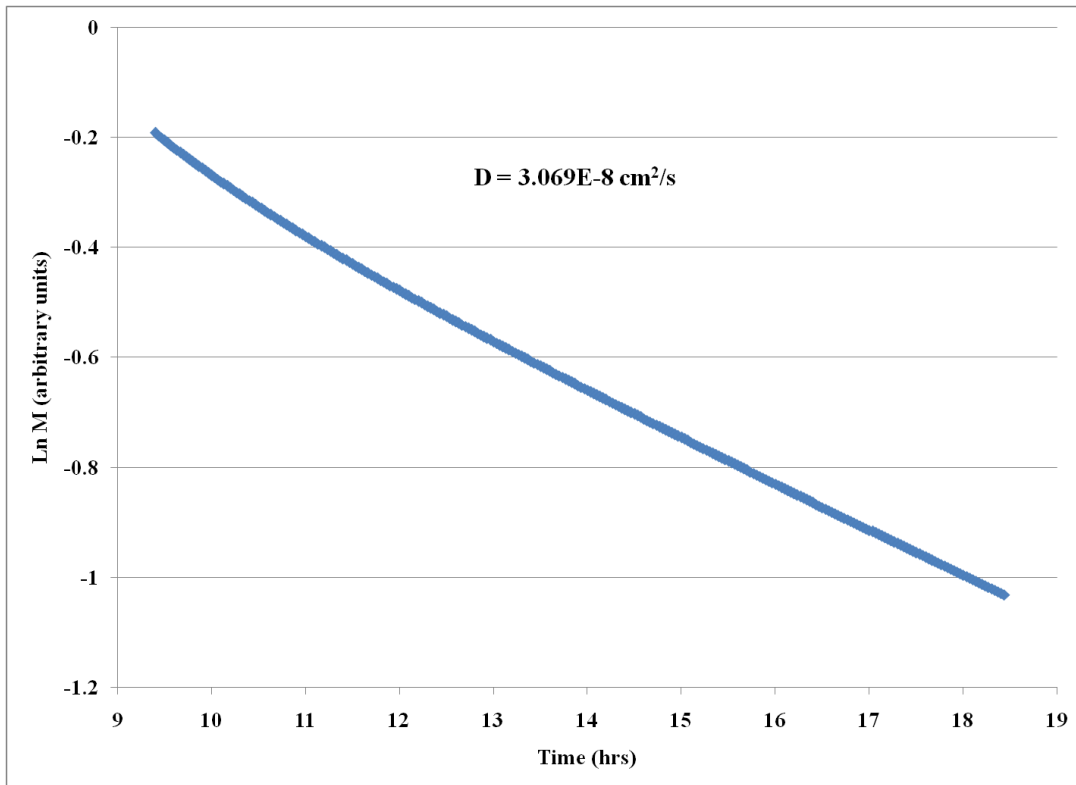


Figure 6.30: Normalised relaxation conductivity for the reduction of Sample A of $\text{La}_{0.2}\text{Sr}_{0.25}\text{Ca}_{0.45}\text{TiO}_3$ at 900°C with the calculated oxygen chemical diffusion coefficient shown.

With the added porosity the oxygen diffusion coefficient of sample A was smaller by an order of magnitude when compared to the dense sample. Sample B has higher porosity than sample A as can be seen from the SEM micrographs in figure 6.31.

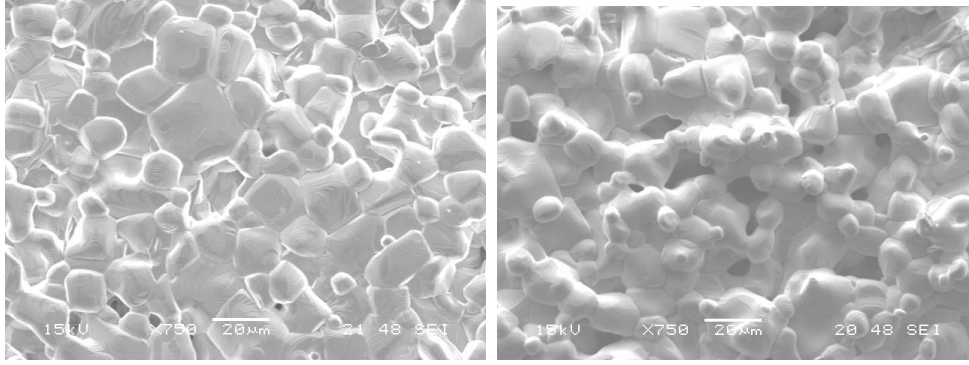


Figure 6.31: SEM micrographs comparing the porosity of sample A and sample B, respectively.

Since sample B showed a lower density than that of sample A, given the higher porosity, the oxygen diffusion coefficient was higher by an order of magnitude, as shown in figure 6.32.

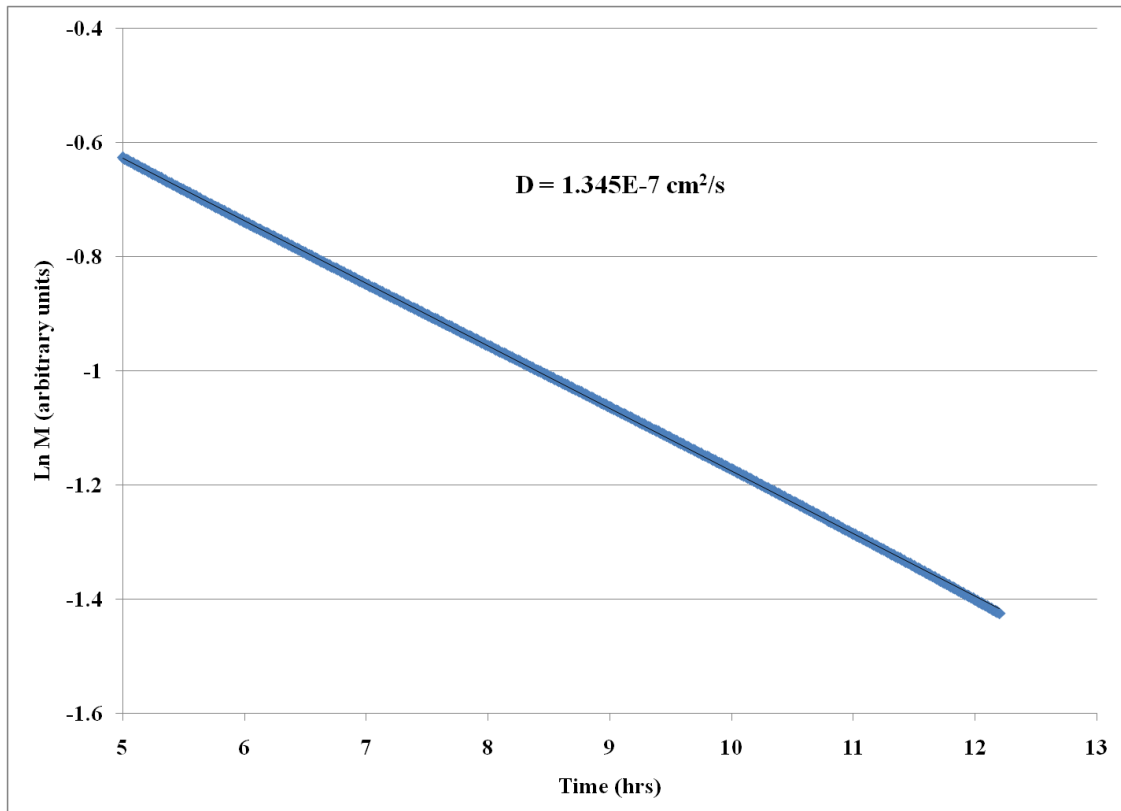
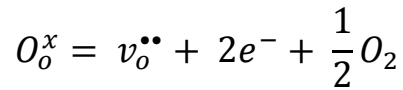


Figure 6.32: Normalised relaxation conductivity for the reduction of Sample B of $\text{La}_{0.2}\text{Sr}_{0.25}\text{Ca}_{0.45}\text{TiO}_3$ at 900°C with the calculated oxygen diffusion coefficient shown.

Since the electrical conductivity of sample A was found to be lower than sample B; having a lower oxygen diffusion coefficient can be explained through the analogy that when an oxygen vacancy is generated on an oxygen lattice point, two electrons are generated according to the reaction:



In the above reaction three mechanisms are involved in the removal of lattice oxygen. These are the formation of an oxygen vacancy on the lattice point involve, removal of electrons and finally the removal of oxygen molecules. Thus, the removal of these generated electrons is equally important to the removal of oxygen molecules. Comparing between sample A and sample B, we find that the oxygen diffusion coefficient in sample B is higher than that of sample A; which can be attributed to increased porosity making the removal of oxygen much easier; as well as, more reduced surface area does result giving higher electronic conductivity. In the dense sample, there is more material for a given surface area; giving higher conductivity when compared to the porous samples. This picture is confirmed with the ceria impregnated sample A; its electrical conductivity was higher with ceria, thus, it can be seen from figure 6.33, that the diffusion coefficient was higher and similar to that of the dense $La_{0.2}Sr_{0.25}Ca_{0.45}TiO_3$ and sample B; i.e. the same order of magnitude.

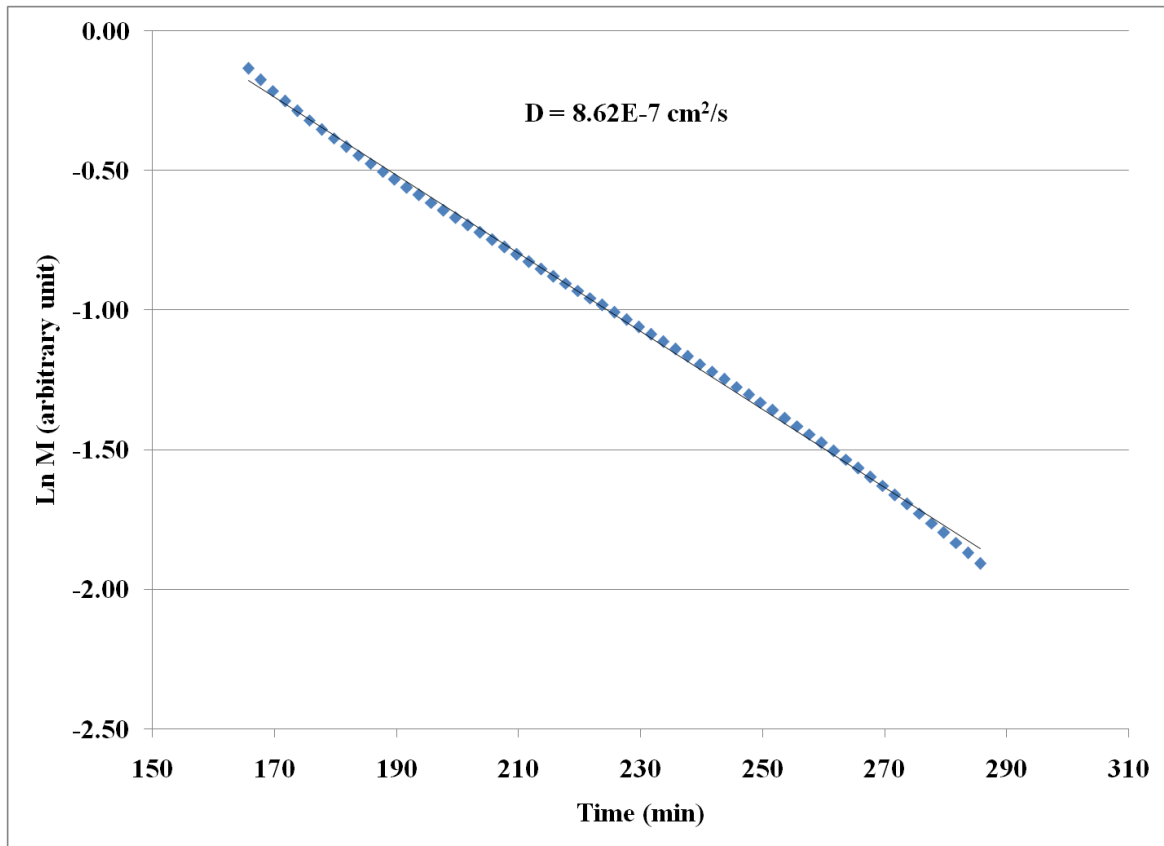


Figure 6.33: Normalised relaxation conductivity for the reduction of the ceria impregnated sample of $\text{La}_{0.2}\text{Sr}_{0.25}\text{Ca}_{0.45}\text{TiO}_3$ (Sample A) at 900°C with the calculated oxygen chemical diffusion coefficient shown.

The above figure shows that there is an improvement in the chemical diffusion of oxygen with ceria, this increase can be a result of a faster diffusion of oxygen that results from the reduction of the ceria; as we have seen in figure 6.28; also, in figure 6.34, it can be seen how ceria impregnation changed the morphology of sample A, where the distribution of ceria is obvious and can be said to dominate the oxygen chemical diffusion. However, the estimation of the oxygen chemical diffusion coefficient was taken over the whole run, thus it can be argued that this is a good approximation of the performance of the system under study here.

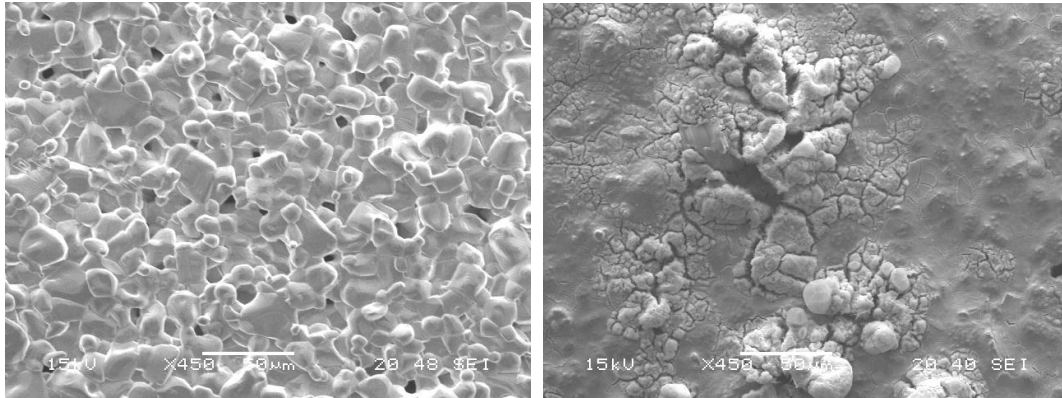


Figure 6.34: SEM micrographs of sample A before (left) and after (right) impregnation with ceria.

The micrographs show that most of the pores have closed up with ceria; which is creating more conducting pathways throughout the pellet. Ceria addition did improve the kinetics through redox cycling, however, from figure 6.33; the diffusion coefficient is slightly higher to that of the dense sample. Having very similar values for most of the tested samples in this work may indicate that the diffusion coefficient measured here is that of the material itself; and porosity has little or no effect. The different oxygen diffusion coefficients obtained in this work are listed in table 6.2.

Sample	$D(O_2)$ (cm ² /s)	Notes
Dense Pellet	3.406E-7	Relative density 90.11%
Sample A	3.069E-8	Relative density 74.28%
Sample B	1.345E-7	Relative density 69.51%
Sample A + Ceria	8.617E-7	Impregnated with 2.81wt% Ceria

Table 6.2: Oxygen chemical diffusion coefficients obtained with different samples of $La_{0.2}Sr_{0.25}Ca_{0.45}TiO_3$.

The diffusion coefficients of the different samples, shown above, are all in the same order of magnitude, except for Sample A. This can indicate an intimate relation between the electrical conductivity, as explained earlier, where as the conductivity increases in this type of titanates the oxygen diffusion increases as well. However, since we are limited with the current setup, a precise determination of the exact factor that affect the oxygen diffusion, whether it is the bulk or the surface that give these values. The diffusion coefficient was slightly affected by the addition of ceria and showed a slightly higher value to the dense sample; this can indicate an improvement in the catalytic activity. As mentioned earlier, most of the samples showed a similar diffusion coefficient to that of YSZ electrolyte and this shows that this material can be considered as a good alternative anode material. This is because in the operation of SOFCs, a continuous oxygen diffusion coefficient profile through the different phases; i.e. electrolyte and anode; will surely increase the efficiency of the whole system through minimising the losses through the different components. Having a similar order of magnitude; 10^{-7} cm²/s; does confirm that the experimental setup and analysis employed in this work was successful in determining the oxygen diffusion coefficient of La_{0.2}Sr_{0.25}Ca_{0.45}TiO₃, despite the different difficulties. Most importantly, with the setup used in this work it was possible to confirm that the electrical conductivity in the A-site deficient perovskite, studied here, is intimately linked with its oxygen diffusion coefficient which indicates that the overall performance of this material is affected by its oxygen content.

6.6 - Conclusions

We have successfully demonstrated a new analytic technique that combines TGA with DC conductivity using an existing TGA instrument with extra modifications. The modifications involved adding four contacts to collect the DC conductivity, an oxygen partial pressure sensor to readily quantify the surrounding atmosphere and changes to the original sample's arm. An A-site deficient perovskite was used as the testing material and showed a strong correlation between weight change, oxygen chemical diffusion coefficient and conductivity. Oxygen content or the lack of it; i.e. oxygen vacancies; governs the electrical conductivity of this type of materials where increasing the oxygen deficiency showed to improve the electrical conductivity, as it was found in chapter 4. Porosity improved the catalytic activity of this material; as well as; impregnation with ceria, where the samples showed faster redox kinetics. Oxygen chemical diffusion coefficient was measured for $\text{La}_{0.2}\text{Sr}_{0.25}\text{Ca}_{0.45}\text{TiO}_3$ successfully using the conductivity relaxation method; which showed a strong correlation between oxygen content and electrical conductivity. The results also indicate little effect by the microstructure of the samples; i.e. porosity; on the oxygen diffusion coefficient, which validates the relaxation method used. Further improvements are needed to better quantify the thermal parameter which will give a good approximation of the oxygen tracer diffusion coefficient of different oxides. This will be the focus of future work.

6.7 - Future Recommendations

The jig showed very good results, however, there are some improvements that can be adopted in the future to make it a more reliable technique. Firstly, without any reference weight measurement and because of the way the instrument was designed, a

simultaneous correction had to be sacrificed. In order to overcome this, the instrument should be operated away from any ambient noise as much as possible. Moving the instrument to a more isolated area and placing it on a vibration free bench can improve the weight reading significantly. Also, it will be possible to run a weight baseline which was tried in this work but failed due to noise that was picked up by the SDT2960.

Secondly, a precise measure of the oxygen partial pressure could not be achieved by using an YSZ tube due to leaks. Using a smaller section of the tube improved the voltage response to temperature. Having an external oxygen sensor was considered; however, that would require an additional furnace which will increase the complexity and cost of this technique. Alternatively, a smaller sensor can be made by using a cell made of YSZ where one side is exposed to the ambient air through a sealed tube. Extra care should be taken in drilling an opening through the cast metal of the meter housing to avoid any fracturing that might lead to further leaks. A precise control of the partial pressure using flow controls will prove very beneficial for conductivity relaxation method in order to determine the oxygen diffusion coefficient. The thermodynamic factor can also be obtained, using equation 11, through a precise measurement of the change in oxygen partial pressure surrounding a sample along with a more sensitive weight change which can give a measure of the oxygen concentration. The thermodynamic factor can be used to measure the oxygen mobility as well. The potential of this novel instrument can increase when it includes the determination of the tracer self diffusion coefficient; which can give a direct measure of the ionic conductivity. This instrument can be an all-in-one machine, where many different electrochemical analytic techniques can be combined together.

6.8 - References

- [1] P. J. Haines, 'Introduction', in *Principles of Thermal Analysis and Calorimetry*, ed. Peter Haines, Cambridge, The Royal Society of Chemistry, **2002**, 1-9.
- [2] B. Wunderlich, *Thermal Analysis of Polymeric Materials*, Springer-Verlag Berlin Heidelberg, **2005**.
- [3] J. C. Ruiz-Morales, D. Marrero-Lo'pez, J. Canales-Va'zquezc and J. T. S. Irvine, *RSC Advances*, 2011, **1**, 1403–1414.
- [4] F. Tietz, I. A. Raj, Q. X. Fu and M. Zahid, *J. Mater. Sci.*, 2009, **44**, 4883-4891.
- [5] C. Elschner, M. Kusnezoff, S. Ziesche, A. Paepcke and A. Michaelis, *J. Membrane Sci.*, 2010, **362**, 545-549.
- [6] T. Ishihara, J. A. Kilner, M. Honda, N. Sakai, H. Yokokawa and Y. Takita, *Solid State Ionics*, 1998, **113-115**, 593-600.
- [7] F. Mauvy, J. M. Bassat, E. Boehm, P. Dordor, J. C. Grenier and J. P. Loup, *J. Eur. Ceram. Soc.*, 2004, **24**, 1265-1269.
- [8] V.V. Vashook, M. AI Daroukh and H. Ullmann, *Ionics*, 2001, **7**, 59-66.
- [9] S. Wang, A. Verma, Y. L. Yang, A. J. Jacobson and B. Abeles, *Solid State Ionics*, 2001, **140**, 125-133.
- [10] G. R. Heal, 'Thermogravimetry and Derivative Thermogravimetry', in *Principles of Thermal Analysis and Calorimetry*, ed. Peter Haines. Cambridge, The Royal Society of Chemistry, **2002**, 10-54.

- [11] D. K. Schroeder, *Semiconductor Material and Device Characterization*, Wiley, **1990**, 1-7.
- [12] S. Z. Tehrani, W. L. Lim and L. Lee, *Measurement*, 2012, **45**, 219-225.
- [13] C. Kasl and M. J. R. Hoch, *Rev. Sci. Instrum.*, 2005, **76**, 033907.
- [14] L. J. Van der Pauw, *Philips Tech. Rev.*, 1958/59, **20**, 220-224.
- [15] L. J. Van der Pauw, *Philips Res. Rep.*, 1958, **13**, 1-9.
- [16] X. ChaoYang, L. XuChen, Y. Yan, W. TiZhuang, Z. ZhiMin and Y. SuPing, *Appl. Surf. Sci.*, 2011, **257**, 7952-7958.
- [17] B. Ma, U. Balachandran, J.-H. Park, and C. U. Segre, *Solid State Ionics*, 1996, **83**, 65-71.
- [18] J. A. Kilner, *Solid State Ionics*, 2000, **129**, 12-23.
- [19] J. A. Lane and J. A. Kilner, *Solid State Ionics*, 2000, **136-137**, 997-1001.
- [20] J. Maier, “*Physical Chemistry of Ionic Materials: Ions and Electrons in Solids*”, John Wiley & sons Ltd., England, **2004**.
- [21] TA Instruments, *SDT2960 Flyer*. Internet, Retrieved from:
<http://www.chem.pku.edu.cn/instlab/pdf/ONLINETRAIN/SDT2960-DSC2010-3.pdf>,
accessed 20 September 2012.
- [22] Y. Ji, J. A. Kilner and M. F. Carolan, *Solid State Ionics*, 2005, **176**, 937-943.
- [23] M. Katsuki, S. Wang, K. Yasumoto and M. Dokiya, *Solid State Ionics*, 2002, **154-155**, 589-595.

Chapter 7

Final Remarks and Future Recommendations

7.1 Final Remarks

As we started this work with the synthesis and characterisation of the A-site deficient $\text{La}_{0.2}\text{Sr}_{0.7-x}\text{Ca}_x\text{TiO}_3$, the end result became very diverse, yet, very connected. We successfully obtained solid solutions of different samples with different calcium content through solid state synthesis. Although very dense, the electrical conductivity showed a positive proportionality with calcium content; which led to decreasing unit cell volume bringing the conduction orbitals closer to each other. However, this increase in conductivity was held to a maximum with the composition $\text{La}_{0.2}\text{Sr}_{0.25}\text{Ca}_{0.45}\text{TiO}_3$ which showed an electrical conductivity just over 27 S/cm at 900°C. The conductivity dropped with increasing calcium content afterwards. During the course of studying these materials, we proved or re-established that the total conductivity for a given composition depends greatly on the oxygen deficiency obtained through reduction. This deficiency was much higher when samples were reduced at higher temperatures; e.g. 1050°C compared to 900°C.

As a novel material, a detailed crystallographic analysis was provided where many interesting findings were obtained. Through X-Ray and neutron diffraction methods, the symmetries of samples in the series $\text{La}_{0.2}\text{Sr}_{0.7-x}\text{Ca}_x\text{TiO}_3$ were found. This helped in lifting some of the ambiguity surrounding the different/conflicting symmetries reported in literature for similar compounds, especially for different samples in the series $\text{Ca}_{1-x}\text{Sr}_x\text{TiO}_3$. These conflicting reports initially led to much debate about the correct symmetries of our system. Nonetheless, it was proven that this system is slightly distorted; i.e. much less than its counterparts in literature. Two symmetries were present, tetragonal $I4/mcm$ and orthorhombic $Pbnm$ for compositions $0.1 \leq x \leq 0.35$ and

$0.4 \leq x \leq 0.7$, respectively. These lower symmetries were a result of tilts and slight distortions to the BO_6 octahedra which were easily removed at high temperatures. Samples that were studied at high temperatures, showed higher symmetries and ended up with the ideal cubic symmetry at 900°C . The interesting finding was that at this temperature, the two samples; i.e. $x = 0.45$ and $x = 0.5$; showed the relatively the same unit cell; however, the composition $\text{La}_{0.2}\text{Sr}_{0.2}\text{Ca}_{0.5}\text{TiO}_3$ showed a lower conductivity although its unit cell volume was smaller than $x = 0.45$. Further investigation led to the finding that traces of the distortions at lower temperatures were still affecting the BO_6 octahedra at the cubic symmetry; where the sample $x = 0.5$ showed higher isotropic parameters which indicate more disruption to the conduction orbitals; which led to the lower conductivity. Unlike much of the reported diffraction results of stoichiometric compounds; e.g. $\text{Ca}_{1-x}\text{Sr}_x\text{TiO}_3$; these A-site deficient compositions showed distortions to the BO_6 octahedra through unequal bond lengths between the titanium and the neighbouring oxygen anions.

Overall the system did show very encouraging properties to be considered as a good alternative anode material for SOFCs. Interesting properties were shown from the close TEC; i.e. compared to that of the most common electrolyte, YSZ; to a very good stability through thermal and redox cycling. Also, phase purity was obtained at lower sintering temperatures which can make processing this material much cheaper and easier. Redox kinetics improvements to this system were obtained through impregnation with ceria and can be further enhanced with different catalysts for better fuel oxidation and electrical performance. It should be mentioned that as this thesis was written, $\text{La}_{0.2}\text{Sr}_{0.25}\text{Ca}_{0.45}\text{TiO}_3$ was chosen to be the material of choice for fuel cell tests that are being conducted jointly between the University of St Andrews and the leading fuel cell

manufacturer HEXIS. The material is showing very encouraging performance as it was impregnated with nickel and ceria; which will be the subject of a publication very soon.

As this work is mainly sponsored by the government of the United Arab Emirates; a study that outlined the best alternative energy technologies and how to best implement fuel cell technology in the country given different aspects was necessary. This is but a small attempt to help decision makers in the Emirates to see a clearer picture of the different options available to them, to keep the development rolling. In chapter 2, we outlined different aspects about the country that should be taken very seriously when planning to implement renewable energy technologies. The most important aspect is the water shortage; which is currently supplied to the population through sea water desalination plants. We argued that desalination at the current and projected rates cannot be sustainable and it can become a very heavy burden on the government in the near future. Given the arid climate of the main body of water; the Gulf; it is only inevitable that salt levels and the sea water temperature will rise; leading to increased cost of desalination. Being one of the largest oil producing countries in the world, the UAE has an advantage; given its healthy economy; to experiment with a new proposed system that combines different technologies that stemmed up from fuel cell development. Indeed, this system is not intended to replace the whole energy and water sector in the country. It is meant to utilise the different infrastructures already existing within the country to increase the efficiency associated with power generation and fresh water production. Combining water electrolysis with fuel cells can be a very good alternative to the current employed mechanisms. As water consumption levels are very high, waste water is abundantly available to be utilised in the production of hydrogen through steam electrolysis. Hydrogen can be pumped or stored taking benefit of the

country extensive oil industry infrastructure; which then can be used in hydrogen fuel cells for cogeneration of power and water. Oxygen was considered to be used in fish farming to provide a major food source; which is declining in natural habitats due to many human actions. Also, direct methane fuel cells can be extensively utilised in current power station; where they will be much more efficient than the currently used gas turbines. Also, water can be relatively easier to extract off the exhaust of the fuel cell stack and collected and transported to consumers. All of this was thought of since we believe strongly that given the climate of the Emirates; i.e. desert climate; solar energy which is a very obvious choice when it comes to renewables; however solar energy might be after all very costly when the very frequent sand storms do hit. Solar energy can be utilised in providing power to waste water treatment plants; where more are being built; and electrolysis units, instead of using it to power large cities and towns. All in all, the UAE has a great potential in exploring many different alternative energy technologies, but it is our belief that fresh water should be at the backbone of the planning phase and that our proposed system can be further improved and it will pose as a very useful alternative, renewable and clean method for cogeneration of water and power. Finally, all the above potential implementations of fuel cells related technologies in the UAE do encourage in the search for alternative materials for SOFCs that will give the optimum utilisation of certain conditions/resources of a given region while providing the best performances. The UAE is one of the leading oil producing countries in the world, thus developing materials that can utilise different hydrocarbon based fuels with minimum degradation is very important for the adoption of fuel cells in these markets.

As with any material research, in many occasions the studied material can end up to be used in a different application than the one it was intended for. Since the prepared samples of $\text{La}_{0.2}\text{Sr}_{0.7-x}\text{Ca}_x\text{TiO}_3$ were intended as anode material for SOFCs; some showed a stable tetragonal perovskite structure; which is thought of to be rare; which diverted the attention to ferroelectricity. Thus, many samples were studied using AC impedance spectroscopy. These studies gave many different indications of the nature of these samples. Most importantly, it showed that most of the samples are homogenous and showed a semiconducting behaviour when these were fully oxygenated. The dielectric constant dropped with increasing calcium indicating more stable phases as calcium content increased. No ferroelectric behaviour was noticed and this confirmed that the symmetry investigations of chapter 3 were correct; since ferroelectricity is associated with non-centrosymmetric space groups. Thus, although this part of the thesis seems off course, it helped in further broaden our understanding of the material given the few experiments that were conducted.

Finally, the most interesting part of this work was the development of the new jig outlined in chapter 6. This part was very interesting since it involved many aspects of the material research world. Through alteration made to an old TGA instrument, it is now possible to measure the DC conductivity and weight change of a sample simultaneously. This method brings together many different analytical techniques into one device. Most importantly, this new setup provides us with a much clearer picture in the different processes; since both measurements are obtained for a single sample. Although we were not successful in obtaining a precise measure of oxygen partial pressure, we successful obtained useful data that can be further improved that linked DC conductivity to changes in the stoichiometry of a sample. This device was also useful in

determining the oxygen diffusion coefficient; using the electrical conductivity relaxation method; of the material studied; which gave very interesting values that were comparable with YSZ. This further convinced us that the system $\text{La}_{0.2}\text{Sr}_{0.7-x}\text{Ca}_x\text{TiO}_3$ is a very good candidate to be an alternative anode material for SOFCs. The results were impressive despite the difficulties endured during the course of developing this jig. Noise that was picked up by the instrument due to traffic and personnel movement and actions in the surrounding area affected many measurements; giving useless weight change measurement. $\text{La}_{0.2}\text{Sr}_{0.25}\text{Ca}_{0.45}\text{TiO}_3$ maximum conductivity depended greatly on its oxygen deficiency; which in turn increased when the sample was reduced at temperatures higher than 900°C . This instrument is being enhanced further to provide further stability and better control and determination of oxygen partial pressure. This can lead to the determination of both the oxygen diffusion coefficient and tracer diffusion coefficient; bringing an extra important parameter in oxides research. Most importantly, this part has resulted in providing a new jig for other users to take advantage of; where effort and time can be saved significantly.

Many publications based on the different findings in this thesis are being prepared and will soon be published. First, a manuscript will be published which will outline the structural changes associated with calcium doping and the effects these led to in terms of electrical conductivity and other features of the material. Another paper is also being prepared that outlines the detailed structural analysis at room temperature of the different compositions, as well as, the structural changes at high temperatures obtained using neutron diffraction as was shown in chapter 3. This shall be an important publication since it establishes a new phase map of the ternary system CaTiO_3 - $\text{La}_{2/3}\text{TiO}_3$ - SrTiO_3 ; which will be very useful in helping to resolve the disputes in the

literature regarding similar compounds. Finally, a paper will discuss the work in chapter 6; outlining the concept and implementation of the novel instrument that combines DC conductivity and TGA in one setup; which will help in protecting our concept from possible imitation. Such a basic setup holds the potential of being adopted by an analytical instruments manufacturer. Some results will be included to show the potential of such a device in the electrochemical community. Moreover, we are looking into the possibility of a potential publication discussing the findings in chapter 5; the ferroelectric study.

All in all, although this thesis may seem to be very diverse, it is essentially very well connected and the end result does provide many unique findings and inputs to the research efforts surrounding the development of new materials for SOFCs in particular and oxides or ceramics development in general.

7.2 Future Recommendations

As we did try to do our best in conducting the different works and analysis within the different chapters of this thesis; there is always room for improvement or details that were overlooked.

Firstly, it can be very useful if more intermediate compositions; between the studied ones; of the system $\text{La}_{0.2}\text{Sr}_{0.7-x}\text{Ca}_x\text{TiO}_3$ can be synthesised in the same manner here in order to study their structures. This is important to validate the outlined phases/symmetries in the phase maps shown in chapter 3. Also, it will be very useful to ascertain the existence of other phases in between; partly to satisfy the doubts coming from different sources in the literature. Also, a sub-ambient study of the different compositions that were examined in chapter 5 for ferroelectricity using diffraction techniques to establish whether there are phase changes that take place at low temperatures; this will help to give a very wide spectrum into the different crystal structures of these perovskites. Investigating different microstructures and their effect on the reduction of these titanates and their electrical conductivity can shed more light into the different key processes that affect the performance. Since we've seen that reducing these samples highly depends on the reduction temperature; and having a high temperature to reduce these samples plus long periods of time can add to the complexity of producing these materials. Thus, a study might be useful into the effects of different microstructures plus the role of different catalysts to the reduction process might give some insights into improving the reduction process. Moreover, since we were mainly concerned with establishing which calcium content gave the highest conductivity and having dense samples; investigation of the defect chemistry involved in these materials

was not possible. Thus, having different microstructure that will facilitate such an investigation will be very useful in understanding this material much better. As mentioned above, studying the performance of these materials with different catalysts in terms of type and concentration, as well as, the effects of different synthesis methods on the performance can further enhance the electrical performance and the electrochemical kinetics as well.

As we've found high conductivity in $\text{La}_{0.2}\text{Sr}_{0.25}\text{Ca}_{0.45}\text{TiO}_3$, this composition can be a basis for new compounds where the B-site is doped with different cations which can improve the catalytic activity and may make reducing these compositions much easier. The possibilities are endless; however, careful considerations and following a consistent plan for the dopants and their concentrations can give a very deep understanding which can help in the development of other materials.

Finally, the scientific research is an endless endeavour, where the areas to be explored are almost infinite. Having a conscious mind and a clear plan is very important in the search for new materials for different applications. With the current scale; fuel cells have a very bright future and soon they will be the main source of energy worldwide.

Appendix A

Simultaneous TGA and DC Conductivity Measurement Jig – TA Instruments SDT2960

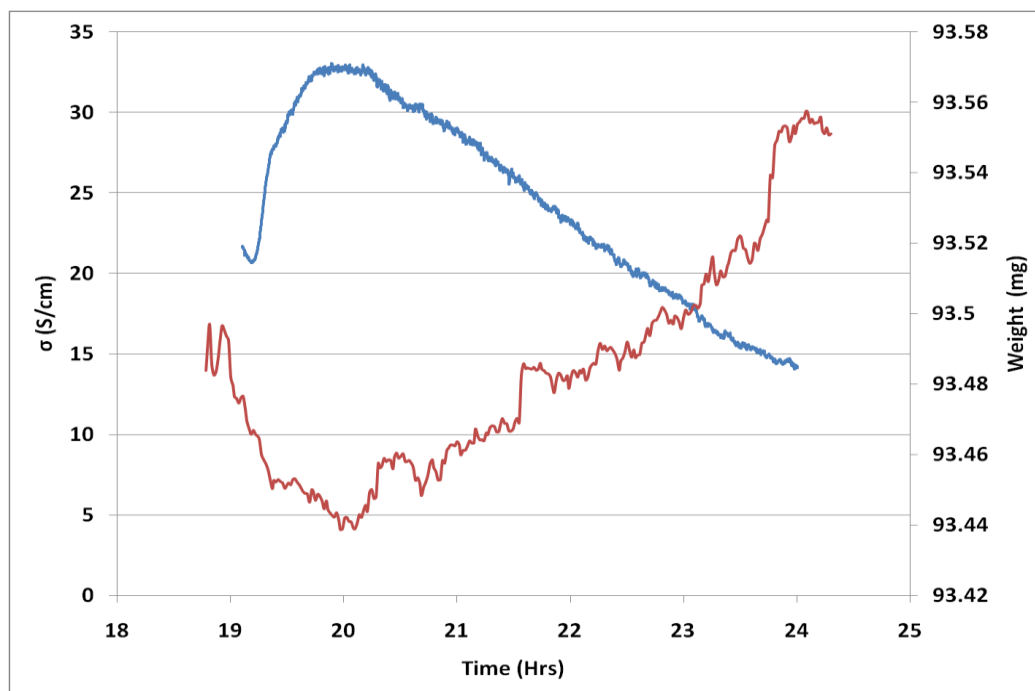
User's Manual



University
of
St Andrews

Simultaneous TGA and DC Conductivity Measurement Jig – TA Instruments SDT2960

User's Manual



John T. S. Irvine Research Group

School of Chemistry

©2012

Introduction

Many materials researchers rely on Thermogravimetric Analysis (TGA) as a necessary tool to study the changes that samples undergo with different experimental conditions. This technique measures minute changes to a sample's mass corresponding to changes in the surrounding conditions. On the other hand, much research is targeted to study electrochemical properties of different materials.

The jig, discussed here, evolved from studying solid oxides that form different components in a fuel cell. For example, studying different oxides that can be used as anodes in a solid oxide fuel cell (SOFC) requires measuring the electrical conductivity at different temperatures and atmospheres. Where in many cases it is clearly straightforward to understand the different mechanisms governing the performance of some oxides, some show different behaviours. And since the conductivity of most of these oxides depends on the oxygen content; TGA is important to quantify the performance of such samples. Thus, it was thought that having a device that performs TGA while measuring the DC conductivity of a sample will prove to be very beneficial.

In the following pages, instructions are given on how to operate an improvised jig that measures the DC conductivity of samples alongside measuring the weight changes; i.e. TGA.

Description:

The jig is based on the TA instruments SDT2960 simultaneous DTA-TGA. This instrument was altered to accommodate necessary components to measure the DC conductivity while maintaining the functionality of TGA. By taking advantage of a malfunctioning circuit that used to measure the reference weight; the weight meter/arm was removed from the housing to give space for inserting an oxygen sensor and its thermocouple. New sample arm was designed with four gold wires running through the whole beam and the pan itself was made flat to accommodate different sample shapes.



Figure 1: The TA Instruments SDT2960 simultaneous DTA-TGA.

Setup:

The new setup for the SDT2960 is shown in figure 2; where the pO₂ sensor can be seen sitting next to an R-type thermocouple next to the sample arm; i.e. to measure the pO₂ sensor temperature. The arm has four wires to measure the conductivity of a sample and a S-type thermocouple positioned underneath the sample.

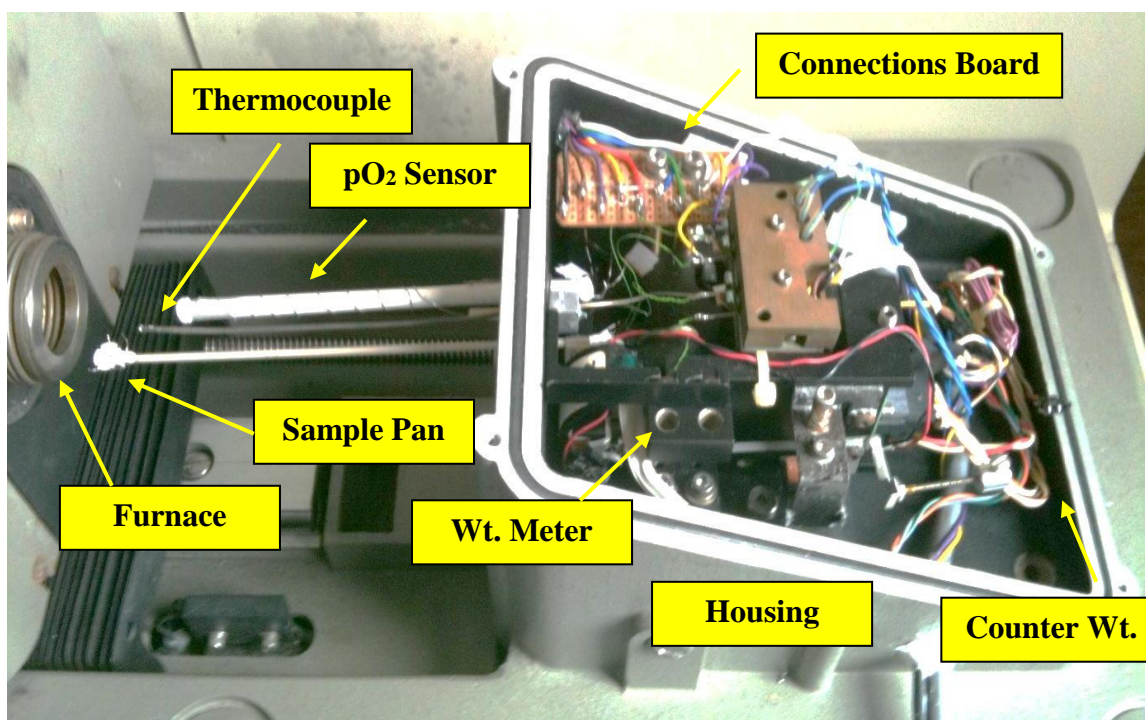


Figure 2: Representation of the new setup.

All Connections are attached to a fixed board to minimise any vibrations that can affect the weight balance. These are taken out through a hole on the side of the meters housing to the different millimetres. The sample pan has an S-type thermocouple in the hole to measure the sample temperature. The counter weight can be changed when using heavier or lighter samples; also it can be moved in and out for smaller adjustments.

Pre-Cautions:

- The new sample arm is very fragile; extra care should be taken when changing samples.
- Handling the gold wires should be with minimum tension to avoid breaking them.
- **Do Not exceed 1000°C** when programming the furnace.
- The YSZ tube/pO₂ sensor is a very fragile tube and can be easily broken; handle with care.
- The end of the sample arm at the meter housing is attached to very thin wires. Under no circumstances these shall be touched or objects are allowed to fall in.
- When adjusting the counter weight; it must be handled carefully in order not to entice large changes to the weight signal. The weight meter is continuously adjusting the position of the arm to keep it in the flat/null position.
- If the weight of the sample is too large for the counter weight; the machine should be turned off before changing it. Then turned on and the counter weight can be slightly moved in or out to make small changes.
- Purging the furnace with pure hydrogen should be avoided; especially at very high temperatures.
- Minimising the level of noise and vibrations is essential to obtain a sensible weight signal. Thus, operating the jig is preferred when there is less activity in the surrounding rooms.
- **Under no circumstances** should the user attempt to replace or fix any components within the meters housing. Contact the administrator immediately if a fault arises **and/or** in doubt of procedure.

OperationProcedure:

- 1- Turn on the SDT2960, PC and the different meters on the side.
- 2- Check all gas connections.
- 3- Open the furnace by pressing the button on the SDT2960. Allow to stop automatically.
- 4- Open the housing top lid/cover by unscrewing all the screws with the proper Allen key.
- 5- Carefully remove previous samples by cutting the thinner gold wires coming from the sample.
- 6- Place the new sample on the pan and carefully attach the wires using some gold paste.

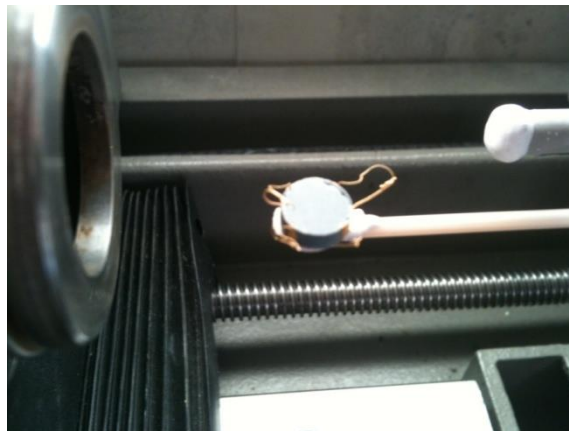


Figure 3: Sample in place on the arm.

- 7- Contacts should be arranged accordingly to the chosen conductivity measurement technique; i.e. current input points and voltage measurement points.
- 8- Leave the arm to stabilise for few minutes. Make any necessary adjustments to the counter weight on the other side; if the instrument shows an “out of range” sample weight reading.

- 9- The sample weight should read between 50-100mg on the instrument display.
Note: This weight does not represent the actual weight of the sample.
- 10- Make sure the function generator is supplying an adequate reading for the reference weight; typically between 0.1-1.5mg. Check by pressing the scroll button on the instrument panel.
- 11- Make sure the pO₂ sensor and its adjacent thermocouple are not touching the sample arm.
- 12- Close the meter housing lid using the screws. Make sure not to apply high pressure at the beginning until all edges are aligned properly.
- 13- Close the furnace by pressing the furnace button on the panel. Make sure to press the button again as soon as the furnace is pressed against the O-ring on the meter housing. **Warning:** Don't leave the furnace pushing in for long time since it won't stop automatically and it might burn the motor.
- 14- Make sure the heating button is switched on.
- 15- Start purging the chosen gas. **Do not** exceed 30ml/min as this might disrupt the weight. There are two flow meters at the inlet and exhaust of the furnace. Matching the two in terms of flow rate ensures there is a good seal.
- 16- Make sure the software key (dongle) is attached between the computer and the SDT2960.
- 17- Start the Thermal Advantage software. Make the necessary changes and make sure to click on the apply button after all changes/inputs.

- 18- Start the logTGA software. Choose a file name and folder. Make sure the triggers are reset; to avoid early termination. Choose the measurement type and input the different parameters. Make sure to press enter after changing the different settings; **except** for the 'notes' box where clicking away is sufficient.
- 19- Click on the start button on the Thermal Advantage software to start heating the furnace.
- 20- Once at an isotherm, allow time for the weight to show a stable signal; i.e. flat line.
- 21- Make any desired changes to the purge gas by changing the connections between the different gas supplies. Depending on the sample, the time to see any changes can vary.
- 22- After finishing a run; make sure to stop purging the furnace, check all connections, and check that both software programmes have stopped.
- 23- Open the furnace and carefully remove the sample for the next user.
- 24- Turn off all instruments from the mains after use.

Note: Data should be interpreted carefully with this setup. Since the SDT2960 has no correction mechanism; taking note of points when any changes to the experiment take place is essential. Also, minimising noise and vibrations when the furnace is at an isotherm is important to pinpoint any weight changes that resulted from chemical changes of the sample.

Software

1- TA Instruments-Thermal Advantage:

This software controls the operation of the furnace and records the weight signal coming from the sample arm. A screen capture of the main window of the software is shown in figure 4, below.

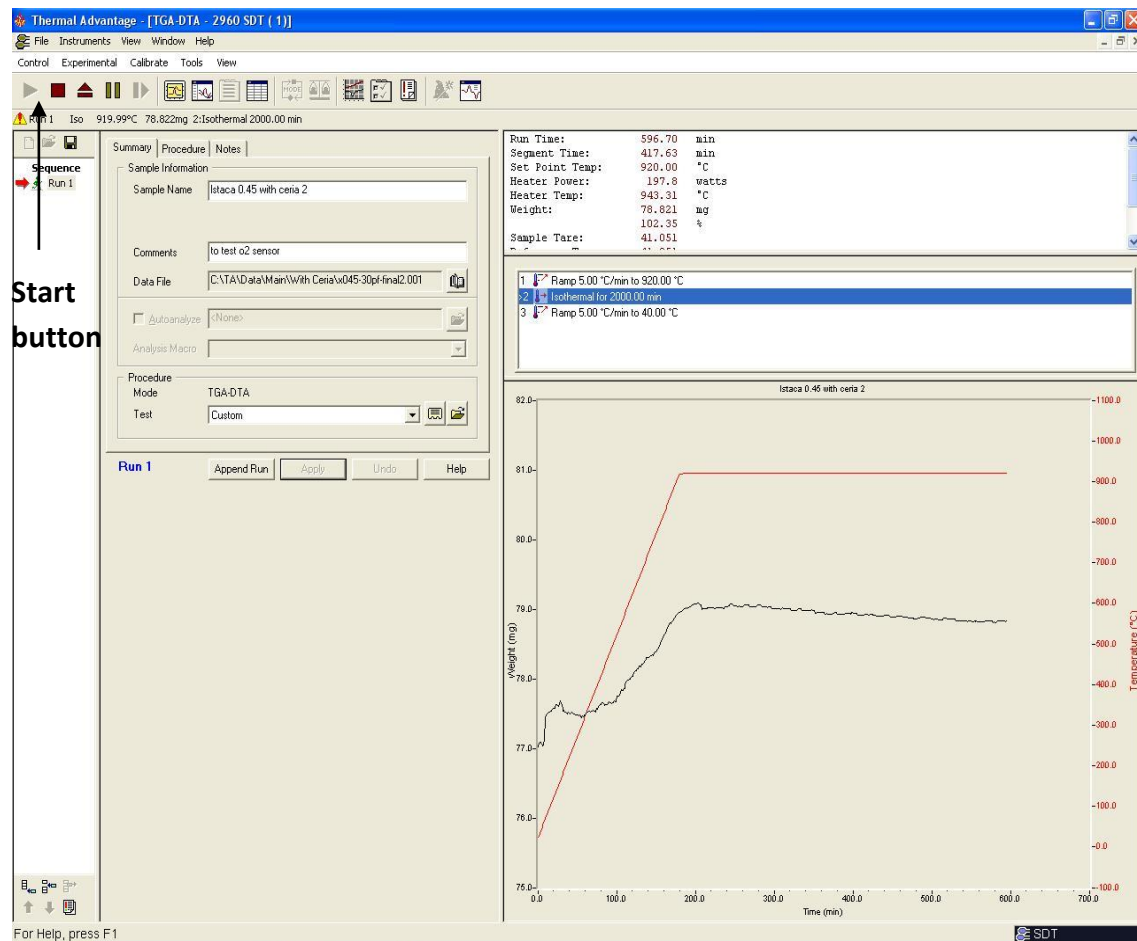


Figure 4: Screen capture of the TA Instruments Thermal Analysis software.

There are three tabs within the main screen. The first is the summary tab where the user can input the sample name, comments, file name and location. The second tab is the procedure tab where a furnace program can be designed. The last tab is an extra information input screen. It is necessary before starting any run to apply all changes by clicking on the apply button before clicking on the start button at the top.

TGA data can be viewed using the supplied analysis software by TA Instruments. Also, data can be exported into different formats to be used in other processing software along with the conductivity data.

2- LabView-logTGA:

The second software to control the new jig is the one shown in figure 5. This is mainly used to log all the different signals concerned with measuring the DC conductivity of a sample.



Figure 5: Screen capture of the LabView-logTGA interface.

Starting from the top left corner, the first input box is for the thickness or the correction factor of the sample under study. In the case of using the Van der Pauw technique, the user inputs the thickness of the sample in cm. On the other hand, if using the conventional 4-point DC conductivity setup, the user simply inserts the correction factor in this box.

Next, there is a button where the user can switch between the VdP or 4-point techniques. Then, the notes box is for the user to insert notes into the data files. The ref

pO₂ box is set to input the oxygen partial pressure inside the sensor; i.e. the pO₂ maintained in the tube by the oxygen buffer. On the top right corner is the stop button, which terminates the software along with the sourcemeter supplying the current to the sample.

The last line of input boxes contains a logging speed trigger which controls how often the software logs a data point in seconds. The green light gives an indication if there is a good contact with the sample. Finally, the cut off settings which force the software to stop after certain number of hours and minutes, or below a certain temperature. The software has three real-time plots that show the conductivity, log pO₂ and the pO₂ sensor temperature respectively.

All data are stored into a text file in a tabulated form which can be easily extracted into any processing software. **ALWAYS** press the stop button on the screen to terminate a run.